Imperial College

London

Experimental Evaluation of Steady and Pulsating Flow Performance of an Asymmetric Double Entry Turbine for an Automotive Turbocharger

By

Balamurugan Annamalai Gurunathan

This thesis is submitted for the award of Doctor of Philosophy (Ph.D.)

Department of Mechanical Engineering

Imperial College London

DECLARATION

This thesis represents my account of the work that I have undertaken over the course of the registration period for this degree. Relevant citations have been included to acknowledge the contribution of others. Parts of the work that has been published in conference proceedings have also been clearly mentioned.



_____

Balamurugan Annamalai Gurunathan

COPYRIGHT DECLARATION

The copyright of this thesis rests with the author and is made available under a Creative Commons Attribution Non-Commercial No Derivatives licence. Researchers are free to copy, distribute or transmit the thesis on the condition that they attribute it, that they do not use it for commercial purposes and that they do not alter, transform or build upon it. For any reuse or redistribution, researchers must make clear to others the licence terms of this work.

ACKNOWLEDGEMENT

My special thanks to my supervisor Professor Ricardo Martinez-Botas who has been constantly providing the support, guidance, advice and encouragement all the way through despite his busy schedule. I would also like to thank Associate Professor Srithar Rajoo for the helpful discussions and ideas especially during the initial stage of the project. Special thanks to Masa Sakai for allowing the use of the asymmetric double entry turbine for this research.

My gratitude is also extended to Universiti Pertahanan Nasional Malaysia (UPNM) and Ministry of Higher Education Malaysia (MoHE) for funding of my studies at Imperial College London.

I would like to thank Dr. Owan Saiful for all the help when I first arrived and interesting discussions that continued along the way. I am grateful to have been surrounded by helpful methodological advisors and support from Dr. Yang MingYang and Dr. Peter Newton, for their continuous support in understanding the rig and instruments. Forever amazed by mechanical specialist Harminder Flora and Anthony Willis, who were instrumental in the experimental aspect of this work. Sincere thanks to Asanka Munasinghe who has been instrumental in setting up the turbocharger test facility and Tariq Rasheed for his assistance in software installations.

I would also like to express deep appreciation to Uswah Khairuddin for her generous time and effort in CFD understanding at the initial part of this work. My thanks are extended to Jose Cortell, Mohd Izzal Ismail, Maria Barrera-Medrano and Allen Cao for their support during the running of the test rig.

To my great spiritual guru and mentor, Shri Brahmathmananda Guruji for his blessings and guidance that has made me the person I am today, I thank him with a humble heart. I wish to thank my wife Subashni for her endless love, patience and support throughout my duration in London and all these years. My children, Tharani and Ekalayen who motivated and gave me the strength to pursue my studies while bringing lots of joy to our stay here in London.

My humble gratitude and love to both my parents, my father Annamalai Gurunathan and my late mother Mallika, who have always supported everything I do. Thanking my siblings, Gangadevi, Usha Rani and Gunaseelon for always being there when I needed them.

This thesis is dedicated to my parents, wife and children.

ABSTRACT

Variable Geometry Turbines are widely used in High Pressure Loop Exhaust Gas Recirculation to enhance positive pressure gradient between turbine inlet and compressor outlet. Multiple-entry turbines (twin or double) can achieve an enhanced pulse energy extraction when compared with single entry devices. However, when EGR takes place, an imbalance of mass flow can lead to significant energy loss. This thesis presents the design and experimental assessment of a novel asymmetric double entry turbine that aims to achieve pulse energy recovery even in the face of high EGR. The asymmetric double entry volute was developed with two different scroll lengths: a small scroll that feeds the rotor between azimuth angle of 0° and 160°, beyond which rotor is fed by the large scroll. A pivoting action is designed to enable an optimisation of the optimum angle in each scroll sector. Extensive testing was carried out to characterise the novel turbine under various steady and unsteady flow conditions (full, partial, unequal, in phase and out of phase).

The peak recorded efficiency for the full admission nozzleless condition was found to be 78%. When nozzle was present in the small scroll, the efficiency had a similar magnitude (77.6%); while when nozzles were present in both scrolls a lower efficiency was found (74.4%). Considering nozzles only on the small sector: as the vane angle opening changes from most open position (51°) to mid open position (71°) an increase in stage efficiency was observed. Under partial admission, the nozzleless unit showed a very significant the deficit in peak efficiency: 17 points with large scroll flowing and 25 points with small scroll flowing. When nozzle vanes are introduced in the small scroll sector a similar drop was found; but when vanes were present in both scrolls the deficit during partial reduced (13.9% for the best performing configuration). During unequal admission the nozzleless and small nozzle setting displayed a symmetrical efficiency characteristic.

During unsteady flow admission at 30k RPM for all frequencies showed that the nozzle configurations recorded higher cycle average efficiency than the base line nozzleless unit. Test results at 20 Hz and 40 Hz have shown higher cycle average efficiency than 60 Hz. Interestingly when nozzles were present on both scrolls the cycle average efficiency increased by almost 13 percentage point higher than nozzleless indicating the value of introducing nozzles.

TABLE OF CONTENTS

CHAPTER	TITLE	PAGE
	DECLARATION	**2**
	COPY RIGHT DECLARATION	**3**
	ACKNOWLEDGEMENTS	**4**
	DEDICATION	**6**
	ABSTRACT	**7**
	TABLE OF CONTENTS	**8**
	LIST OF FIGURES	**13**
	LIST OF TABLES	**22**
	NOMENCLATURE	**24**
1	**INTRODUCTION**	**30**
	1.1 Engine Downsizing and Turbocharging	30
	1.2 Turbocharging Principles and History	31
	1.3 Exhaust Gas Recirculation	35
	1.4 Research Motivation	38
	1.5 Thesis Objectives	43
	1.6 Thesis Outline	44

Chapter 1: Introduction 44

Chapter 2: Literature Review 44

Chapter 3: Asymmetric Double Entry Turbine Design 44

Chapter 4: Experimental Setup and Procedures 44

Chapter 5: Steady Flow Experiment 45

Chapter 6: Unsteady Flow Experiment 45

Chapter 7: Conclusion and Future Work 45

2 LITERATURE REVIEW 46

2.1 Mixed Flow Rotor research 46

2.2 Variable Geometry Turbine research 49

2.3 Double entry research 60

2.4 Pulsating flow testing in radial turbine 70

2.5 Pulsating flow simulation in radial turbine 75

2.6 Summary 80

3 ASYMMETRIC DOUBLE ENTRY TURBINE DESIGN 83

3.1 Asymmetric Volute Design 83

3.1.1 Optimum circumferential division 84

3.1.2 Volute cross sectional area (A/R) 88

3.1.3 Volute 3D geometry and dimension 93

3.2 Nozzle Vane Design 97

3.2.1 Vane Aerofoil and Conformal Transformation 98

3.2.2 Number of nozzle vanes 100

3.3 Nozzle vane ring mechanism 100

3.4 Summary 111

4 EXPERIMENTAL SETUP AND PROCEDURES 112

4.1 Test Facility 112

4.1.1 Cold flow equivalent condition and air supply 112

4.1.2 Test-rig layout 113

4.1.3 Rig Control and safety 118

4.1.4 Instrumentation, data acquisition and monitoring hardware 119

4.2 Steady flow measurement 120

4.2.1 Pressure 120

4.2.2 Temperature 121

4.2.3 Mass flow 122

4.2.4 Rotor Speed 124

4.2.5 Torque 124

4.3 Unsteady flow measurement 125

4.3.1 Pressure 125

4.3.2 Temperature 125

4.3.3 Mass flow 126

4.3.4 Rotor speed 129

4.3.5 Torque 129

4.3.6 Polar Moment of Inertia 130

4.4 Performance Parameter 130

4.4.1 Steady flow 130

4.4.2 Unsteady flow 136

4.5 Uncertainty 139

5 STEADY FLOW EXPERIMENT 142

5.1 Full Admission characteristic 144

5.1.1 Nozzleless 144

5.1.2 Nozzle Vanes in small scroll 146

5.1.3 Nozzle Vanes in both scrolls 156

5.2 Partial Admission characteristics 163

5.2.1 Nozzleless 163

5.2.2 Nozzle Vanes in small scroll 169

5.2.3 Nozzle Vanes in both scrolls 175

5.3 Unequal Admission characteristics 181

5.3.1 Nozzleless 182

5.3.2 Nozzle Vanes in small scroll 184

5.3.3 Nozzle Vanes in both scrolls 187

5.4 Summary 188

6 UNSTEADY FLOW EXPERIMENT 190

6.1 Nozzleless 190

6.2 Nozzle Vanes in small scroll 200

6.3 Cycle Average Parameters 219

6.4 Summary 221

7 CONCLUSIONS 222

7.1 Conclusion 222

7.1.1 Asymmetric double entry turbine design 222

7.1.2 Steady flow experiment 223

7.1.3 Unsteady flow experiment 223

7.2 Future Work 224

7.2.1 Computational model 224

7.2.2 Active Control Turbocharger 225

7.2.3 Exhaust Gas Recovery 226

8 REFERENCES 227

LIST OF FIGURES

1.1	Example of a turbocharger for a spark ignition engine *(extract from Japikse and Baines[5])*	33
1.2	Components of the typical turbocharger *(extract from Kusztelan et al [6])*	33
1.3	Schematic of an engine turbocharging system *(extract from Rajoo [7])*	34
1.4	Turbine enthalpy-entropy diagram *(extract from Moustapha. H. et al [8])*	34
1.5	Turbine expansion velocity triangle *(extract from Moustapha. H. et al [8])*	34
1.6	Low Pressure EGR schematics *(extract from Wei et al [14])*	36
1.7	High Pressure EGR schematics *(extract from Wei et al [14])*	37
1.8	Exhaust pulse timing for 3 cylinder of an ICE *(extract from Watson and Janota [11])*	38
1.9	Exhaust pulse timing for 4 cylinder of an ICE *(extract from Watson and Janota [11])*	38
1.10	Double entry turbine cross section	39
1.11	Twin entry turbine cross section	39
1.12	Exhaust pulse timing for 6 cylinder of an ICE *(extract from Watson and Janota [11])*	39
1.13	Compressor and turbine cross section	40
1.14	Velocity triangle	41
1.15	Flow separation due to inlet flow angle and Coriolis force *(extract from Rajoo [7])*	41
1.16	HPL EGR layout in 6 cylinder engine coupled to double entry turbine *(extract from Muller et al [16])*	42
1.17	P – V diagram	43
2.1	Two distinct types of turbine rotor *(extract from Newton [18])*	46
2.2	Meridional view of a radial and a mixed flow turbine rotor *(extract from Rajoo [7])*	47

2.3 Mass flow improvement of mixed flow turbine at various pressure ratios *(extract from Wallace and Pasha [20])* 48

2.4 Engine performance improvements with VGT *(extract from Watson and Janota [11])* 51

2.5 Effect of variable area control on BMEP *(extract from Flaxington and Szezupak [29])* 51

2.6 VGT superiority in engine transient response *(extract from Walsham [30])* 52

2.7 Engine torque and NOx emission under limiting torque *(extract from Hawley et al [31])* 52

2.8 Straight nozzle vane used for (a) a radial turbine and (b) a mixed flow turbine *(extract from Rajoo [7])* 56

2.9 Possible options of nozzle vanes for a mixed-flow turbine (a) vane with inclined hub/shroud surface (b) vane with flat hub/shroud surface *(extract from Rajoo [7])* 56

2.10 Lean nozzle vane with pivoting disc and shaft *(extract from Rajoo and Martinez-Botas [43])* 58

2.11 Dimensional matching between lean nozzle vane and rotor leading edge *(extract from Rajoo [7])* 58

2.12 Lean nozzle vane dimensions *(extract from Rajoo [7])* 59

2.13 Efficiency improvement of a VGT with lean nozzle vane *(extract from Rajoo and Martinez-Botas [43])* 59

2.14 Efficiency comparison between lean and staright nozzle vane *(extract from Rajoo and Martinez-Botas [43])* 60

2.15 Three different admission conditions 61

2.16 Comparison between experimental and calculated mass flow characteristic of a double entry turbine under different unequal admission condition *(extract from Wallace, Cave and Miles [48])* 62

2.17 Comparison between experimental and calculated torque characteristic of a double entry turbine under different unequal admission condition *(extract from Wallace, Cave and Miles [48])* 63

2.18 Isentropic flow area comparison between double (Do) and twin (Zw) entry turbine for different ratio of pressure *(extract from Pischinger and Wunsche [49])* 64

2.19 Efficiency comparison between double (Do) and twin (Zw) entry turbine *(extract from Pischinger and Wunsche [49])* 65

2.20 180° circumferential nozzle passage in single entry turbine blocked off to simulate double entry turbine under partial admission condition *(extract from Mizumachi, Yoshiki and Endoh [50])* 66

2.21 Influence of velocity ratio on the circumferential pressure distribution around a rotor with half of the nozzles passage blocked to simulate double entry turbine under partial admission condition *(extract from Mizumachi, Yoshiki and Endoh [50])* 66

2.22 Mass flow characteristic of a single entry turbine with half of the nozzles passage blocked to simulate double entry turbine under partial admission condition *(extract from Mizumachi, Yoshiki and Endoh [50])* 67

2.23 Novel 3 dimensional performance plot of a double entry turbine *(extract from Copeland et al [51])* 68

2.24 Effect of pulse frequency on the unsteady and quasi-steady cycle averaged efficiency of a double entry turbine under pulsating flow condition *(extract from Copeland et al [52])* 69

2.25 Instantaneous mass flow characteristic under in phase pulsating condition *(extract from Dale and Watson [57])* 71

2.26 Instantaneous efficiency characteristic under in phase pulsating condition *(extract from Dale and Watson [57])* 72

2.27 Instantaneous mass flow characteristics for various nozzle vane angles *(extract from Rajoo and Martinez-Botas [45])* 74

2.28 Computational domain modelled by Hellstrom *[69]* 77

2.29 Computational Stream line plot in double entry turbine *(extract from Copeland et al [70])* 78

2.30 Computational entropy rise comparison between equal and partial admission condition in a double entry turbine *(extract from Copeland et al [70])* 78

2.31 Computational instantaneous efficiency vs. incidence angle in a single entry turbine *(extract from Padzillah et al [71])* 79

2.32 Rotor blade passage domain dissected in theblade-to-blade orientation; Suction Side (SS), Pressure Side (PS) *(extract from Newton [18])* 80

2.33 Rotor passage and volute domain dissected in the meridional view *(extract from Newton [18])* 80

3.1 Mean line model sub-station in asymmetric double entry turbine 85

3.2	Mixed Flow Rotor ‘A’ *(extract from Rajoo [7])*	86
3.3	Velocity triangle at inlet and outlet of the blade	87
3.4	Mean line model predicted *(extract from Sakai et al [17])*	88
3.5	Turbine Volute’s Radius And Velocities *(extract from Rajoo [7])*	89
3.6	Asymmetric Double Entry Turbine cross section	90
3.7	A/r : Asymmetric double entry turbine vs. single entry turbine *(extract from Sakai et al [17])*	92
3.8	Typical volute cross sectional shapes *(extract form Rajoo [7])*	93
3.9	Velocity distribution in the single entry turbine *(extract from Padzillah [74])*	94
3.10	Volute inlet to volute tongue cross sectional change *(extract form Rajoo [7])*	94
3.11	Coupling of Volute to Test-rig with important dimensions *(extract form Rajoo [7])*	95
3.12	Volute geometry	96
3.13	3D solid model of the asymmetric double entry volute	97
3.14	A/r : Mean line calculation vs CAD solid modeling	97
3.15	NACA airfoil profile *(extract from Abbott et al [75])*	98
3.16	NACA 0015 airfoil profile *(extract from Abbott et al [75])*	99
3.17	Nozzle vane terminologies, conformal mapping and rotor inlet velocity triangle *(extract from Rajoo [7])*	99
3.18	Actual shape of polar coordinated nozzle vane	99
3.19	3D solid model of the nozzle vane pivoting mechanism	102
3.20	(a) 3D Isometric view (b) Machined component assembled to Asymmetric double entry turbine	102
3.21	Concept 1	104
3.22	Concept 2	104
3.23	Final (a) small scroll ring (b) large scroll ring	105

3.24	3D solid model of the dual ring Nozzle vane control – Isometric view 1	105
3.25	3D solid model of the dual ring Nozzle vane control – Isometric view 2	106
3.26	3D solid model of the dual ring Nozzle vane control – Exploded view	106
3.27	S51_L91 setting (a) front view (b) back view	108
3.28	S91_L51 setting (a) front view (b) back view	109
3.29	Final machined component assembled to Asymmetric double entry turbine	110
3.30	Asymmetric double entry turbine coupled to the dynamometer	110
4.1	Cold flow turbocharger test rig schematic *(extract from Wan Salim [76])*	115
4.2	Front view of rotating chopper plate (a) In phase flow (b) Out-off phase flow	116
4.3	Chopper plate opening area versus phase angle	116
4.4	Magnetic rotor and stator plate assembly *(extract from Syzmko [58])*	117
4.5	Eddy current dynamometer cross section extract from *(extract from Syzmko [58])*	118
4.6	V-cone flow meter cross section *(extract from McCrometer Inc.[78])*	123
4.7	Rotor speed vs. Voltage	124
4.8	Traversing mechanisms: 2 axis and 36 points hotwire measurement in flow duct *(extract from Rajoo [7])*	127
5.1	Total to static efficiency plot for Nozzleless configuration	145
5.2	Overall swallowing capacity plot for Nozzleless configuration	145
5.3	Total to static efficiency plot for various S nozzle configuration	147
5.4	Trend showing variation in peak efficiency as S nozzle vane closes for different turbine speeds	147
5.5	Overall turbine swallowing capacity plot for various S nozzle configuration	150
5.6	Total to static efficiency plot comparison between S nozzle and nozzleless configuration	155

5.7	Overall turbine swallowing capacity plot comparison between S nozzle and nozzleless configuration	156
5.8	Total to static efficiency plot for various SL nozzle configuration	158
5.9	Overall turbine swallowing capacity plot for various SL nozzle vane opening	159
5.10	Total to static efficiency plot comparison between SL nozzle and nozzleless configuration at 30k RPM	160
5.11	Overall turbine swallowing capacity plot comparison between SL nozzle and nozzleless configuration at 30k RPM	161
5.12	Total to static efficiency plot for various nozzle vane configuration under full admission condition at 30k RPM	165
5.13	Overall turbine swallowing capacity plot various nozzle vane configuration under full admission condition at 30k RPM	166
5.14	Total to static efficiency plot comparison between full and partial admission condition for nozzleless configuration	166
5.15	Total to static efficiency plot comparison between full and partial admission condition at 30k RPM for nozzleless configuration	167
5.16	Nozzleless configuration	168
5.17	Overall turbine swallowing capacity plot comparison between full and partial admission condition for nozzleless configuration	169
5.18	Total to static efficiency plot comparison between full and partial admission condition for two S nozzle configuration	170
5.19	Total to static efficiency plot comparison between full and partial admission condition at 30k RPM for S51 configuration	170
5.20	a) S nozzle configuration (b) S66 detail view B	173
5.21	Partial Admission Perfomance comparison map between S nozzle and nozzleless configuration when small scroll is flowing at 30k RPM	174
5.22	Partial Admission Perfomance map comparison between S nozzle and nozzleless configuration when large scroll is flowing at 48k RPM	175
5.23	Total to static efficiency plot comparison between full and partial admission condition at 30k RPM for S66_L66 configuration	176

5.24	Comparison Between Full And Partial Admission Efficiency Of Symmetric Double Entry Turbine At 30k RPM *(extract from Newton [18])*	177
5.25	Total to static efficiency plot comparison between nozzleless and SL nozzle configuration with small scroll flowing at 30k RPM	178
5.26	Partial Admission Perfomance map for various nozzle vane configuration with small scroll flowing at 30 k RPM	178
5.27	(a) SL nozzle configuration (b) S66_L66 detail view B (c) S66_L51 detail view B	179
5.28	Total to static efficiency plot comparison between nozzleless and SL nozzle configuration with large scroll flowing at 30k RPM	181
5.29	Partial Admission Perfomance map for various nozzle vane configuration with large scroll flowing at 30 k RPM	181
5.30	Normalised efficiency	182
5.31	Unequal Admission normalized efficiency for nozzleless configuration	184
5.32	Unequal Admission normalized efficiency for S nozzle configuration at 30k RPM	186
5.33	Comparison between nozzleless and S nozzle configuration at 30k RPM	186
5.34	Unequal Admission normalized efficiency for S nozzle configuration at 42k RPM	187
5.35	Unequal Admission normalized efficiency for SL nozzle configuration at 30k RPM	188
5.36	Unequal Admission normalized efficiency for various nozzle vane configuration at 30k RPM	188
6.1	In-Phase Small Scroll Instantaneous Swallowing Capacity for nozzleless configuration	192
6.2	In-Phase Large Scroll Instantaneous Swallowing Capacity for nozzleless configuration	194
6.3	Out of phase Small Scroll Instantaneous Swallowing Capacity for nozzleless configuration	196
6.4	Out of phase Large Scroll Instantaneous Swallowing Capacity for nozzleless configuration	197

6.5	Small Scroll Instantaneous Isentropic Power for nozzleless configuration	198
6.6	Large Scroll Instantaneous Isentropic Power for nozzleless configuration	199
6.7	In Phase Instantaneous Actual power for nozzleless configuration	200
6.8	Out of Phase Instantaneous Actual power for nozzleless configuration	200
6.9	In-Phase Small Scroll Instantaneous Swallowing Capacity for S51 configuration	202
6.10	In-Phase Large Scroll Instantaneous Swallowing Capacity for S51 configuration	203
6.11	Out of phase Small Scroll Instantaneous Swallowing Capacity for S51 configuration	204
6.12	Out of phase Large Scroll Instantaneous Swallowing Capacity for S51 configuration	207
6.13	In-Phase Small Scroll Instantaneous Swallowing Capacity for S66 configuration	208
6.14	In-Phase Large Scroll Instantaneous Swallowing Capacity for S66 configuration	209
6.15	Out of Phase Small Scroll Instantaneous Swallowing Capacity for S66 configuration	210
6.16	Out of Phase Large Scroll Instantaneous Swallowing Capacity for S66 configuration	211
6.17	In-Phase Small Scroll Instantaneous Swallowing Capacity for S71 configuration	213
6.18	In-Phase Large Scroll Instantaneous Swallowing Capacity for S71 configuration	214
6.19	Out of Phase Small Scroll Instantaneous Swallowing Capacity for S71 configuration	215
6.20	Out of Phase Large Scroll Instantaneous Swallowing Capacity for S71 configuration	216
6.21	Instantaneous Swallowing Capacity for various S nozzle nozzleless configuration at 60Hz	217

6.22 In-Phase Instantaneous Swallowing Capacity for S66 nozzle configuration 218

LIST OF TABLES

3.1	Mean line model stations	84
3.2	Losses according to station	85
3.3	Rotor ‘A’ Geometrical Dimension	86
3.4	Volute final dimensions	96
4.1	Equivalent cold flow test condition	113
4.2	Parameters and respective safety limits	119
4.3	Turbocharger test-rig instrumentation	120
4.4	CTA platinum plated tungsten wire probe technical data	126
4.5	Steady State Parameters	131
4.6	Constants of specific heat	132
4.7	Uncertainty in measurement	141
5.1	Steady flow experiment configuration	144
5.2	List of peak efficiency and corresponding velocity ratios for S nozzle configuration	148
5.3	List of swallowing capacity and pressure ratio corresponding to peak efficiency of S nozzle configuration	151
5.4	List of peak efficiency and corresponding velocity ratios for SL nozzle configuration	159
5.5	List of swallowing capacity and pressure ratio corresponding to peak efficiency of SL nozzle configuration	160
5.6	Drop in partial admission efficiency relative to full admission for nozzleless configuration	168
5.7	Drop in partial admission efficiency relative to full admission for S nozzle configuration	171
5.8	Drop in partial admission efficiency relative to full admission for SL nozzle configuration	177
6.1	Cycle Average properties at 20Hz In Phase	219
6.2	Cycle Average properties at 40Hz In Phase	219

6.3 Cycle Average properties at 60Hz In Phase 220

6.4 Cycle Average properties at 40Hz Out of Phase 221

6.5 Cycle Average properties at 60Hz Out of Phase 221

NOMENCLATURE

Roman Characters

A	area hotwire calibration constant	m^2
a	acoustic velocity	ms^{-1}
A.C.T.	Active Control Turbocharger	
ASME	American Society of Mechanical Engineers	
b_{nv}	radial chord length	m
b	rotor inlet width	m
B	hotwire calibration constant	
BDC	Bottom Dead Centre	
C	absolute flow velocity	ms^{-1}
c_{nv}	chord length	m
CAD	Computer Aided Design	
CFD	Computational Fluid Dynamics	
CO_2	Carbon Dioxide	
c_p	Specific heat of air	$J/kg.K$
CTA	Constant Temperature Anemometer	
D	rotor's diameter	m
E	CTA voltage	$Volts$
EGR	Exhaust Gas Recirculation	
FGT	Fixed Geometry Turbine	
f, *freq*	frequency	Hz

h	enthalpy	J
I	polar moment of inertia	kgm^2
iEGR	Ideal Exhaust Gas Recirculation	
K	constant	
k	Thermal conductivity of air	$W/(m.K)$
L	characteristics length large scroll	m
LDV	Laser Doppler Velocimetry	
LE	leading edge	
m	temperature loading factor (hotwire correction)	
$\dot{m}$	mass flow rate	$kg\ s^{-1}$
Ma	Mach number	
MFP	mass flow parameter	$(kg\ s^{-1}.\sqrt{K}\ )/Pa$
MSt.	Modified Strouhal number	
n	number of samples hotwire calibration constant	
N	rotational speed	*RPM, rpm or* *RPS, rps*
NOx	Nitrogen oxide	
o_{nv}	throat width	m
P	pressure	Nm^{-2} *or* Pa
PID	Proportional Integral Derivative controller	
PMSt.	Pressure modified Strouhal number	
PR	pressure ratio	

Pr	Prandtl Number	
ps	Pressure surface	
r	recovery factor radius	 *m*
R	Gas constant of air	*J/(kg.K)*
Re	Reynolds Number	
RPM, rpm	revolutions per minute	
RPR	Ratio of pressure ratio	
RPS, rps	revolutions per second	
RSS	Root Sum Square (uncertainties analysis)	
s_{nv}	nozzle pitch	*m*
ss	suction surface	
S	small scroll Configuration with nozzle vanes in small scroll circumference	
SL	Configuration with nozzle vanes in small and large scroll circumference	
St.	Strouhal number	
t	values for instant in time	
T	temperature	*K*
TDC	Top Dead Center	
TE	trailing edge	
U	rotor's tip velocity	ms^{-1}
VGT	Variable Geometry Turbocharger	
VR	velocity ratio	

W	Relative flow velocity	*ms-1*
$\dot{W}$	power	*W(Watts)*
x	distance or length	*m*

Greek Characters

ϕ	pulse fraction rotor's camber angle	 *Deg*
θ	circumferential angle	*Deg*
α	angular acceleration absolute flow angle	$rad.s^{-2}$ *deg*
ω	angular speed circular frequency	$rad.s^{-1}$ $rad.s^{-1}$
ψ	azimuth angle	*Deg*
i	incidence angle	*Deg*
β	relative flow angle	*Deg*
β_b	inlet blade angle	*Deg*
λ	mixed-flow rotor's cone angle	*Deg*
η	efficiency	
ø	diameter	*M*
ωt	phase	*deg or rad*
ζ	tangential lift coefficient	
τ	torque	*Nm*
ρ	density	kgm^{-3}
μ	dynamic viscosity	$kg.m^{-1}s^{-1}$
υ	kinematic viscosity	m^2s^{-1}
γ	specific heat ratio	

Subscripts

0	Total condition	
1	volute inlet	
2	nozzle inlet / volute exit	
3	nozzle exit (upstream)	
4	interspace inlet / nozzle exit (downstream)	
5	rotor inlet / interspace exit	
6	rotor exit (upstream)	
7	rotor exit (downstream)	
act	actual condition	
ave	averaged value	
b	blade	
calib	calibrated	
cold	equivalent cold condition (cold flow test rig)	
cyc	cycle	
exp	experimental/measured value	
f	mean-film values (hotwire measurement) flow	
fluct	fluctuating components	
hot	actual hot condition	
inst	instantaneous condition components	
is	isentropic conditional components	
L	large scroll	
le	leading edge	
m	meridional directional components	
nv	nozzle vane components	
r	radial directional components	
S	small scroll	
s	static condition	
te	trailing edge	
t-s	total-to-static	
TI	Turbine Inlet (measurement plane)	

w	Wire wall	
θ	tangential component or circumferential direction	
ψ	Azimuth directional components	
$\psi=0$	volute's tongue location	
η	Efficiency	

CHAPTER 1

INTRODUCTION

1.1 Engine downsizing

Automotive manufacturers across the globe have been tasked to meet ever-growing stringent emission legislation, whilst not compromising engine power. This has resulted in vehicles with less CO_2 emission and correspondingly improved fuel economy in the last two decades. Average vehicle tailpipe CO_2 has decreased from 186gCO_2/km in 1995 to 136.6 gCO_2/km in 2011, a reduction of 26.6% [1]. Besides that, vehicle fuel consumption in recent years has recorded a reduction of more than thirty three percent of the total fuel consumption since the 1990s [2]. Hybrid and electric vehicle technology have made a small contribution to this decrease; the major contributor comes from improvements to the conventional internal combustion engine as it dominates the current automotive market. The current trend towards highly downsized engines can be considered the major trend in technology improvements in recent years and it is likely to remain as a major player in the future.

The key enabler for lower vehicles CO_2 emission is enhanced vehicle fuel economy. Improved fuel economy is accomplished when kinetic energy resulting from combustion process is converted to useful work without being lost; when energy is utilized efficiently. To date, the most effective method employed to reduce energy losses is engine downsizing, made possible with boosting technology. In engine downsizing, engine with larger capacity is replaced with that of a smaller one; this reduces number of cylinders. This results in net decrease in engine friction. Furthermore, as a consequent of fewer cylinders, net pumping loss is also reduced, especially at smaller throttle opening.

Engine downsizing necessitates high levels of boost and thus needs as a key enabling technology the use of advanced supercharging/turbocharging systems. It is therefore essential to continue to improve the efficiency of the turbocharger and associated air management systems in the diesel and gasoline powered engines. Owing to cost, engine package limitations and wider flow range, the nozzleless turbine has been the preferred candidate [3]. However, this trend has started to change and it is leading to the need to

introduce variability to achieve engine performance rage with the use of Variable Geometry Turbines (VGT). Martinez-Botas et al. [4] reported that two third of diesel engine powered turbocharger in Europe are fitted with VGT. The VGT systems thus need to cope with unsteady exhaust gas at different operating condition and in high Exhaust Gas Recirculation (EGR) modes. It is this thesis that trying to address this additional requirement with the introduction of an asymmetric double entry turbine with variable nozzle configuration. The research presented uses a mixed flow turbine that has been shown to enable better energy extraction from the pulse energy. Thus, two novel aspects are introduced: asymmetry in the double entry for better EGR extraction and a turbine more capable of achieving pulse energy extraction; this thesis is centered on achieving the former. The ability of EGR to bring down combustion chamber peak temperature, which subsequently reduces production of NOx and heat transfer losses, is the foremost motivation for its usage in asymmetric double entry turbine. Apart from that, having EGR extraction taking place in one scroll of the asymmetric double entry turbine, reduces pumping losses, that would otherwise have intensified if both scrolls of the symmetric turbine were connected to EGR loop.

VGT research in mixed flow turbine is relatively new and its fullest potential remains unexplored. Since as high as seventy five percent of gasoline engines in the current automotive market are still naturally aspirated [4], VGT fitted mixed flow turbine has a promising future in this segment of the market. According to Martinez-Botas et al. [4], additional hood space required by VGT fitted turbocharger is only 12% compared to a 10% requirement for Fixed Geometry Turbocharger (FGT), using naturally aspirated engine as the baseline. Due to these factors, VGT would continue to remain as major source of turbocharging to meet future engine demands. This in turn would make turbocharger to be relevant in the development of modern automotive engines.

1.2 Turbocharging Principles and History

A turbocharger facilitates an internal combustion engine to achieve more power density by forcing high density air into the engine. This higher density can be utilized to achieve higher output power or alternatively it can be used to achieve an engine size reduction while maintaining the desired level of power. In other words, for a given engine size, a turbocharger significantly increases power and torque compared to a naturally aspirated

engine with same displacement volume. It is possible to achieve a smaller and lighter engine that can produce the same power compared again with the naturally aspirated engine. A classic example of turbocharger and its components are shown in Figures 1.1 and 1.2 respectively.

Turbocharging working principles are best understood by referring to Figure 1.3. Highly pulsating flows from two different banks of cylinders, are channelled to the turbine inlets via two separate pipes. This arrangement allows flow in each pipe to enter each half of the turbine volute (housing) as shown in Figure 1.2. Due to swirling motion in the scroll, the flow arrives at the nozzle inlet with considerable level of kinetic energy, $\frac{1}{2}C_1^2$.This kinetic energy is being the difference between total and static enthalpies as shown in Figure 1.4. The kinetic energy in the flow is further increased to $\frac{1}{2}C_2^2$ through expansion in the nozzle passage. The rotor sees this flow in the rotating frame as W_2, as shown by velocity triangle in Figure 1.5. The corresponding relative kinetic energy is $\frac{1}{2}W_2^2$.The flow then accelerates through the rotor passage and exits the rotor with kinetic energy of $\frac{1}{2}W_3^2$. Both change in radius and the expansion of the flow through rotor passage provide the required shaft power to drive the compressor. In Figure 1.4, this work output is shown as the change in absolute total enthalpy across the stage. It should be noted that total enthalpy change across the nozzle passage is zero, as shaft work is not produced in the nozzle passage. Based on Figure 1.5, the absolute flow at rotor exit is given by C_3. It would be desirable to have the exit flow to be as close as possible in the axial direction, to avoid residual swirl. This is normally achieved with the aid of a diffuser. The work output minus the friction in the bearing is delivered to the compressor. Ambient air drawn through the inlet of the rotating compressor wheel, is pressurised prior to entering the intake port of the internal combustion engine. This results in increase in the density of the charged-air into the engine cylinders.

It is crucial that pressure of air charge entering the engine intake port is maintained higher than that of the exhaust flow leaving the exhaust port. In a VGT, the turbine inlet geometry can be varied to regulate the back pressure, to avoid negative pressure gradient. In contrary, owing to the fixed geometry of the FGT, maximum exhaust flow through the turbine

becomes restricted and this increases back pressure which leads to negative pressure gradient. One way to reduce the build-up in back pressure is by letting the excess exhaust to flow through a wastegate in a FGT. Unfortunately, this comes with a penalty. Inadequate exhaust flow requires finite time to overcome the rotating component inertia and deliver the power required to meet driver's demand. This is known as the turbo-lag phenomena. Fitting a smaller turbine, although might alleviate the turbo-lag problem, on the other hand will expose the rotor to over-speeding and intake manifold over-boosting. Therefore, correctly matched engine-turbocharger is essential not only to overcome the over boosting and turbo-lag problem, but it is also key in achieving higher engine power, by minimising pumping losses.

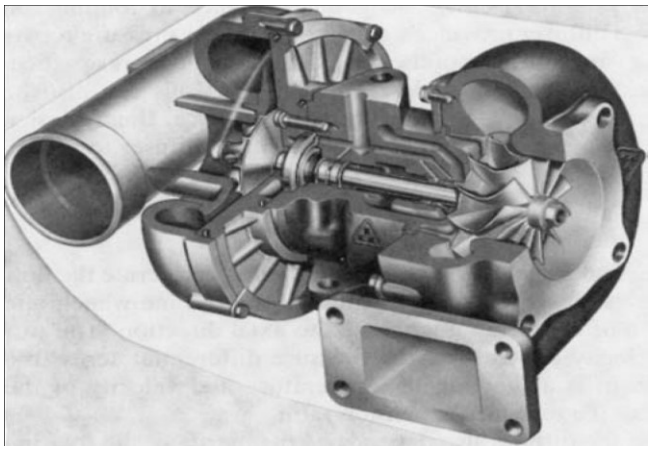


Figure 1.1 Example of a turbocharger for a spark ignition engine
(extract from Japikse and Baines [5])

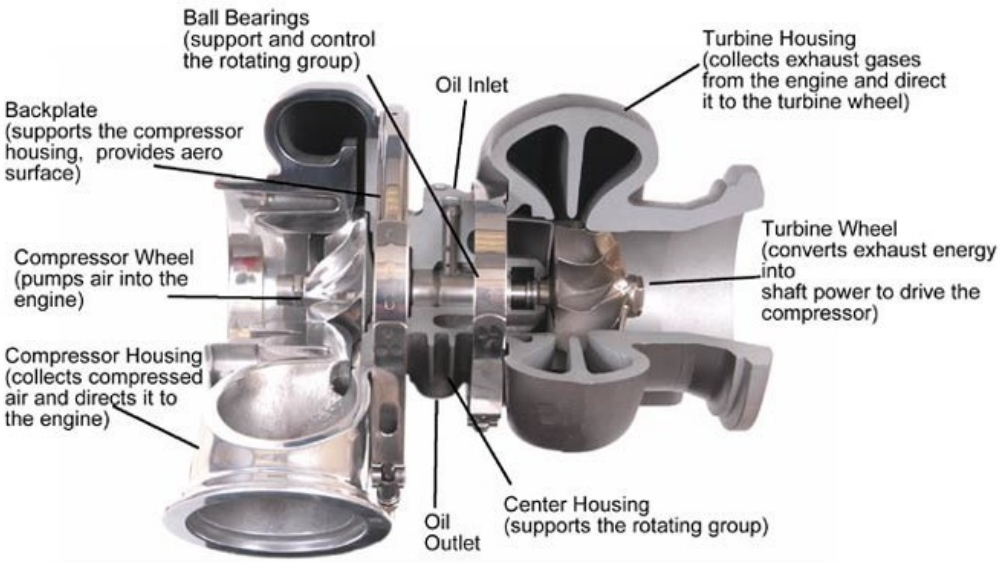


Figure 1.2 Components of the typical turbocharger *(extract from Kusztelan et al [6])*

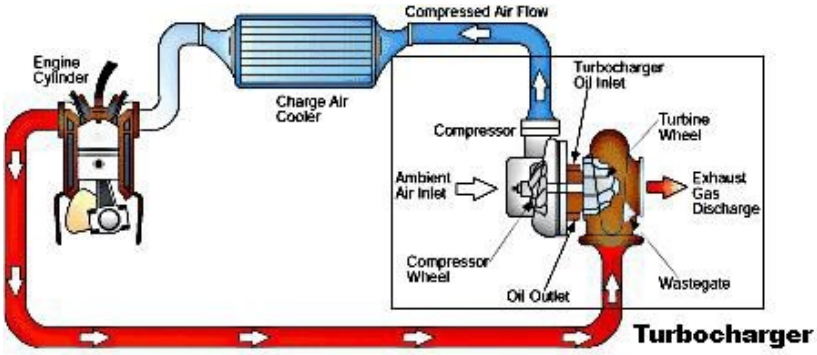


Figure 1.3 Schematic of an engine turbocharging system *(extract from Rajoo [7])*

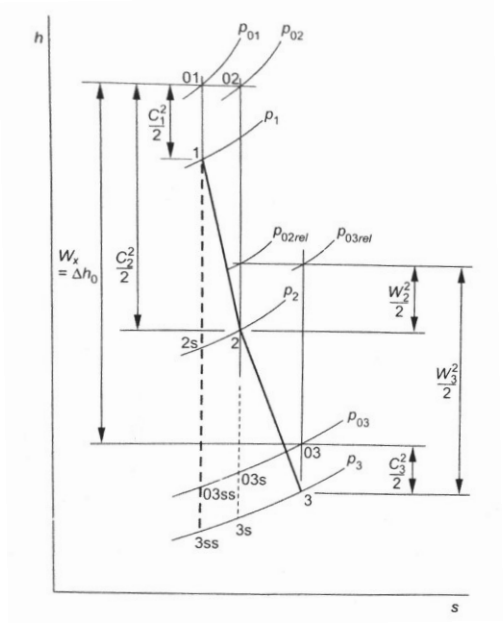


Figure 1.4 Turbine enthalpy-entropy diagram *(extract from Moustapha. H. et al [8])*

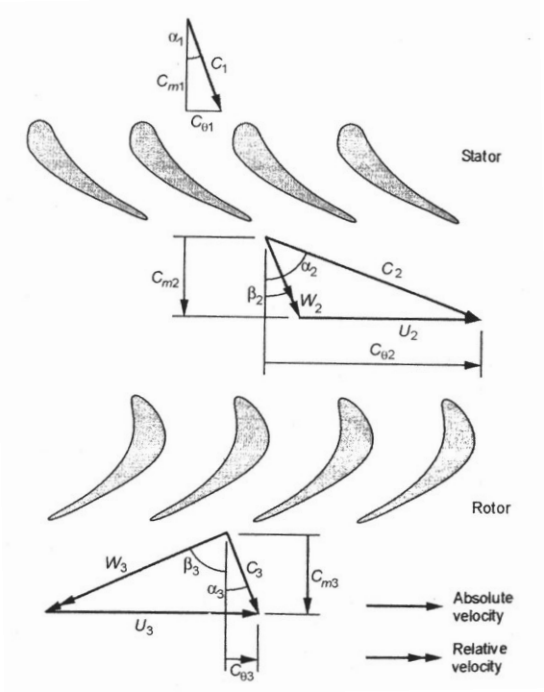


Figure 1.5 Turbine expansion velocity triangle *(extract from Moustapha. H. et al [8])*

Although the commercialization of large turbocharged ship engine started much earlier, mass production for land vehicles was only realized in 1938 when the first diesel truck engine fitted with turbocharger rolled out form Swiss Machine Works Saurer factory. After four decades since the first successful exhaust gas turbocharging, the Chevrolet Corvair Monza and Oldsmobile Jetfire became the first production passenger car to be fitted with turbocharger between 1962 and 1963. Owing to significant events of engine combustion knocking, as a result of very high compression ratio, these two models did not last very long. Oil crisis in 1973 has forced automobile manufacturers to adopt turbocharged engine for commercial diesel vehicle segment. Since the initial higher investment for a turbocharged diesel engine was compensated by the savings obtained from better fuel economy, turbocharged passenger car became the preferred choice by early 1980s. Stringent emission legislation requirement in Europe by end of 1980s the level of turbocharging in passenger vehicles. In the current European market, almost every diesel engine is turbocharged. From the 1990s, automotive producers started pay greater attention to turbocharging the gasoline engine passenger car market. These days, almost twenty five percent of gasoline engines in the automotive market are turbocharged [4], and this number is expected to grow as more research and development are underway to realize the full potential of turbocharger in gasoline engine application, [9, 10, 11].

1.3 Exhaust Gas Recirculation

Policy makers have further tightened emission standards in order to reduce NOx emissions. Permissible NOx level of 0.50 g/km under Euro 3, has been reduced to 0.08 g/km, under Euro 6 standards for diesel passenger vehicles [12,13]. For petrol operated passenger vehicles, the gradual transition from Euro 3 to Euro 6, has recorded drop of 60% requirement from 0.15 g/km [12,13]. Exhaust Gas Recirculation, EGR, is often used as a NOx mitigation strategy whereby exhaust gas is recirculated into intake manifold. This brings down oxygen concentration and combustion chamber peak temperature, which subsequently reduces the formation of NOx. Two different EGR scheme that can be incorporated into the exhaust and intake manifold are Low Pressure Loop (LPL) and High Pressure Loop (HPL) EGR ; the choice being influenced by after treatment of the recirculated soot, fouling of compressor and dead gas volume.

Figure 1.6 shows schematics of LPL EGR configuration. In this system, exhaust gases are taken downstream of the turbine and recirculated in the intake manifold before being channeled into the compressor together with fresh air. Since the pressure difference between the turbine outlet, (p_4) and the compressor inlet, (p_1) is low in this scheme, the EGR cooler and EGR valve need to have low pressure loss to ensure EGR flow. Also, since EGR cooler is located between turbine exhaust and compressor inlet, over cooling in EGR cooler could bring down temperature of the exhaust gas that leads to condensation. Any droplet caused by condensation has the potential to damage the compressor wheel. Apart from that, EGR cooler is exposed to substantial risk of being clogged due to soot particulate. This eventually leads to inefficient operation of EGR cooler and subsequently pose damaging threat to the compressor blades. Furthermore, dead gas volume created inside engine cylinder is large. All this demands an intricate system with gas and coolant temperature control capable of regulating the EGR cooler temperature, besides an advanced after treatment filter to minimise droplet impact on the compressor blades. Likewise, to prevent intake air overheat and reduce volumetric efficiency, high efficiency of EGR cooler is required. Unfortunately, with the current readily available technology, conventional compressors and inter-coolers are unable to cope with high temperature and fouling of exhaust gases, thus limiting the use of low pressure (LPL) EGR in the turbocharging application.

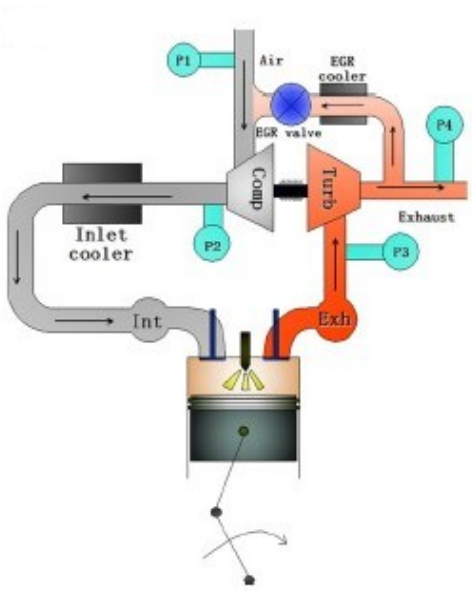


Figure 1.6 Low Pressure EGR schematics *(extract from Wei et al [14])*

In the high pressure (HPL) EGR scheme, exhaust gases emanating from engine are taken upstream of the turbine and channeled into the intake circuit downstream of the compressor (Figure 1.7). High Pressure Loop EGR depends entirely on the pressure difference between the turbine inlet, (p_3) and the compressor outlet, (p_2). The turbine pressure needs to be higher than boost pressure to ensure EGR flow. However, due to low speed and high load condition, negative pressure difference is generated between turbine inlet and compressor outlet. Thus, EGR flow needs to be assisted either by increasing turbine inlet pressure or reducing compressor outlet pressure. One way of achieving this is by installing a throttle valve in the downstream of the compressor or upstream of the turbine. Another way is by having a VGT. With the VGT, the turbine inlet is adjusted to allow a flow towards the compressor, without significantly effecting the turbine efficiency.

Since exhaust gas is routed directly to post inlet cooler, the route for exhaust gas is relatively shorter than LPL EGR. Owing to this reason, the compressor durability is very high as it is not subjected to any droplet impact due to condensation. Therefore, control strategy to regulate gas and coolant temperature in the EGR cooler can be of a simple feedback loop. Apart from that, dead gas volume created inside engine cylinder is minimized due to the short-route scheme between pre-turbine and post compressor. Thus, this simple scheme provides fast response to the engine, achieving high torque demand, especially at low speed engine speed operation. All these advantages outweigh the risk of soot deposition in the EGR cooler and makes the HPL EGR a widely adopted strategy in engine turbocharging system.

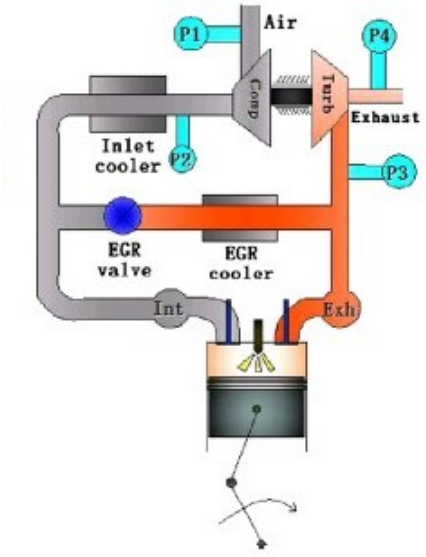


Figure 1.7 High Pressure EGR schematics *(extract from Wei et al [14])*

1.4 Research Motivation

The Internal Combustion Engine (ICE) produces pulsating exhaust gas with the opening and closing of the exhaust valves. To preserve the exhaust pulse and allow maximum energy extraction, proper mating between the ICE and turbocharger turbine is necessary. ICE with 3 cylinders produces pulses at 240° intervals. Very little overlap between exhaust gases occurs when these three cylinders are connected to a single entry turbine (Figure 1.8). On the other hand, when 4 or more cylinders of the ICE is connected to a single scroll turbine, there is significant overlap between exhaust pulses emanating from different cylinders before the turbine rotor (Figure 1.9). In such a single entry turbine, pulse separation between cylinder events cannot take place. This pulse interference creates unsteady mixing prior to the turbine rotor, which subsequently results in decrease in pulse energy extraction and increase in pumping losses. Thus, single entry turbines are unable to maximize pulsating exhaust gas energy recovery.

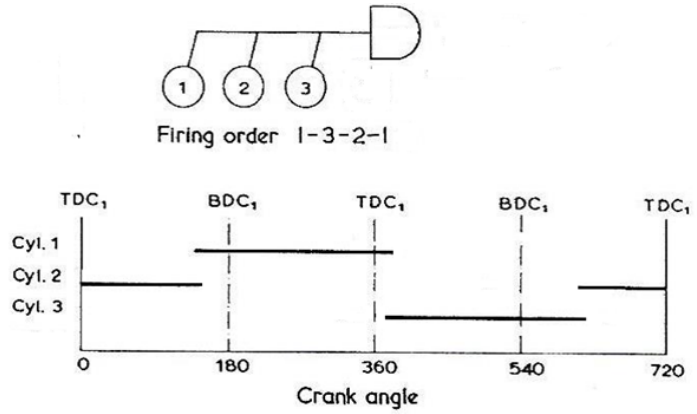


Figure 1.8 Exhaust pulse timing for 3 cylinder of an ICE
(extract from Watson and Janota [11])

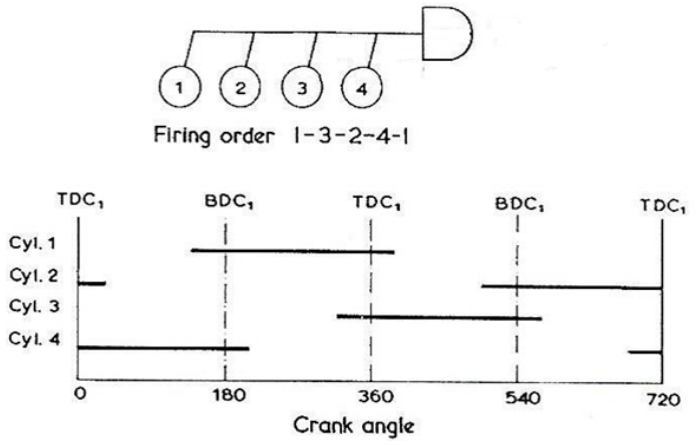


Figure 1.9 Exhaust pulse timing for 4 cylinder of an ICE
(extract from Watson and Janota [11])

Therefore pulse division is required to prevent flow mixing before the turbine rotor. Multiple entry volutes can alleviate this effect of mixing by ducting the engine cylinder flows to two or more separate turbine inlets. The most common multiple entry configuration is a twin-entry volute, followed by a circumferentially divided volute or double-entry volute. These multiple entry volutes are shown in Figure 1.10 and 1.11. Six cylinders of an ICE connected to a twin entry turbine is shown in Figure 1.12.

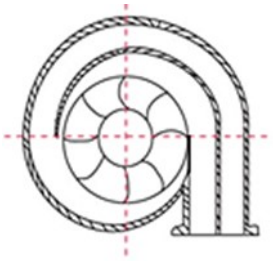


Figure 1.10 Double entry turbine cross section

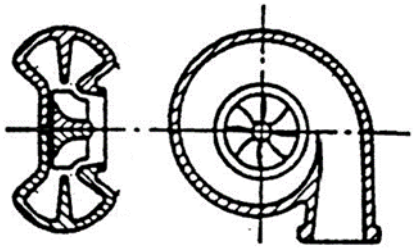


Figure 1.11 Twin entry turbine cross section

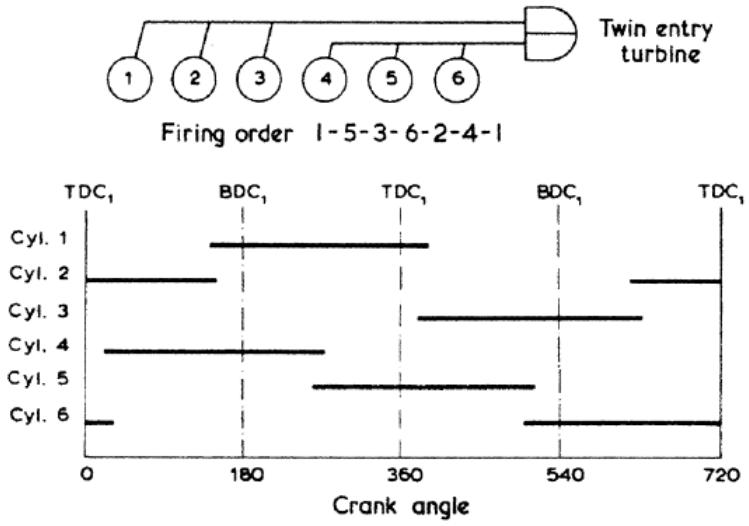


Figure 1.12 Exhaust pulse timing for 6 cylinder of an ICE
(extract from Watson and Janota [11])

Whether twin or double entry turbine, taking EGR flows from one side of the two entries, leads to a mass imbalance in the turbine. Consider the symmetric turbine presented in Figure 1.13. When EGR is extracted from the inner scroll, mass flow rate in that scroll decreases relative to outer scroll. The mass flow in each scroll is given by equation 1.1.

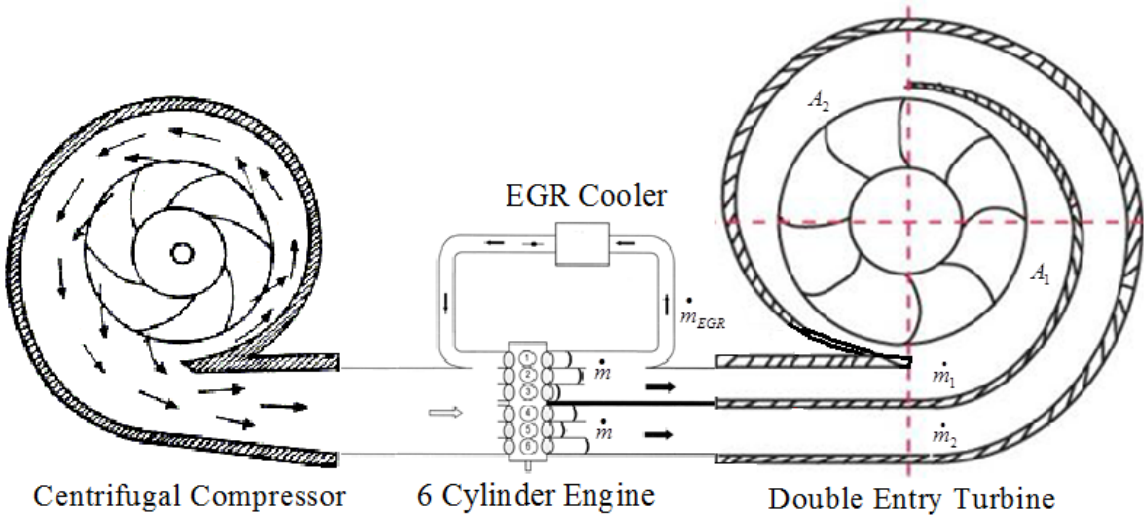


Figure 1.13 Compressor and turbine cross section

$$\dot{m}_1 = \dot{m} - \dot{m}_{EGR}$$
$$\dot{m}_2 = \dot{m} \qquad (1.1)$$

It is clear from Equation 1.1, that $\dot{m}_1 < \dot{m}_2$. The turbine has a symmetrical circumferential geometry configuration, therefore the rotor circumferential area in each scroll are identical, $A_1 = A_2 = A$. These clearly shows distinct absolute velocity component at the rotor periphery of each scroll, $C_1 < C_2$, assuming incompressible flow.

For a given rotor speed, the velocity triangles for each scroll is depicted in Figure 1.14. Apparent relative flow component, in magnitude and angle, is experienced in each scroll. These different relative flow angles, creates non-uniform incidences angle around the entire rotor periphery of the symmetric double entry turbine when EGR is extracted from only one scroll. The incidence angles are expressed in equation 1.2.

$$i_1 = \beta_1 - \beta_b$$
$$i_2 = \beta_2 - \beta_b \qquad (1.2)$$

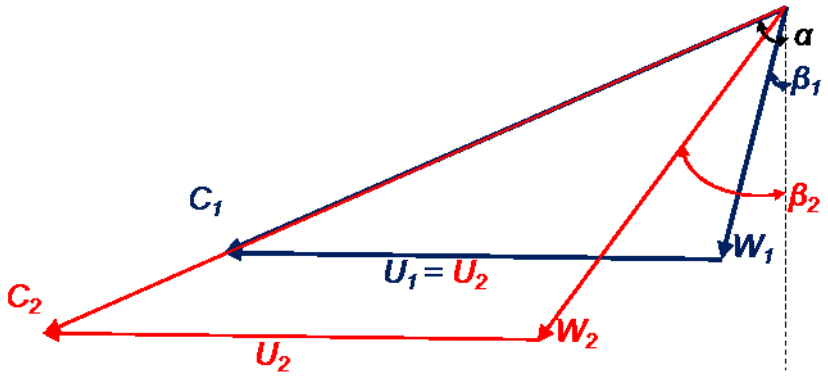


Figure 1.14 Velocity triangle

Wooley's and Hatton's [15] work on flow visualisation has shown that radially inwards flow (more positive incidence angle) separates at rotor blade suction surface, while tangential flow (more negative incidence angle) separates at pressure surface (Figure 1.15). Since flow separation on either side contributes to rise in overall turbine losses, both extremes are detrimental to the turbine. Furthermore, the turbine rotor is subjected to changing relative inlet flow angle as it rotates from one scroll to another. This causes unsteady effect in the rotor performance, and contributes further to turbine losses. Clearly EGR extraction in one scroll of the symmetric turbine will lead to mass imbalance, which in turn creates non-uniform and unsteady flow phenomena in the turbine, while it is operated in steady condition. The twin entry reduces this potential imbalance by an asymmetric configuration, as reported by Muller et al. [16].

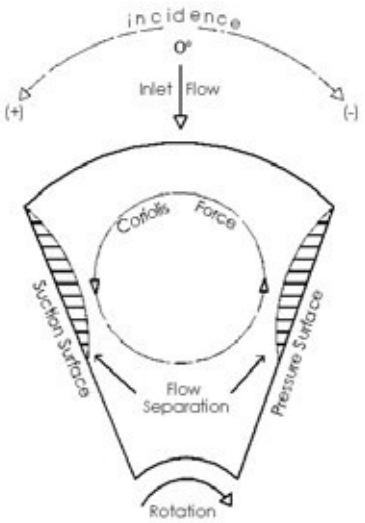


Figure 1.15 Flow separation due to inlet flow angle and Coriolis force
(extract from Rajoo [7])

One way to overcome this flow non-uniformity in double entry turbine is by extracting identical amount of EGR from both scroll. As explained in section 1.2, the effectiveness of a turbocharger depends on its ability to maintain positive pressure gradient across an engine intake-to-exhaust. When EGR is operated by extracting mass from one scroll of the symmetric double entry turbine, a negative pressure gradient is created between engine intake and exhaust. This negative pressure gradient causes p_2 to be lower than p_3 in just one of the two exhaust branches as shown in Figure 1.16. Therefore, negative pumping work is generated as indicated by the Indicator Diagram (P-V) in Figure 1.17. This pumping loss needs to be debited from the indicated mean power, together with other losses already present in the engine (power to overcome friction, power to drive valve gear, water and oil pump to name a few). Ultimately this reduces the brake power of the cylinder 1,2,3. If EGR were to be extracted from both scrolls, all six cylinder would be experience pumping loss, and eventually resulting in reduced net brake power of the engine. For this reason, EGR cannot be extracted from both scrolls of the conventional double entry turbine. To overcome this problem, an asymmetric double-entry turbine is proposed here, to maximize pulse energy extraction even under high EGR condition, and limiting/confining pumping losses only to the cylinders connected to the EGR loop.

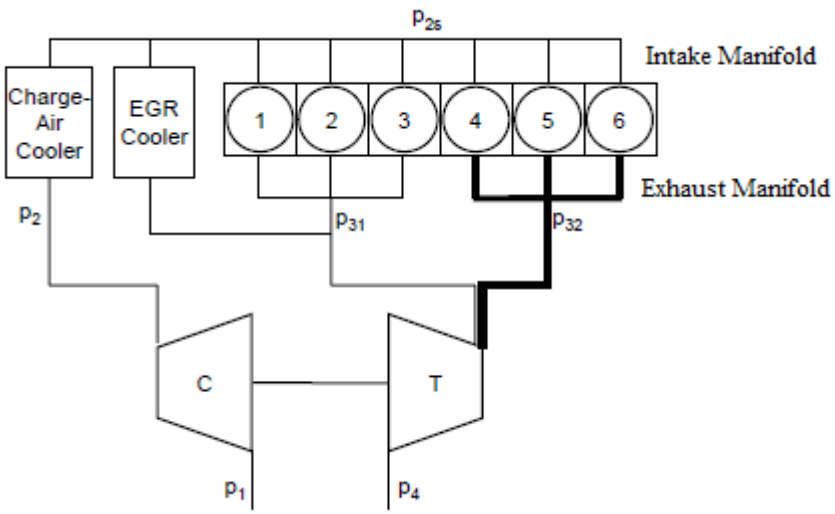
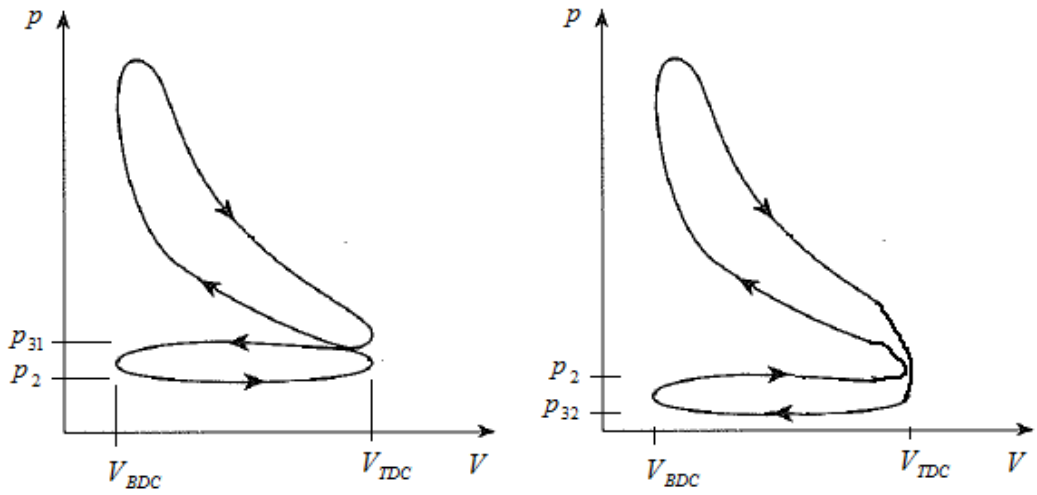


Figure 1.16 HPL EGR layout in 6 cylinder engine coupled to double entry turbine
(extract from Muller et al. [16])



(a) Negative Pumping work (b) Positive pumping work

Figure 1.17 P – V diagram

1.5 Thesis Objective

This thesis will provide fundamental understanding of asymmetric double entry turbine under both steady and unsteady flow condition. Apart from that, the research work in this thesis will also encompass the influence of nozzle vane opening on an asymmetric double entry turbine, with unequal circumferential division. All steady and unsteady flow characterization of the asymmetric double entry turbine with different vane opening will be addressed via extensive laboratory measurement.

The objectives of this Ph.D research are :

1. To characterize the steady-state performance of an asymmetric double entry turbine with different vane setting and configuration, under full, partial and unequal admission condition.
2. To provide an understanding of the unsteady flow performance of an asymmetric double entry turbine with different vane angle and configuration, under in phase and out of phase pulsating flow for various pulsation frequency and turbine speed.

3. To explore the influence of nozzle vane angle on the steady state and unsteady state performance of the asymmetric double entry turbine.

1.6 Thesis Outline

CHAPTER 1 *INTRODUCTION*

In this chapter, the importance of downsizing and turbocharging are introduced in the beginning, to lay the foundation for this PhD research. This is followed by brief overview of pulse flow turbocharging, Exhaust Gas Recirculation and double entry turbine, which sets the tone for research motivation. A summary of main objectives of the thesis and outline are also included in this chapter.

CHAPTER 2 *LITERATURE REVIEW*

The review of literature most relevant to this thesis are presented in this chapter. These are mixed flow rotor, variable geometry turbine, double entry turbine, experimental and computational pulsating flow research. The available literatures in these fields would be instrumental in discussion of the entire thesis and to highlight the gap in the current knowledge.

CHAPTER 3 *ASYMMETRIC DOUBLE ENTRY TURBINE DESIGN*

The methodology and procedures adopted by Sakai et al [17] to design this novel asymmetric double entry turbine is discussed in this chapter. This includes asymmetric volute design and nozzle vane design. This chapter also includes, the design of dual ring nozzle vane control mechanism, a brainchild of the author, which allows extensive testing with different vane angle setting.

CHAPTER 4 *EXPERIMENTAL SETUP AND PROCEDURES*

This chapter describes the cold flow test rig facility at Imperial College London. Safety operation and control of rig are also highlighted here. All the instrumentations employed in steady and unsteady flow measurements are presented, together with their respective

uncertainties. All performance parameter involved in the experimental work are also included at the end of the chapter.

CHAPTER 5 *STEADY FLOW EXPERIMENT*

Steady-state experimental results and discussion are contained in this chapter. This results includes full, partial and unequal admission condition for various nozzle vane configuration, including the nozzleless setting. The nozzleless setting is used as the base line for the nozzle vane configurations. Besides that, partial and unequal admission efficiency are compared to full admission, to quantify the drop in performance. Some CFD computational results from Chapter 2 are referred to further understand the flow phenomena which causes change in steady flow characteristics.

CHAPTER 6 *UNSTEADY FLOW EXPERIMENT*

In this chapter, pulsating flow characteristics of the asymmetric double entry turbine is presented and analyzed. This includes experimental results obtained under in phase and out of phase condition. Influence of nozzle vane angle, pulse frequency and turbine speed are also analyzed. The instantaneous quantities are presented first, followed by cycle average properties.

CHAPTER 7 *CONCLUSION*

This chapter contains the conclusion pertaining to the work presented in this thesis. The conclusion starts off with discussion on whether the outcome of this thesis has fulfilled objective set in the beginning. This is then followed by proposal for future work and recommendations.

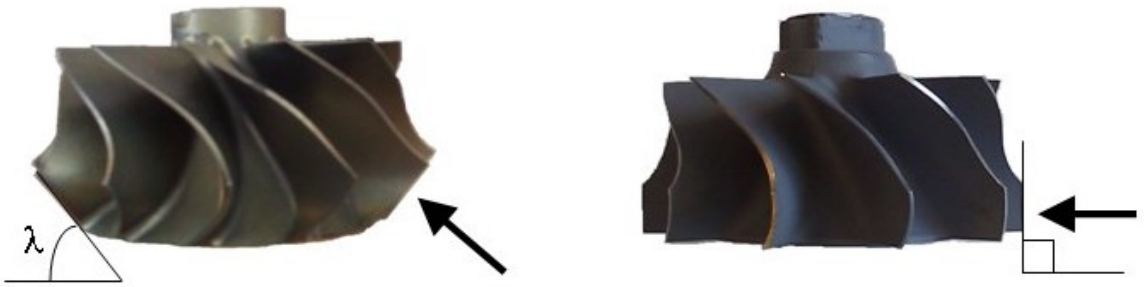
CHAPTER 2

LITERATURE REVIEW

This chapter presents the literature review related to the work covered in this thesis. The literature review has been categorized into several sections. Development overview of mixed flow rotor is presented in the first section. The second section covers key published literature on the variable geometry turbine. Double entry turbine research review is presented in the third section. And pulsating flow related publications, experimental and computational work are reviewed in section four and five respectively. Finally, the lesson learnt from all these sections are summarized to demonstrate the gap in the current literature.

2.1 Mixed Flow Rotor research

Literature review of mixed flow turbine will be well appreciated by first understanding its geometry and inlet condition. Figure 2.1 (a) shows a mixed flow turbine rotor. A mixed flow turbine is indeed a radial turbine, but with a different rotor inlet condition. As shown in Figure 2.1 (b), flow enters the rotor at 90º relative to the turbine axis, possessing both radial and tangential velocity component, in a radial flow turbine. Where else, in a mixed flow turbine, the flow at the rotor inlet has an additional velocity component in axial direction, compared to its radial counterpart. Figure 2.2 shows the major geometrical difference between a radial and a mixed flow turbine rotor, in a meridional perspective.



(a) Mixed flow turbine rotor (b)Radial flow turbine rotor

Figure 2.1 Two distinct types of turbine rotor *(extract from Newton [18])*

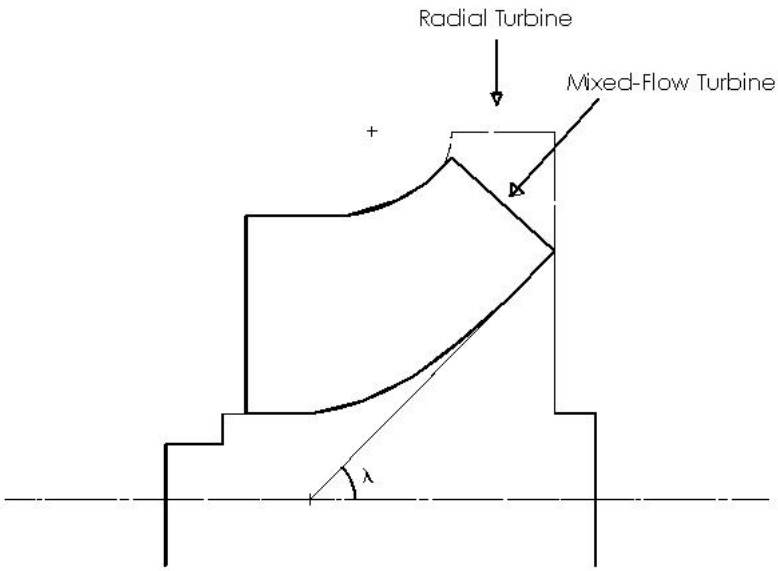


Figure 2.2 Meridional view of a radial and a mixed flow turbine rotor
(extract from Rajoo [7])

The quest for improved mixed flow turbine performance especially in the aspect of automotive turbocharger and engine efficiency has motivated research and development engineers to come up with new and innovative ideas in fulfilling the above requirements. Although the radial turbine has been in existence for almost a century and has been the ideal preference for automotive turbocharger, tremendous research has been going on since 1970s as reported by Rajoo [19] to investigate the suitability of the mixed flow turbine as an alternative. This is due to the fact that the mixed flow turbine has higher swallowing capacity and ability to achieve peak efficiency at lower velocity compared to an equal radial turbine. Peak efficiency at lower velocity would ensure turbocharger turbine to operate efficiently at higher pressure ratio to accommodate pulsating flow of exhaust gases into the turbine. This justifies the shift in attention in studying mixed flow turbine ever since the first experimental work carried out by Wallace and Pasha [20] in 1972.

An important aspect of a radial turbine is the radial fiber configuration which ensures an acceptable level of blade stresses in the face of a very hot gas environment. Wallace and Pasha [20] designed a mixed flow turbine to enable a different design process while still maintaining the radial fiber requirement. They used a pseudo three-dimensional method to gather more information about internal flow conditions in the mixed flow turbine since their design is based on one dimensional analytical analysis. The mixed flow turbine was designed to have the same rotor dimension as the original radial flow turbine, but with a swept leading

edge and a mean cone angle of 45º. Analytical and experimental work have indicated that the mixed flow turbine designed by Wallace and Pasha [20], has recorded increase in swallowing capacity at various pressure ratio regions as shown in Figure 2.3. Despite substantial amount of swallowing capacity improvement in the higher speed and pressure ratio region, where the radial turbine shows a drastic drop in the swallowing capacity, the mixed flow turbine design only managed to record marginally improved efficiency for the same wheel rotational speed.

The design documented by Wallace and Pasha [20] was implemented in two mixed flow turbines tested by Baines et al. [21], with an additional loss factor included in the design. Performance map obtained by Baines et al. [21] agreed well with those documented by Wallace and Pasha [20]. Abidat et al. [22] improved further the work of Baines et al. [21], by considering blade incidence effect in the design and adopted Bezier polynomial to generate rotor geometry profile. Baines et al. [21] used Lame oval technique to produce the rotor geometry profile. Although results obtained by Abidat et al. [22] were similar to the performance results reported by Wallace and Pasha [20] and Baines et al. [21], Abidat et al. [22] work has been found to be beneficial in understanding the effects of the inlet incidence.



Figure 2.3 Mass flow improvement of mixed flow turbine at various pressure ratios *(extract from Wallace and Pasha [20])*

The initial success in development of mixed flow turbine by Wallace and Pasha [20] and Baines et al. [21], has prompted researchers in 1980s and early 1990s to pay more attention in matching the mixed flow turbine to an internal combustion engine. Yamaguchi et al. [23], Chou and Gibbs [24], Naguib [25], and Minegashi et al. [26] pioneered the research work to design a mixed flow turbine for internal combustion engine application, adopting the same

design method as Wallace and Pasha [20] and Baines et al. [21]. Their effort was inspired by the fact that mixed flow turbine produces higher swallowing capacity compared to an equal radial flow turbine having same rotor tip dimension, thus a smaller mixed flow turbine could be used to give the same swallowing capacity that would be produced by a bigger radial turbine. A smaller turbine means reduction in turbine rotor inertia which could subsequently improve turbocharger response.

After more than two decades of research and development in mixed flow turbine, research direction again took a different approach in mid 1990s. Researchers started spending more resources and time in reducing the loss by means of turbine optimization. Chen and Baines [27] conducted investigation and presented optimization technique to reduce losses in the mixed flow turbine. The method employed by them focused on the turbine loading factor and the exit loss. The fundamental principle used by Chen and Baines [27] in loss reduction optimization, by minimizing velocity components at the rotor inlet and exit, was also extensively used by Whitfield [28] in his design of a radial turbine. Contrary to the standard practice of assuming zero exit swirl angle as in the case of radial turbine, Chen and Baines [27] used a positive swirl angle at exit. This unconventional assumption has proven to reduce overall turbine losses greatly but with a penalty in specific power.

2.2 Variable Geometry Turbine Research

A VGT is used as a boost control so that turbocharger can be matched to the engine to obtain the desired performance. It controls the turbine inlet opening to regulate the turbocharger boost. Ever since its' inception in early 1960s, VGT has gone through great deal of improvement in performance and reliability with regards to radial turbine. This has led to the usage of VGT as a standard component in commercial diesel applications such as heavy duty trucks, ships, off-road vehicles, and power generators. Two most commonly used methods in VGT are pivoting nozzle vanes and the sliding wall.

Figure 2.4 shows the benefits of using a VGT over a FGT in diesel powered road vehicle. These two separate research work, as reported by Watson and Janota [11], clearly shows substantial improvement in brake power, specific fuel consumption and reduced emission with the implementation of VGT. Unfortunately, the wider application of VGT has not been

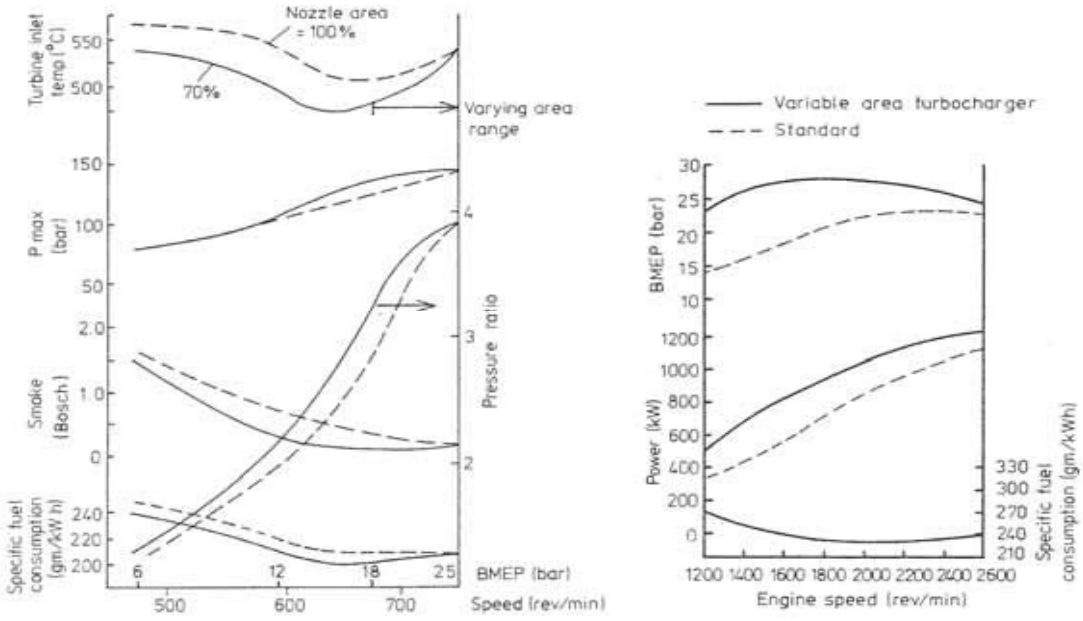
very successful owing to high cost and reliability issues of VGT at that time, which outweighs its benefits to the engine.

In pursuit to investigate influence of varying turbine inlet geometry on engine performance, Flaxington and Szezupak [29] studied three different methods; varying rotor exit area, volute exit area and volute tongue area. They conducted laboratory work by regulating volute exit area and volute tongue area to obtain optimum Brake Mean Effective Pressure (BMEP). Their findings are shown in Figure 2.5. According to them, both methods have demonstrated an improved torque, wider speed range and enhanced transient response. Although Flaxington and Szezupak [29], examined boost control, engine speed control and optimum full/part load control as control strategy for VGT, they were unable to point out the single superior control strategy amongst the three.

Investigation carried out by Walsham [30] has demonstrated superiority of VGT compared to waste-gated turbine and turbo compounding, in term of transient response and transient emission. This is shown in Figure 2.6. However, VGT has recorded significant drop in efficiency at closed position. Walsham [30] echoed Watson and Janota [11], by concluding that complexity of VGT outweighs it benefits when it comes to mass commercialization consideration.

Hawley et al. [31] performed laboratory testing by coupling a turbocharger with pivoting nozzle vane turbine to a direct injection diesel engine. The outcome of this investigation is demonstrated in Figure 2.7. Comparing VGT against FGT, the former has recorded 45% improvement in NOx emission reduction and 10% in limiting torque. Owing to significant research contribution to overcome VGT problems since 1980s, VGT has become a standard component in almost all diesel powered engine during early 1990s.

The design of nozzle vane is essential in order to obtain good performing pivoting vane VGT system. To date numerous analytical, experimental and numerical investigation have been reported in the public domain on nozzle vane passage design in pursuit of improving the radial turbine stage efficiency. Changing the nozzle vane geometry, varying the interspace between nozzle and rotor, and varying the number of nozzle vane in a particular turbine are the most common method adopted by researchers in reducing loss in radial flow turbine stage performance.



Kunberger (1980) Berenyi and Raffa (1979)

Figure 2.4 Engine performance improvements with VGT
(extract from Watson and Janota [11])

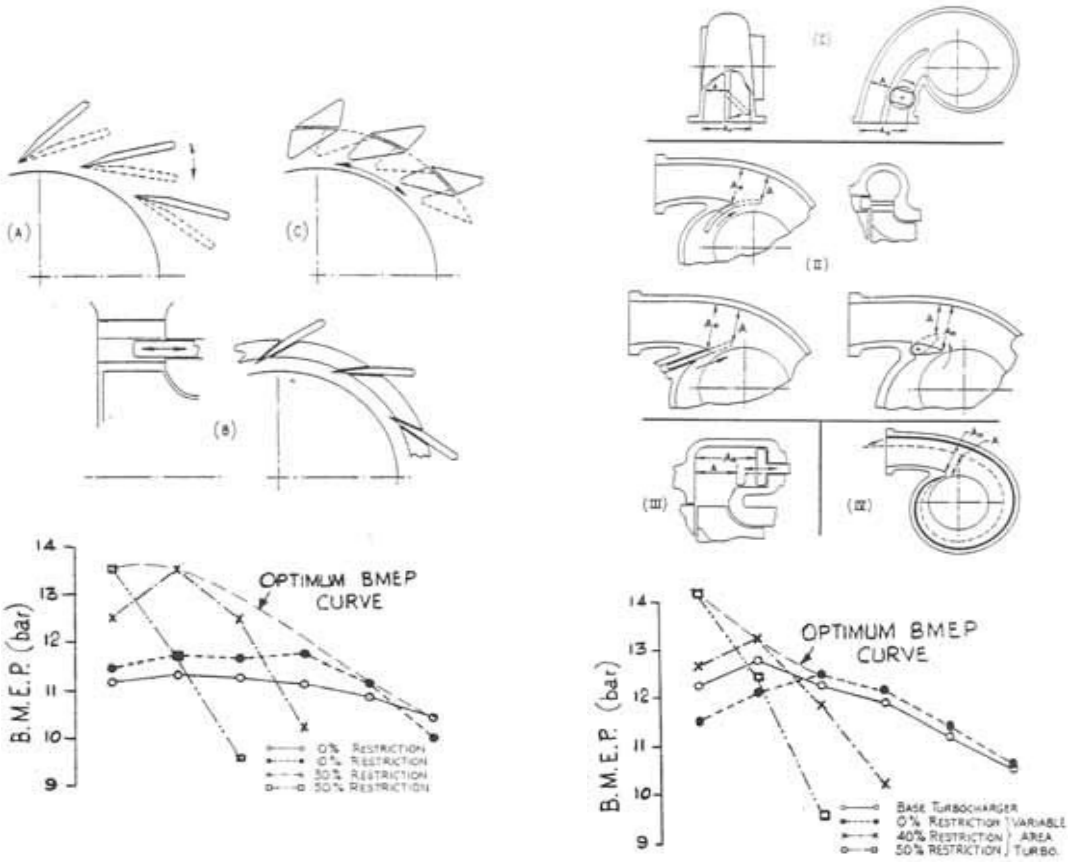


Figure 2.5 Effect of variable area control on BMEP
(extract from Flaxington and Szezupak [29])

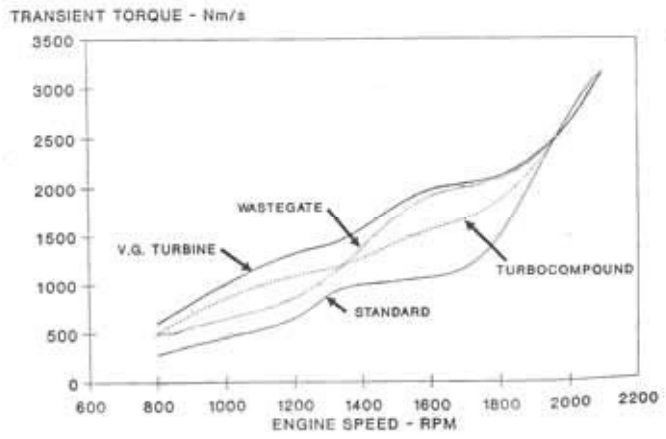


Figure 2.6 VGT superiority in engine transient response
(extract from Walsham [30])

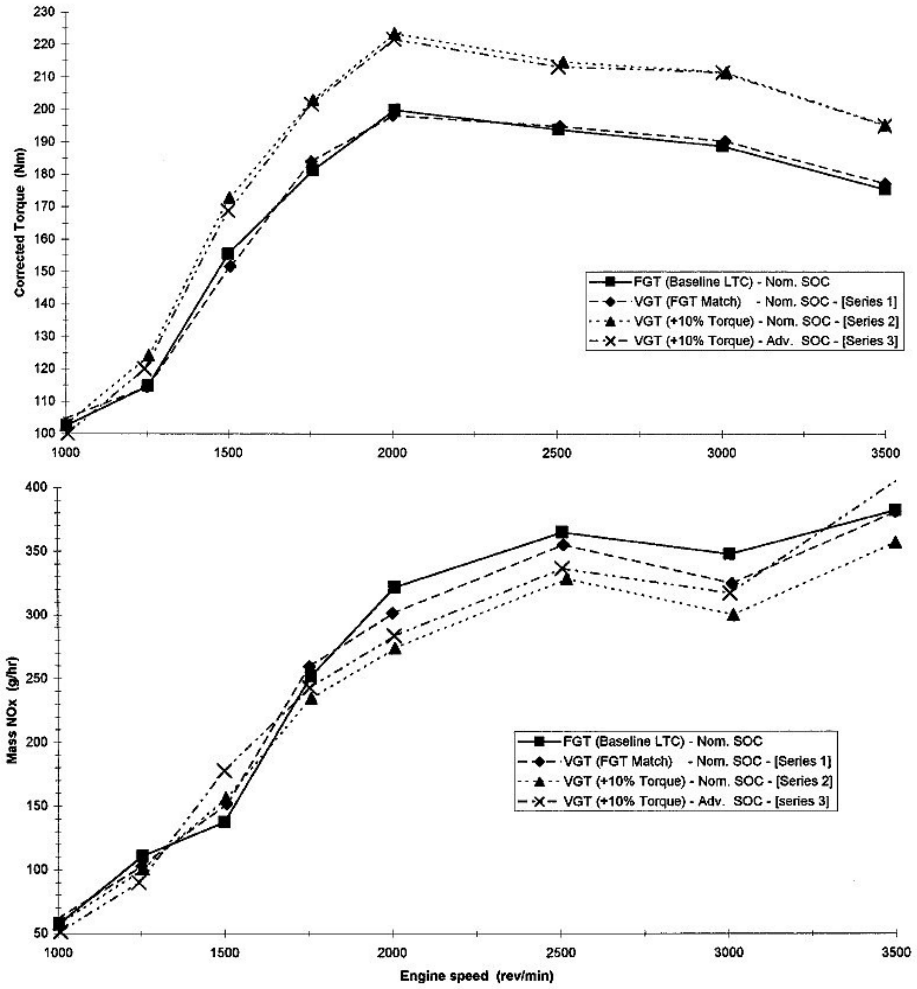


Figure 2.7 Engine torque and NOx emission under limiting torque
(extract from Hawley et al. [31])

Ricardo PLC conducted extensive radial turbine test programme using uncambered vane geometry with robust trailing edge and this investigation was reported by Hiett and Johnston [32]. In this test programme, seventeen vanes with vane angles ranging between 60º and 80º were tested. On the same test programme, Hiett and Palmer [33] concluded that cambered vane geometry has recorded significant improvement compared to the straight (uncambered) vane when both geometry tested at 60º vane angle setting. Investigation revealed that the vane exit flow angle for both geometry configuration was different. To this the authors suggested that the straight vane geometry should be adjusted to guide the flow into rotor at identical angle as the cambered vane geometry, if direct comparison of vane passage loss were to be made.

The success in incorporating cambered vane profile as reported by Hiett and Johnston [32], has prompted Maki and Mori [34] to conduct experimental work on a radial turbine using three different vane geometries; a straight vane, a concave vane and a convex vane. Although, experimental test conducted for each vane geometry managed to record static pressure measurements and some flow visualization, unfortunately correlation of vane geometry to losses in vane passage and subsequent rotor blade passage were not made. As such no concrete conclusion could be drawn from this research.

Besides experimental work, few researchers used numerical methods to investigate the impact of vane geometry in radial turbine. One of them is Ribaud and Mischel [35]. To investigate the effectiveness of adopting purely nozzle geometry used in axial stage turbine, conformal mapping method was used by Ribaud and Mischel [35], to transform high efficiency axial cascade into a circular row of vanes in a radial stator volute. Although no experiments were carried out, authors managed to demonstrate numerically that the circular row of vanes achieved via conformal mapping has been successful in avoiding positive pressure gradient built up in the vane passage.

Reichert and Simon [36] deployed CFD to improve design and offer in-depth understanding of vane passage internal flow. These authors favored a H-C grid in this research work as this grid provides good resolution at the trailing edge and low distortion at vane exit. One dimensional analysis was used to design the vane prior to in-viscid CFD analysis to validate the design. The strong curvature of the channel at exit has caused undesirable supersonic region on the suction side, which was detected by CFD calculation. Although the region of

curvature was moved towards the leading edge to improve the design, authors concluded that only a fully viscous CFD simulation would be able to evaluate the actual losses in vane passage.

Simpson et al. [37] conducted experimental and numerical investigation to study the impact of varying number of nozzles and nozzle geometry in a radial turbine. Three different vane geometry that were tested are uncambered (baseline) vane, cambered 2D vane and flat plate vane. All tests were carried out on a volute with a constant cross-sectional area that did not change with azimuth angle, as opposed to the conventional volute. Experimental tests show that increasing number of nozzle for the same nozzle geometry from 11 to 17 has improved stage efficiency by 0.5%. As for varying nozzle geometry experiment, the uncambered nozzle geometry has recorded an improvement in stage efficiency of 4% over flat plate nozzle tested for the same number of nozzle. Although numerical analysis agrees well with experimental results qualitatively, the efficiency recorded are 0.9% higher when number of nozzles are varied and 0.8% lower when nozzle geometry is varied. Authors concluded that failure of numerical analysis to predict the full extent of separation at rotor inlet contributed to the difference between experimental and numerical results. It is very apparent that nozzle size has less impact compared to nozzle passage geometry as far as the stage efficiency is concerned.

Since vane nozzle geometry has been found to be more influential in improving radial turbine stage efficiency as reported by Simpson et al. [37], a further experimental and numerical investigation on nozzled and nozzleless turbine volute was undertaken by Simpson et al. [38] with an aim to study the flow fields delivered to the inlet of a radial turbine rotor. A volute with nozzles has a constant circular cross-sectional area, regardless of azimuth angle, as opposed to a nozzleless volute, which has cross-sectional area that varies with azimuth angle. The nozzle used in the study has a straight uncambered geometry with a nozzle trailing edge radius to rotor leading edge radius ratio, R_{te}/r_{le} of 1.10. Nozzleless volute has been found to deliver flow to the rotor inlet more uniformly than volute with nozzles, which produces high level of non-uniformity. Jet and wakes did not mix out significantly and have been discovered to be the attributing factor to non-uniformity and pressure loss at rotor inlet in volute with nozzles. This subsequently causes overall pressure losses and higher variation of rotor inlet incidence. For nozzleless volute, main source of

flow non-uniformity and pressure losses occurs at tongue region. Simulation results is in agreement with measured experimental results.

Having gained sufficient understanding of nozzle vane geometry contribution to stage efficiency and subsequent flow field generated at rotor inlet, Simpson et al. [39] conducted experimental and simulation work to examine the impact on stage efficiency by varying vaneless space (interspace between vane nozzle trailing edge and rotor leading edge) and number of vanes in a radial turbine. A nozzle vane profile was designed using Bezier curves in order to produce accelerating flow constantly all through the vane passage. Configuration with 15 vanes and $R_{te}/r_{le} = 1.13$ was set as the baseline. In order to understand the impact of varying number of nozzles on stage efficiency, volute with 12, 18, 24 and 30 number of nozzles, with the same vane profile, were tested. Simulation results yields volute having 15 number of vanes gives the highest turbine stage efficiency. Thus, volute with 15 number of vanes was set as baseline for subsequent simulation to study effect of varying vaneless interspace, having $R_{te}/r_{le} = 1.05, 1.175, 1.20$ and 1.25. Numerical work to study impact of varying vaneless space shows that increase in R_{te}/r_{le} has no significant influence on stage efficiency. Experimental and numerical results complement each other quantitatively, but with deviation between 3% and 4%. Aerodynamically optimum values of the vaneless space R_{te}/r_{le} and solidity, c_{nv}/s were found to be 1.175 and 1.25 respectively. Authors concluded that increase in vaneless space has been found to contribute to a more circumferentially uniform flow state around the rotor periphery despite contributing to reduction in static pressure variation at the rotor inlet.

VGT has been successfully implemented in radial turbines automotive turbochargers powered by diesel engines [4]. Owing to the benefit of achieving better swallowing capacity and peak efficiency at lower velocity ratio, it would be beneficial to study the effectiveness of having VGT in a mixed flow turbine. Wallace and Pasha [20], has indicated that swallowing capacity, torque and efficiency of mixed flow turbine can be enhanced further with the aid of a specially design 'ideal' vane ring. Indication by Wallace and Pasha [20], was echoed by Karamanis et al. [63]. Karamanis et al. [63] suggest that a specially designed volute and nozzle rig were needed to optimize the unsteady flow direction into mixed flow turbine rotor. Suggestion by Karamanis et al. [63] was validated through a three-dimensional full unsteady flow analysis by Palfreyman and Martinez-Botas [40]. According to

computational investigation by Palfreyman and Martinez-Botas [40], the unsteady flow was poorly guided at the rotor inlet of mixed flow turbine at high pressure ratio.

In view of this and motivation gained due to subsequent promising results over the years, researchers in recent years have embarked on investigation to explore the feasibility and advantages of incorporating VGT in mixed flow turbine. These reported investigations which were more focused on achieving an optimal VGT nozzle vane design, will be presented after a brief explanation to distinguish vane nozzle geometry in a mixed flow turbine as opposed to a radial one. This explanation, which is aided by Figure 2.8 and Figure 2.9, is instrumental in understanding how VGT can be adopted in a mixed flow turbine.

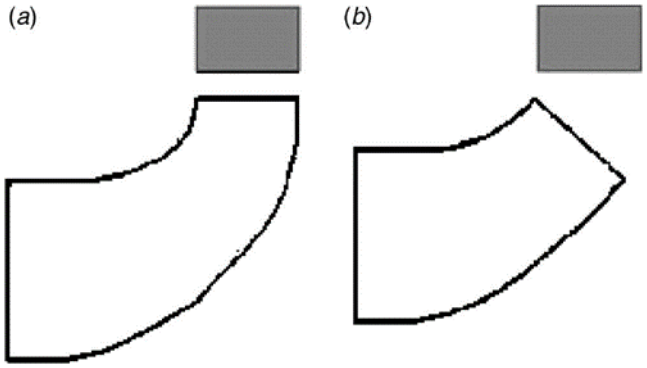


Figure 2.8 Straight nozzle vane used for (a) a radial turbine and (b) a mixed flow turbine *(extract from Rajoo [7])*

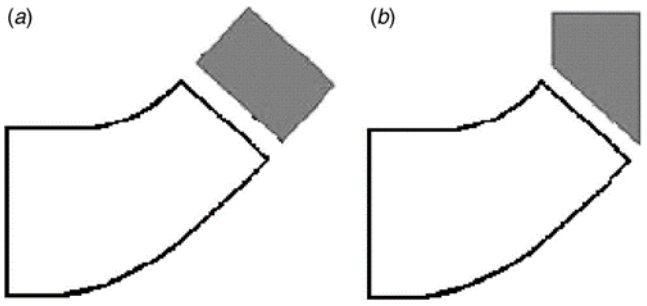


Figure 2.9 Possible options of nozzle vanes for a mixed-flow turbine (a) vane with inclined hub/shroud surface (b) vane with flat hub/shroud surface *(extract from Rajoo [7])*

Figure 2.8(a) depicts a straight nozzle vane arrangement in a radial turbine. This configuration creates a uniform interspace between the vane trailing edge and rotor leading edge. When the same straight nozzle vane is fitted into a mixed flow turbine, assuming both turbine in Figure 2.8 has same rotor tip diameter, an uneven interspace is created as shown

in Figure 2.8(b). This uneven interspace contributes to the existing non-uniformity flow at rotor inlet in the spanwise direction besides increasing the friction loss due to the longer unguided path, especially at the hub. Two possible design to overcome the above problem are shown in Figure 2.9. Although both configuration creates uniform interspace, which in turn would provide better flow direction into the rotor, it would be impractical to build a nozzle ring on a concave inclined surface as shown in Figure 2.9(a). Thus, configuration in Figure 2.9(b) is preferred for practical application, especially when it involves VGT, either for sliding or pivoting operation.

Both Figure 2.8 and 2.9 were presented in meridional view of a turbine, thus they do not represent the actual rotor, vane and the entire vane passage geometry. Furthermore, the above method is one of the few possible ways to optimize nozzle vane design. Therefore, in order to design an optimum nozzle vane by matching spanwise nozzle vane geometry to a specific mixed flow turbine, attention should be given to internal flow in nozzle vane passage and the three-dimensional variation of the rotor leading edge.

To study the viability of commercializing VGT in the mixed flow turbine turbocharger, Baets et al. [41] conducted a research using straight nozzle vanes pivoted to nozzle ring arranged uniquely to reduce the clearance leakage. Although the efficiency is slightly lower, research conducted by Baets et al. [41] has shown improvement in part load fuel consumption and exhaust smoke of a diesel engine. A distinct conclusion on practical benefit of mixed flow turbine could not be drawn as authors did not highlight the comparison against a radial counterpart and the benefits of the VGT in mixed flow turbine.

In order to geometrically match the leading edge of a mixed flow turbine rotor, Ishino and Bessho [42] adopted a radially slanted straight nozzle vane. The turbine was fitted with alternate pivoting and fixed nozzle vanes to minimize clearance leakage loss. The test results show 14% improvement in efficiency using the new VGT mixed flow turbine, especially at lower exhaust flow conditions.

Adopting the same approach as Ishino and Bessho [42] to geometrically match the leading edge of the rotor, Rajoo and Martinez-Botas [43], used NACA airfoil 0015, uncambered profile as a guideline to design a nozzle vane. A lean nozzle vane, which makes 50° with the hub surface, was finally designed to ensure the trailing edge of the nozzle vane matches the

three-dimensional leading edge of the mixed flow rotor (Figures 2.10 and 2.11). This resulted in an elongated shroud profile compared to the hub profile (Figure 2.12). Number of nozzles was determined based on; Zweifels criterion [44], adopting optimum tangential lift coefficient between 0.75 and 0.85, and suitable nozzle space for pivoting within the circumferential perimeter. Experimental test was carried out with vane pivoting angle between 40º and 70º. Steady state experiment conducted at 80% of the design speed using the new lean nozzle vane design demonstrates higher peak efficiency compared to an equivalent nozzleless turbine, especially for vane pivoting angle between 60º and 70º. On the other hand, vane pivoting angle of 40º and 50º have recorded drop in peak efficiency and increase in swallowing capacity. Vane angle setting of 65º has been found to be the optimum pivoting angle as it has shown best performance at both peak and higher velocity region. This is shown in Figure 2.13. Comparison between new lean nozzle and equivalent straight nozzle design, both pivoted at an angle of 65º, reveals that peak efficiency remains same while the swallowing capacity has increased in the new design (Figure 2.14). As far for the 40Hz pulsating unsteady flow, turbine performance deviated significantly from the equivalent quasi-steady state assumption when compared to a nozzleless mixed flow turbine. However, at 60Hz pulsating flow condition, the turbine has recorded high cycled averaged efficiency.

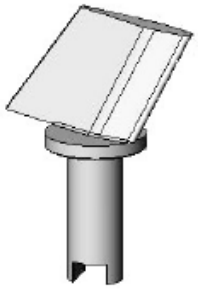


Figure 2.10 Lean nozzle vane with pivoting disc and shaft
(extract from Rajoo and Martinez-Botas [43])

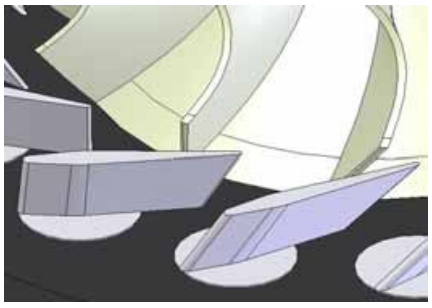


Figure 2.11 3-Dimensional matching between lean nozzle vane and rotor leading edge *(extract from Rajoo [7])*

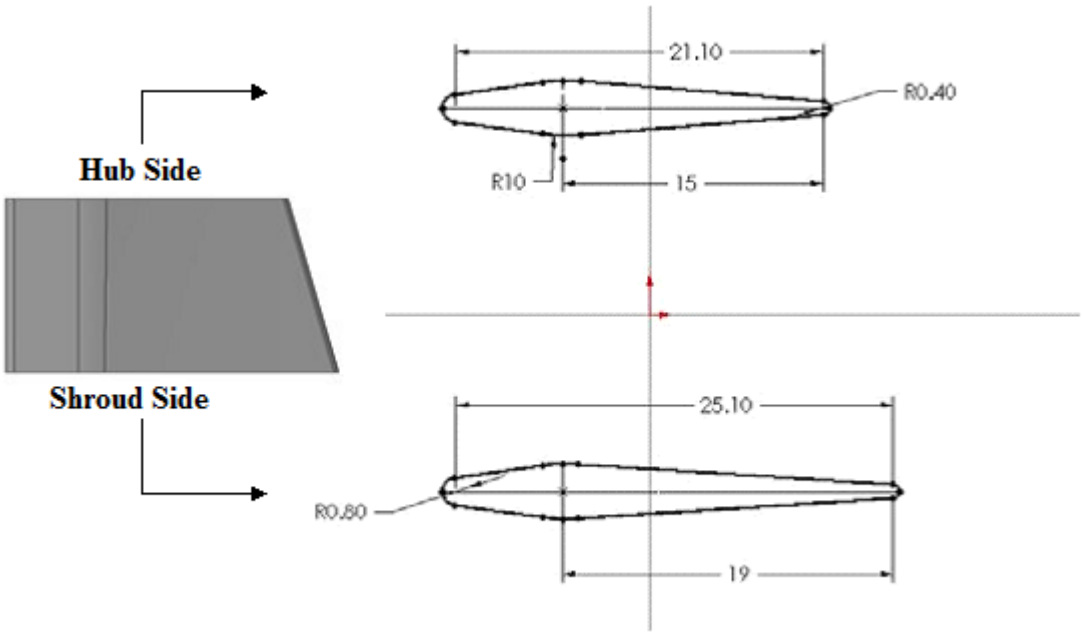


Figure 2.12 Lean nozzle vane dimensions *(extract from Rajoo [7])*

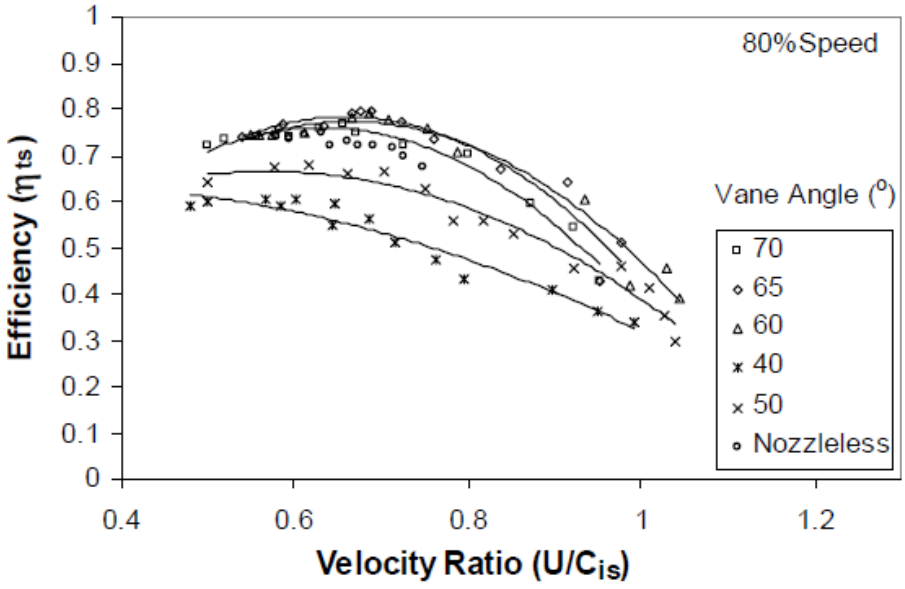


Figure 2.13 Efficiency improvement of a VGT with lean nozzle vane
(extract from Rajoo and Martinez-Botas [43])

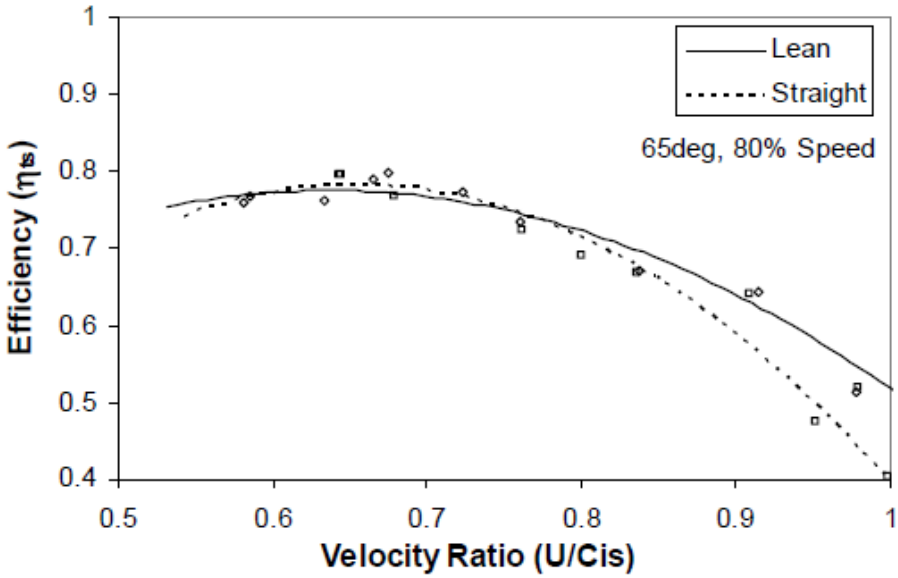


Figure 2.14 Efficiency comparison between lean and staright nozzle vane
(extract from Rajoo and Martinez-Botas [43])

Prompted by their earlier findings, Rajoo and Martinez-Botas [45] tested a specially designed volute with additional nozzled stator volume of 48% and VGT in a mixed flow turbine. Their study shows that the peak efficiency reduces while swallowing capacity increases as the straight vanes are opened, from 70º to 40º in a steady state condition. This decrease in peak efficiency has forced velocity ratio to assume higher values, between 0.53 and 0.62 corresponding to vane opening between 70º and 40º respectively. Under pulsating condition of 40Hz and 60 Hz at 50º vane opening, the swallowing capacity is the same as a nozzleless turbine. Turbine isentropic power plot demonstrates that 60Hz flow is more dynamic than 40Hz flow owing to the more fluctuation experienced by the 60Hz pulsating flow. On the other hand, comparison of these two pulsating conditions on a turbine actual power plot reveals that 40Hz has a higher peak. This indicates that the nozzle ring acts as a damping body which dampens the dynamic flow characteristics resulting from higher pulsating frequency and at more open vane positions.

2.3 Double Entry Research

Double entry turbine research normally involves measurements of turbine performance at three different admission conditions; full, unequal and partial admissions. Since all three admission conditions involve different inlet conditions (mass flow and pressure), it is

important that they are defined here to complement the literature review in the proceeding paragraphs. In full admission testing, both limbs of double entry will be flowing with either equal mass flow rate or total stagnation pressure. In other words, both limb possess equal amount of energy at the measurement plane; which is why it is also known as equal admission condition. As for the unequal admission testing, each limb of the double entry turbine is subjected to different pressures and mass flow rates. This is to replicate the actual gas flow in a multiple entry turbine coupled to an engine, in the steady state flow condition. The extreme of the unequal admission is known as partial admission. In partial admission state, one limb is fully flowing while the other limb is not flowing. All three conditions are illustrated in Figure 2.15.

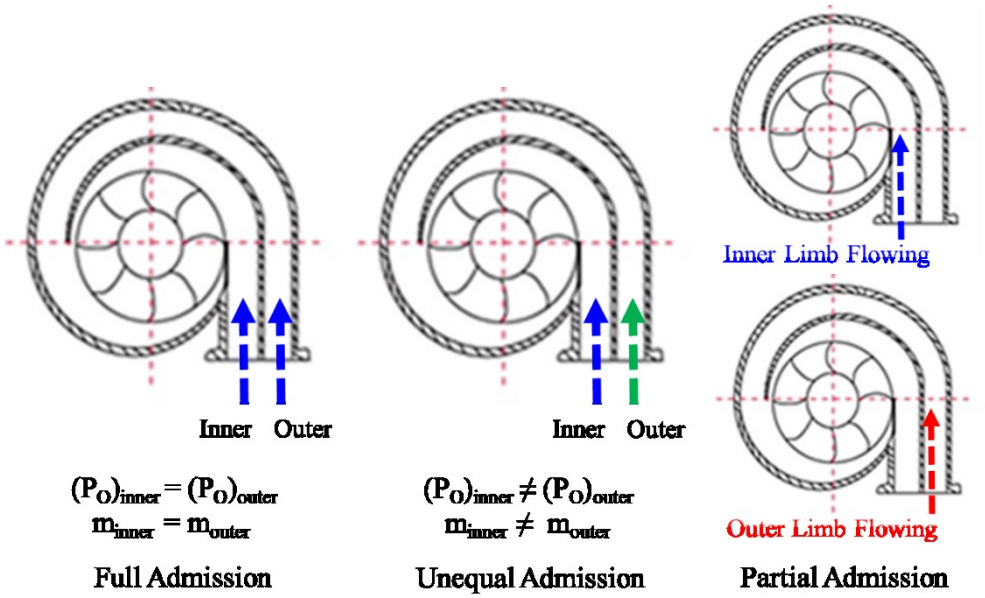


Figure 2.15 Three different admission conditions

The wide application of double entry scroll in a pulse flow environment has seen substantial benefits in turbine performance. Owing to this reason, most of the available literature in the public domain are very much inclined towards unsteady performance of the double entry turbine. First published experimental work on double entry turbine took place exactly 5 decades ago when Benson and Scrimshaw [40] reported their full and partial admission investigation findings. They attempted to find correlation between quasi-steady flow and unsteady flow performance, but were not successful as they could not completely characterize the unequal admission behavior of the double entry turbine in quasi-steady state and observed 11 point drop in peak efficiency under partial admission. They were the first

ones to conclude that turbine has negative impact if it operates only partial or full admission for the quasi-steady state analysis, thus will operate mostly between full admission and partial admission during steady state condition.

This motivated Timmis [47] to pursue unequal admission experimental work on double entry turbines, using Benson and Scrimshaw [46] work as base for his investigation. Timmis analyzed and reported mass flow characteristics for each limb, varying the mass flow ratio. Definition for mass flow ratio is specified as ratio of mass flow through one limb against the other. Timmis presented the flow interdependence between both limbs of a double entry turbine and intelligently concluded that the flow behavior is most likely due to mixing in the interspace region. His work has successfully demonstrated effect of inequality between entries on efficiency deficit. His data was adequately presented by Wallace, Cave and Miles [48] as shown in Figure 2.16 and Figure 2.17, as there were constraints re-producing charts by Timmis [47] in his thesis.

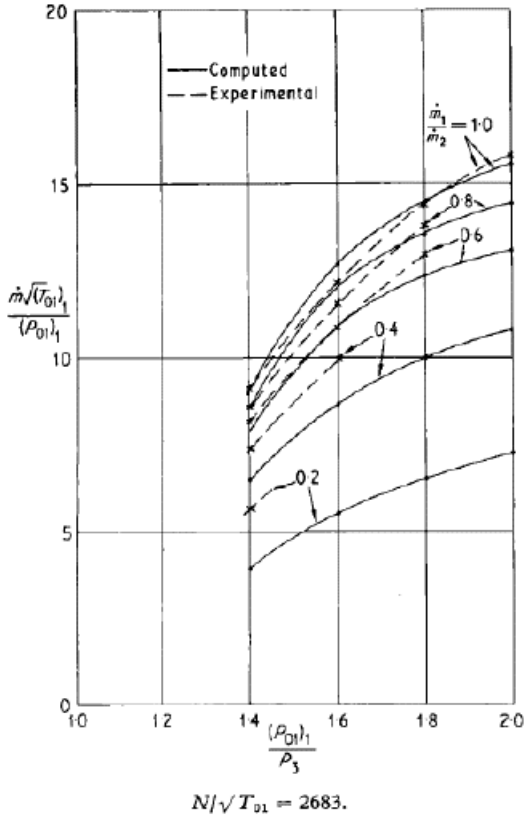


Figure 2.16 Comparison between experimental and calculated mass flow characteristic of a double entry turbine under different unequal admission condition
(extract from Wallace, Cave and Miles [48])

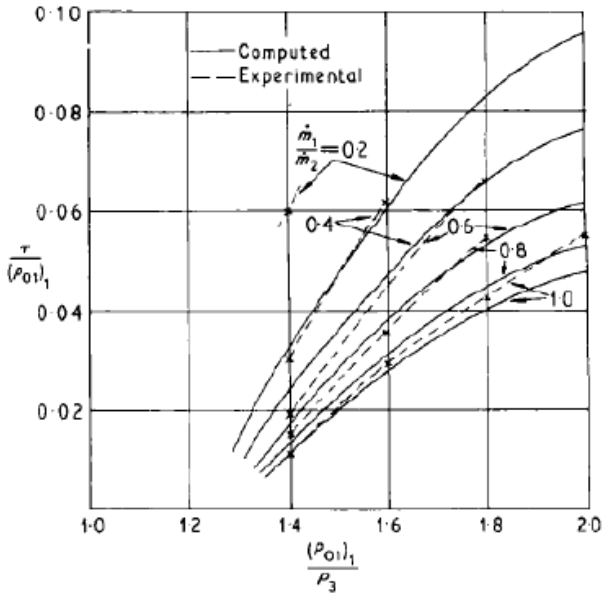


Figure 2.17 Comparison between experimental and calculated torque characteristic of a double entry turbine under different unequal admission condition
(extract from Wallace, Cave and Miles [48])

Later, Pischinger and Wunsche [49] revealed in their publication, that twin-entry turbines had better performance compared to double-entry turbines with same rotor assembly in unequal admission environment. Equal mass flow rate in both entries of the turbine was used as the criteria to match and compare turbine with different volutes. Contrary to the method used by Timmis [47], Pischinger and Wunsche [49] used pressure ratio rates between limbs instead of ratio of mass flow rates, to demonstrate the inequality between entries. In pursuit to define the space that the mass flow goes through when it expands under isentropic process, they identified isentropic flow zones within the plot area of each limb. The impact of pressure ratio inequality between limbs, on the isentropic flow zones can been clearly seen in Figure 2.18. The chart depicts the results for twin entry volute (Zw) and double entry (Do) in solid and broken lines respectively. The test is done under the same average pressure ratio all through the test. It is observed that the lines intersect at exact point of the full admission condition with isentropic flow area of about 3.8 cm^2. Pischinger and Wunsche [49] has good agreement with Timmis [47] findings, whereby isentropic zone for high pressure limb increases as opposed to a decrease in the low pressure limb counterpart, as inequality changes from full admission to extreme unequal admission state. The plot also points out an abrupt gradient in the lines of the twin entry volute than that of the double entry, demonstrating the significance of unequal admission impact on twin entry geometry.

In order to investigate level of symmetry of efficiency characteristic in the unequal admission condition, total to-static efficiency against pressure ratio of both geometries are presented in Figure 2.19. A flat efficiency curve is seen for twin entry geometry compared to double entry volute, due to the ability of the former to maintain uniform circumferential rotor inlet condition, whereas the inlet condition in the latter constantly changes between low and high pressure. However, the twin entry volute is seen to have a peak on both sides of the unequal admission condition with uneven efficiency deficit in each limb. Despite higher efficiency deficit, double entry volute tested by Pischinger and Wunsche [49] exhibited good degree of symmetry between the two limbs, with a single peak point.

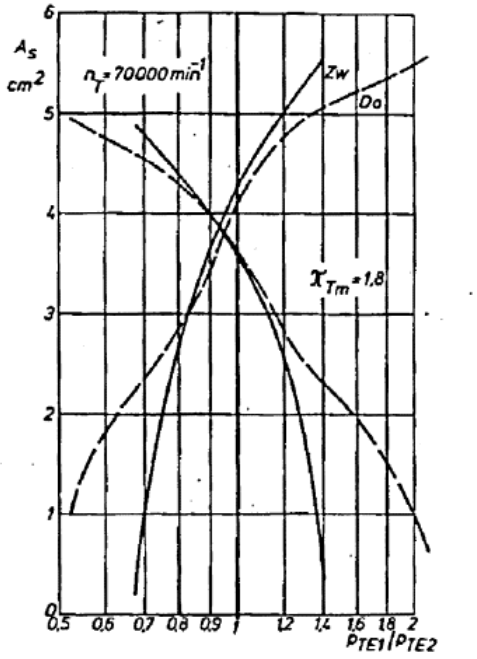


Figure 2.18 Isentropic flow area comparison between double (Do) and twin (Zw) entry turbine for different ratio of pressure *(extract from Pischinger and Wunsche [49])*

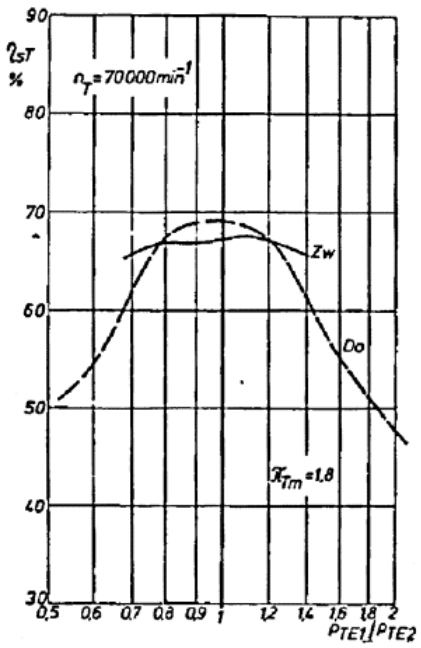


Figure 2.19 Efficiency comparison between double (Do) and twin (Zw) entry turbine
(extract from Pischinger and Wunsche [49])

Like Benson and Scrimshaw [46], Mizumachi, Yoshiki and Endoh [50] investigated the performance of the radial turbine in partial admission condition. While the former tested an actual double entry turbine, the latter blocked half of a single entry nozzle passage to simulate the partial admission condition due to lack of an actual double entry turbine, as shown in Figure 2.20. Most of their finding contradicts researches done in this area mainly due to the method used to simulate the partial admission condition. However, their findings are still valid with some exciting points in their analysis. They postulated that as the fluid flows from the open to the blocked off section, the initial momentum provides the fluid the ability to flow through. However due to centrifugal acceleration, the fluid then stopped flowing through the passage. In order to verify this prediction, Mizumachi, Yoshiki and Endoh [50] performed testing by measuring pressure fields around the rotor circumference using a sequence of 38 static pressure tappings in the nozzle-rotor interspace. Figure 2.21, shows the results of the theoretical centrifugal head (Pc) which is calculated using the pressure field measurements at the rotor periphery by assuming the fluid within the rotor is stationary in a relative frame. As the pressure ratio across the limb fixed at 2.0, the 5 different values of velocity ratio translate to 5 different speed conditions used in the experiment. The volute pressure increases gradually as rotor rotates from non-flowing section to the flowing section. This causes drop in in fluid velocity, which in turn increases the centrifugal head. The experimental findings have lent some support to their prediction.

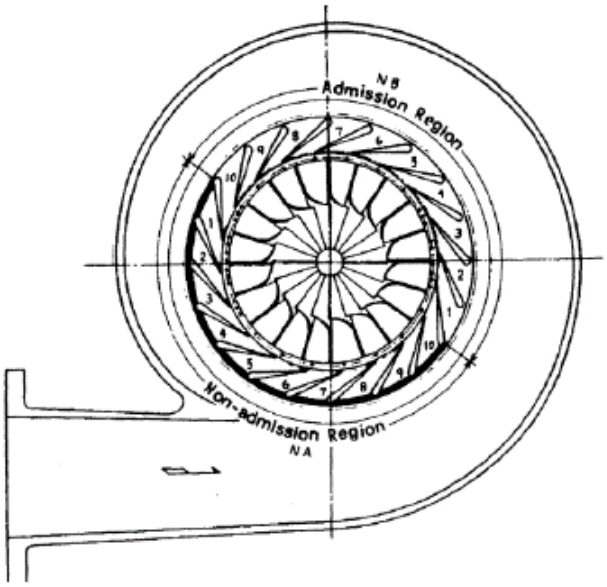


Figure 2.20 180° circumferential nozzle passage in single entry turbine blocked off to simulate double entry turbine under partial admission condition
(extract from Mizumachi, Yoshiki and Endoh [50])

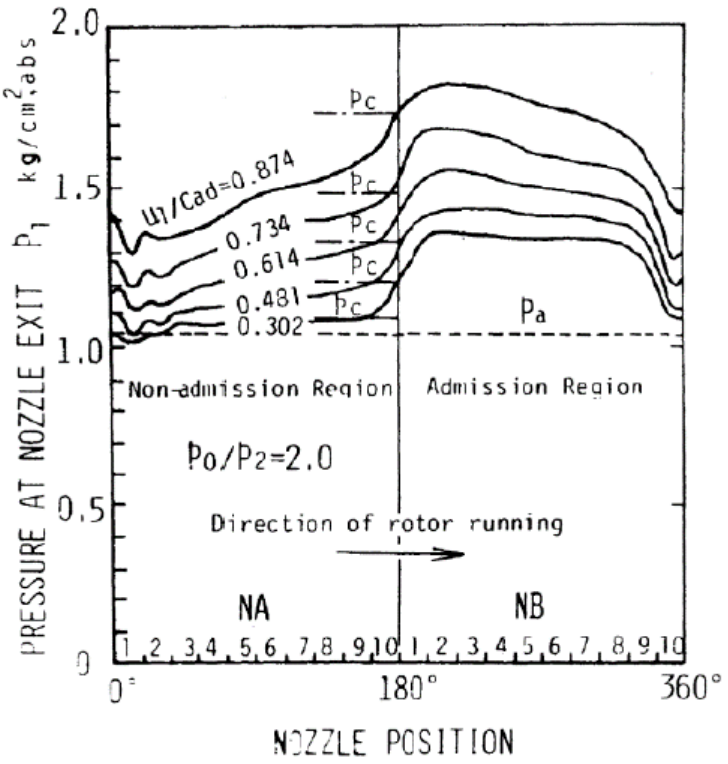


Figure 2.21 Influence of velocity ratio on the circumferential pressure distribution around a rotor with half of the nozzles passage blocked to simulate double entry turbine under partial admission condition *(extract from Mizumachi, Yoshiki and Endoh [50])*

With regards to turbine performance, their conclusion is in agreement with Benson and Scrimshaw [46] as both see an efficiency drop under partial admission. Mizumachi, Yoshiki

and Endoh [50] saw a 19% efficiency drop compared to an 11% drop as reported by Benson and Scrimshaw [46]. Mizumachi, Yoshiki and Endoh [50] also reported that the mass flow characteristic of partial admission surpasses half of that of the full admission measurement at low velocity ratio and the reverse is true at high velocity ratio. This result is definitely interesting as in all experimental work of double entry turbine, the flowing section in partial admission has shown to have higher mass flow rate than half the full admission value for the entire velocity ratio range. Figure 2.22 depicts the corrected mass flow rate against velocity ratio. This condition could have surfaced due to the way the partial admission was simulated using a single entry turbine.

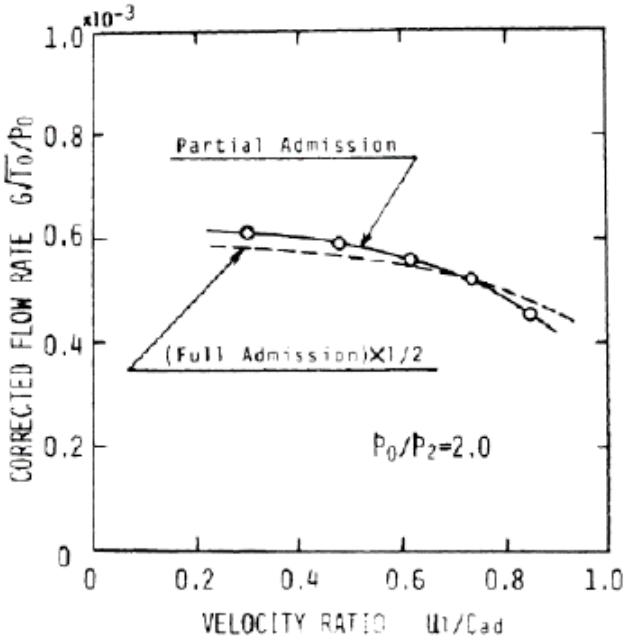


Figure 2.22 Mass flow characteristic of a single entry turbine with half of the nozzles passage blocked to simulate double entry turbine under partial admission condition
(extract from Mizumachi, Yoshiki and Endoh [50])

Copeland et al. [51,52] and Copeland [53] tested extensively a double entry turbine in a cold flow condition, loaded by an eddy current dynamometer at the Imperial College turbocharger test-rig facility. A comprehensive turbine map was developed covering both full and partial admission, besides covering important unsteady operation points. Copeland et al. [51] findings for full admission performance has identical phenomenon as mixed flow turbine, as the efficiency peaks between 0.67-0.68 velocity ratios. During the unequal admission, the pressure ratio is maintained at 2.0 in one entry while varying the other entry from zero to a maximum pressure ratio of 2.6, and maintaining a velocity ratio of 0.65 identical to peak efficiency value under full admission. Similar unequal admission testing was carried out by

reversing the volute scrolls. The unequal admission steady state testing showed good agreement with the findings of Pischinger and Wunsche [49], whereby a 35% efficiency drop is observed between partial and full admission under the same velocity ratio of 0.65 while showing high symmetrical characteristics between two limbs. The major contribution was seen in the unsteady performance assessment of the double entry turbine. They discovered that the cycle averaged unsteady flow efficiency is always lower than the equivalent steady state point and the difference between the two states continued to widen as the turbine speed and pulse frequency decreases.

Copeland et al [51] developed a novel 3-dimensional plot to fully defined operating space of a double entry turbine. This is shown in Figure 2.23, where two axis represents pressure ratio in each limb, and the third characterizes velocity ratio, all measurement obtained in steady flow condition. Comparison with unsteady operating characteristic plotted on the same 3-dimensional space reveals two interesting relationships; operation of in phase unsteady flow stays closer to the full steady condition, while that of out of phase pulsating flow hovers close to the unequal admission.

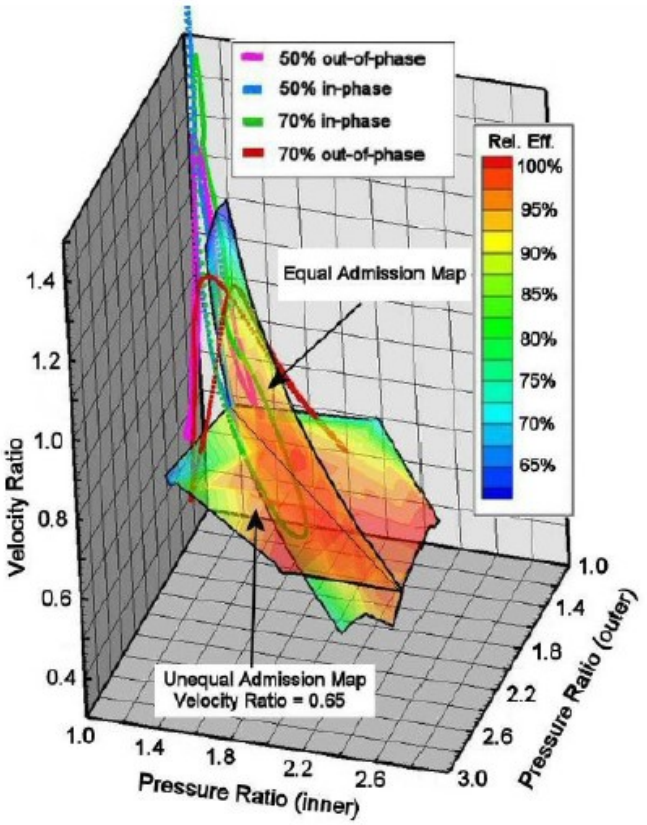


Figure 2.23 Novel 3 dimensional performance plot of a double entry turbine
(extract from Copeland et al [51])

Copeland et al. [52] included additional unequal measurement points at various velocity ratios, to the existing 3-dimensional plot. With this new extension, the plot now represents a full quasi-steady state. This quasi-steady result is compared against cycle averaged unsteady testing results as shown in Figure 2.24. In phase and out of phase have almost similar influence on overall unsteady turbine performance. However, the difference between in phase and out of phase quasi-steady is very significant, with the former recording at least 3 points higher than latter. They postulated that the reduced interaction between the two limbs caused the higher efficiency during unsteady operation than if one presumed a quasi-steady operation.

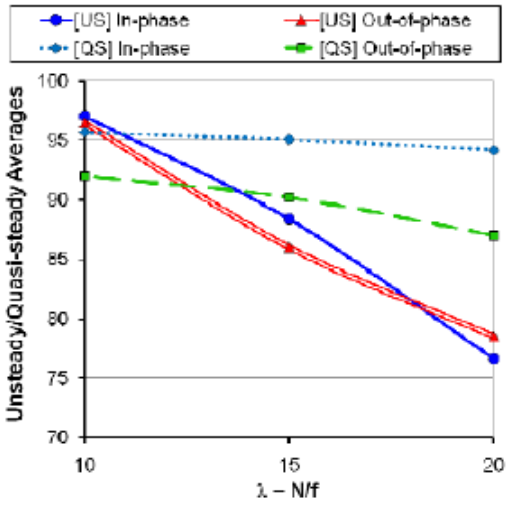


Figure 2.24 Effect of pulse frequency on the unsteady and quasi-steady cycle averaged efficiency of a double entry turbine under pulsating flow condition
(extract from Copeland et al [52])

Newton [18] tested double entry turbine using three different nozzles in steady and pulsating conditions. Unlike the flow inequality which has great influence on turbine performance, nozzle geometry did not seem to create any impact on the efficiency. Interaction between the two limbs increased as nozzle throat area reduced. Nozzle geometry continued to influence the unsteady operation, with the largest throat area recording best cycle average efficiency.

2.4 Pulsating flow testing in radial turbine

Early researchers were limited by many technical limitations, mainly due to the instrumentation available to measure pulsating flow during that point of time. The response time of the instruments was a challenge for parameters such temperature, turbine speed, mass flow rate and torque. As such, these parameters were only measured on an average time basis. On the other hand, pressure was the only parameter that could be measured on a time resolved basis. Going by these limitations, significant number of papers were still published and presented to evaluate the reliability of quasi-steady hypothesis. The assumption states that during quasi-steady state for unsteady flow, the turbine has the identical flow characteristics as in the steady state manner for the same conditions and any point of time. Quasi-steady performance of the turbine and equivalent steady state operating point is calculated using instantaneous static pressure ratios on a time resolved basis whereas temperature and speed are measured using average time for all through the experiments for a pulse cycle. Time averaged turbine performance is thus compared to the cycle average quasi-state values which are integrated using instantaneous quasi-steady state performance of the turbine.

Various studies and research were carried out to evaluate turbine performance in quasi-steady state for unsteady flow using wide range of parameters, pulse frequency, pulse form, pulse amplitude, turbine speed, nozzle angle, pipe length and area, as done by Wallace and Blair [54]. Others were more focused in their parameter selection, Benson and Scrimshaw [46] looked at pulse frequency, while Kosuge et al [55] evaluated the effects of pulse amplitude and Strouhal number and later Benson [56] on pulse shape. Most studies and analysis on the plots were inconclusive and inconsistent, mainly due to the limitations in experimental set ups and instruments available at that time.

A break through was finally seen exactly 30 years ago, when Dale and Watson [57] published unsteady performance of the turbine using the Turbocharger test rig at Imperial College. The rig was equipped with instruments to measure instantaneous mass flow rate and turbine shaft power, and the authors used the adiabatic relationship with pressure to calculate instantaneous temperature. This assumption was later proven valid by Szymko [58]. Turbine loading was provided by an eddy current dynamometer, which has the capability to measure the average torque. With the knowledge of polar moment of inertia and differentiation of the

speed signal, the instantaneous torque is then evaluated. Both torque readings were then added up to provide the values of fluctuating torque delivered by the turbine. A hotwire anemometer was installed and used to measure the mass flow rate across the flow area. Instantaneous non-dimensional mass flow in one limb for a twin entry turbocharger under unsteady flow condition at 40 Hz is presented in Figure 2.25. The unsteady mass flow of mixed flow turbine is shown as a loop around the steady state operations in dashed line, moving away from quasi-steady. Even though, the mass flow average for unsteady is calculated to be close to the quasi-steady flow curves, nonetheless it is one of the initial findings produced to prove that the turbine instantaneous and quasi-steady characteristics are different.

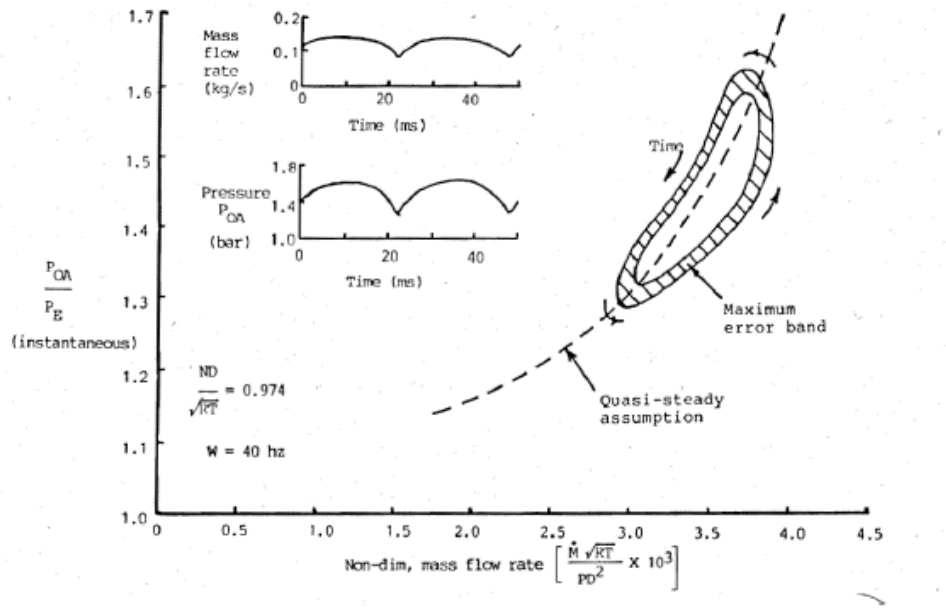


Figure 2.25 Instantaneous mass flow characteristic under in phase pulsating condition *(extract from Dale and Watson [57])*

In the same paper, Dale and Watson [57] has presented the instantaneous efficiency of the turbine under unsteady flow at 40Hz as shown in Figure 2.26. It again produces similar behavior as unsteady mass flow whereby, the instantaneous efficiency of unsteady flow is seen to be forming a loop around steady state, moving away from quasi-steady characteristics. They conclude that the reduction in turbine inlet pressure brings about higher peak efficiency in the unsteady flow region in comparison to steady flow.

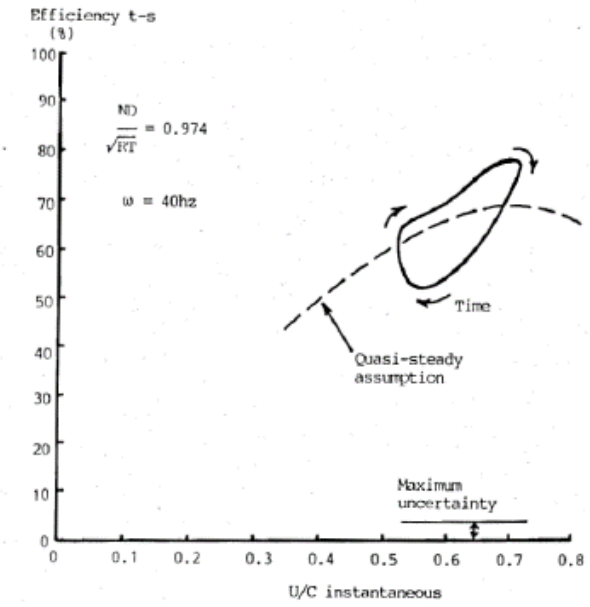


Figure 2.26 Instantaneous efficiency characteristic under in phase pulsating condition *(extract from Dale and Watson [57])*

A few years later, Dale [59] conducted another experiment to review the performance of twin entry turbine under unsteady flow conditions. His findings show a similar hysteresis loop around the steady flow performance plot. According to Dale [59], the main reason behind this observation is due to volute filling and emptying effect.

Using the test-rig setup by Dale [59], Yeo and Baines [60] initiated experimental work to understand internal fluid dynamics inside a twin entry turbine subjected to pulsating flow. Using a Laser-2-Focus (L2F) velocimetry system, the instantaneous measurements were carried out immediately upstream of the rotor leading edge. In order to understand unsteady flow behavior from a steady flow point of view, Yeo and Baines [60] conducted unequal admission testing in steady state condition. As part of the experimental analysis, inlet flow angles of the rotor for different level of flow inequality between two entries were assessed. High variation was seen in the incidence angle when the flow inequality is altered between the limbs. This variation of incidence angle was believed to be responsible for twin entry turbine efficiency deficit. Similar incidence angle variation characteristic was observed in the out-off phase pulsation testing of the twin entry turbine. Additionally, Yeo and Baines [60] discovered that velocity components measured in out of phase conditions are similar to steady flow conditions. It was also observed that the turbine rotor passing frequency is two orders of magnitude larger than pulse frequency. These evidences made remarkable advancement in unsteady flow behavior characterization, which proves that the turbine rotor

is operating under quasi-steady condition, further strengthening the hypothesis produced by Dale [59] that the significant behavior of unsteady flow is due to the filling and emptying of the volute and the rotor wheel has minimal or no impact, a view that is upheld till today. These experimental findings set the foundation for development of an unsteady twin entry turbine model by Baines et al [61], which was found to be in good agreement with former. Although instantaneous swallowing capacity plot for each limb of the twin entry turbine shows similar hysteresis loop as Dale and Watson [57], a secondary loop was noticed within the low pressure region of each curve presented by Baines et al [61].

The first ever measurement of instantaneous performance of a mixed flow rotor under unsteady flow conditions was carried out by Arcoumanis et al [62]. According to them, instantaneous performance loops of a mixed flow rotor under pulsating flow shows similar trend as that of a radial inflow turbines; with the former recording, higher overall efficiency than the latter. The increase in efficiency was mainly attributed to the rotor geometry at the leading edge of the mixed flow turbine.

The Imperial College test rig was later fitted with a Laser Doppler Velocimetry (LDV) system in 2001 by Karamanis, Martinez-Botas and Su [63] to measure instantaneous velocity components at the inlet and outlet of the rotor, with a sole purpose of investigating and understanding unsteady flow inside a mixed flow turbine. The LDV was used to measure both steady and unsteady inlet conditions in a mix flow turbine. Again, a large variation in incidence angle of -80° to +40° was observed at inlet to the rotor during entire pulse cycle of the unsteady operation, depicting similar results as radial flow turbine reported by Yeo and Baines [60]. The effect includes a loop of the unsteady operating line around the steady performance curve.

Szymko et al [64] made a major development in 2002, to the Imperial College test rig when a new eddy current dynamometer was installed to enable wider range of loading on the turbine than a conventional compressor. This is essential in studying the turbocharger characterization when dealing with pulsating flow, as the boundary conditions for the turbine extends intermittently beyond the range of steady turbine maps. Szymko [58] in his thesis indicates that this revolution provides an insightful and “true” quasi-steady state performance under pulsating flow, which was never done before.

In pursuit to define level of unsteadiness in turbocharger turbine subjected to pulsating flow, Szymko [58] defined 3 modes of unsteady criterion. The first mode, with ***St* <0.1***, is defined as quasi-steady operation, where the unsteady hysteresis loop overlaps the steady state characteristic curves. In the second mode, presence of hysteresis loop encapsulating the steady state curve is clearly seen. This mode which represents filling and emptying of the turbine volute, is given by ***St*>0.1>PMSt***. Finally, the hysteresis loop goes through significant shape change in the third mode, moving away from the steady state line and defined by ***PMSt > 0.1***. In this mode, unsteadiness is significantly dominated by wave dynamics in the turbine volute.

Costall et al [65] used a 1 dimensional computational model to verify the unsteady flow findings by Szymko [58]. 1D wave action calculation, shows good agreement with experimental result, at 20 Hz pulse frequency. However, the disparity between computational and testing values becomes wider with increase in pulse frequency. Building on the pressure modified strouhal ***PMSt*** number suggested by Szymko [58], Rajoo and Martinez-Botas [45] investigated the effect of vane angle opening on level of unsteadiness in a mixed flow turbine. According to them, level of unsteadiness is determined by vane angle setting, and concluded that this does not fit into unsteady criterion proposed by Szymko [58]. This is depicted in Figure 2.27.

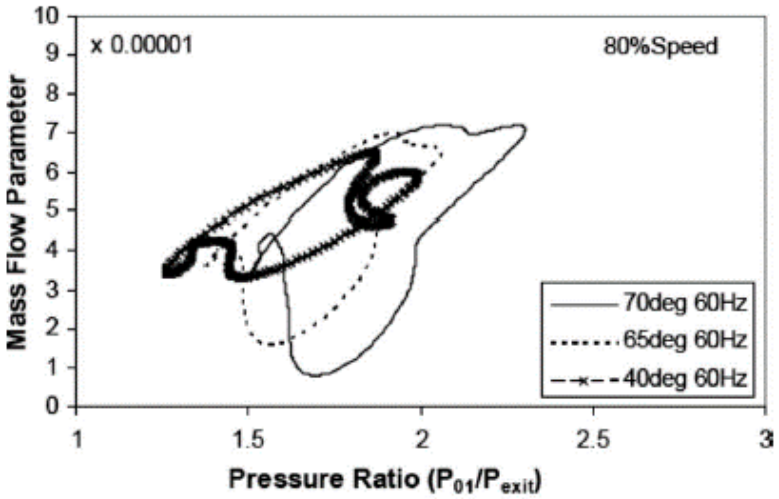


Figure 2.27 Instantaneous mass flow characteristics for various nozzle vane angles
(extract from Rajoo and Martinez-Botas [45])

2.5 Pulsating flow simulation in radial turbine

Research, in the 1970s and 1980s, on mixed flow turbine has only focused on steady state exhaust gas flow. Measurement techniques and computational resource were limited to investigate, experimentally and numerically, unsteady flow at that time due to the complexity of pulsating flow. However, owing to the advances in instrumentation and computational code in the last 2 decades, it has been possible to determine unsteady flow characteristics and performance through experimental and numerical work. The advances in computational resources are largely influenced by the growing need to understand the unsteady flow effects in an automotive turbocharger during the said period.

Chen and Winterbone [66] developed a one-dimensional unsteady code to model and analyze the flow in a radial turbine. Chen et al. [67] modified the one-dimensional unsteady code developed by Chen and Winterbone [66] to model the flow in a scroll and a mixed flow rotor. Although the rotor was assumed to behave in a quasi-steady manner, due to limitation in computational resources at that time, the numerical prediction obtained by Chen et al. [67] was at good agreement with experimental measurements. Adopting an analysis model with a four step Runge–Kutta scheme, Abidat et al. [68] managed to prove that closer prediction to that of the measurement can be obtained. According to Abidat et al. [68], the improvement in his prediction is contributed by the second order accuracy in time of the four step Runge-Kutta scheme, as opposed to first order accuracy in method used by Chen et al. [67]. Unsteady turbine performance obtained in an experiment takes the form of hysteresis loop. Abidat et al. [68] successfully duplicated this hysteresis loop by purely using one dimensional code and taking into account difference in phase between mass flow and the pressure pulse in unsteady condition.

Although the one-dimensional codes developed by [68, 67] were successful in predicting unsteady performance in a mixed flow turbine with good accuracy, but the actual three-dimensional flow phenomena in a mixed flow rotor, which is vital in rotor design, remains unexplained. The internal flow measurements in the region just upstream of the rotor and the rotor passage were impossible despite having very accurate instrumentation during that period and it remains the case today due to high speed rotation of the rotor. If the entire three-dimensional domain of the volute and mixed flow rotor were modelled correctly, numerical simulation would provide an accurate flow model. This comes with huge

computational and design time resources, which indeed requires a high amount of investment.

Palfreyman and Martinez-Botas [40] were among the first workers to model a true three-dimensional full unsteady flow analysis in a mixed flow turbine. In order to identify minimum mesh density required for convergence and accurate results, Palfreyman and Martinez-Botas [40] simulated the unsteady effect using four mesh densities; 50,000, 200,000, 850,000, and 1,750,000 cells. The simulation model and boundary condition were based on Karamanis et al. [63] mixed flow turbine geometry and measured parameters, respectively. The computation which was conducted using two domains; the stationary nozzleless volute domain and rotating rotor domain, captured unsteady flow phenomena in mixed flow turbine.

Detail comparison by Palfreyman and Martinez-Botas [40] revealed that computed torque to be higher than the measured value by Karamanis et al. [63]. According to the authors, the inertia of the rotating assembly has 'dampened' the experimentally measured torque and this has been identified as the main reason for the difference. Furthermore, the blade torque and loading were found to fluctuate in accordance with the pulse frequency. These findings are a true representation of unsteady pulsating flow effect on a turbine operation. Thorough understanding of the simulation results has revealed that during high pressure ratio operation, the flow at the rotor inlet was found to be poorly guided. These findings agree with the Laser Doppler Velocimetry (LDV) measurement made by Karamanis et al. [63]. This clearly shows that a specially designed nozzle rig was needed to optimize the unsteady flow direction into the rotor of mixed flow turbine, as the nozzleless volute in the analysis has been proven to be insufficient in guiding the flow into the rotor. However, the computational prediction of instantaneous mass flow parameter and efficiency has deviated from the experimental characteristics. Besides the valuable scientific findings, Palfreyman and Martinez-Botas [40] has demonstrated that with proper availability of computational and time resources, unsteady flow computation in the mixed flow rotor is achievable.

Hellstrom [69] unsteady calculation findings has excellent resemblances to that of Palfreyman and Martinez-Botas [40]. Although his pulsating flow boundary condition is based on engine operating parameter, as shown in Figure 2.28, the computational model has shown significant incidence angle variation that spreads over the pulse cycle. According to

him, due to the phase shift difference between pressure pulse and mass flow pulse, the turbine cannot be treated as quasi-steady. Apart from this observation, his findings also conclude that nature of pressure field and acceleration state of the rotor wheel dictates the flow dynamics within the rotor passage.

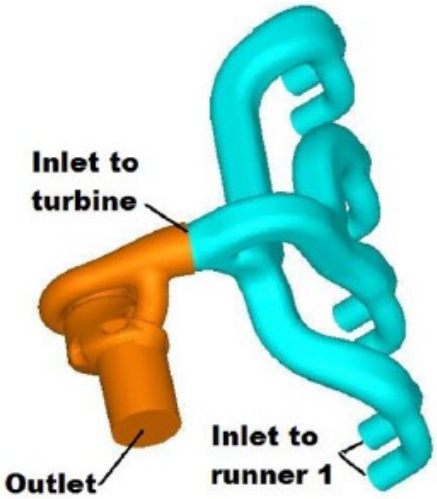


Figure 2.28 Computational domain modelled by Hellstrom *[69]*

Copeland et al [70] presented the findings of the very first 3 dimensional CFD calculation of flow inside a double entry turbine. Although the calculated efficiency is lower than that of the measurement [51,52], the former follows the trend of the latter very well. On the other hand, for the mass flow parameter, CFD calculation predicted well the measured values. In order to investigate mass flow interaction between two limbs, they presented streamline plot as shown in Figure 2.29. Comparing streamlines emanating from final nozzle vane in the high pressure limb (unequal admission) and equal admission, they concluded that the capability of the turbine to pass more mass in the high limb is due to the interaction between two limbs. Finally, they divided the turbine into several divisions to determine entropy change in each division for both partial and full admission condition. The entropy increase is shown in Figure 2.30. Overall entropy generated in the partial admission state is twice that for the full admission, mainly due to high entropy increase in rotor domains, interspace and nozzle divisions.

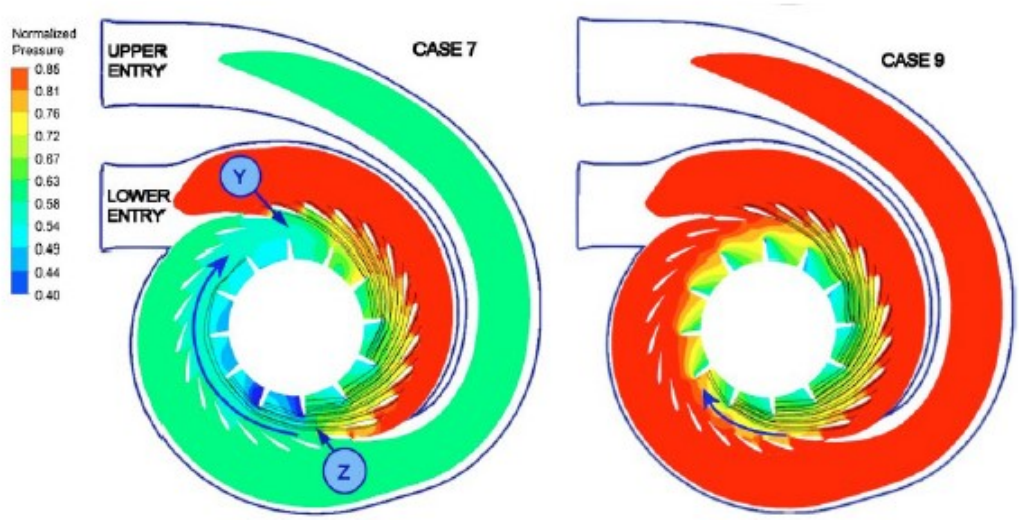


Figure 2.29 Computational Stream line plot in double entry turbine
(extract from Copeland et al [70])

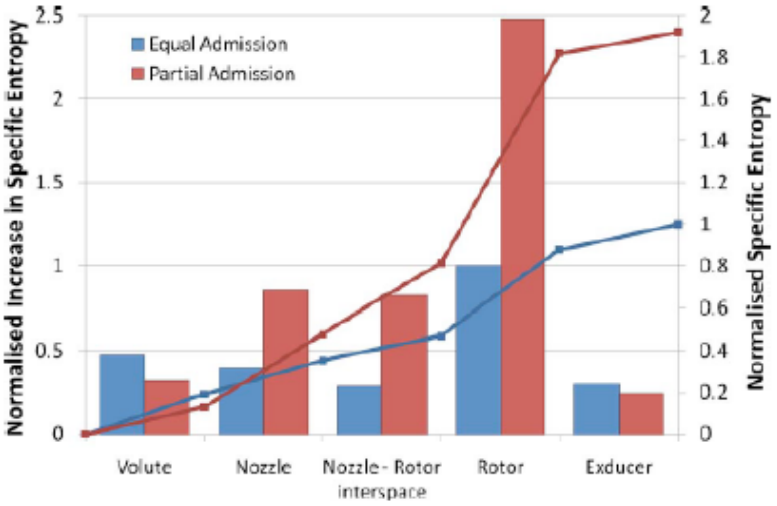


Figure 2.30 Computational entropy rise comparison between equal and partial admission condition in a double entry turbine *(extract from Copeland et al [70])*

Padzillah et al [71] took advantage of the vast test measurement data obtained by Rajoo and Martinez-Botas [45], to validate their CFD and thus understand flow field in a single entry turbine with lean nozzle vanes designed by the latter. Excellent agreement existed between the calculation and the experimental results. As for the unsteady flow analysis, for the very first time, authors used two different method to determine instantaneous efficiency by referring isentropic and measured power at the same axis. They found that disparity between the two methods is very small. Apart from that, their computational work also shows that the incidence angle variation causes deficit in turbine instantaneous performance. This is

clearly shown in Figure 2.31. Also shown in this figure is two different zone of incidence angle, region of which corresponds to region of peak efficiency and region where maximum pulse energy is contained.

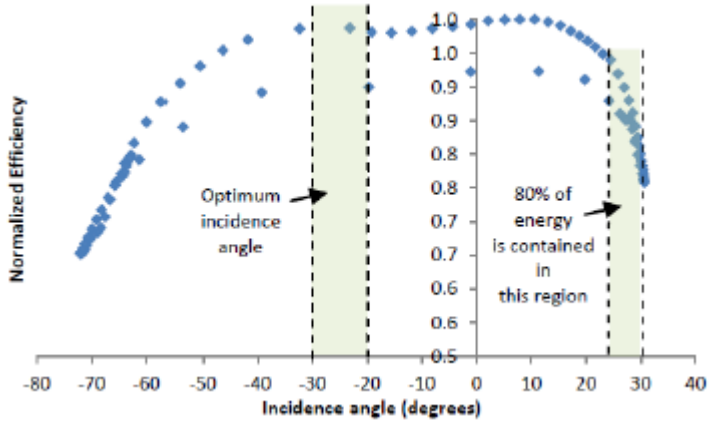


Figure 2.31 Computational instantaneous efficiency vs. incidence angle in a single entry turbine *(extract from Padzillah et al [71])*

Newton [18] undertook detailed CFD calculations to investigate further the entropy generation in the double entry turbine, advancing the work done by Copeland [53]. Although Newton [18] investigated three different nozzles and measured their respective steady and unsteady condition parameters, the computational simulation was only undertaken for one of the nozzle configuration. Steady state 3D calculation has over predicted the efficiency characteristic, while has reasonably good agreement with the swallowing capacity. As for the pulsating flow calculation, model has predicted very well the instantaneous mass flow parameter. Newton [18] has divided the turbine into very detail section, one step further to the work done by Copeland [53], to carry out turbine loss auditing. This is shown in Figure 2.32 and 2.33. His unsteady flow entropy generation is higher than the steady state counterpart, owing to increase in the nozzle-rotor interspace region. Furthermore, Newton [18] echoed Copeland's [53] postulation that the rotor behaves almost close to quasi-steady.

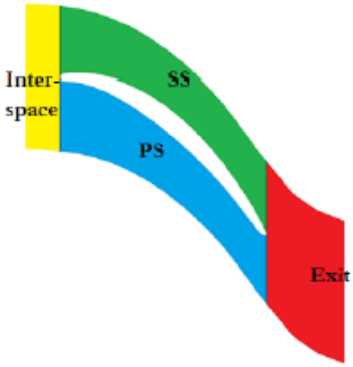


Figure 2.32 Rotor blade passage domain dissected in the blade-to-blade orientation; Suction Side (SS), Pressure Side (PS) *(extract from Newton [18])*

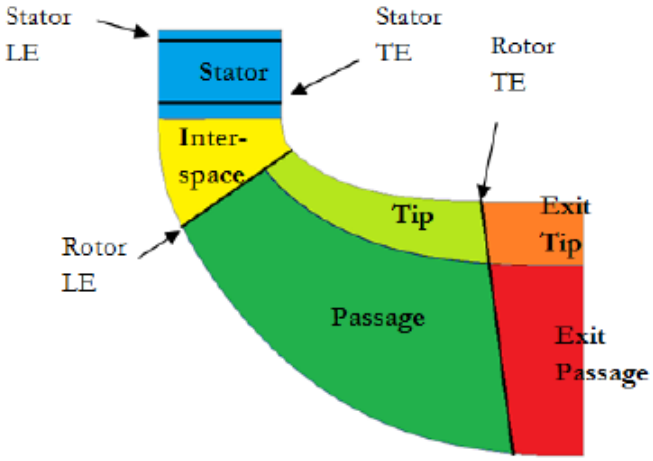


Figure 2.33 Rotor passage and volute domain dissected in the meridional view *(extract from Newton [18])*

2.6 Summary

Based on the review in the preceding section, it has been found that the mixed flow turbine has been proven to operate efficiently in high pressure ratio compared to its radial counterpart [20, 21]. This has driven numerous research works to further realize and enhance the full potential of a mixed flow turbine. One of the most recent and widely explored technologies in turbocharging is VGT. Although many studies were carried out on VGT, only a handful of them [42,43,45] actually investigated the lack of flow guidance arising from the uneven interspace between the trailing edge of the nozzle vane and the leading edge of the mixed flow rotor. Initiated by Wallace and Pasha [20] and Karamanis et al. [63],

Palfreyman and Martinez-Botas [40] computational work has clearly indicated the need for VGT to properly guide the flow into a mixed flow turbine under pulsating flow conditions. However, all the research work pertaining to VGT were very focused on enhancing the flow incidence angle in a single entry turbine, especially in pulsating flow conditions, where pulse energy extraction takes place.

In the actual turbocharger turbine coupled to an ICE, exhaust pulses emanating from different cylinders of the engine needs to be separated, to maximize pulse energy extraction by the turbine rotor. This in turn prevents flow mixing, which if not taken care would be detrimental to the stage performance. This is something that single entry turbines cannot achieve, as the exhaust manifolds from different banks of the ICE merges into one before being coupled to the turbine entry. Hence, the turbine with multiple entries, namely double entry, are preferred over single entry.

Research on double entry turbines commenced 5 decades ago, when Benson and Scrimshaw [46] conducted full and partial admission experimental work and reported performance deficit in partial admission relative to the full admission efficiency. This motivated a great deal of double entry performance map characterization to be made available in the public domain as a result of extensive research work conducted under various steady and unsteady flow configuration. The similarity among all these research work is the significant drop in efficiency when the turbine is operated between the full admission and partial admission condition. The pressure or mass flow inequality between entries increases efficiency drop in steady state conditions. Additionally, double entry turbine measurement in pulsating flow conditions too reveals a performance deficit; but with a very small disparity in cycle averaged efficiency between in phase and out of phase.

Unfortunately, the research conducted to date, was only motivated to understand the flow phenomena in a double entry turbine with equal circumference divisions. Apart from work done by Newton [18], there is no information available in the public domain to address the influence of nozzle vane opening on double entry turbine stage performance, operated in both steady and unsteady flow environment. Furthermore, none has attempted to study the effect of having distinct nozzle vane angle setting in each circumferential division. What more, when the circumferential division is unequal as in the case of asymmetric double entry turbine. Owing to the unequal circumferential division, the asymmetric double entry would

behave in unequal admission condition when one entry has more mass than the other, in the presence of additional extraction, such as when EGR is widely operated in one manifold. Apart from that, influence of inequality between entries and thus interaction between them, when operated in unequal and partial admission is not currently available in the public domain. Furthermore, unsteadiness caused by this unequal scroll division under pulsating flow environment is expected to be different than conventional double entry turbine. Until complete steady and unsteady characterizations are made available via extensive laboratory measurement, the gap in literature on asymmetric double entry turbine is to remain for years to come. This will not only hinder the advancement of double entry turbine scientific finding, but also constraint the engine downsizing and turbocharger – engine matching effort.

CHAPTER 3

ASYMMETRIC DOUBLE ENTRY TURBINE DESIGN

This chapter presents the design of a novel asymmetric double entry turbine volute and vane angle control mechanism. The new volute geometry was derived from Rotor 'A' specification, which was designed by Abidat [72]. Mean line analysis was used to determine stage performance for various circumferential divisions, before arriving at the current unequal scroll design. The original design consisted of a single vane control ring mechanism to regulate the vane angle setting in the turbine. A dual ring control mechanism was later designed and fabricated to enable testing of different vane angle settings in the turbine.

3.1 Asymmetric Volute Design

The rotor and volute are the two principal features of a turbocharger turbine. The primary function of a rotor is to convert exhaust gas energy into shaft rotational energy to power a compressor. The volute is responsible for distributing the flow around the circumference of the rotor as well as to accelerate the flow. In a turbine fitted with a nozzle vane ring, nozzle vanes accelerate the flow into the rotor at the correct incidence angle. Meanwhile, in a nozzleless turbine, it is the sole responsibility of the volute to maintain the swirl component already present in the flow while setting the flow angle at the rotor inlet. In either configuration, nozzled or nozzleless, the volute is a vital component as it determines the volute exit flow angle to the next downstream component; nozzle vanes in former and rotor in latter. Since the volute design is central in the overall turbine development, significant attention has been given in this thesis for this purpose.

3.1.1 Optimum circumferential division

The current design practice in the turbomachinery industry still relies on steady state analysis of the turbocharger. Additionally, matching of the turbocharger to the engine is done by assuming the turbine to be a steady flow device. This makes the mean line method a suitable choice in performance prediction of turbines as it only relies on solution of turbomachinery equations in the steady state condition. Furthermore, the mean line model relies on very little geometrical conditions of the turbine and requires less computational resources than existing CFD calculations. This makes the mean line analysis the most widely used method in the automotive turbocharging industry in the initial design stage. Due to these considerations, the mean line method has been adopted in the preliminary design stage of this asymmetric double entry turbine. Sakai et al [17] used the mean line model developed and validated by Romagnoli and Martinez-Botas [73] in selecting the optimum circumferential divisions between scrolls.

The turbine is divided into four main stations and eight sub-stations as shown in Table 3.1. The eight stations are shown in Figure 3.1. The loss model used in each station are listed in Table 3.2.

Table 3.1 Mean line model stations

Main Station	Sub-Station Number		Description
	Large scroll	Small scroll	
Volute	0-L	0-S	Turbine inlet
	1-L	1-S	Volute inlet (tongue)
Vane	2-L	2-S	Vane inlet
	3-L	3-S	Vane exit (upstream)
	4-L	4-S	Vane exit (downstream)
Rotor	5-L	5-S	Rotor inlet
	6-L	6-S	Rotor exit (upstream)
Rotor exit	7-L	7-S	Rotor exit (downstream)

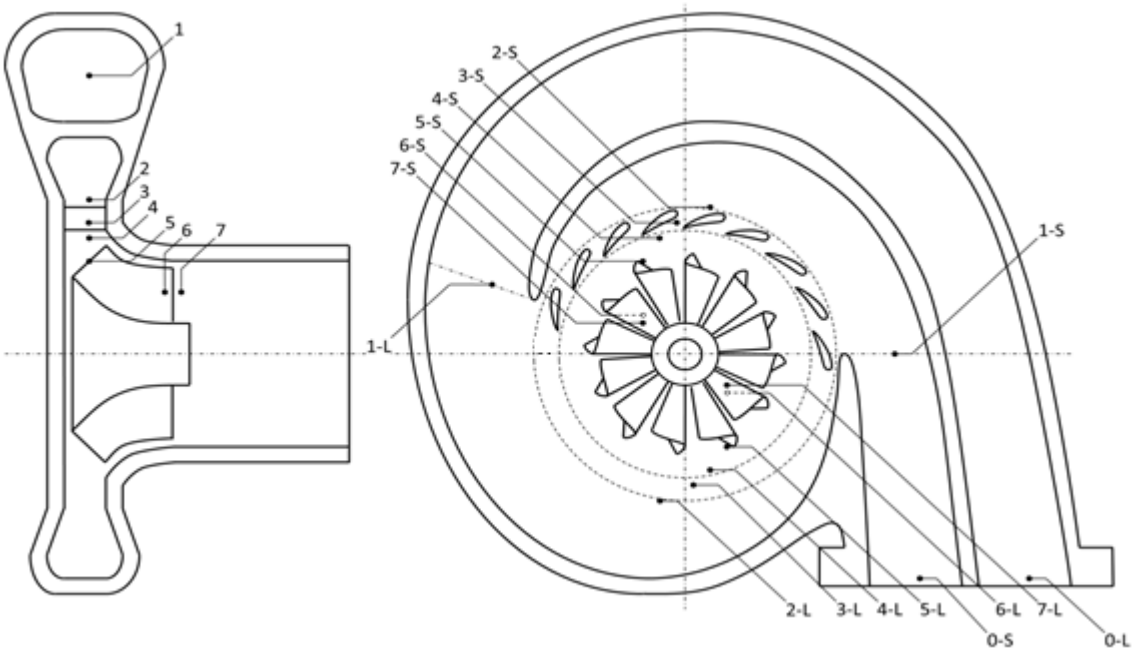


Figure 3.1 Mean line model sub-station in asymmetric double entry turbine

Table 3.2 Losses according to station

Loss models	Station (Sub station)	Actual loss accounted
Pressure loss	Volute (0 – 2)	Pressure loss
Friction loss	Volute (0 – 2)	Pressure loss
Secondary flow and boundary layer growth loss	Vane (2 – 3)	Pressure loss
Nozzle loss	Vane (2 – 3)	Pressure loss
Nozzle leakage loss	Vane (2 – 3)	Pressure loss
Incidence loss	Rotor – Leading edge (5)	Power loss
Clearance loss	Rotor (5 – 6)	Power loss
Passage loss	Rotor (5 – 6)	Power loss
Disc friction loss	Rotor (5 – 6)	Power loss

Sakai et al [17] used a mixed flow rotor (known as rotor 'A' by the Imperial College Turbocharger group, Abidat [72]) for this optimisation of the volute geometry. The geometry details of rotor 'A' are given in Table 3.3 and is shown in Figure 3.2. Velocity triangles, at inlet and exit of the rotor is depicted in Figure 3.3.

Table 3.3 Rotor 'A' Geometrical Dimension

Geometric Feature	Dimension
Leading Edge Tip Diameter	95.14mm
Leading Edge Span Height	18mm
Rotor inlet width (axial direction)	13.79mm
Trailing Edge Tip Diameter	78.65mm
Trailing Edge Span Height	25.79mm
Cone Angle	40°
Leading Edge Blade Angle	20°
Root Mean Radius at Trailing Edge Blade Angle	52°
Length of Axial Chord	40mm
Number of rotor blades	12
Tip Gap Height (% blade span)	3%

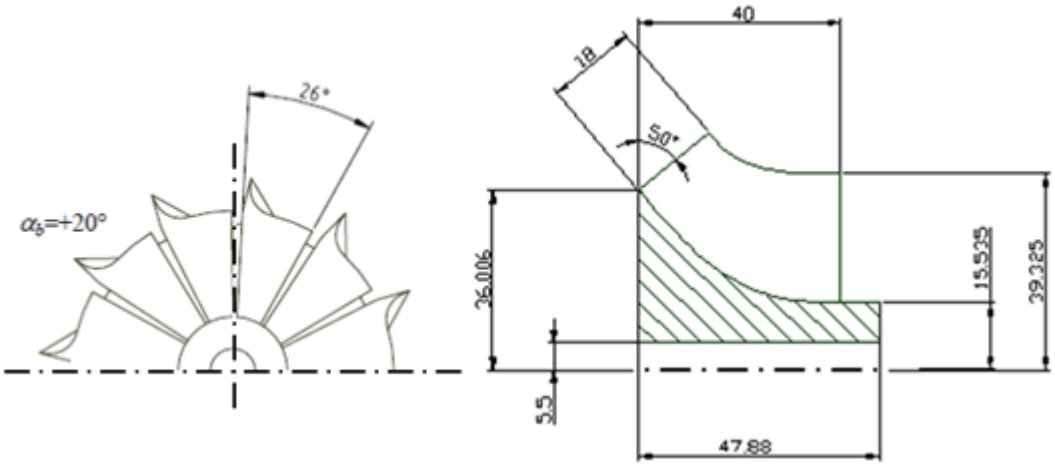


Figure 3.2 Mixed Flow Rotor 'A' *(extract from Rajoo [7])*

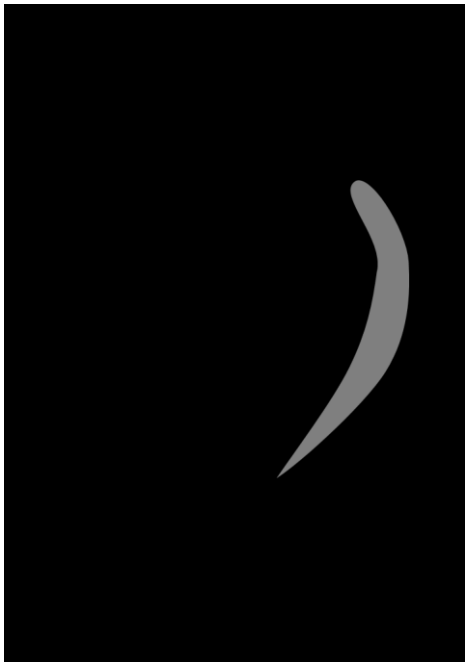


Figure 3.3 Velocity triangle at inlet and outlet of the blade

Sakai et al [17] modified the mean line by Romagnoli and Martinez-Botas [73], to evaluate the preliminary performance of the asymmetric double entry turbine. In his model, Sakai et al [17] calculated the efficiency of the small and large scroll individually before evaluating the overall stage efficiency using mass flow weighted average method, as given by equation (3.1).

$$\eta = \frac{\dot{m}_S (\eta_{ts})_S + \dot{m}_L (\eta_{ts})_L}{\dot{m}_S + \dot{m}_L} \tag{3.1}$$

Efficiency of several circumferential divisions were calculated and compared with that of a single entry VGT [7], fitted with the same rotor wheel. A new term ideal Exhaust Gas Recirculation (iEGR) is defined and used here instead of EGR. Since the latter is concerned with the actual mass flow that varies with engine condition, the former is more appropriate to be used here as the mass flow conditions in this research are assumed on a fixed engine condition. Top three configurations with optimum mass weighted efficiency for a range of iEGR rates are shown in Figure 3.4. Configuration 180 : 180 refers to a symmetric double entry turbine (with equal circumferential division), while setting 135 : 225 corresponds to an asymmetric double entry turbine with 135° and 225° circumferential division in the small and large scroll respectively. It is very apparent that 160 : 200

configuration maintains a constant optimum performance for wide range of iEGR rates. This configuration has recorded an improvement close to 3% for iEGR rates between 0% and 40%. Therefore, small scroll with 160° and large scroll with 200° circumferential division are selected as the final configuration for this asymmetric double entry turbine.

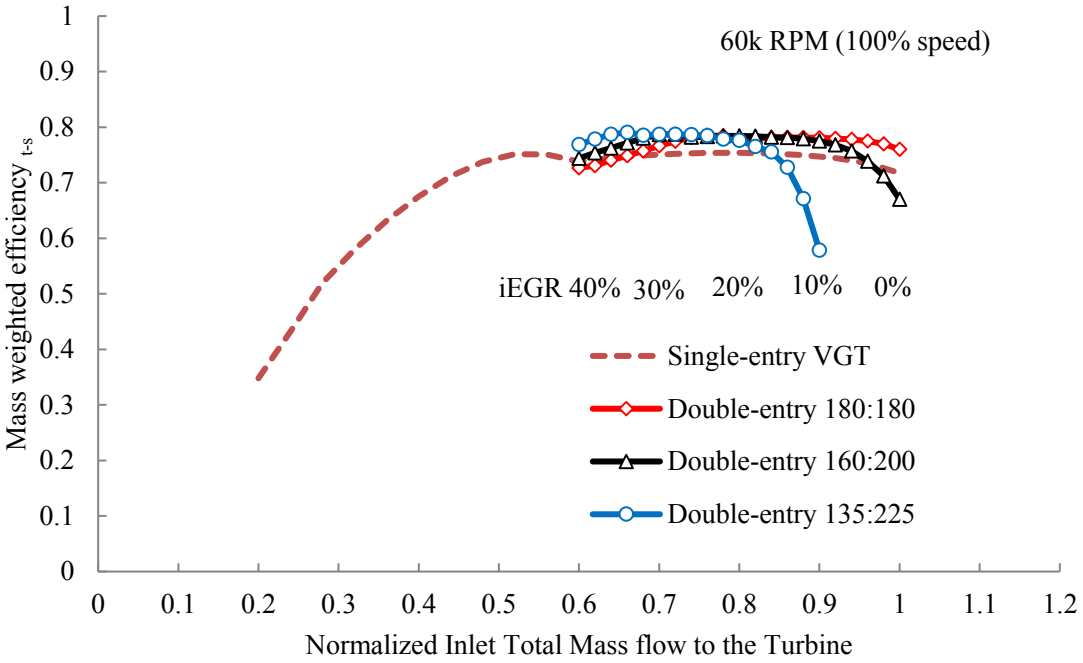


Figure 3.4 Mean line model predicted *(extract from Sakai et al [17])*

3.1.2 Volute cross sectional area (A/R)

Since the aim of this research is to characterize asymmetric double entry turbine, the volute was not designed to meet any existing symmetric turbine scroll specification as a baseline. The volute design, namely $\frac{A}{r}$ ratio is derived from optimum circumferential divisions and volute exit flow angle in [7].

Equation (3.2) shows the conservation of angular momentum when applying free vortex conditions. Volute tongue at azimuth angle, $\psi = 0$, has been fixed as station 1 as shown in Figure 3.5. At the volute tongue, $C_{\psi=0} = C_1$, leading to equation (3.3):

$$r_\psi C_\psi = K \tag{3.2}$$

$$r_1 C_1 = r_{\psi 2} C_{\psi 2} \tag{3.3}$$

where $r_{\psi 2}$ is the centroid radius of cross sectional area at azimuth angle ψ .

The flow is assumed to be evenly distributed around the periphery of the rotor by the volute, equation (3.4)

$$\dot{m}_\psi = \dot{m}\left(1 - \frac{\psi}{2\pi}\right) \tag{3.4}$$

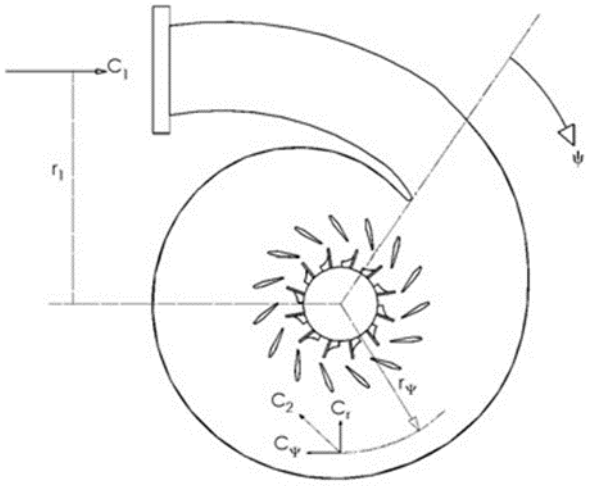


Figure 3.5 Turbine Volute's Radius And Velocities *(extract from Rajoo [7])*

Combining the above equations with the conservation of mass, it is possible to obtain the relation below that governs the local distribution of $\frac{A}{r}$:

$$\frac{A_\psi}{r_\psi} = \frac{\dot{m}}{\rho_\psi K}\left(1 - \frac{\psi}{2\pi}\right) \tag{3.5}$$

Equation (3.5) shows that in order to achieve a uniform mass flow distribution along the volute passage, the area-radius ratio must change with azimuth angle ψ . This provides the fundamental guideline for the volute cross sectional area around the rotor.

It is then possible to show that the volute exit angle is directly related to the $\frac{A}{r}$ of the volute, as per equation (3.6); this analysis has assumed a constant density flow.

$$\tan\alpha_2 = \frac{\left(\frac{A_2}{r_2}\right)}{\left(\frac{A_1}{r_1}\right)} \tag{3.6}$$

For a double entry turbine, a similar approach is possible by considering each volute entry separately, in here the interaction between the entries is not accounted for. Additional subscript S (small) and L (large) are employed to represent the two entries in the volute, as shown in Figure 3.6. The purpose of the new proposed design is to achieve uniform inlet conditions to the rotor, this is shown in equation (3.7). When this equation is set in terms of area-radius ratio, one arrives at equation (3.8).

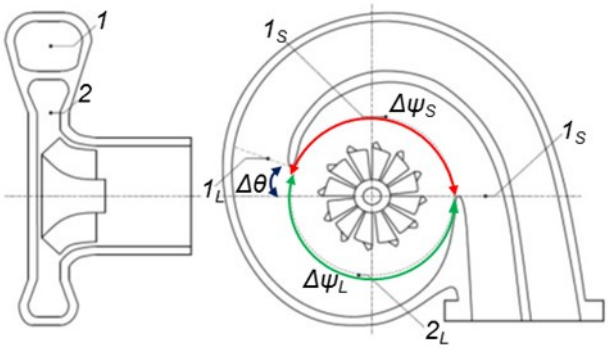


Figure 3.6 Asymmetric Double Entry Turbine cross section

$$\tan(\alpha_2)_S = \tan(\alpha_2)_L \tag{3.7}$$

$$\frac{\left(\frac{A_2}{r_2}\right)_S}{\left(\frac{A_1}{r_1}\right)_S} = \frac{\left(\frac{A_2}{r_2}\right)_L}{\left(\frac{A_1}{r_1}\right)_L} \tag{3.8}$$

Numerators on both sides of equation (3.8) can be simplified as in equation (3.9) and (3.10),

$$\left(\frac{A_2}{r_2}\right)_S = \frac{\Delta\psi_S (r_2)_S b_2}{(r_2)_S} = \Delta\psi_S b_2 \tag{3.9}$$

$$\left(\frac{A_2}{r_2}\right)_L = \frac{\Delta\psi_L (r_2)_L b_2}{(r_2)_L} = \Delta\psi_L b_2 \tag{3.10}$$

It is now possible to introduce the azimuthal location of the tongue of the two volutes ($\Delta\psi_S, \Delta\psi_L$). Equation (3.11), below governs the location of the volute tongue in a double entry turbine.

$$\frac{\left(\frac{A_1}{r_1}\right)_S}{\left(\frac{A_1}{r_1}\right)_L} = \frac{\left(\frac{A_2}{r_2}\right)_S}{\left(\frac{A_2}{r_2}\right)_L} = \frac{\Delta\psi_S}{\Delta\psi_L} \tag{3.11}$$

The optimum volute exit flow angle obtained by Sakai et al [17] from his mean-line analysis is $70.9°$. Therefore substituting $\alpha_2 = 70.9°$ into equation (3.7) yields equation (3.12).

$$\frac{\left(\frac{A_2}{r_2}\right)_S}{\left(\frac{A_1}{r_1}\right)_S} = \frac{\left(\frac{A_2}{r_2}\right)_L}{\left(\frac{A_1}{r_1}\right)_L} = \tan(70.9°) \tag{3.12}$$

Since unequal circumferential division of 160° and 200° has proven to give 3 point higher efficiency in the previous section, $\Delta\psi_S = 160°$ and $\Delta\psi_L = 200°$ together with rotor width $b_2 = 13.79mm$ (from Table 3.3) are substituted into equations (3.9) and (3.10) to give the following equations (3.13) and (3.14),

$$\left(\frac{A_2}{r_2}\right)_S = \left(\frac{160}{180}\pi\right)(13.79mm) = 38.51mm \tag{3.13}$$

$$\left(\frac{A_2}{r_2}\right)_S = \left(\frac{200}{180}\pi\right)(13.79mm) = 48.13mm \tag{3.14}$$

Substituting equations (3.13) and (3.14) into equation (3.12), yields the following $\left(\frac{A_1}{r_1}\right)$ for each scroll

$$\left(\frac{A_2}{r_2}\right)_S = 13.33mm \tag{3.15}$$

$$\left(\frac{A_2}{r_2}\right)_S = 16.67mm \tag{3.16}$$

Figure 3.7 shows $\frac{A}{r}$ plotted against azimuth angle, ψ. $\frac{A}{r}$ for a single entry turbine [7] has been shown on the same scale for comparison purpose. Since same rotor 'A' and volute exit flow angle are used, $\frac{A}{r}$ for asymmetric double entry turbine is parallel to that of the single entry. This relationship between A and r is used in the next section to determine volute geometry and dimensions.

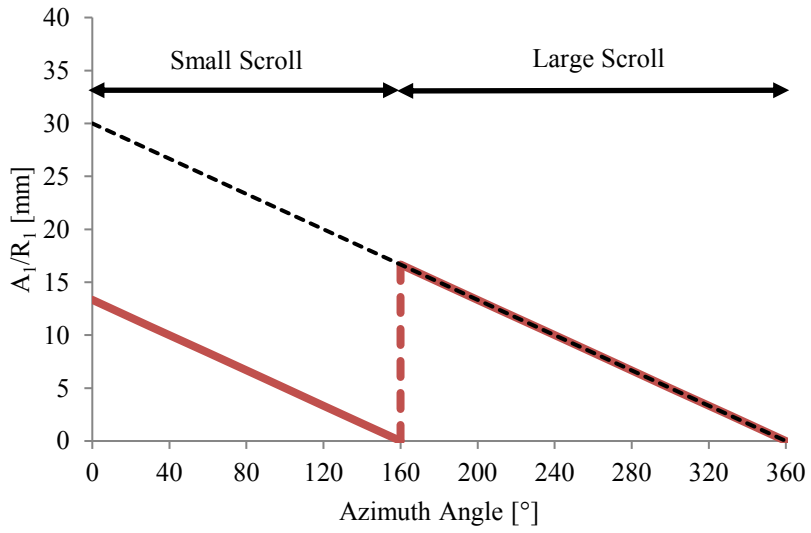


Figure 3.7 A/r : Asymmetric double entry turbine vs. single entry turbine
(extract from Sakai et al [17])

3.1.3 Volute 3D geometry and dimensions

In order to ensure smooth flow of air without significant separation at the exit section, selection of volute cross sectional shape requires good design guidance. Some of the typical cross sectional shapes for turbine volutes are shown in Figure 3.8. Volute with profile shape (I) in Rajoo [7] has been proven by Padzillah [74] to preserve smooth air flow throughout the volute cross section. This is shown in Figure 3.9, where the velocity is evenly distributed along the volute circumference, with an exception at tongue area. Therefore, as for the asymmetric double entry volute design, the cross-sectional shape (I) in Figure 3.8 is chosen. Since the volute inlet is of a rectangular cross section and volute tongue is of a profile shape (I), a converging passage between the former and latter is generated as shown in Figure 3.10.

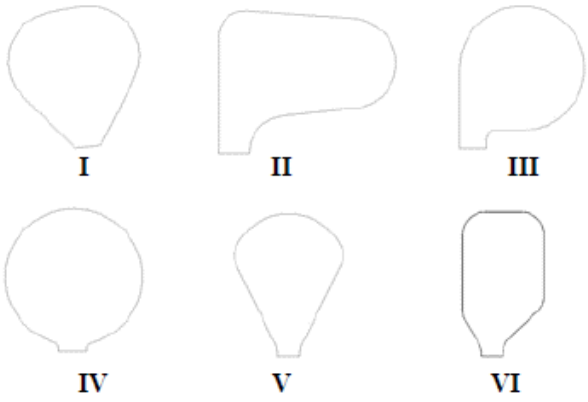


Figure 3.8 Typical volute cross sectional shapes *(extract form Rajoo [7])*

$\frac{A}{r}$ in equation (3.15) and (3.16) are used in calculating cross sectional dimension in each scroll of the volute. This is achieved by first locating the tongue position of the small scroll. Once this has been done, large scroll tongue positon can be positioned at an azimuth location of 160° relative to small scroll tongue. Based on the test-rig physical dimension (refer Figure 3.11), the small scroll tongue is positioned at 0°, parallel with volute inlet plane. Now that the position of first and second tongue location has been determined, the next step would be to decide the appropriate value for $r_{\psi=0}$ in both scrolls.

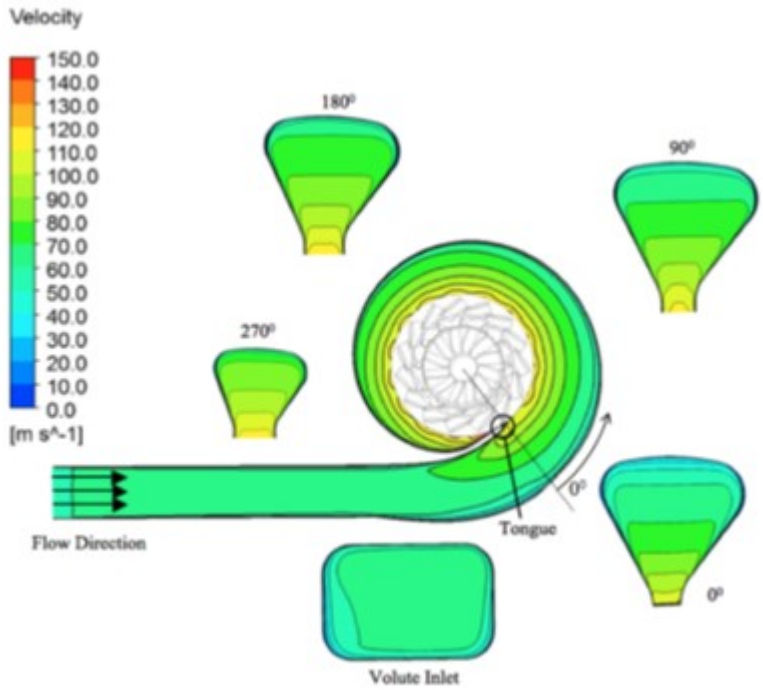


Figure 3.9 Velocity distribution in the single entry turbine *(extract from Padzillah [74])*

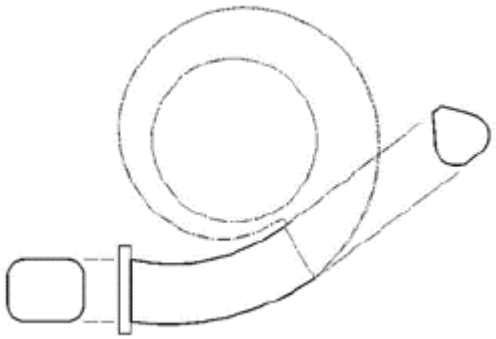


Figure 3.10 Volute inlet to volute tongue cross sectional change *(extract form Rajoo [7])*

The choice of $r_{\psi=0}$ in the small scroll is important, as it would also influence $r_{\psi=0}$ in the large scroll and subsequently the overall volute dimension. Based on $r_{\psi=0}=100\ mm$ used by Rajoo [7], $r_{\psi=0}=95\ mm$ was selected in the small scroll. The equivalent $A_{\psi=0}$ in the small scroll is $1266.35\ mm^2$. Unfortunately, the exact value of this area could not be achieved in Solid Works sketch plane, due to constraint in sketching spline curves. The closest value that the spline curve could provide is $A_{\psi=0}=1322.02\ mm^2$ in the small scroll. The corresponding $r_{\psi=0}$ is $96.45\ mm$. Other values of A and r, at different azimuth location in the small scroll are determined in the same way. Based on $r_{\psi=0}=70$

mm and $A_{\psi=0} = 0 \ \ mm^2$ in the small scroll , $A_{\psi=0} = 1749.27\ mm^2$ and $r_{\psi=0} = 101.32$ mm in large scroll are determined using similar approach. The final dimension of the volute is given in Figure 3.12 and Table 3.4. 3D solid model of asymmetric volute is presented in Figure 3.13. Figure 3.14 shows comparison between $\frac{A}{r}$ obtained from mean line calculation, equations (3.15) and (3.16), and that of the CAD solid model generated using Solid Works. The imperfect match between mean line and CAD solid model, is due to capability of Solid Works to produce identical cross sectional area (compared to mean line model), especially at the tongue region as clearly shown in Figure 3.14. However, this mismatch is very small, and will not affect the flow distribution throughout the volute cross section.

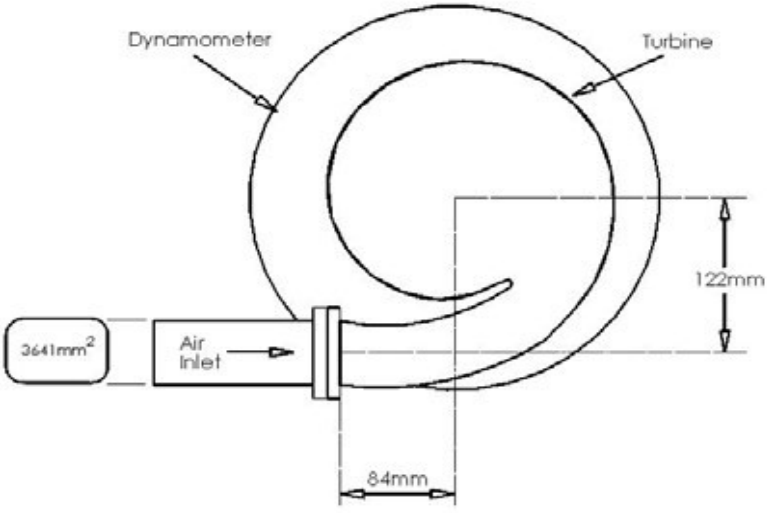


Figure 3.11 Coupling of Volute to Test-rig with important dimensions
(extract form Rajoo [7])

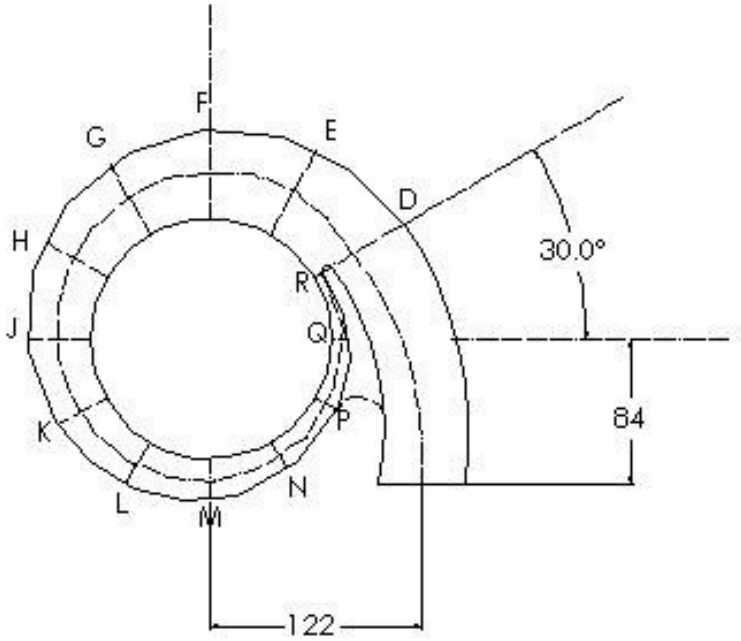


Figure 3.12 Volute geometry

Table 3.4 Volute final dimensions

Scroll	Section	Azimuth angle, °	r, mm	A, mm^2
Small	S Section 0	0	96.45	1322.02
	S Section 30	30	90.34	1007.77
	S Section 60	60	86.24	734.90
	S Section 90	90	81.92	484.86
	S Section 120	120	77.27	259.37
	S Section 140	140	73.86	123.45
	S Section 160	160	70.00	0.00
Large	L Section 160	160	101.32	1749.27
	L Section 180	180	96.85	1511.79
	L Section 210	210	92.99	1201.95
	L Section 240	240	88.99	914.12
	L Section 270	270	84.83	648.93
	L Section 300	300	80.42	407.11
	L Section 330	330	75.61	189.97
	L Section 360	360	70.00	0.00

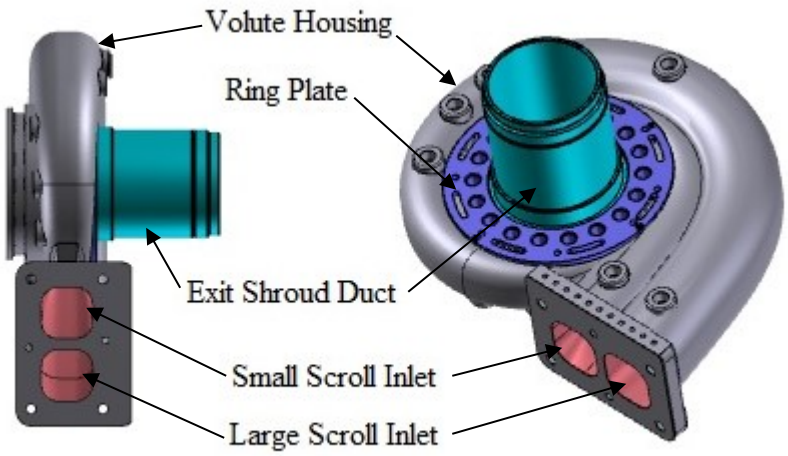


Figure 3.13 3D solid model of the asymmetric double entry volute

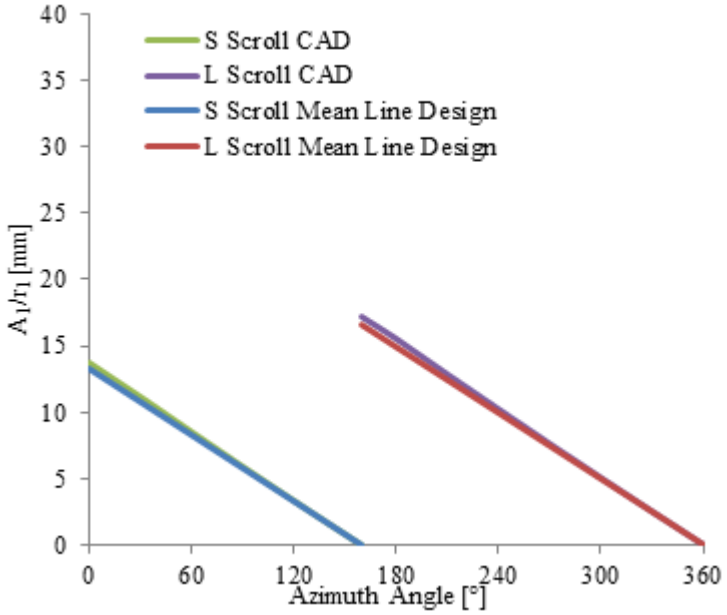


Figure 3.14 A/r : Mean line calculation vs CAD solid modeling

3.2 Nozzle Vane Design

Nozzle vanes are introduced in the rotor circumference of the small scroll in order to redress stagnation pressure imbalance created by different EGR extraction. It is prudent to state here that the nozzle vanes are not meant to drive EGR as commonly practiced in a turbocharger. Therefore, fixed geometry nozzle vanes in small scrolls are investigated in this thesis to evaluate the effectiveness in preserving the performance and where it is

impossible to do so, it helps to reduce the penalty in efficiency. This would in turn provide adequate performance data for the nozzle vanes to be used as Variable Geometry Turbine (VGT) to compensate for different EGR rate.

3.2.1 Vane Aerofoil and Conformal Transformation

The volute is responsible for producing the required amount of swirl and as well as to accelerate the flow. As such nozzle vanes are only required to accelerate the flow into the rotor, with almost no turning, Japikse and Baines [5]. However, the effect of using straight vanes at the exit of the volute would provide an undesired free vortex flow to the vaneless section. Hence, a highly desirable curved nozzle vane with the same inlet and outlet angles is recommended here. NACA 0015 is used as the base to determine the nozzle vane profile. Figure 3.15 provides a general description of the NACA airfoil profile. In Figure 3.16, thickness profile and theoretical pressure distribution of NACA 0015 are shown.

Conformal mapping is adopted to convert the annular cascade to circumferential nozzle ring, as shown Figure 3.17. It is also expected that incidence loss at the vane leading edge is optimum when flow angle is matched with the vane inlet angle. The actual nozzle vane fabricated in this thesis is shown in Figure 3.18.

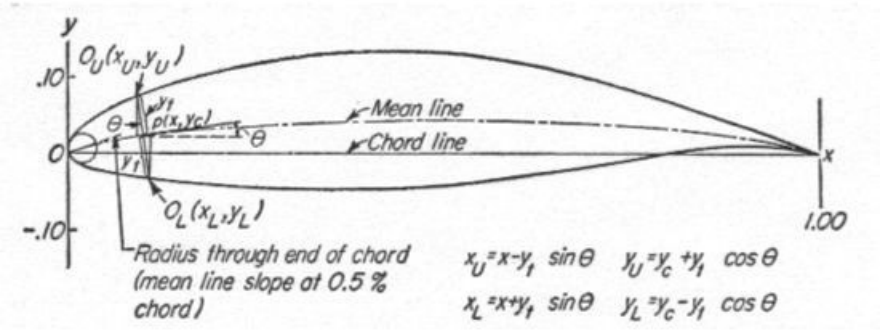
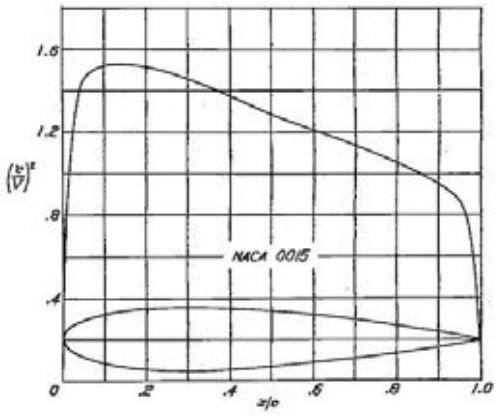


Figure 3.15 NACA airfoil profile *(extract from Abbott et al [75])*



NACA 0015 BASIC THICKNESS FORM

x (percent c)	y (percent c)	$(y/V)^2$	y/V	$\Delta r_a/V$
0	0	0	0	1.600
.5	----------	.546	.739	1.312
1.25	2.267	.933	.966	1.112
2.5	3.203	1.237	1.112	.900
5.0	4.443	1.450	1.204	.676
7.5	5.250	1.498	1.224	.557
10	5.853	1.520	1.233	.479
15	6.682	1.520	1.233	.381
20	7.172	1.510	1.229	.320
25	7.427	1.484	1.218	.274
30	7.502	1.450	1.204	.239
40	7.254	1.369	1.170	.185
50	6.617	1.279	1.131	.146
60	5.704	1.206	1.098	.115
70	4.580	1.132	1.064	.090
80	3.279	1.049	1.024	.065
90	1.810	.945	.972	.041
95	1.008	.872	.934	.027
100	.158	0	0	0

L. E. radius: 2.48 percent c

Figure 3.16 NACA 0015 airfoil profile *(extract from Abbott et al [75])*

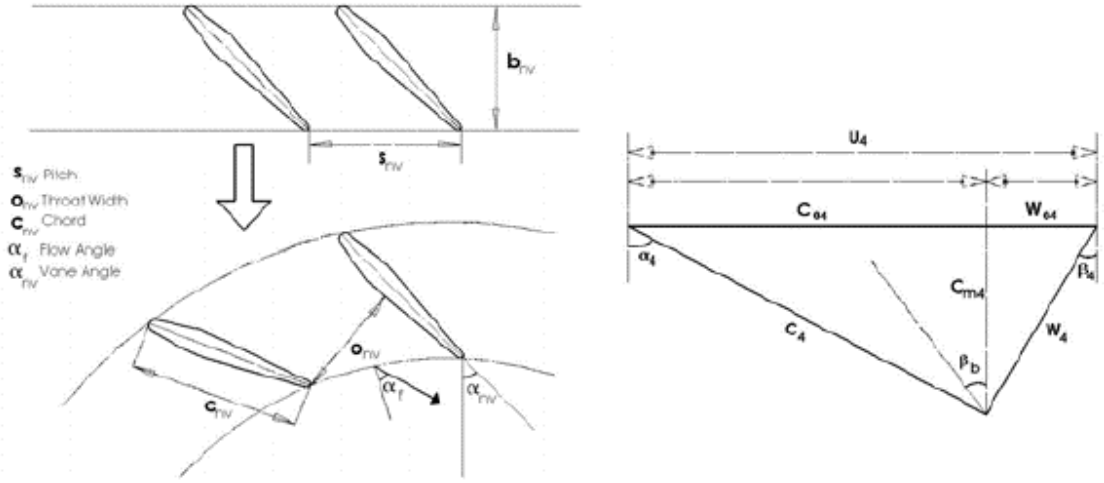


Figure 3.17 Nozzle vane terminologies, conformal mapping and rotor inlet velocity triangle *(extract from Rajoo [7])*



Figure 3.18 Actual shape of polar coordinated nozzle vane

3.2.2 Number of nozzle vanes

According to Hiett and Johnston [32], if nozzle exit flow angle is assumed to be equal to the rotor inlet angle, the flow angle can be expressed as a function of nozzle geometry, as given by equation (3.17).

$$\alpha_4 = \cos^{-1}\left(\frac{o_{nv}}{s_{nv}}\right) \tag{3.17}$$

Based on Figure 3.17, it is clear that nozzle throat and pitch are influenced by number of nozzle vanes and vane angle. Thus number of nozzle vanes (blade spacing) is crucial in loss contribution. Zweifels criterion [44] is used to determine blade spacing, as given by equation (3.18)

$$\varsigma = 2\left(\frac{s_{nv}}{c_{nv}\cos\alpha_{nv}}\right)(\cos\alpha_3)^2\left|\tan\alpha_2 - \tan\alpha_3\right| \tag{3.18}$$

where $\varsigma =$ tangential lift coefficient

Since there are two tongues in a double entry turbine volute, the distance from the tongue of the small volute and the distance from the tongue of the large volute should be identical. Therefore, the number of the vane is thought to be an integral multiple of the least integral ratio between the circumferential division angles.

3.3 Nozzle Vane Ring Mechanism

With the completion of asymmetric volute and nozzle vane design, a specially designed nozzle vane ring mechanism is now required to allow pivoting of the latter into the former, within the pivoting range. This is normally achieved by having a unison ring which retains all the nozzle vanes and synchronously allows them to rotate to the desired opening angle. Asymmetric double entry volute has identical nozzle interspace volume (bounded by nozzle vane and hub wall) as that of the single entry turbine designed by Rajoo [7]. As such similar nozzle vane pivoting mechanism [7] is adopted in this thesis.

This nozzle vane pivoting mechanism consists of a nozzle vane, sliding lever, connecting pin, vane retainer and a M3 bolt, as shown in Figure 3.19. The main purpose of the vane seat is to secure and concentrically position the nozzle vanes into the step hole of the stainless steel shroud plate. Two *SKF* plain bearings *PCMF 081007.5 B* are inserted into each hole of the shroud plate to support and allow free rotation of vane stem. The exposed end of the vane stem has a groove to secure sliding lever with a stainless steel vane retainer and M3 bolt. This prevents the sliding lever from having any axial motion. The oblong slot on the *brass* sliding lever allows it to slide in the radial direction. Dowel pin is inserted at the free end of the sliding lever. This dowel pin is connected to a unison ring, which controls the opening and closing operation of the nozzle vane. A single *SKF* plain bearing *PCM 040510 E/VB055* inserted into the hole of unison ring, supports and allows the dowel pin to rotate freely. This unison ring is supported on the shroud duct by *SKF* bearing *61818-2RZ*. Sakai et al [17] designed a similar unison ring as [7], shown in Figure 3.20.

The unison ring designed by Sakai et al [17], connects all 18 nozzle vanes and controls them simultaneously. This only permits equal nozzle vane angle setting around the entire rotor circumferential area. When EGR is extracted from the small scroll, mass flow rate in that scroll decreases relative to large scroll. If extraction remains within ideal EGR (iEGR) rate of 10% at design point, the geometry of the asymmetric volute (unequal rotor circumferential area) will be sufficient to redress the magnitude of mass imbalance created. On the other hand, iEGR rate greater or lower than 10% demands nozzle vane angle setting in each scroll to be distinct. The nozzle vane angle in small scroll need to be different than that of large scroll, to create a uniform incidence angle. Furthermore, in a pulsating flow environment, instantaneous flow angle changes dynamically, thus demanding a system which could match the incoming flow at different frequency. Owing to these reasons, independent nozzle vane control mechanism is presented here.

The first step in the design of the novel nozzle vane control mechanism would be to identify the requirement specification. Since vane angle settings in each scroll are to be distinct, two unison rings are required in this design. The operation of each unison ring must be independent with respect to each other at all time. Besides that, the operating range of the ring will be limited by the actual nozzle vane opening angle (between fully opened and fully closed angles). The rotation of the unison rings must translate to the desired nozzle vane angle setting, similar to [17]. Since the nozzle vane angle setting will

be done manually during testing, rotational speed and the material of the unison rings are immaterial in this design. However, the selected material should allow the unison ring to function according to design intent, within the operating pressure and temperature of the test rig. Finally, number of nozzle vanes for each unison ring must be decided. Although the circumferential division between the scrolls are unequal, nine vanes fit well in each scroll periphery.

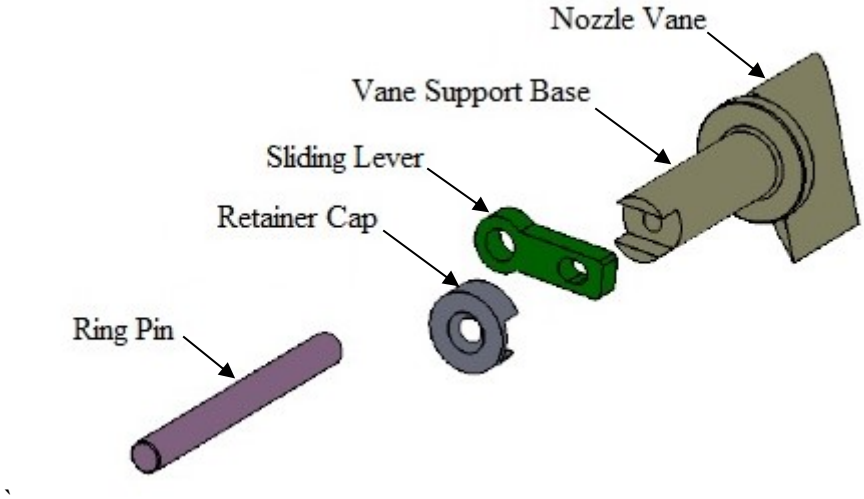
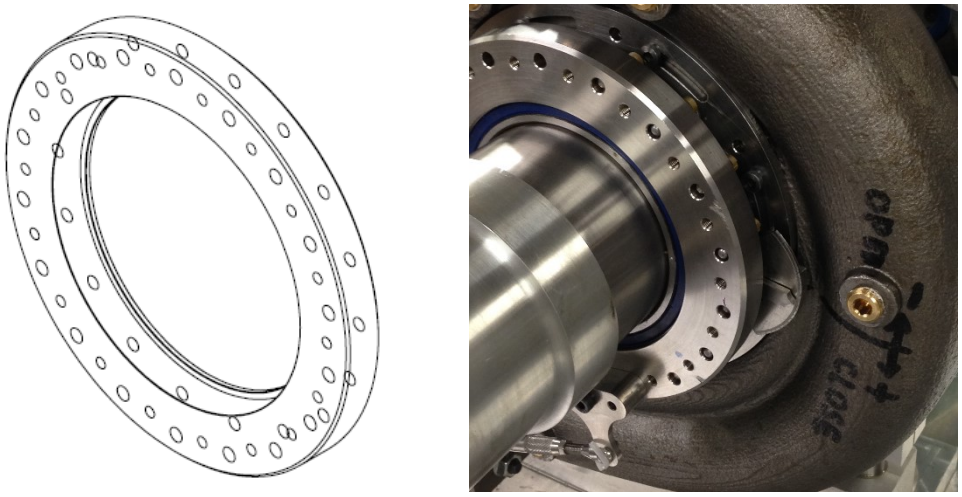


Figure 3.19 3D solid model of the nozzle vane pivoting mechanism



(a) (b)

Figure 3.20 (a) 3D Isometric view (b) Machined component assembled to Asymmetric double entry turbine

To conceptualize the above requirements, two ideas were generated, as shown in Figures 3.21 and 3.22. In the first concept, the same unison ring as [17] was adopted to drive the nozzle vanes in the large scroll periphery. Small scroll ring design was derived from [17]

to allow the operations of the large scroll ring. This was achieved by removing some material on the side which would otherwise overlap with large scroll ring pins (Figure 3.21). Unfortunately, longer ring pins as seen in Figure 3.21, has few disadvantages. Since the rotational motion are achieved by applying some level of torque, the long unsupported portion of the ring pin would be subjected to turning load, which could subsequently twist the pins. Besides that, the ring pins would be subjected to angular displacement while delivering the desired vane angle setting, due to the long-exposed segment. To overcome these shortcomings, the second concept was generated.

In the second concept, the gap between both unison rings had been significantly reduced as shown in Figure 3.22. This was made possible by redesigning the large scroll ring; removal of material on the side where small ring pin protrudes out. This not only brought the two unison rings closer, but also reduced the absolute length of the large scroll ring pins. Apart from this improvement, the exposed segment of the ring pins was reduced tremendously, thus eliminating the angular displacement and twisting of the ring pins. Thus, concept 2 was selected as the final concept. Both unison rings were subjected to some cosmetic changes before arriving at the final design as shown in Figure 3.23. Final dual ring nozzle vane control unit is shown in Figures 3.24 and 3.25.

This dual nozzle vane control mechanism consists of bearing clamp, bearing – clamp spacer, large scroll ring, bearing spacer, small scroll ring and 2 *SKF* bearings as shown in Figure 3.26. *SKF* bearings *61818-2RZ* are assembled onto the stainless-steel exit shroud duct. Small scroll and large scroll rings are individually secured on these bearing, which allow free rotation of the rings. While the bearing spacer keeps the bearings apart at required design distance, bearing – clamp spacer absorbs the force applied by the bearing clamp, thus preventing force being transmitted directly to the bearings and damaging them. Each nozzle vane pivoting mechanism module (Figure 3.19) are attached to every hole in the small scroll and large scroll rings.

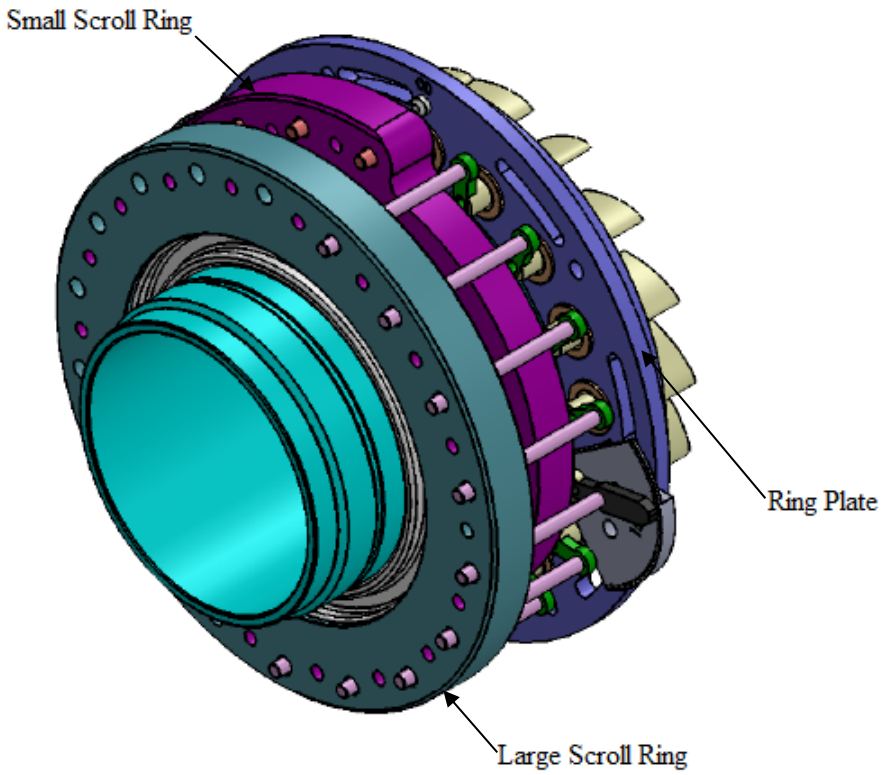


Figure 3.21 Concept 1

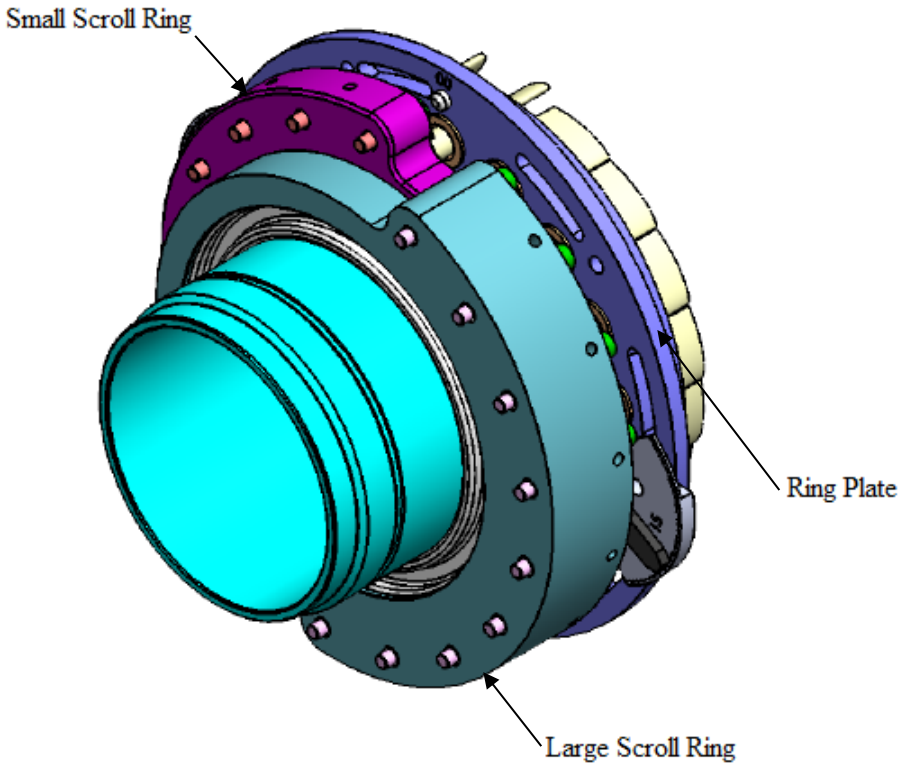
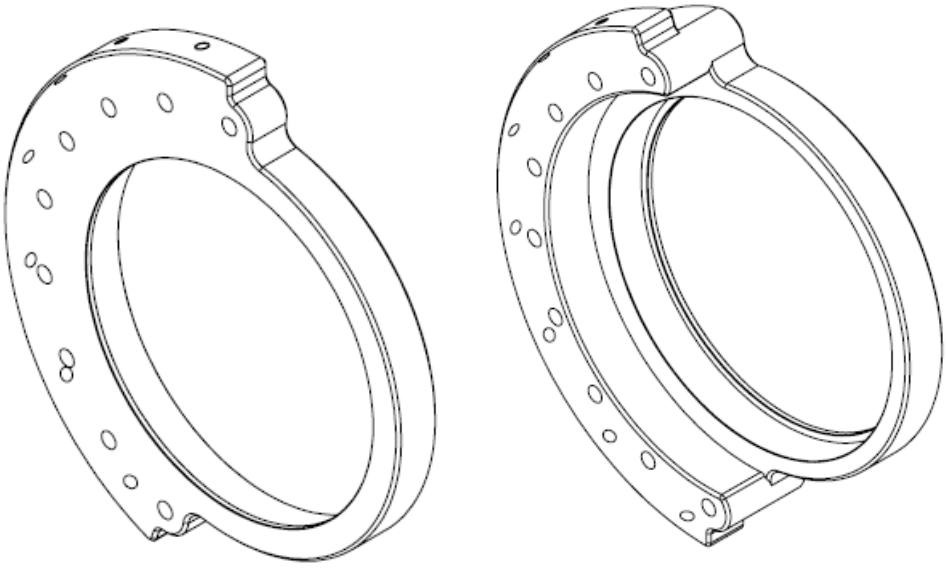


Figure 3.22 Concept 2



(a) (b)

Figure 3.23 Final (a) small scroll ring (b) large scroll ring

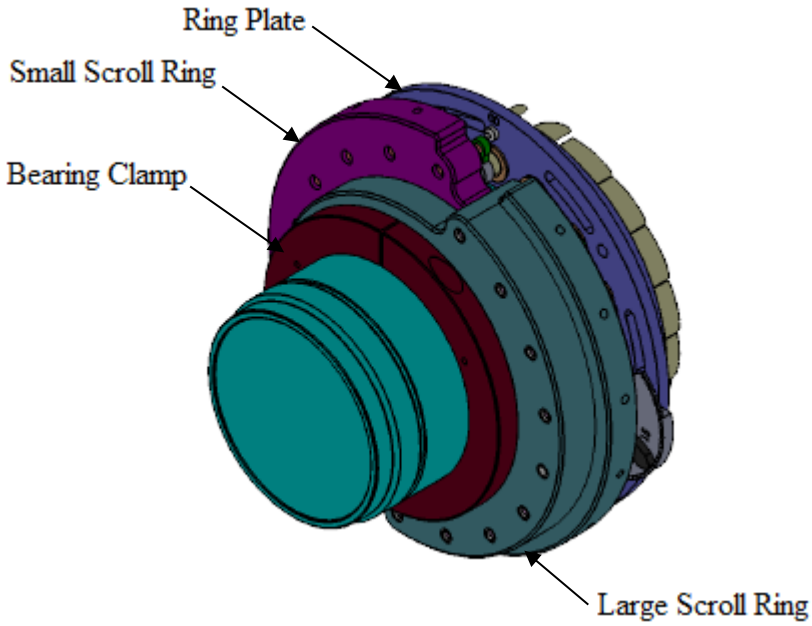


Figure 3.24 3D solid model of the dual ring Nozzle vane control – Isometric view 1

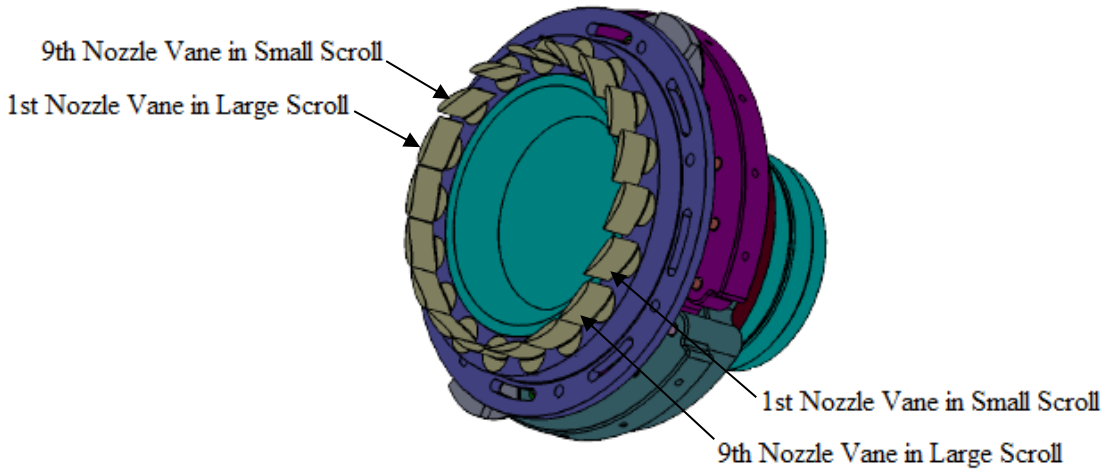


Figure 3.25 3D solid model of the dual ring Nozzle vane control – Isometric view 2

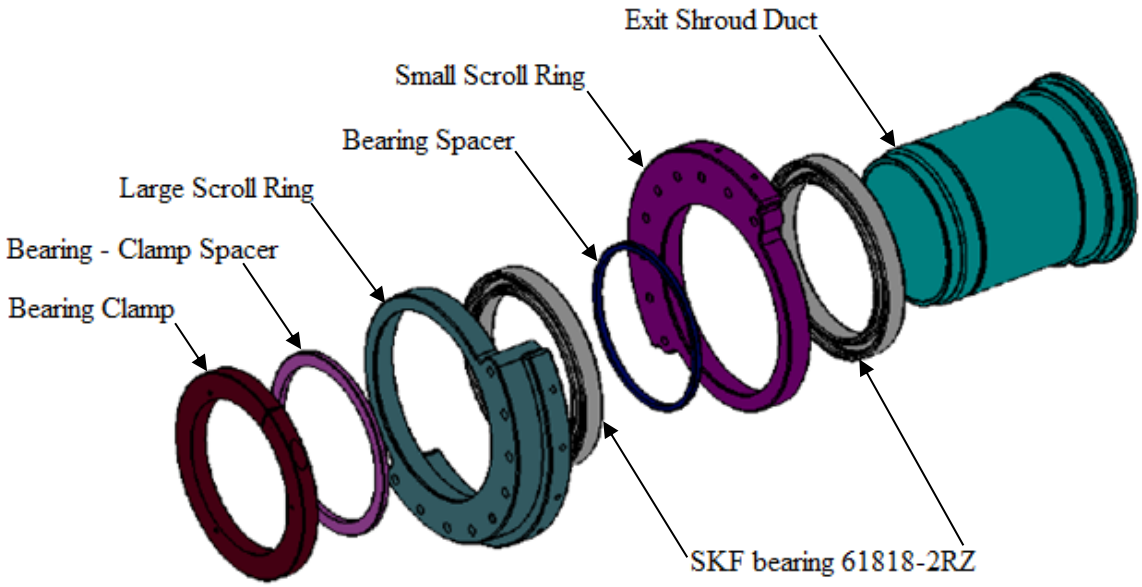
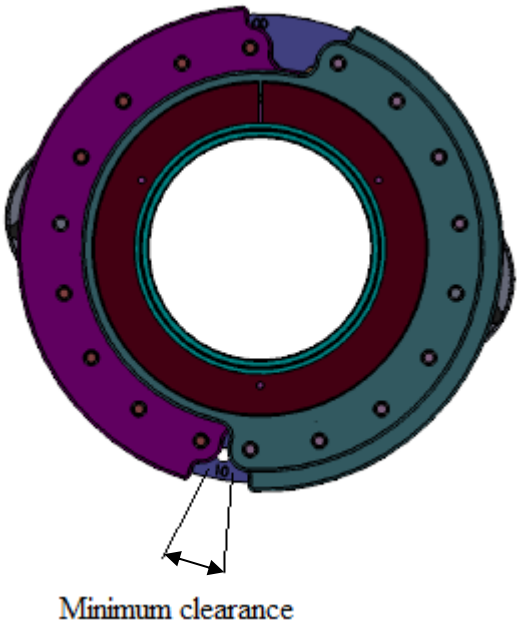


Figure 3.26 3D solid model of the dual ring Nozzle vane control – Exploded view

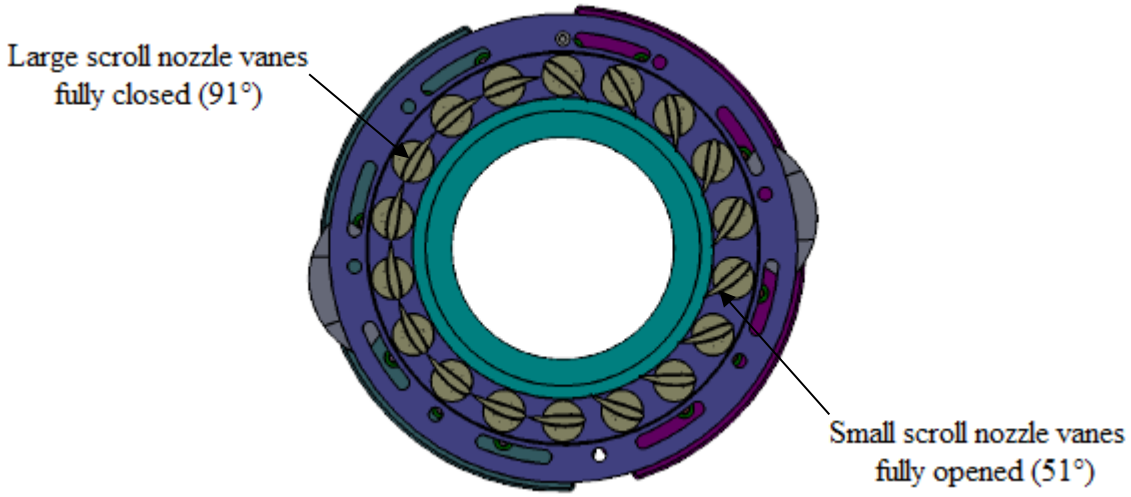
The operating range of dual nozzle vane control mechanism is depicted in Figures 3.27 and 3.28. Figure 3.27 shows S51_L91 configuration (nozzle vane in small scroll with an angle of 51° and nozzle vane in large scroll with an angle of 91°). S91_L51 setting shown in Figure 3.28 represents nozzle vane in small scroll with an angle of 91° and nozzle vane in large scroll with an angle of 51°. 51° and 91° vane angle settings correspond to fully opened position and fully closed position respectively. Minimum clearance shown in these figures demonstrates that both rings have sufficient gap between them, which keeps them

from clashing while in operation. This is to safeguard the components when nozzle vanes angles are set to extreme nozzle vane opening in each scroll.

All components of dual nozzle vane control mechanism shown in Figure 3.26 (with exception of the *SKF* bearings *61818-2RZ*) were machined and assembled in the Mechanical Engineering Workshop, Imperial College London. The final dual nozzle vane control mechanism fitted to asymmetric double entry turbine is shown in Figure 3.29. Figure 3.30 shows the test rig, where the entire asymmetric double entry turbine assembly is coupled to the dynamometer, and ready for testing.

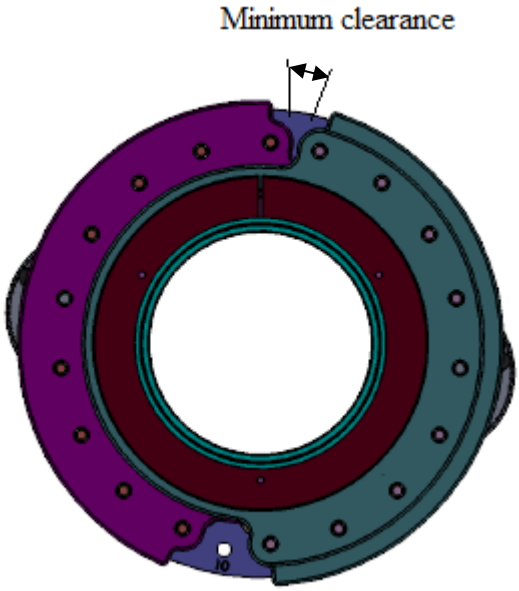


(a)

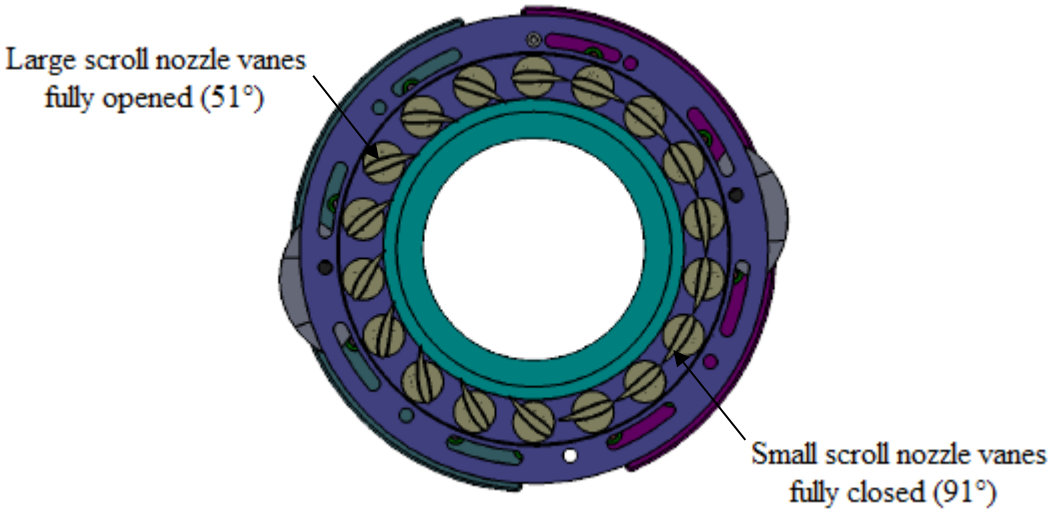


(b)

Figure 3.27 S51_L91 setting (a) front view (b) back view



(a)



(b)

Figure 3.28 S91_L51 setting (a) front view (b) back view

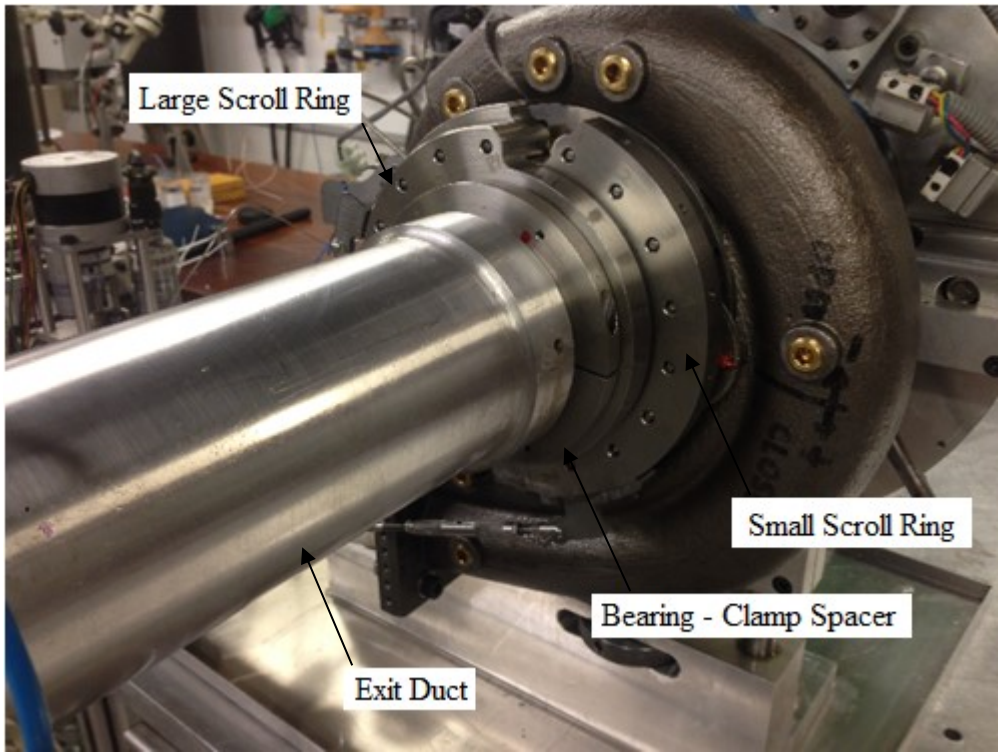


Figure 3.29 Final machined component assembled to Asymmetric double entry turbine

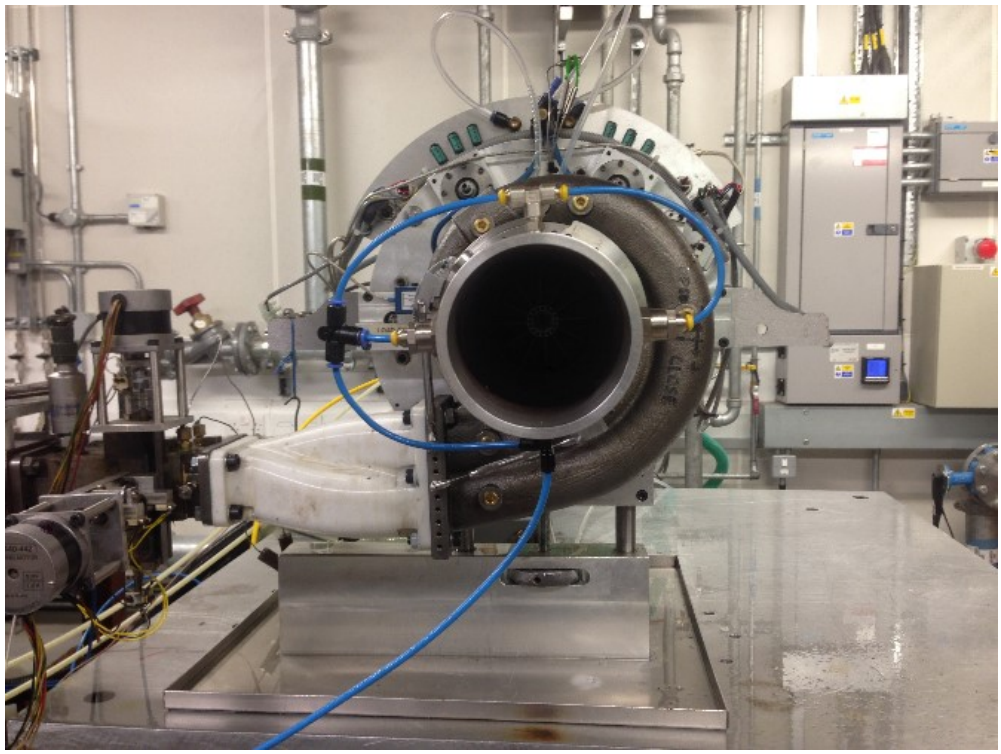


Figure 3.30 Asymmetric double entry turbine coupled to the dynamometer.

3.4 Summary

A novel asymmetric double entry volute was designed with ratio $\frac{A}{r}$ of 13.33 and 16.67 in the small and large scroll respectively. The small scroll covers circumferential sector between azimuth angle of 0° and 160°, while the remaining 200° rotor periphery belongs to the large scroll. Each scroll has an equal volute exit flow angle of 71°. NACA 0015 specification was used to design a novel nozzle vane with equal inlet and exit flow angle. The pivoting range of the nozzle vane between 51° and 91°, is achieved via a specially designed dual ring pivoting mechanism. This dual ring pivoting mechanism has the capability to regulate the vane angle opening in each scroll independently, something that has never been attempted before. Each ring consists of 9 nozzle vanes. Rotor used in this investigation is a mixed flow rotor consisting 12 blades with a constant inlet blade angle of +20°, a cone angle of 50° and tip diameter of 95.2 mm.

CHAPTER 4

EXPERIMENTAL SETUP AND PROCEDURES

An asymmetric double entry turbine was tested under various flow conditions in the turbocharger test rig Cell 123H at the Mechanical Engineering Department of Imperial College London. The available instrumentation and data acquisition system makes it possible to measure and log relevant parameters valuable in the stage performance analysis. This chapter presents the technical details of the turbocharger test rig, which includes the instrumentations, data logging method, measurement uncertainties and the performance parameters calculated based on the measured data.

4.1 Test Facility

In this section, first a brief introduction is presented about the test rig and the equivalence conditions. This is followed by detailed description of key features of the turbocharger test-rig.

4.1.1 Cold flow equivalent condition and air supply

This state of the art test rig, initiated by Dale and Watson [57] is a cold flow test facility, where the turbine inlet is fed with considerably lower temperature air, away from its actual hot condition. In reality, exhaust gas emanating from a spark ignition internal combustion engine (ICE) could go up to 1330 K. Thus, the capability of the cold flow test-rig to measure equivalent on-engine condition is achieved by similitude approach. Adopting this similarity method, the relationship between the actual hot condition and the equivalent measured cold condition parameter is given by equations (4.1) and (4.2).

$$\left(\frac{N}{\sqrt{T_{01}}}\right)_{cold} = \left(\frac{N}{\sqrt{T_{01}}}\right)_{hot} \tag{4.1}$$

$$\left(\frac{\dot{m}\sqrt{T_{01}}}{P_{01}}\right)_{cold} = \left(\frac{\dot{m}\sqrt{T_{01}}}{P_{01}}\right)_{hot} \tag{4.2}$$

Table 4.1 shows the equivalent cold flow condition attained using equations (4.1) and (4.2) for a given hot condition. It can be noticed that the pressure ratio is similar in both the cases, but the lower temperature and speed condition is compensated by higher mass flow rate.

There are three *Ingersoll-Rand* screw type compressors in the department of Mechanical Engineering of Imperial College London. Each compressor is capable of supplying 0.4 kg/s of air at a maximum absolute pressure of 500 kPa (5 bar). At any time, two compressors are operated simultaneously, supplying total mass flow rate of 0.8 kg/s. This is sufficient to feed the demanding asymmetric double entry turbine requirement as given in Table 4.1.

Most turbine rotor operates in excess of 100k RPM in the actual condition. However the maximum hot condition speed for asymmetric double entry turbine has been confined to 98k RPM. This is mainly due to the application of the asymmetric double entry turbine in the truck diesel engine vehicle segment; owing to the higher wheel inertia of the former and lower speed range of the latter. This combination requires the turbine to operate in low speed range, thus justifying the lower speed test choice as shown in Table 4.1.

Table 4.1 Equivalent cold flow test condition

	Hot condition	Equivalent Cold condition
Pressure ratio	2.91	2.91
Inlet Temperature (K)	923	346
Mass flow rate (kg/s)	0.4	0.653
Rotational speed (RPM)	98000	60000

4.1.2 Test-rig layout

The schematic of the test facility is shown in Figure 4.1. The key features of the test facility are heater, independently controllable twin-limbs (suited for multiple entry

turbines), a pulse flow generator and a high speed eddy-current dynamometer. The steady state air is delivered from the compressors through a pipe work with internal diameter of 101.6 mm. There are two valves installed at the end of this pipe work; primary and secondary air valve which are remotely controlled from outside the test cell 123H. These valves, regulates the total air flow rate into the test rig. Air then passes through a 72kW heater, which has the capacity to heat up the air to 373K. There are two reasons for the air temperature to be raised using the heater. Foremost reason is to avoid water vapour condensation at the exit of the turbine due to expansion process. Another incentive of having the heater is to maintain the desired turbine inlet temperature, in the range of 333K ~338K during the entire testing process according to the equivalent cold condition. The heater is controlled by a single loop PID controller, *West 6001+* which is remotely operated from main control computer.

Heated air enters the two limbs, each with internal diameter of 76.2 mm. Each limb is equipped with *McCrometer* V-cone flow meters that measure the mass flow rate. This type of flow meter is preferred over a conventional orifice-plate system as they provide better flow measurement over a wide range of steady operations. These limbs are also fitted with individual valve that has the ability to independently adjust the mass flow rate, allowing either full or unequal admission testing. Prior to the full admission test, flow control valve attached to the outer limb (connected to large scroll) is kept fully open, while that off at the inner limb (connected to small scroll) is adjusted until the inlet stagnation pressure in both the limbs are equal. This configuration of flow control valves is then fixed for the entire testing of full admission condition. On the other hand, during unequal admission testing, flow control valve at one limb is kept fully open, while the valve at the other limb is varied for each data point. This would allow different level of inequality between both the limbs, hence the inequality between both the scrolls.

Downstream of the V-cone meter, flow in both the limbs goes through the pulse generator. A motor that drives a pair of chopper plates, one for each limb, is responsible for the unsteady flow generation in the pulse generator. The Chopper plates are shown in Figure 4.2. The chopper plate pulse generator has a profile shown in Figure 4.3, creating the pulsating flow emulating the exhaust condition in an internal combustion engine. The speed of the motor can be remotely controlled to achieve a pulse frequency between 0 Hz and 85 Hz. Also, the position of the plates with respect to each other can be adjusted

manually to create different phase angle between them, namely in-phase and out-of-phase condition. In the steady flow test, the chopper plate remains static in fully opened position.

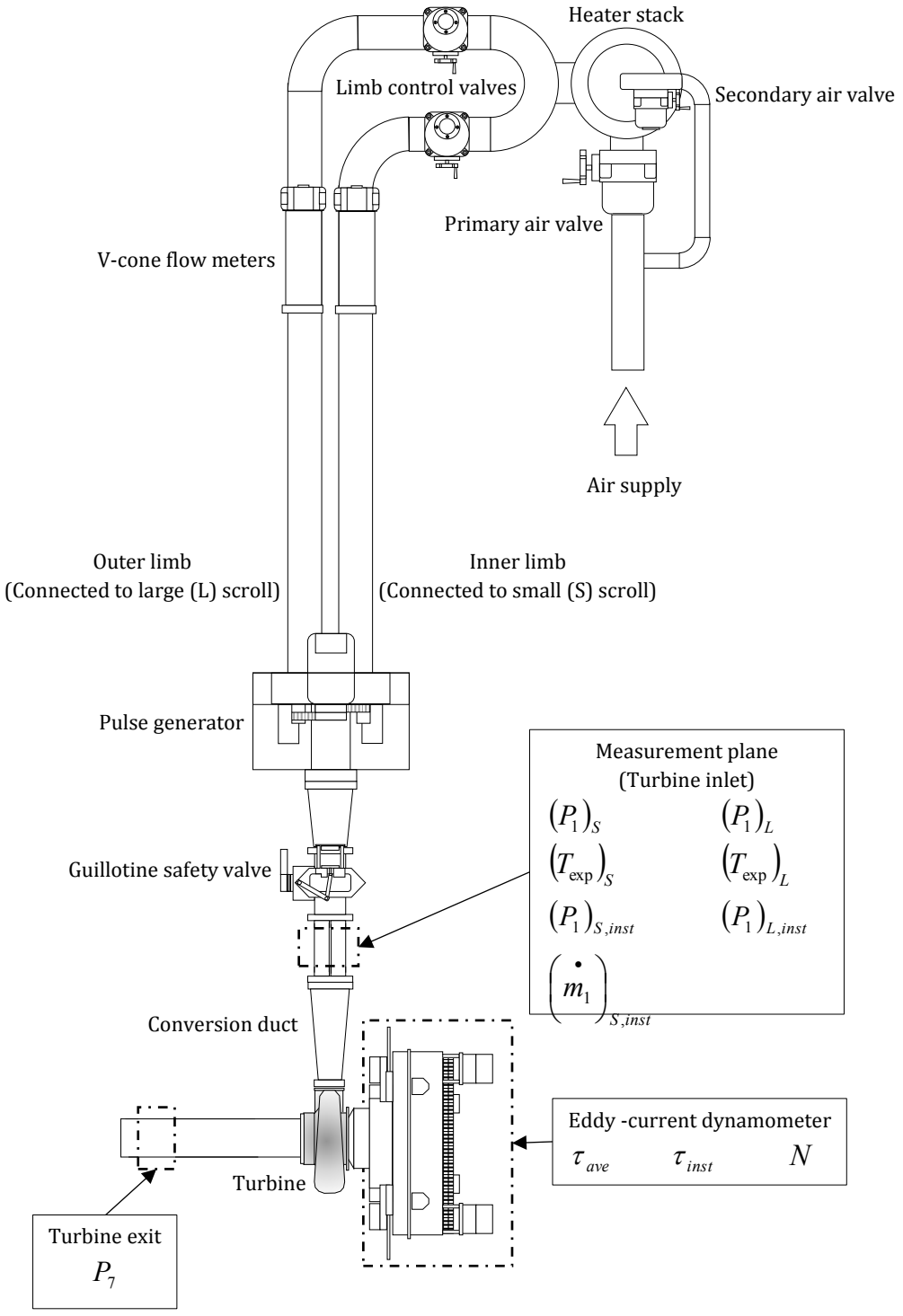
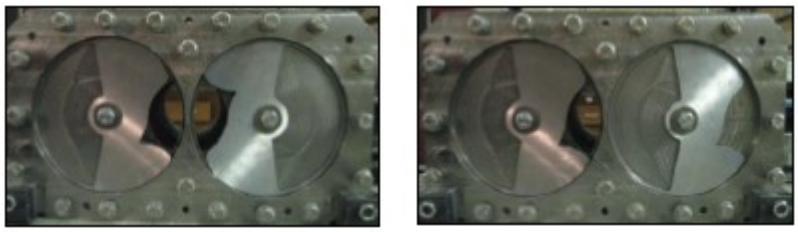


Figure 4.1 Cold flow turbocharger test rig schematic *(extract from Wan Salim [76])*



(a) (b)

Figure 4.2 Front view of rotating chopper plate

(a) In phase flow (b) Out-off phase flow

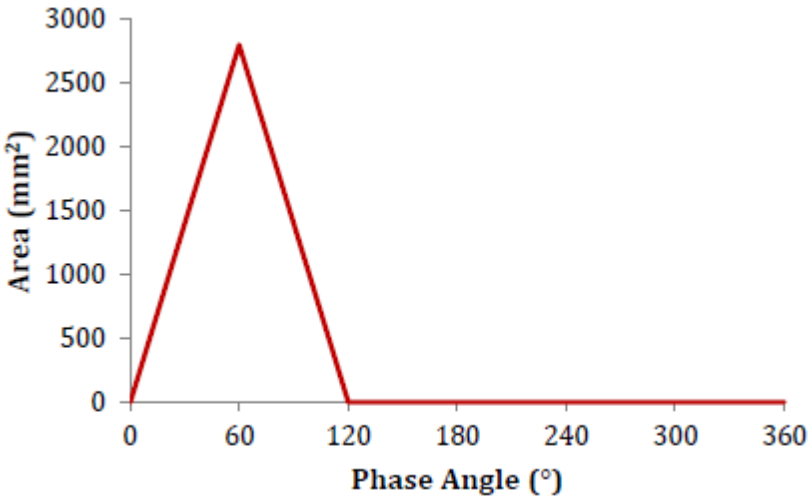


Figure 4.3 Chopper plate opening area versus phase angle

After the pulse generator, air passes through the guillotine valve, which acts as a safety device during testing. This spring loaded valve, is manually magnetized to allow flow to pass through during testing, and automatically demagnetized if any of the safety limits of the test rig is breached, forcing air flow to the turbine shut off immediately. The guillotine valve has two passages to preserve the flow from inner and outer limbs.

The air leaving the guillotine safety valve then flows through the measurement plane. This measurement plane is an instrumented section, within which each limb remains separated from each other. Each section is equipped with pressure transducer, static pressure tapping, thermocouples and hotwire system. The hotwire system in the outer measurement plane is able to be traversed, while that in the inner limb is fixed. Hotwires are used to measure the instantaneous mass flow rate during the unsteady flow testing.

Finally, air enters the turbine and drives the rotor. The turbine is coupled to an eddy-current dynamometer designed by Szymko [58], which enables turbine performance measurement over the wide range of velocity ratios. This could be achieved because without the compressor loading there is no surge and choke limitations. The dynamometer permits testing speeds up to 60k RPM, with a maximum power absorption of 62kW. The core of the dynamometer is shown in Figure 4.4. The entire dynamometer housing is suspended on a set of gimbal bearings which allows the turbine loading to react against a load cell. The gimbal bearing is shown in Figure 4.5. Owing to this novel support system, the bearing frictional losses are also accounted for in the turbine loading. Therefore, the load cell provides the absolute value of the aerodynamic torque produced by the turbine.

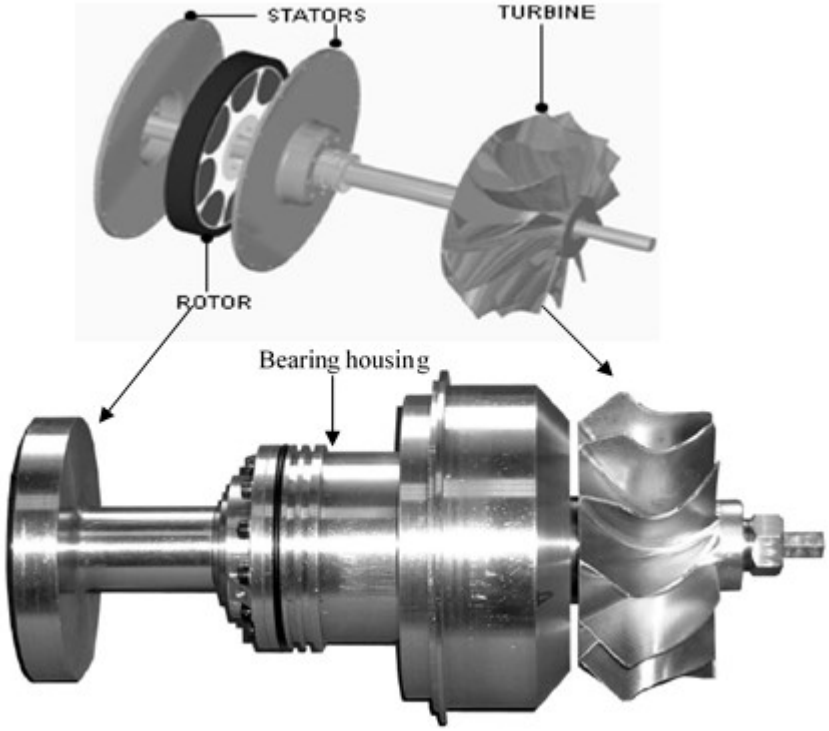


Figure 4.4 Magnetic rotor and stator plate assembly *(extract from Syzmko [58])*

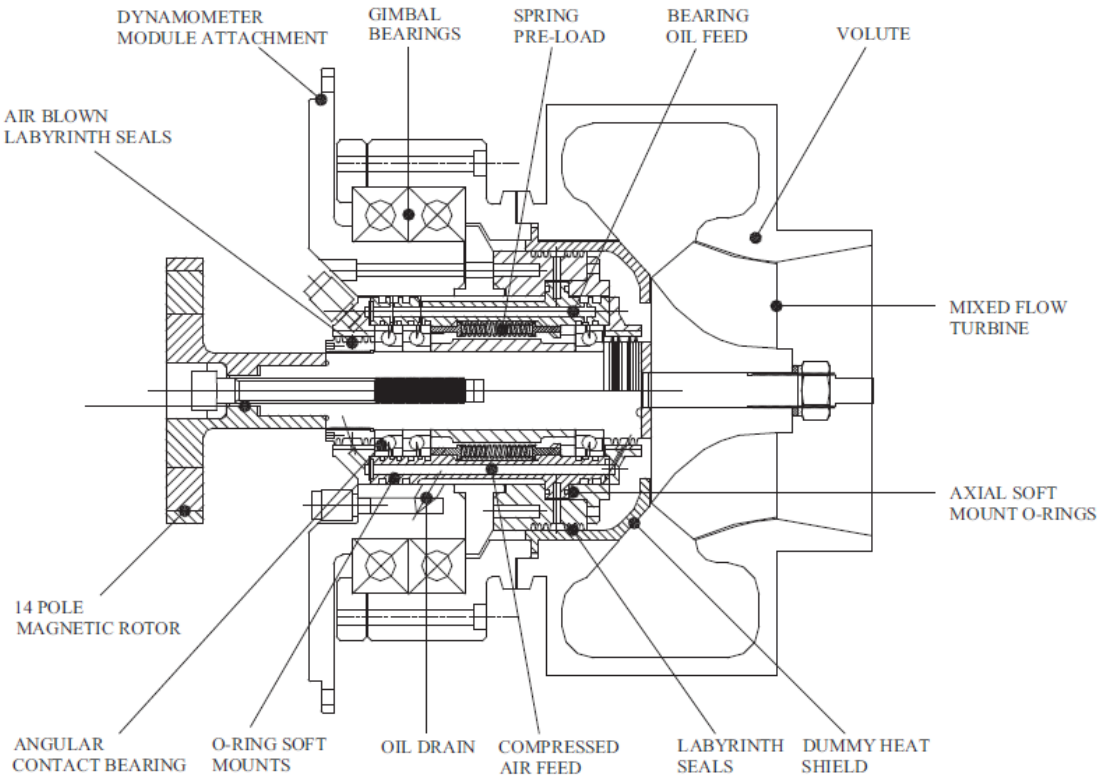


Figure 4.5 Eddy current dynamometer cross section extract from
(extract from Syzmko [58])

4.1.3 Rig Control and Safety

An operator should not be present inside the test-cell during experiments due to the presence of highly pressurised pipe work, high temperature heater and turbine speed up to 60k RPM. The entire test-rig facility is controlled from outside the cell 123H via a *LabVIEW* interface. The setup which involves 3 display monitors connected to the CPU, is known as the control centre. The *LabVIEW* interface is programmed with an integrated safety loop that immediately demagnetized the guillotine valve when safety limits of designated parameters are breached. This is to protect the user and also safeguard the equipment in the event of a breakdown. The parameters and their respective safety limits are shown in Table 4.2.

Table 4.2 Parameters and respective safety limits

Parameter	Safety Limits		Action
	Min	Max	
Turbine Speed *(rps)*	-	1,050	Rig Shut-down
Turbine Bearing Temperature *(K)*	-	373	Rig Shut-down
Magnetic Rotor Temperatures *(K)*	-	323	Rig Shut-down
Vibration Level *(mm/s)*	-	1.5	Rig Shut-down
Cooling Water Flow Rate *(l/min)*	150	-	Rig Shut-down
Bearing Oil Flow Rate *(l/hr)*	11	-	Rig Shut-down
Air Mass Flow Rate *(kg/s)*	0.05	-	Rig Shut-down
Heater Air Temperature *(K)*	-	373	Rig Shut-down

4.1.4 Instrumentation, data acquisition and monitoring hardware

Accurate measurement of different quantities in the test-rig is essential to enable complete steady and unsteady turbine characterization. These measurements can be categorized into two distinct groups; measurement for safe operation of the test-rig and measurement for performance analysis, as described in section 4.1.3. These quantities together with the instruments used to achieve the measurements are shown in Table 4.3. Explanations about these instruments are provided in sections 4.2 and 4.3.

National Instruments CompactRIO system (cRIO) comprising a real-time (RT) controller, a field programmable logic array (FPGA) chassis and eight C-series I/O modules forms the core of data acquisition and monitoring hardware. All the instruments listed in Table 4.3 are connected to the I/O modules, which are directly accessible by the FPGA. The FPGA uses a high speed bus based on a FIFO (first in, first out) queuing system to send the signal to the RT controller. The data from RT controller is then relayed to the control centre, which is then communicated to the user for rig control and data logging via the *LabVIEW* interface.

Table 4.3 Turbocharger test-rig instrumentation

Measuring Location	Physical Property	Instumentation		Purpose
		Steady	Unsteady	
Atmosphere	Temperature	Wall Thermometer		Performance Characterization
	Pressure	Mercury Barometer		
V- Cone flow meter	Upstream Pressure	Scanivalve		
	Pressure difference	Scanivalve		
	Uptream Temperature	K-type Themocouples		
Pulse Generator	Rotational Speed		Shaft Encoder	
Measurement plane (Turbine inlet)	Pressure	Scanivalve		
	Temperature	T - type Thermocouples		
	Instantaneous Pressure		Strain gauge pressure	
	Instantaneous Mass flow		CTA probe	
Turbine exit	Pressure	Scanivalve		
Dynamometer	Rotational Speed	Optical sensor		
	Torque	Load Cell	Load Cell	
			Optical sensor	
	Stator and bearing temperature	K - type Thermocouples		Test-rig Health and Safety Monitoring
	Water temperature	T - type Thermocouples		
	Vibration	Velometer		
Electric Heater	Temperature	K-type Themocouples		

4.2 Steady flow measurement

4.2.1 Pressure

In steady flow experiments, the flow static pressure is measured at the inlet and exit of the turbine. A *Scanivalve* with 24 channels consisting of positive and negative pneumatic inputs are used to measure the pressure at each limb using static-hole tapings. Four DSA3016 modules with eight pressure connections are used to measure 32 pressure readings simultaneously. Two strain gauge pressure transducers are coupled to the *Scanivalve* for low pressure and high pressure measurement. The low pressure range varies between 0 and 6894.75 Pa, whereas the high pressure range is between 0 and 689475 Pa. The *Scanivalve* system is remotely connected to the host PC via Ethernet connection. A

LabVIEW interface program with Transmission Control Protocol (TCP) connection is used to obtain the static pressure flow readings during the test logging period.

4.2.2 Temperature

Temperatures are measured with K-type and T-type thermocouples, at various locations in steady flow testing for performance and safety evaluations. The thermocouples are linked to a module on the *cR10* chassis. Table 4.3 provides detailed locations of the all the thermocouples used in the test rig.

The air temperature in the heater is measured and monitored using K-type thermocouples to avoid risk of overheating. For the purpose of safeguarding the turbine and relevant components, the pre-set temperature is maintained via *PID* controller incorporated within the heater power supply. Further downstream, inside the V-cone flow meter, K-type thermocouples are also used to measure air temperature. Apart from that, K-type thermocouples are again utilised in measuring temperature of the stator plates to safeguard the operation of the dynamometer and bearing housing. On the other hand, T-type thermocouples are used to measure and monitor cooling water temperature and air temperature at the measurement plane (turbine inlet), essential for evaluating turbine performance.

The isentropic relationship between the static (T) and stagnation temperatures (T_0) is given by equation (4.3).

$$T_0 = T\left[1 + \frac{(\gamma - 1)}{2} Ma^2\right] \tag{4.3}$$

The measurement of temperature $(T_{\exp})$ in a moving flow is subjected to compressibility effect. The compressibility of the flow causes the temperature measurement to drop between the static (T) and stagnation temperatures (T_0) and needs to be corrected when the Mach number *(Ma)* exceeds 0.3, Yahya [77]. As such, the measured temperature $(T_{\exp})$ is corrected with a recovery factor, *r* as shown in equations (4.4) and (4.5).

$$T = \frac{T_{\exp}}{1 + r\left(\frac{\gamma - 1}{2}\right)Ma^2} \tag{4.4}$$

where $r =$ recovery factor and given in equation (4.5)

$$r = \frac{T_{\exp} - T}{T_0 - T} \tag{4.5}$$

4.2.3 Mass flow rate

A *McCrometer* V-cone differential pressure flow meter is used to measure the mass flow rate during steady state experiments, shown in Figure 4.6. It is located downstream of the limb control valves. The pressure is measured at two locations, upstream high pressure port (P_1) and downstream low pressure port of the cone (P_1). A cone which is centrally located within the *McCrometer* accelerates the flow inside the pipe creating a low pressure region at the downstream causing pressure difference between the two locations. The mass flow rate of gas accelerating through the V-cone can be calculated using equation (4.6).

$$\dot{m} = F_a C_D Y k_1 \sqrt{\Delta P \rho} \tag{4.6}$$

where, $F_a =$ material expansion factor

$C_D =$ discharge coefficienct

$Y =$ gas expansion factor

$k_1 =$ flow constant

$\Delta P =$ pressure difference

$\rho =$ air density

The differential pressure, (ΔP) is measured via the high and low ports of the V-cone. Thermal expansion factor, (F_a), which typically approaches a value of unity, is the material geometrical change that varies with temperature. The discharge coefficient (C_D) is taken as constant of 0.8385 and 0.8472 in the individual limbs during testing, between Reynolds

number (Re) range of 17000 and 430000. This range of Reynolds number (Re) translates to a mass flow rate of 20 g/s to 50 g/s through the meters.

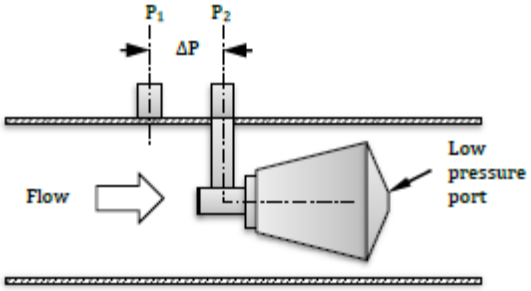


Figure 4.6 V-cone flow meter cross section *(extract from McCrometer Inc.[78])*

The gas expansion factor (Y) in equation (4.6) is obtained by the expression in equation (4.7).

$$Y = 1 - \left(0.649 + 0.696\beta^4\right)\frac{U_1 \Delta P}{P} \tag{4.7}$$

where, $U_1 =$ unit conversion factor

Flow constant, (k_1) is defined in equation (4.8).

$$k_1 = \frac{\pi\sqrt{2U_3}}{4U_2}\left(\frac{D^2\beta^2}{\sqrt{1-\beta^4}}\right) \tag{4.8}$$

where, U_2 , U_3 = unit conversion constants set by *McCrometer*

$D =$ pipe internal diameter

$d =$ cone external diameter

$$\beta = \sqrt{1 - \frac{d^2}{D^2}}$$

V-cones in both flow limbs of the test rig have a k_1 value of 0.0139

4.2.4 Rotor speed

Rotor speed is an essential parameter to determine the turbine performance. The rotational speed is obtained using an infra-red reflective optical sensor mounted to the turbine shaft integrated with an amplifier, type *Omron EE-SX4101*. The optical signal is triggered by a 10-toothed encoder at the end of the rotor shaft. The speed is then derived from the pulses produced by the encoder which is then converted into DC voltage. An increase in the turbine speed results in decrease of the output voltage, as shown in Figure 4.7.

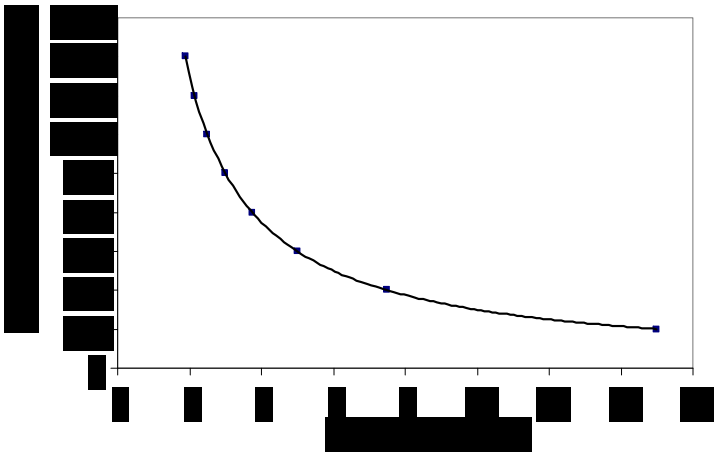


Figure 4.7 Rotor speed vs. Voltage

4.2.5 Torque

The torque coupled with the turbine speed is used in the evaluation of actual turbine power, as shown in equation (4.9). The turbine torque is directly measured via a load cell fixed on the body of the eddy-current dynamometer. The load cell is *Interface Miniature Beam* force transducer with a capacity of 11.3 kg.f, which is connected to a bridge module of a *cR10* system. During the experiment, load cell reading is logged together with other relevant parameters when the turbine speed stabilizes for a particular test condition. And as soon as the logging of other parameter completes, the main air valve is shut down to bring the rotor to rest. The torque reading at this point is taken as the zero offset for the actual torque calculation.

$$Power = W_{act} = 2\pi N\tau \tag{4.9}$$

4.3 Unsteady flow measurement

4.3.1 Pressure

Strain gauge pressure transducers, *Schaevitz* type *P704-0001* are used to measure the instantaneous static pressure at the measurement plane. The transducers are connected to a high speed bridge input module *NI 9237* through individual signal conditioner and amplifier modules, which are *Fylde FE-492-BBS Mini-Bal* conditioner and *Fylde FE-351-UA Uni-Amp* amplifier. The measurement signals are channelled to the *cR10* chassis, and it has measurement range from 0 to 3.5 bar gauge pressure. The *LabVIEW* program records the pressure reading and all related parameters, at a consistent triggered event by a single pulse per revolution of the pulse generator encoder.

4.3.2 Temperature

Steady and unsteady flow temperature measurement at the measurement plane uses the same T-type thermocouples. However, the instantaneous temperature evaluation is more elaborate compared to the steady flow calculation. This is due to the presence of thermal inertia in the thermocouples, which makes it impossible to directly measure instantaneous temperature of the unsteady flow. Therefore, temperature measurement obtained from the T-type thermocouple is taken as a mean temperature (T_{ave}), and used together with the instantaneous (P_{inst}) and mean pressure (P_{ave}) measurements through adiabatic relationship presented in equation (4.10). This approximation was initially proposed by Dale and Watson [57] and later validated by Szymko [58].

$$\frac{T_{inst}}{T_{ave}} = \left(\frac{P_{inst}}{P_{ave}} \right)^{\frac{\gamma-1}{\gamma}} \tag{4.10}$$

4.3.3 Mass flow rate

The instantaneous mass flow rate feeding the turbine is measured using a constant-temperature type hot-wire anemometer (CTA) located at measurement plane (turbine inlet). The probe is a 10 μm diameter platinum plated tungsten type, coupled to the *StreamLine* CTA system by *Dantec Dynamic*. The response rate is indirectly measured using a 'square-wave' with yield of 7.7k Hz. Table 4.4 provides the list of technical data of the probe.

Table 4.4 CTA platinum plated tungsten wire probe technical data

Temperature coefficient of resistance (TCR), α_o	0.36%/^{o}C
Sensor's cold resistance	0.589 Ω
Total resistance, sensor+lead+cable+support	2.129 Ω
Over-heat ratio	0.85
Over temperature	239 ^{o}C
Typical sensor temperature	262 ^{o}C

The CTA is designed using a Wheatstone bridge, whereby the hotwire is maintained constant through voltage balance. The measuring principle is purely dependent on the voltage balance to maintain the hotwire temperature. When subjected to airflow, the hotwire reduces temperature due to heat transfer, thus unbalancing the electronic bridge. As such, the voltage required to balance the bridge is related to the velocity of the flow, using both the Nusselt number and Reynolds number, resulting in King's Law (Lomas [79] and Brun, [80]). The through flow velocity and mass flux is measured by placing the hotwire perpendicular to the flow direction, in accordance to British Standard (BS1042, [81]). This traversing procedure is achieved by measuring 36 points through an in-house made 2 axes traversing mechanism as shown in Figure 4.8.

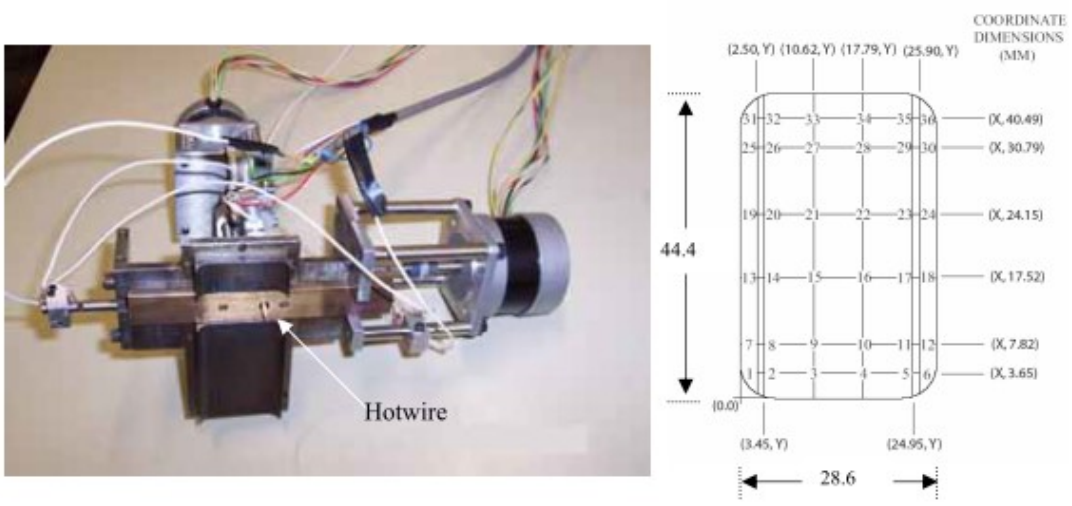


Figure 4.8 Traversing mechanisms: 2 axis and 36 points hotwire measurement in flow duct *(extract from Rajoo [7])*

Hotwire calibration CTA is done in two stages prior to measuring the instantaneous mass flow rate in pulsating flow. First, a 15 point calibration is done using a *StreamLine* system to obtain the transfer function of the recorded voltage for the flow velocity between 3 m/s to 300 m/s and then mass flux. The streamline calibrator unit produces high pressure air stream at room temperature (~24 ^{o}C), at a fixed point. The air static temperature varies in the hotwire sensor according to Mach number and a calibration curve corrected to the averaged room temperature is plotted, to be used as a reference temperature at the second part of the calibration. The transfer function is then obtained through curve fitting, a method established by King's Law and shown in equation (4.11). The typical value for A_{calib} and B_{calib} is 4.61 and 0.46.

$$E^2 = A_{calib} + B_{calib}.(\rho U)^n \tag{4.11}$$

Whereby, E = CTA voltage (volts)

A, B, n = Power law coefficients (cuve-fit)

ρU = Mass flux ($kg/m^2.s$)

The second part of calibration includes all 36 points at the measurement plane, whereby the voltage is taken under steady flow for a range of mass flow rates that would be used during the turbine testing. Using equation (4.11), the voltage is then converted to mass flux

producing readings for all 36 points as specified by BS 1042 [81]. It is then spread into 6 rows and 6 columns as show in Figure 4.8. The integration technique using equation (4.12) as adapted by BS 1042 [81] specification for regular duct is used. The integration is done for the 6 points in each row followed by the 6 points in the column to result in the final velocity value. The distance between the walls, L is as shown in Figure 4.8 and the value of m_w is between 4 (rough) and 10 (smooth).

$$
\begin{aligned}
(\rho U)_i = {} & v_1\left[\left(\frac{m_w}{1+m_w}.j_1\right)+\left(\frac{1}{12.m_w}.\frac{j_2^2}{j_1}\right)+\left(\frac{7}{12}.j_2\right)-\left(\frac{1}{12}.j_3\right)\right]+ \\
& v_2\left[\left(\frac{1}{2}.j_2\right)+\left(\frac{7}{12}.j_3\right)-\left(\frac{1}{12}.j_4\right)\right]+v_3\left[\left(\frac{7}{12}(j_3+j_4)\right)-\left(\frac{1}{12}.(j_2+j_5)\right)\right]+ \\
& v_4\left[\left(\frac{7}{12}.(j_4+j_5)\right)-\left(\frac{1}{12}.(j_3+j_6)\right)\right]+v_5\left[\left(\frac{1}{2}j_6\right)+\left(\frac{7}{12}.j_5\right)-\left(\frac{1}{12}.j_4\right)\right]+ \\
& v_6\left[\left(\frac{m_w}{1+m_w}.j_7\right)+\left(\frac{1}{12.m_w}.\frac{j_6^2}{j_7}\right)+\left(\frac{7}{12}.j_6\right)-\left(\frac{1}{12}.j_5\right)\right]
\end{aligned}
\tag{4.12}
$$

Whereby $j_1 .... j_6 = \frac{l_i - l_{i-1}}{L}$; $j_7 = \frac{L - l_6}{L}$

$(\rho U)_i$ = integrated mass flux *(kg/m².s)*

v_i = single point mass flux *(kg/m².s)*

m_w =wall roughness factor

l_i = distance of point to the reference wall *(m)*

L = distance between the walls *(m)*

Graphical interpolation of the near-wall measurements (BS 1042, [81]) is used to determine the wall roughness factor, whereby in this case it was found to be 8. The instantaneous mass flow rate, $\dot{m}$ is calculated using the duct area, A_{TI} as shown in equation (4.13).

$$\dot{m} = (\rho.U)_i.A_{TI} \tag{4.13}$$

The temperature of the pulsating flow has high tendency to fluctuate away from the hotwire calibration temperature. As such, it is extremely crucial to calibrate the hotwire to the actual testing temperature range, as done in the second part of the calibration. Knowing this fact, the *StreamLine* CTA system is set up at an over-heat ratio during calibration and actual measurement period. The main properties that influences the hotwire are density (ρ), Mach number (Ma), Prandtl number (Pr), thermal conductivity (k) and dynamic viscosity (μ). These properties are used to determine the A_{calib} and B_{calib} to solve the mass flow rate. The mass flow rate is measured using the hotwire is then compared against V-cone to develop consistent transfer function for all the conditions expected during the actual testing. It provides a confidence level of 95% of uncertainty in CTA.

4.3.4 Rotor speed

The instantaneous turbine speed is important to measure the turbine performance under pulsating flow. All 10 pulses per revolution from the optical sensor are measured and recorded during testing at consistent trigger point as generated from the pulse generator via the shaft encoder. Hence, the time for a turbine to rotate at a given angle can be calculated, resulting in turbine rotational speed.

4.3.5 Torque

In pulsating flow, instantaneous torque is produced by adding the fluctuating and the mean torques, resulting in equation (4.14).

$$\tau_{inst} = \tau_{fluc} + \tau_{ave} \tag{4.14}$$

The mean torque (τ_{ave}) is obtained from the load cell, similar to the steady flow torque calculation. However, a rotating shaft produces fluctuating torque, (τ_{fluc}) which is the result of rotor acceleration (α) and polar moment of inertia (I)as shown in equation (4.15).

$$\tau_{fluc} = I\alpha = I\left(\frac{d\omega}{dt}\right) \tag{4.15}$$

The angular acceleration of the rotating component is calculated with the first central difference numerical technique as shown in equation (4.16).

$$\frac{d\omega}{dt} = \frac{\omega_n - \omega_{n-1}}{t_n - t_{n-1}} \tag{4.16}$$

4.3.6 Polar Moment of Inertia

The *tri-filar suspension method* is used to assess the polar moment of inertia of the rotating component. Polar moment of inertia (I), of the whole assembly is 4.563 x 10^{-4} kgm^2 and that of the turbine wheel is 9.858 x 10^{-5} kgm^2. The Root-Sum-Square RSS uncertainty is used to calculate the polar moment of inertia, giving a value of ± 1.55 x 10^{-5} kgm^2 .

4.4 Performance Parameter

In this section, calculations of the performance parameters for an asymmetric double entry turbine are shown. Parameters which form the foundation of turbine in turbomachine analysis are presented first in order to provide coherent link between single entry and double entry turbine.

4.4.1 Steady flow

Single entry turbine performance in steady state operations are defined by four standard parameters, which are total to static isentropic efficiency, velocity ratio, mass flow parameter and pressure ratio, as shown in Table 4.5.

Table 4.5 Steady State Parameters

Parameter	Formula
Total to-static efficiency	$\eta_{ts} = \frac{\dot{W}_{act}}{\dot{W}_{is}}$
Velocity Ratio (VR)	$\frac{U}{C_{is}}$
Mass Flow Parameter (MFP)	$\frac{\dot{m}\sqrt{T_{01}}}{P_{01}}$
Pressure Ratio (PR)	$\frac{P_{01}}{P_5}$

4.4.1.1 Total-to-static Efficiency vs. Velocity ratio

The total-to-static efficiency of a single entry turbine, as shown in Table 4.5, is defined as the ratio between the actual power transferred to the shaft compared to a theoretical power that would be available should the working fluid follow an ideal process. Actual power transferred from the working fluid to the shaft is acquired from the load cell measurement as mentioned in section 4.2, while the available isentropic work is calculated using measurements from the measurement plane. To understand this, total to-static efficiency is rewritten in terms of enthalpy difference between two states, as given by equation (4.17).

$$\eta_{ts} = \frac{\dot{W}_{act}}{\dot{W}_{is}} = \frac{h_{01} - h_{07}}{h_{01} - h_{7,is}} \tag{4.17}$$

For a double entry turbine, actual shaft power measurement remains the same as that of a single entry; however, the isentropic power is measured at two turbine inlets. This is shown in equations (4.18) to (4.20).

$$\eta_{ts} = \frac{\dot{W}_{act}}{\dot{W}_{is}} = \frac{\dot{W}_{act}}{\left(\dot{W}_{is}\right)_S + \left(\dot{W}_{is}\right)_L} \tag{4.18}$$

$$\dot{W}_{is} = \dot{m}_S\left(h_{01} - h_{7,is}\right)_S + \dot{m}_L\left(h_{01} - h_{7,is}\right)_L \tag{4.19}$$

$$\dot{W}_{is} = \dot{m}_S\left[\int_{7,is}^{1} c_p dT + \frac{1}{2}C_1^2\right]_S + \dot{m}_L\left[\int_{7,is}^{1} c_p dT + \frac{1}{2}C_1^2\right]_L \tag{4.20}$$

It should be noted that exit condition with subscript S and L are both referring to the turbine exit, therefore they are identical quantities. Mass flow rate $(\dot{m}_S)$ and $(\dot{m}_L)$ are obtained from direct measurement as described in section 4.2.

Evaluation of specific heat integral term in equation (4.20) requires the knowledge of the inlet static temperature $\left(T_1\right)$ and exit isentropic static temperature $\left(T_{7,is}\right)$ as shown in equation (4.21). The formula for specific heat constant $\left(c_p\right)$ is given in equation (4.22) and all five coefficients are presented in Table 4.6.

$$\int_{7,is}^{1} c_p dT = f\left(T_1, T_{7,is}\right) \tag{4.21}$$

$$c_p = A_0 + A_1 T + A_2 T^2 + A_3 T^3 + A_4 T^4 + A_5 \tag{4.22}$$

Table 4.6 Constants of specific heat

A_0	0.10831165×10^{4}
A_1	0.68388122
A_2	$0.17875137 \times 10^{-2}$
A_3	$0.11323656 \times 10^{-5}$
A_4	$0.82943324 \times 10^{-9}$
A_5	$0.11100191 \times 10^{-11}$

Equations (4.3), (4.4) and (4.5) are solved iteratively for the Mach number (Ma) and subsequently for static (T_1) and total (T_{01}) temperature using the measured static temperature $(T_{\exp})$ at turbine inlet. Calculation of exit isentropic static temperature $(T_{7,is})$ is shown in equation (4.23).

$$T_{7,is} = T_{01}\left[\frac{P_7}{P_1}\left(\frac{T_1}{T_{01}}\right)^{\frac{\gamma_1}{\gamma_1 - 1}}\right]^{\frac{\gamma_{1,7}-1}{\gamma_{1,7}}} \tag{4.23}$$

Inlet $(P_1)$and exit (P_7) static pressure are obtained from direct measurement while iteration is used in solving equation (4.23) to determine the mean specific heat ratio, $\gamma_{1,7}$, between the inlet and exit conditions, using all the quantities obtained above.

The inlet dynamic enthalpy term appearing in equation (4.20) can be evaluated using static (T_1) and total temperature (T_{01}) as shown in equation (4.24). The solution obtained from equation (4.21) to (4.24) is substituted into equation (4.20) to evaluate inlet isentropic power in both limbs.

$$\frac{1}{2}C_1^2 = c_{p,1}(T_{01} - T_1) \tag{4.24}$$

With the knowledge of turbine rotor speed (N), rotor inlet diameter (D_5) and inlet isentropic power $\dot{W}_{is}$, the velocity ratio of the turbine can be calculated with equation (4.25).

$$\frac{U_5}{C_{is}} = \frac{\pi D_5\left(\frac{N}{60}\right)}{\sqrt{2\left(\frac{\left(\dot{W}_{is}\right)_S + \left(\dot{W}_{is}\right)_L}{\dot{m}_S + \dot{m}_L}\right)}} \tag{4.25}$$

4.4.1.2 Mass Flow parameter vs. Pressure ratio

Calculated quantities obtained in the previous section, together with direct measurement are substituted into equations (4.26) and (4.27).

$$MFP_S = \frac{\dot{m}_S \sqrt{(T_{01})_S}}{(P_{01})_S} \tag{4.26a}$$

$$MFP_L = \frac{\dot{m}_L \sqrt{(T_{01})_L}}{(P_{01})_L} \tag{4.26b}$$

$$PR_S = \frac{(P_{01})_S}{P_7} \tag{4.27a}$$

$$PR_L = \frac{(P_{01})_L}{P_7} \tag{4.27b}$$

In addition, equations (4.28) to (4.31) are used to calculate overall mass flow parameter and pressure ratio in full admission condition. As highlighted by Copeland [53], these equations would be meaningless if the inlet conditions are different for both the scrolls. Nevertheless, stagnation inlet pressure for both the inlets is identical in the full admission testing. Therefore, the overall mass flow parameter and pressure ratio are still valid and representative of the turbine swallowing capacity, in the full admission condition.

$$MFP = \frac{\left(\dot{m}_S + \dot{m}_L\right)\sqrt{T_{01}}}{P_{01}} \tag{4.28}$$

$$T_{01} = \frac{\dot{m}_S (T_{01})_S + \dot{m}_L (T_{01})_L}{\dot{m}_S + \dot{m}_L} \tag{4.29}$$

$$P_{01} = \frac{(P_{01})_S \left(\dot{W}_{is}\right)_S + (P_{01})_L \left(\dot{W}_{is}\right)_L}{\left(\dot{W}_{is}\right)_S + \left(\dot{W}_{is}\right)_L} \tag{4.30}$$

$$PR = \frac{PR_S \left(\dot{W}_{is}\right)_S + PR_L \left(\dot{W}_{is}\right)_L}{\left(\dot{W}_{is}\right)_S + \left(\dot{W}_{is}\right)_L} \tag{4.31}$$

There are numerous methods available to average the stagnation pressures; the most common averaging means being Area Average, Mass Average and Energy Average. According to Cumpsty and Horlock [82], the choice of suitable averaging scheme is dependent on the application; in this case a turbine with asymmetric double entry in the full admission condition. Since the First Law of Thermodynamics is one of the fundamental equations used in deriving performance parameter of turbines, the same law has been chosen to enforce energy conservation between the non-uniform flow and equivalent uniform flow. Equation (4.29) which shows Mass Averaging procedure adopted on T_{01} is the only available method which satisfies the conservation of energy, Japikse and Baines, [5]. To be consistent with this law, Energy Average for P_{01} was adopted in equation (4.30) and subsequently for PR in equation (4.31).

Based on Energy Average method, P_{01} is calculated as in equation (4.32).

$$P_{01} = \frac{\dot{m}_S (C_{is})_S^2 (P_{01})_S + \dot{m}_L (C_{is})_L^2 (P_{01})_L}{\dot{m}_S (C_{is})_S^2 + \dot{m}_L (C_{is})_L^2} \tag{4.32}$$

And using definition of $(C_{is})^2 = 2C_P(T_{01})\left(1 - \left(\frac{P_7}{(P_{01})}\right)^{\frac{\gamma-1}{\gamma}}\right)$, and $\left(\dot{W}_{is}\right) = \dot{m}\, C_P(T_{01})\left(1 - \left(\frac{P_7}{(P_{01})}\right)^{\frac{\gamma-1}{\gamma}}\right)$ the relationship between them is obtained as

$\left(C_{is}\right)^2 = 2\frac{\dot{W}_{is}}{\dot{m}}$. Based on this relationship, P_{01} has been simplified to equation (4.30), which is the Isentropic Power Average (Energy Average).

4.4.2 Unsteady flow

Performance parameter calculation of a double entry turbine in the perspective of unsteady flow is discussed in this section. Two methods are used to characterize the unsteady flow, namely instantaneous (time resolved) and cycle average approaches. Both methods require the measurement of average temperature, instantaneous static pressure and mass flow rate.

4.4.2.1 Total-to-static Efficiency vs. Velocity ratio

Definition of total to-static efficiency for unsteady flow remains the same as given by equations (4.17) and (4.18). The difference in the pulsating flow calculation is that time resolved measurement of the actual and isentropic inlet power are used instead of the steady flow quantities. This is presented in equation (4.33).

$$\eta_{ts,inst} = \frac{\dot{W}_{act,inst}}{\dot{W}_{is,inst}} = \frac{\dot{W}_{act,inst}}{\left(\dot{W}_{is,inst}\right)_S + \left(\dot{W}_{is,inst}\right)_L} \tag{4.33}$$

The instantaneous actual shaft work is calculated in accordance to the instantaneous torque definition in section 4.3.5. This is shown in equation (4.34).

$$\dot{W}_{act,inst} = 2\pi N\left(\tau_{fluc} + \tau_{ave}\right) \tag{4.34}$$

The instantaneous isentropic inlet power is calculated as given by equation (4.35).

$$\dot{W}_{is,inst} = \left(\dot{m}_{inst}\right)_S \left[\int_{7,is}^{1} c_p dT + \frac{1}{2}C_1^2\right]_{inst,S} + \left(\dot{m}_{inst}\right)_L \left[\int_{7,is}^{1} c_p dT + \frac{1}{2}C_1^2\right]_{inst,L} \tag{4.35}$$

Evaluation of equation (4.35) requires knowledge of instantaneous mass flow rate, specific heat integral and inlet dynamic enthalpy. Instantaneous mass flow rate is obtained from the hot wire measurement.

Exit isentropic instantaneous static temperature $\left(T_{5,is}\right)$ is calculated based on equation (4.23) using steady exit measurement condition. Instantaneous inlet static temperature $\left(T_{1,inst}\right)$ and stagnation temperature $\left(T_{01,inst}\right)$ are calculated using average temperature $\left(T_{ave}\right)$ and pressure $\left(P_{ave}\right)$ as stipulated in section 4.3.2. Instantaneous stagnation pressure, which is required to calculate the instantaneous stagnation temperature, is obtained from instantaneous pressure using the relationship in equation (4.36).

.

$$P_{0,inst} = P_{inst}\left(1 + \frac{(\gamma - 1)}{2}Ma^2\right) \tag{4.36}$$

Mach number (Ma) in equation (4.36) is calculated from the hot wire measurement.

With the knowledge of turbine rotor speed $\left(N\right)$, rotor inlet diameter $\left(D_5\right)$ and inlet isentropic power $\dot{W}_{is,inst}$, the velocity ratio of the turbine can be calculated with equation (4.37).

$$\left(\frac{U_5}{C_{is}}\right)_{inst} = \frac{\pi D_5\left(\frac{N}{60}\right)}{\sqrt{2\left(\frac{\left(\dot{W}_{is,inst}\right)_S + \left(\dot{W}_{is,inst}\right)_L}{\left(\dot{m}_{inst}\right)_S + \left(\dot{m}_{inst}\right)_L}\right)}} \tag{4.37}$$

4.4.2.2 Mass Flow parameter vs. Pressure ratio

Substitution of time resolved measurements of mass flow rate, pressure and temperature into equations (4.26) and (4.27), yields instantaneous mass flow parameter and pressure ratio as given in equation (4.38) and (4.39).

$$MFP_{inst,S} = \frac{\left(\dot{m}_{inst}\right)_S \sqrt{\left(T_{01,inst}\right)_S}}{\left(P_{01,inst}\right)_S} \tag{4.38a}$$

$$MFP_{inst,L} = \frac{\left(\dot{m}_{inst}\right)_L \sqrt{\left(T_{01,inst}\right)_L}}{\left(P_{01,inst}\right)_L} \tag{4.38b}$$

$$PR_{inst,S} = \frac{\left(P_{01,inst}\right)_S}{P_{7,inst}} \tag{4.39a}$$

$$PR_{inst,L} = \frac{\left(P_{01,inst}\right)_L}{P_{7,inst}} \tag{4.39b}$$

4.4.2.3 Cycle-averaged efficiency vs. Velocity ratio

Cycle-averaged total to-static efficiency of the turbine stage is given by equation (4.40), while that of velocity ratio is provided in equation (4.41).

$$\left(\eta_{ts}\right)_{cyc-ave} = \frac{\sum_1^n \dot{W}_{act,inst}}{\sum_1^n \dot{W}_{is,inst}} \tag{4.40}$$

$$\left(\frac{U_5}{C_{is}}\right)_{cyc-ave} = \frac{\sum_1^n \left[\left(\frac{U_5}{C_{is}}\right)_{inst} \cdot \dot{W}_{is,inst}\right]}{\sum_1^n \dot{W}_{is,inst}} \tag{4.41}$$

4.4.2.4 Strouhal Number

Strouhal Number is a dimensionless parameter to quantify the unsteadiness level in a pulsating flow. It is basically the ratio between the centrifugal force and inertial force (Potter and Wiggert, [83]). As such, it calculates the rate of changes of a moving particle in comparison to its propagation. It is widely used in turbochargers to calculate the unsteady dynamics in volume compared to the pulsating incident of the flow. The Strouhal Number is modified for turbocharges due to the pulse waveform which is not sinusoidal and called Modified Strouhal number, MSt (Szymko [84]), as given by equation (4.42)

$$MSt = \left(\frac{f \cdot L}{C} \right) \frac{1}{2\phi} \tag{4.42}$$

The above is then used as a base to calculate the, Pressure Modified Strouhal number (PMSt) is defined in equation (4.43). It is basically the velocity at which the pressure waves propagate, by adding the gas velocity, C to the sonic speed, a.

$$PMSt = \left(\frac{f \cdot L}{C + a} \right) \frac{1}{2\phi} \tag{4.43}$$

4.5 Uncertainty Analysis

The instruments in the test facility, where measurements are obtained are subjected to a degree of uncertainly or error which influences the final results. As such, it is extremely essential to account for all errors in measurement of individual parameters when analysing the data. Hence, all variables are deduced through a statistical-based approach as proposed by Kirkup [85] and adopted by Newton [18]. The propagated uncertainty of the parameters during the calibration process is defined as parameter Y as a function of variable x, $Y = f(x)$. The calculation of the standard deviation for data points for each parameter is defined as function (σ) for *n* number of data is expressed in equation (4.44).

$$\sigma_Y = \sqrt{\frac{\sum_1^n [Y_i - f(x_i)]^2}{n - v}} \tag{4.44}$$

Whereby v is defined as number of degrees of freedom given as the number of data points minus the number of restrictions to be found on possible Y values for a given function $f(x)$. Linear function of $Y = mx + c$ decreases the value of v to two. The uncertainty is expected to be twice the standard deviation for the variable Y as shown in equation (4.45):

$$U_Y = \pm 2\sigma_Y \tag{4.45}$$

If a normal distribution is realised from the trend of the deviation of the measurement, this provides an outcome of 95.4% probability that the true value lies within the calculated uncertainty. For instances where the measured parameter is a function of several other independent quantities $X_1, X_2, ..., X_k$. The equation is described in (4.46).

$$Y = f(X_1, X_2, ..., X_k) \tag{4.46}$$

The British Standards [81] for standard deviation for Y is given as equation (4.47).

$$\sigma_Y = \sqrt{\left(\frac{\partial Y}{\partial X_1}\sigma_1\right)^2 + \left(\frac{\partial Y}{\partial X_2}\sigma_2\right)^2 + ... + \left(\frac{\partial Y}{\partial X_k}\sigma_k\right)^2} \tag{4.47}$$

Partial derivatives of Y with respect to X are, $\frac{\partial Y}{\partial X_1}, \frac{\partial Y}{\partial X_2}, ... \frac{\partial Y}{\partial X_k}$. As such, a combined uncertainty measurement is applied to measure Y parameter using Root Sum Square (RSS) method. Sysmko [58] and Newton [18] both regularly used this estimation method as it provides thorough uncertainty analysis explicit to the current test facility. The RSS method of uncertainty ($URSS$) for parameter Y is given below in equation (4.48) and used as a basis throughout the current thesis.

$$U_{RSS,Y} = \sqrt{\left(\frac{\partial Y}{\partial X_1}U_1\right)^2 + \left(\frac{\partial Y}{\partial X_2}U_2\right)^2 + ... + \left(\frac{\partial Y}{\partial X_k}U_k\right)^2} \quad \textbf{(4.48)}$$

Where $U_{RSS,Y}$ = *RSS* uncertainty of parameter

U_k = individual variable uncertainty

$\frac{\partial Y}{\partial X_k}$ = sensitivity coefficient

Table 4.7 list the uncertainty associated with individual measurements of the physical properties given in Table 4.3.

Table 4.7 Uncertainty in measurement

Physical Property	Measurement	Uncertainty	
		Steady	Unsteady
V- Cone flow meter	Upstream Pressure	± 257 Pa	NA
	Pressure difference	± 120 Pa	
	Upstream Temperature	± 0.67 K	
	Mass flow	± 1.62 g/s	
Measurement plane (Turbine inlet)	Pressure	± 238 Pa	NA
	Temperature	± 0.5 K	± 3 K
	Instantaneous Pressure	NA	± 613 Pa
	Instantaneous Mass flow (Inner limb)		± 13.2 g/s
	Instantaneous Mass flow (Outer limb)		± 9.7 g/s
Turbine exit	Pressure	± 238 Pa	± 238 Pa
Dynamometer	Rotational Speed	± 1 RPM	± 8 RPM
	Torque	± 0.0620 Nm	± 0.0620 Nm

CHAPTER 5

STEADY FLOW EXPERIMENT

The asymmetric double entry turbine experimental findings and analysis under wide range of steady flow test conditions are presented in this chapter. Although actual flow into the automotive turbine inlet is unsteady, extensive experimental points based on steady flow inlet conditions were measured for a number of reasons. The foremost reason is the absence of steady state experimental results available in the public domain, that of a double entry turbine with an unequal scroll division. The availability of wide extending steady flow results would be essential for laying the fundamental characteristics of this asymmetric double entry turbine. In the state of the art turbine testing facility at Imperial College London, turbine loading can be varied by adjusting the gap between magnetic rotor and stator in the dynamometer. The turbine loading dictates the amount of mass flow rates into the turbine, thus momentum imparting the rotor blades. Therefore, by varying the turbine load, broader range of the turbine map will be available. Unsteady experimental points are primarily measured at several velocity ratios (VR) or pressure ratios (PR), corresponding to low, mid and high load. Hence a complete steady state characteristic would serve as a comparison to the cycle average properties calculated at these unsteady points for a given turbine speed.

Secondly, in the out of phase pulsating flow, the rotor wheel is driven by two unequal unsteady flow. This out of phase flow adds complexity to the unsteadiness already present in the flow. Therefore, in depth understanding of the influence that this unsteady flow has on the rotor wheel is crucial. The equivalent steady state analysis will be beneficial in complementing the basic knowledge of the effect of this out of phase unsteady flow. The steady state equivalent conditions are known as unequal admission and partial admission conditions. Furthermore, in this asymmetric turbine, the unequal division between scrolls creates another degree of freedom that requires understanding of steady state analysis.

Apart from these reasons, the current design practice in the turbomachinery industry still relies on steady state analysis of the turbocharger. As such, availability of vast steady state

data will be valuable in the design phase of the turbocharger turbine. In addition to that, matching of a turbocharger to an engine is done by assuming the turbine to be a steady flow device. Finally, Computational Fluid Dynamics (CFD) validation exercise becomes efficient with the steady flow results. This is especially true when the turbine is being investigated for the very first time, under various configuration and test conditions. CFD calculation validation based on a single unsteady point requires more CPU resources and takes almost a month to reach convergence level; as an example at the time of writing this this, a single steady state point CFD validation would require only 12 hours to converge.

One of the hypothesis in this thesis is whether the presence of nozzle vanes, with distinct opening angle in each scroll of an asymmetrically divided double entry turbine, would reduce the losses encountered in equally set nozzle vanes. In order to investigate this research question, various nozzle vane openings and configurations between two scrolls were explored as shown in Table 5.1. Each of these configurations were evaluated at three different admission conditions commonly practiced in any double entry turbine test program. Full admission test was first conducted in all configuration, followed by partial and unequal admission experiments. This testing sequence allows important parameter obtained from full admission performance map, such as pressure ratio and velocity ratio, to be used as the control parameter in the unequal admission condition. Apart from varying the admission conditions of the two independent turbine inlets, the testing was also conducted at different rotor speeds, between 50% and 90% of the equivalent turbine speed.

As spelt out in the preceding chapter, asymmetric double entry turbine has been narrowed to large diesel engine vehicle segment application; owing to the higher rotor inertia of the former and lower speed range of the latter. In the large diesel engines, turbine is only required to operate in low speed range, unlike other smaller turbines which operate more than 100k RPM speed. Therefore, it comes as no surprise the need to investigate the turbine at 90% equivalent turbine speed in this research. However, the choice of test setup as low as 30k RPM (50% equivalent turbine speed) is simply to provide a comprehensive performance map for this novel turbine.

Table 5.1 Steady flow experiment configuration

Vane Angle in Small Scroll Circumference (degrees)	Vane Angle in Large Scroll Circumference (degrees)	Designation
Vaneless	Vaneless	Nozzleless
51	Vaneless	S51
66	Vaneless	S66
71	Vaneless	S71
51	51	S51_L51
51	66	S51_L66
51	71	S51_L71
66	51	S66_L51
66	66	S66_L66
66	71	S66_L71
71	51	S71_L51
71	66	S71_L66
71	71	S71_L71

5.1 Full Admission Characteristic

5.1.1 Nozzleless

Among the various nozzle vane angles and configurations presented in Table 5.1, the nozzleless settings serves as the baseline. The reduction of skin friction loss in this configuration, due to the absence of nozzles in the stator, makes it the suitable candidate to understand the influence of nozzle vane in other configurations. Therefore nozzleless settings results are presented first in each admission condition of this thesis. To begin with, the nozzleless full admission steady test results are presented in Figure 5.1 and 5.2.

Figure 5.1 shows plot of total-to-static efficiency against velocity ratio for two speeds, 30k RPM and 48k RPM. The measured peak efficiency for the two speed lines occurs in the velocity ratio range of 0.64 – 0.72, close to velocity ratio of optimum operating condition for a purely radial inflow turbine as indicated by Watson and Janota [9]. Within this velocity ratio range, the peak efficiency increase with speed is noticeable. The measured

peak efficiency of 77% at 30k RPM has increased to 78% at 48k RPM, an increase of 1 percentage point. At higher velocity ratio, both speed lines overlaps each other, especially in the velocity ratio region between 0.75 and 0.95.

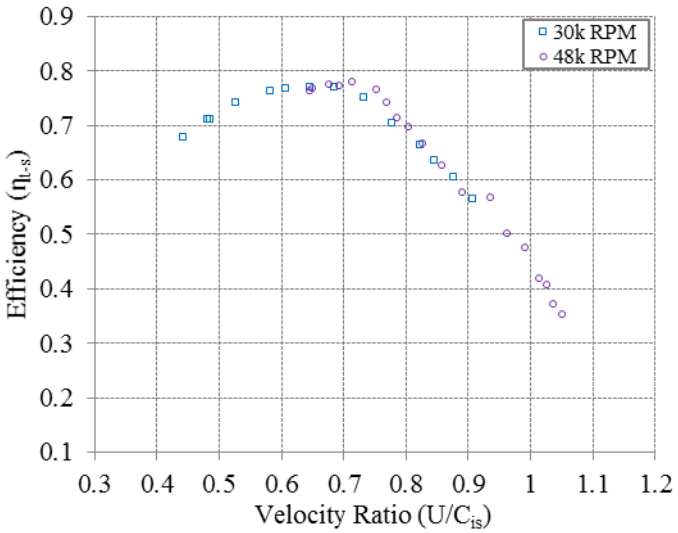


Figure 5.1 Total to static efficiency plot for Nozzleless configuration

Figure 5.2 presents the mass flow characteristic of the nozzleless asymmetric double entry turbine in the full admission condition. The measured mass flow rate in each scroll is used to calculate turbine overall mass flow parameter as given by equation (4.28). The choking limit is asymptotic about 3 x 10^{-5} ($kgs^{-1}K^{1/2}$).Pa^{-1} and 2.5 x 10^{-5} ($kgs^{-1}K^{1/2}$).Pa^{-1} for the large scroll and small scroll respectively. The overall turbine mass flow parameter approaches an asymptote value of 5.5 x 10^{-5} ($kgs^{-1}K^{1/2}$).Pa^{-1}.

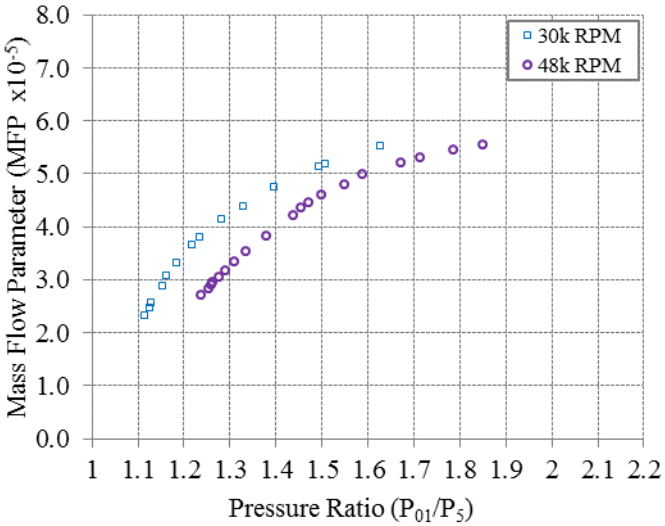


Figure 5.2 Overall swallowing capacity plot for Nozzleless configuration

5.1.2 Nozzle Vanes in small scroll (S nozzle configuration)

An Ideal Exhaust Gas Recirculation (iEGR) rate of approximately 10% is achieved in the nozzleless setting when both scrolls of asymmetric double entry are subjected to full stagnation pressure. Any extraction beyond 10% iEGR rate (either higher or lower) would result in unequal stagnation pressure distribution between the two scrolls, as shown in Chapter 3. As a consequence, the turbine ends up operating in unequal admission condition, which would be detrimental to the overall stage performance. Thus, nozzle vanes are introduced in rotor circumference of the small scroll in order to redress stagnation pressure imbalance created by different EGR extraction. It is prudent to state here that the nozzle vanes are not meant to drive EGR as commonly practiced in turbocharger. Therefore fixed geometry nozzle vanes in small scrolls are investigated in this thesis to evaluate the effectiveness in preserving the performance and where it is impossible to do so, it helps to reduce the penalty in the efficiency. This would in turn provide adequate performance data for the nozzle vanes to be used as Variable Geometry Turbine (VGT) to compensate for different EGR rate. Three different fixed geometry nozzle vane angle openings were investigated in the range of 50% to 90% equivalent turbine speed, these are 51°, 66°, and 71°. Efficiency characteristics of the S nozzle (nozzle vanes arranged in the small scroll) configuration for all five equivalent speed lines are presented in Figure 5.3.

A clear trend is observed in the peak efficiency range (between 30k RPM and 48k RPM) as the nozzle vane setting changes; from most open position (51°) to mid open position (71°). This trend is shown in Figure 5.4. S71 (nozzle vanes on small scroll with an angle of 71°) configuration recorded the optimum peak efficiency, which varies approximately between 72% – 78%. Peak efficiency of S66 (nozzle vanes on small scroll with an angle of 66°) configuration varies approximately between 71% and 76%, while S51 (nozzle vanes on small scroll with an angle of 51°) setting peak efficiency is in the region of 65% - 66%. Table 5.2 shows the peak efficiencies and the corresponding velocity ratios for the setting in Figure 5.3. Efficiency plot of S51 configuration shows little change as the turbine speed increases, with all the speed lines overlapping on each other. Although speed effect of open nozzle vane settings in the S51 configuration is similar to that of Rajoo [7], it is worth mentioning here that his work primarily focused on conventional variable geometry turbine (nozzle vanes arranged around the full circumference of rotor ‘A’) while this work here

focuses on the double entry configuration.

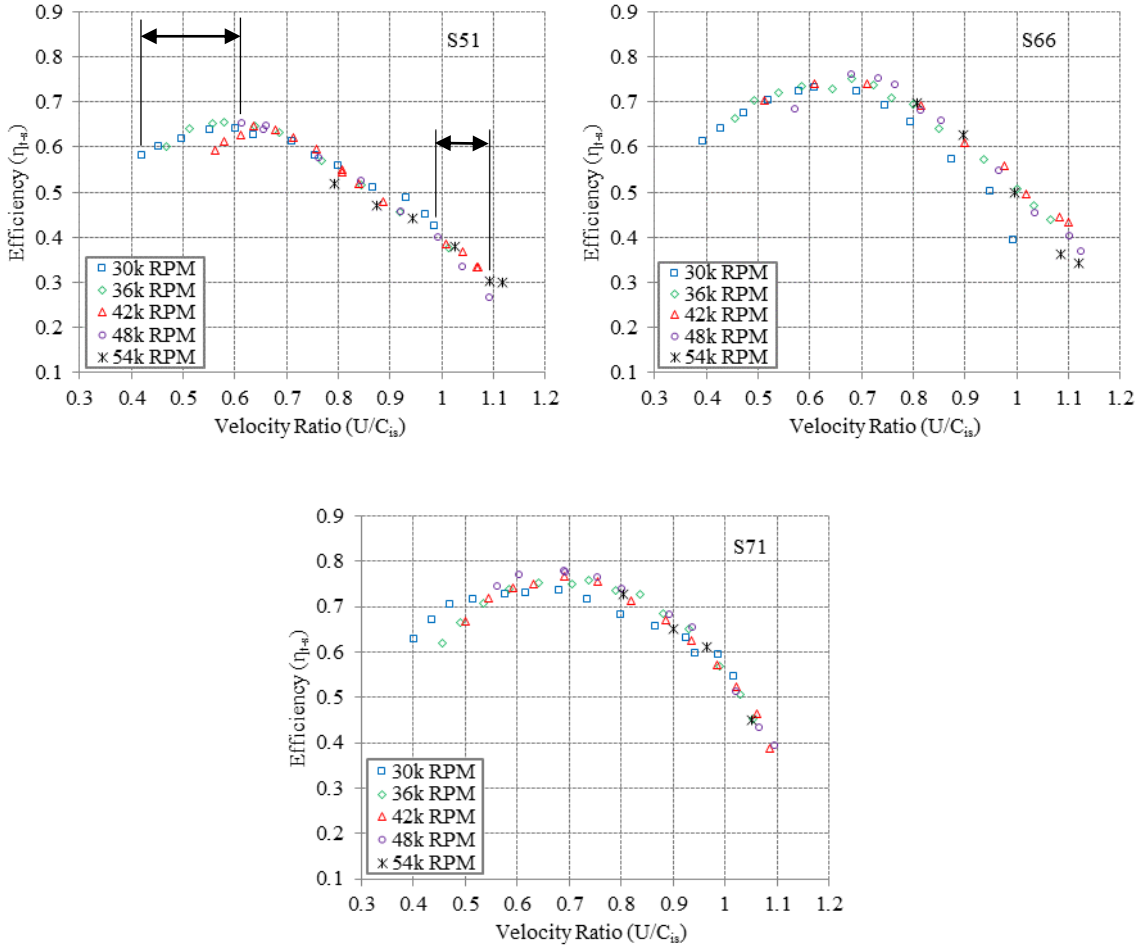


Figure 5.3 Total to static efficiency plot for various S nozzle configuration

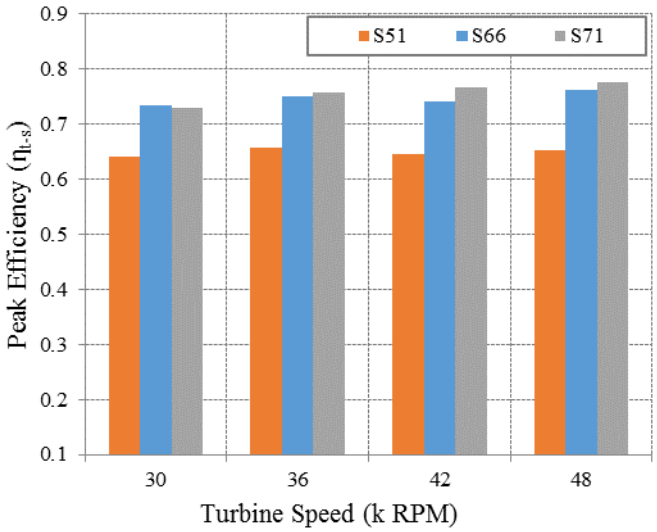


Figure 5.4 Trend showing variation in peak efficiency as S nozzle vane closes for different turbine speeds

One similarity between all configurations presented in Figure 5.3 is that the velocity ratio range gets narrower as the turbine speed increases. As one may expect, the efficiency curve shifts to the right (higher velocity ratio region) with the increase in turbine speed. This would have resulted in velocity ratio range of each speed line of a particular configuration to remain approximately the same. Unfortunately, the shift experienced at both extremes of the curve presented in Figure 5.3 are not equal. Refer zones marked in the right and left of Figure 5.3. This is mainly due to limitation in the current test facility. The existing facility only allows testing between dynamometer gap of 1 mm and 9 mm, and this restricts the efficiency curve to be extended to the left (lower velocity ratio range). Furthermore, overall system vibration increases with turbine speed, and as a consequence it becomes impossible to make any measurements at these high equivalent speeds. This is especially significant at 48k RPM speed and beyond.

Table 5.2 List of peak efficiency and corresponding velocity ratios for S nozzle configuration

Rotor Speed (RPM)	Vane Configuration	$(\eta_{t\text{-}s})_{peak}$	$(U/C_{is})_{\eta\text{-}peak}$	iEGR rate (%)
30k	S51	0.641	0.602	6.1
	S66	0.733	0.609	12.1
	S71	0.729	0.618	16
36k	S51	0.656	0.6	5.5
	S66	0.751	0.68	11.9
	S71	0.757	0.705	16.1
42k	S51	0.646	0.637	5.1
	S66	0.742	0.711	11.7
	S71	0.767	0.69	15.6
48k	S51	0.652	0.613	4.9
	S66	0.761	0.68	10.4
	S71	0.776	0.694	15.4

Figure 5.5 presents overall turbine swallowing capacity characteristics of the asymmetric double entry turbine, with S nozzle configuration for all five speed lines. The horizontal asymptote is evident in all vane angle setting indicating the choking condition of the turbine. The overall mass flow parameter ranges between 5.46 x 10^{-5} ($kgs^{-1}K^{1/2}$) .Pa^{-1} and

6.72 x 10^{-5} ($kgs^{-1}K^{1/2}$) .Pa^{-1}, lower limit being for the mid open nozzle vane position (S71) and the higher limit for the most open nozzle vane angle setting (S51). Table 5.3 lists the swallowing capacity and pressure ratio corresponding to peak efficiency point for configuration presented in Figure 5.5.

The turbine speed has greater influence on the swallowing capacity: the mass flow parameter decreases as equivalent speed increases for a given pressure ratio. This is a typical characteristic of a radial flow turbine and it is the result of the centrifugal pressure head (created by rotating rotor) which opposes the flow and increases as rotor speed increases. This causes the mass flow parameter of different rotor speed (of the same configuration) to appear as distinct curves, as observed in Figure 5.5.

As the nozzle vane setting changes; from most open position (51°) to mid open angle (71°), the mass flow parameter curve moves closer to each other. When the nozzle vane closes, the nozzle throat area becomes smaller and causes the absolute velocity to increase in magnitude. Velocity increases lead to an increase importance of compressible flow conditions, once a Mach number of unity is reached where no more flow moves through the nozzle vane throat. As the nozzle vane chokes at sonic condition, all the swallowing capacity curves at different speed collapse into a single curve. Despite not displaying the a clear vane choking phenomena for S71 (Figure 5.5), there is a clear trend towards a chocking indicated by the gradient of the line at high pressure rations. have clearly shown the combined effect of flow velocity increase and flow density decrease. Therefore it is believed that this pseudo-choking (almost choking) occurrence is more dominant compared to centrifugal pressure head influence as nozzle vane closes.

The narrower pressure ratio range, which increases in speed, for a given configuration is due to the limitation of the testing facility; as discussed there is an upper and lower limit in the power absorption capability. As observed in Figure 5.3, the shorter efficiency characteristics in the low velocity ratio region corresponds to high pressure ratio region, as given by equation (4.25). This explains why 54k RPM speed lines terminates close to pressure ratio of 1.6.

Figure 5.6 shows efficiency characteristics of all three nozzle vane openings in S nozzle configuration, for two equivalent turbine speeds. Nozzleless efficiency curve which is

plotted on the same axis, serves as the baseline as explained in the beginning of the section. It is worth stating here that, nozzleless configuration represents one particular EGR rate, of 10%. Therefore, nozzleless configuration should not be viewed as the optimum setting due to its superior efficiency characteristics.

Figure 5.6 (a) shows total to static efficiency plotted against velocity ratio for constant speed line of 30k RPM. All the nozzle vane openings in S nozzle setting has underperformed in terms of efficiency. Peak efficiency of S51, S66 and S71 configuration are 64.1%, 72.1% and 73.3% respectively. In principle, nozzle vanes are introduced to accelerate the flow further at a particular flow angle into the rotor. Flow acceleration causes the absolute flow velocity component to increase, and subsequently raising the turbine output power. This is clearly shown in Euler turbomachinery equation (5.1). Nevertheless, this benefit comes with a drawback, an increase in absolute flow velocity also means rise in kinetic energy at the nozzle vane throat, as a result, skin friction drag grows. This is one reason why all the S nozzle configurations have recorded drop in efficiency compared to the nozzleless setting.

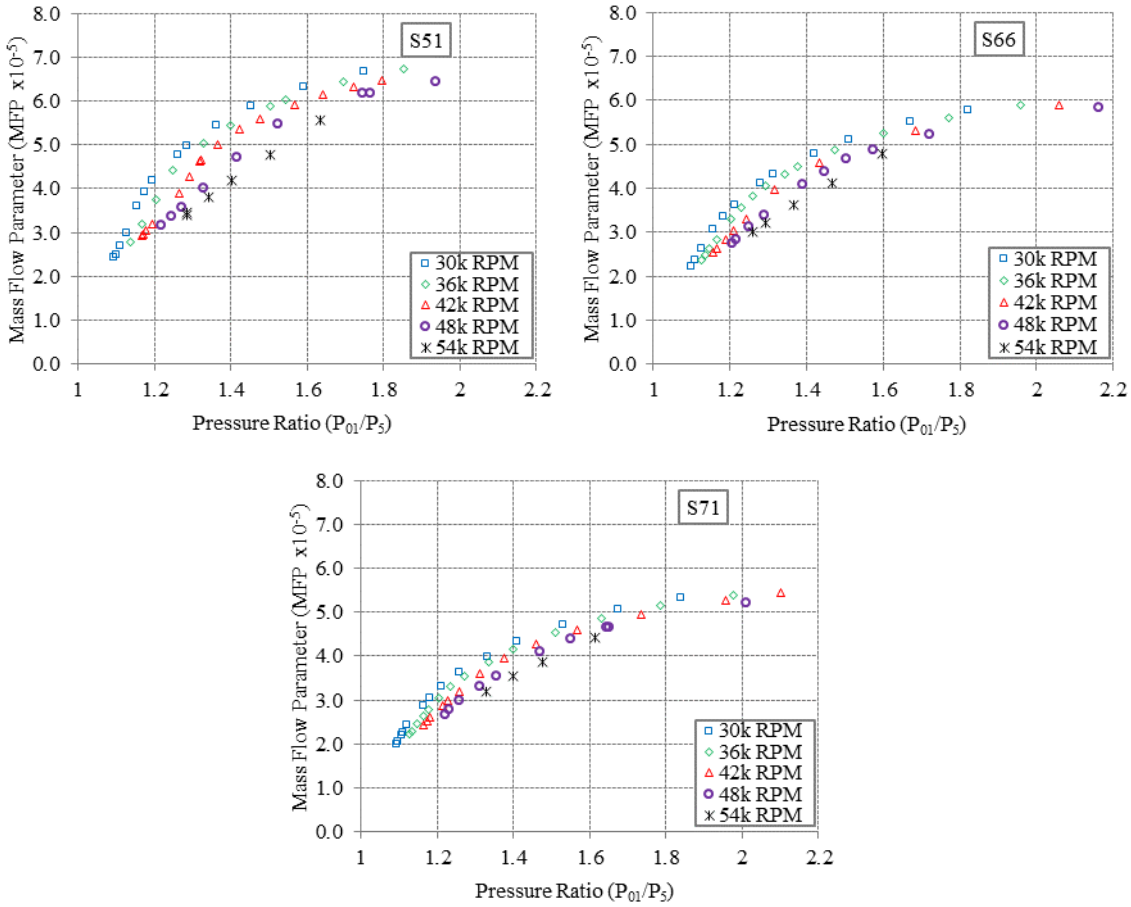


Figure 5.5 Overall turbine swallowing capacity plot for various S nozzle configuration

Table 5.3 List of swallowing capacity and pressure ratio corresponding to peak efficiency of S nozzle configuration

Rotor Speed (RPM)	Vane Configuration	$(MFP)_{\eta\text{-peak}}$ (x 10^{-5})	$(P_{01}/P_5)_{\eta\text{-peak}}$
30k	S51	4.99	1.287
	S66	4.12	1.281
	S71	3.63	1.26
36k	S51	5.9	1.505
	S66	4.31	1.342
	S71	3.87	1.337
42k	S51	5.92	1.567
	S66	4.59	1.436
	S71	4.29	1.462
48k	S51	6.47	1.936
	S66	5.24	1.721
	S71	4.68	1.645

With a drop in peak efficiency of less than 5 percentage point, S66 and S71 configuration performance are the closest to the nozzleless configuration. S71 and S66 settings has outperformed the nozzleless configuration at a velocity ratio of 0.8 and beyond. According to flow visualizations by Woolley and Hatton [15], radially inwards flow (more positive incidence angle) separates at rotor blade suction surface, while tangential flow (more negative incidence angle) separates at pressure surface. Both extremes are unfavorable to the turbine, as flow separation on either side contributes to rise in overall turbine losses. The optimum suggested incidence angle by Japikse and Baines [5] is in the region of -20° and -40°. Since S66 and S71 nozzle vane angle settings are away from two extreme ends of the flow (based on vane angle opening), flow in both configuration are expected to pass through rotor passage smoothly, without separation. The optimum efficiency characteristic displayed by these two settings further strengthen the above explanation and indicates that the flow is within the suggested incidence angle range.

With the presence of nozzle vane in the small scroll, the turbine rotor is subjected to a changing relative inlet flow angle, as it rotates from one scroll to another. This unequal relative flow angle causes an unsteady effect on the rotor performance. Although a detailed flow field analysis using CFD will be required to understand this phenomenon, a preliminary physics analysis of this occurrence is suggested here. Consider one passage of the rotor rotating between the scrolls in the S51 setting. In the small scroll sector with nozzle vane angle at 51°, flow enters the rotor radially, and flow separates on suction surface, as explained above. When the same passage rotates to the nozzleless large scroll sector, flow with more negative incidence angle moves through the rotor, with minimized separation. The passage is subjected to rapid change in flow velocity magnitude and direction as it rotates from the small scroll to large scroll sector. Since each scroll swallowing capacity is different, the passage does not only subject to sudden change in flow velocity direction, but also in its magnitude, as it rotates from small scroll (160°) to large scroll (200°) sector. This rapid change creates unsteadiness in flow. A similar observation by Copeland [53] and Newton [18] of an unequal admission condition in a conventional double entry turbine suggest that the resulting unsteadiness in flow is a function of the ratio of pressure ratio and frequency, which increases with rotational speed. In this asymmetric double entry turbine under a non-uniform state with equal stagnation pressure inlet condition, the ratio of pressure ratio does not dictate the unsteadiness. Instead it is the unequal time spent in each scroll, speed, abrupt incidence angle and mass difference between scrolls govern the unsteadiness. This is true for all S nozzle configuration, with exception in S71 setting; in this case, the flow in each scroll approaches the rotor leading edge inlet with approximately similar absolute flow angle, assuming flow angle in nozzleless large scroll is equivalent to volute exit flow angle.

The magnitude of nozzle vane skin friction force increases as the nozzle vane setting changes from most open position (51°) to mid open position (71°). Considering equal wetted area (nozzle vane planform area) and constant skin friction coefficient (Re and Ma dependency remains unchanged), highest and lowest drag force are expected in S71 and S51 configuration respectively. However, peak efficiency recorded by each setting in Figure 5.6 (a) does not seem to represent this trend. As the nozzle vane closes from 51° to 71°, rotor inflow condition changes from radial (former) to tangential (latter). As a result, flow separation occurs in S51 settings; on rotor suction surface. Separation loss clearly has more profound influence than skin friction loss in the asymmetric double entry turbine

performance for a given rotor speed. This is believed to be the main reason why S51 has the lowest efficiency.

Losses due to skin friction, secondary flow phenomena and non-uniform admission condition, changes as turbine speed increases. In order to appreciate the effect of speed on turbine performance and correlate the losses, efficiency characteristics of various S nozzle configuration at 48k RPM is presented in Figure 5.6 (b). S71 shows overall highest turbine efficiency within the operating condition of the turbine. S71 peak efficiency is similar to that of nozzleless setting. S66 setting exhibit 1% drop in peak efficiency, in the velocity ratio region between 0.65 and 0.75, but outperforms the nozzleless configuration for the entire turbine operating condition. S51 setting did not show any efficiency improvement at 48k RPM.

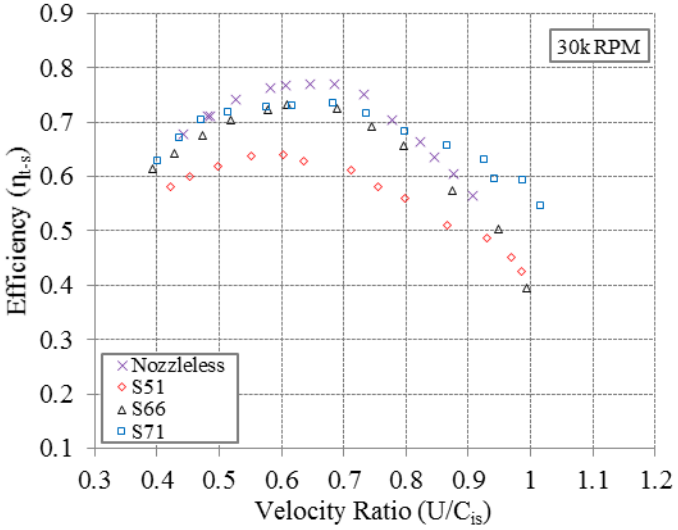
The centrifugal pressure head which opposes the flow and increases with rotor speed, causes the turbine to swallow less for a given nozzle vane configuration. The reduction in mass flow parameter subsequently reduces absolute velocity magnitude, which in turn decreases the kinetic energy. Therefore, skin friction force is expected to decrease as turbine speed increases. Based on swallowing capacity characteristics shown in Figure 5.4, the highest drop in skin friction force is anticipated in S51 setting, while the lowest is in S71 nozzle vane arrangement. With this insignificant variation, S71 remains as the configuration with highest skin friction force.

Increase in turbine speed would have caused the incidence angle to become more negative. This can be easily deduced from a velocity triangle. What remains unknown is whether the incidence angle at higher turbine speed is within the optimum flow condition that could minimize secondary flow in the rotor passage. Peak efficiency points in all S nozzle configuration have moved to velocity ratio of less than 0.7. This obvious change, suggests that incidence angle is within the desired optimum flow condition in these settings. As the rotor passage rotates from one circumferential division to another, it will be subjected to change in unequal incidence angle and mass flow. This mismatch creates unsteadiness in the flow as turbine continues to rotate, whose frequency is a function of turbine speed. Since level of incidence angle inequality and mass difference between scrolls are greatest in S51 settings, rotor passage is exposed to greater level of unsteadiness. Therefore, the increased unsteadiness in the higher turbine speed cancels out the gain obtained from

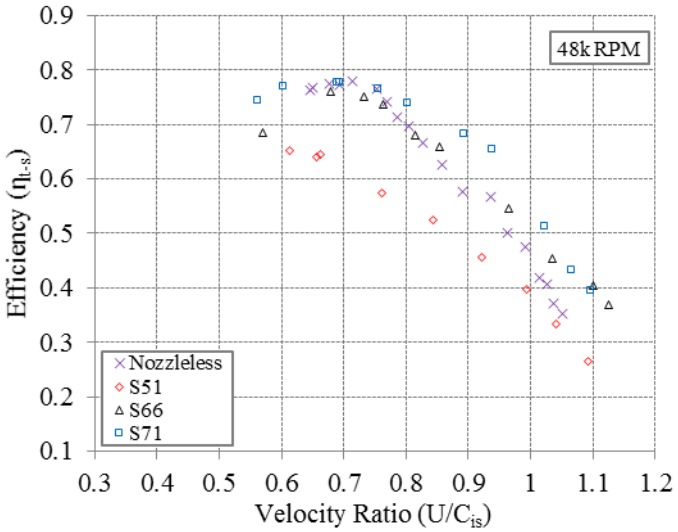
reduced secondary flow in the rotor passage. As a result, constant peak efficiency characteristic observed in S51 settings (when 48k RPM is compared against 30k RPM).

As turbine speed increases, closer to actual optimum operating speed, S71 and S66 configuration are expected to have similar performance characteristic as 48k RPM speed line. Increase in turbine speed would not have caused significant changes to peak efficiency point velocity ratio, which suggest similar optimum flow angle matching to rotor inlet as that of 48k RPM speed. As a result,, higher torque measurement is expected at higher turbine speed, especially at the peak efficiency point (high load region). But this higher useful shaft work would have been defused by increase in sudden turbine back pressure with increase in turbine speed, especially above 54k RPM. In order to understand this suggested trend, one needs to examine the swallowing capacity curve in Figure 5.5. As turbine speed increases, S66 and S71 setting curve is less steep. Due to this flatter gradient characteristic, there is a sudden increase in pressure ratio than would be anticipated from a steeper curve for a given mass flow rate. In other words the increase in back pressure is very sudden as turbine speed increases. This causes increase in isentropic power, which is compensated by useful shaft work extraction from flowing fluid, thus achieving optimum efficiency approximately equal to 48k RPM speed line.

Figure 5.7 shows overall swallowing capacity of all the settings presented in Figure 5.6. The discussion provided previously compared the efficiency characteristics without making reference to the mass flow parameter. Nozzleless and S66 settings have exhibited similar overall swallowing capacity characteristic, at both equivalent turbine speed. The equal mass flow rate parameter between two settings; nozzleless and S66, enables fair comparison between them, as both theoretically imparts equal momentum on the rotor to enable power extraction from the flow.



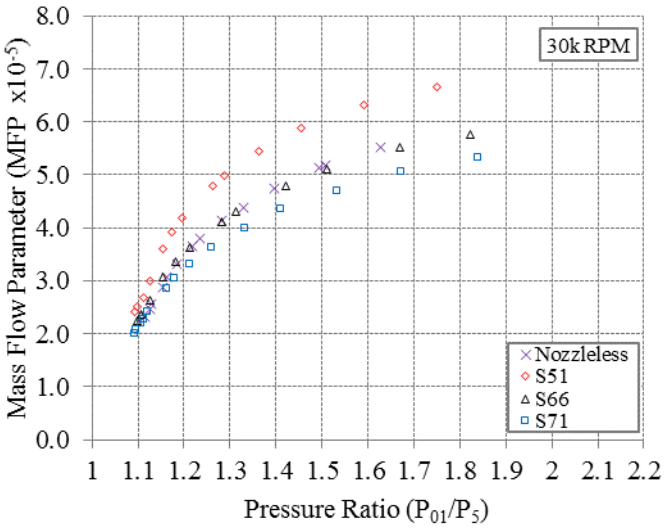
(a)



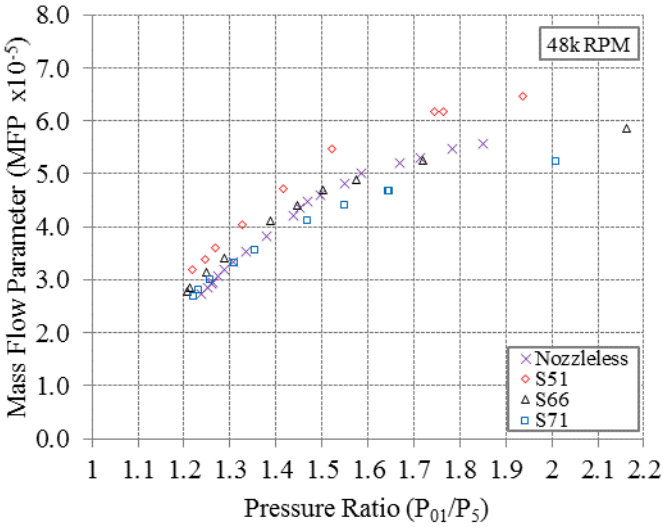
(b)

Figure 5.6 Total to static efficiency plot comparison between S nozzle and nozzleless configuration

$$W_x = \frac{1}{2}\left[\left(U_5^2 - U_7^2\right) - \left(W_5^2 - W_7^2\right) + \left(C_5^2 - C_7^2\right)\right] \tag{5.1}$$



(a)



(b)

Figure 5.7 Overall turbine swallowing capacity plot comparison between S nozzle and nozzleless configuration

5.1.3 Nozzle Vanes in both scrolls (SL nozzle configuration)

A conventional turbine has nozzle vanes arranged around the entire circumference of the turbine rotor. Testing data presented thus far has characterized the asymmetric double entry turbine with nozzle vanes only in the small scroll. Therefore, performance map of asymmetric double entry turbine with nozzle vanes around the entire rotor periphery has to be made available, so that a suitable evaluation against conventional turbine can be made. Two different combinations of nozzle vane configurations are presented in this section. In

the first combination, nozzle vanes with equal opening angles are arranged in both scrolls, while nozzle vanes with distinct opening angles in each scroll are set in the other combination. This gives a total of 9 SL nozzle (nozzle vanes arranged around full circumference of rotor inlet) configurations, derived from basic 3 nozzle vane angles evaluated in section 5.1.2; opening angles of 51°, 66°, and 71°. These configurations were assessed at 2 constant turbine speed. Table 5.4 shows the peak efficiencies and the corresponding velocity ratios for the SL nozzle setting.

Turbine speed has little influence on efficiency characteristic of S66_L66 (nozzle vane with an angle of 66° around full circumference of rotor inlet) and S71_L71 (nozzle vane with an angle of 71° around full circumference of rotor inlet) configuration presented in Figure 5.8. In both settings, peak efficiency improvement is only about 2%, at 48k RPM, compared to 30k RPM. For the rest of the operating condition of the turbine, both speed lines in S66_L66 setting tend to overlap on each other, especially for velocity ratio higher than 0.8. As for S71_L71 configuration, distinct speeds lines are noticed until velocity ratio of 0.9, beyond which, two speed lines merge together.

In contrast, S66_L71 (nozzle vane in small scroll with an angle of 66° and nozzle vane in large scroll with an angle of 71°) and S71_L66 (nozzle vane in small scroll with an angle of 71° and nozzle vane in large scroll with an angle of 66°) configurations exhibit distinct efficiency curves at different turbine speeds. In S66_L71, 48k RPM speed lines has shown 2% peak efficiency improvement over 30k RPM. 48k RPM speed line in S71_L66 has recorded peak efficiency improvement of 5%, at 74.2%.

Distinct speed lines presented in Figure 5.9 clearly exhibit speed dependency swallowing capacity characteristic. Among the configuration shown, S66_L66 and S66_L71 swallowing capacity curve spread away from each other further than that of other two settings. Going by the same suggestion in S nozzle swallowing capacity discussion, smaller nozzle throat area around the entire rotor periphery in the S71_L71 configuration seems like the reason for this difference. However, a closer look at S66_L71 mass flow parameter reveals that this may not be the case, as curves of different turbine speeds are spread away in this settings, despite having smaller nozzle throat area in the large scroll. The more closed nozzle vane angle position in the small scroll is most likely causing the swallowing capacity curve of different speed lines moves closer to each other, as noticed in the S

nozzle mass flow parameter. Rise in rotor speed causes the flow absolute velocity through the smaller nozzle throat area to increase, to a point close to sonic condition. This phenomenon is more dominant in the small scroll owing to the relatively smaller circumferential area.

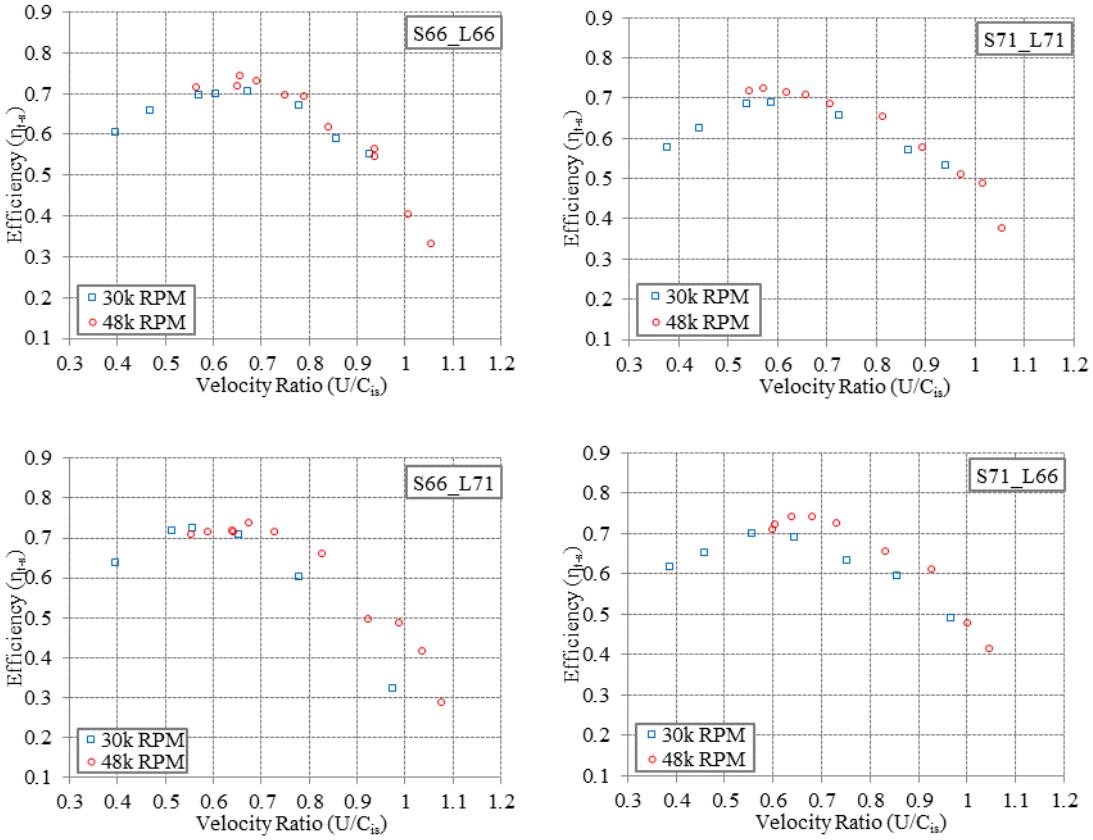


Figure 5.8 Total to static efficiency plot for various SL nozzle configuration

Figure 5.10 shows total to static efficiency plot for configuration with equal nozzle vane opening in both scrolls at 30k RPM. Nozzle vane settings with an angle of 66 ° (S66_L66) and 71° (S71_L71) have shown similar efficiency characteristic, with peak efficiency of 70%, penalty of 7 efficiency point compared to nozzleless setting. Both configurations has wider operating range, in the range of 0.378 – 0.940, compared to that of the nozzleless setting. Configuration with the most open nozzle vane angle has the lowest efficiency characteristic, with peak efficiency of 60%. All the three nozzle vanes setting in Figure 5.10 exhibit peak efficiency at velocity ratio of 0.6, approximately in the same range as the settings presented in Figure 5.6 at 30k RPM speed. Table 5.5 lists the swallowing capacity and pressure ratio corresponding to peak efficiency point for SL nozzle configuration.

Table 5.4 List of peak efficiency and corresponding velocity ratios for SL nozzle configuration

Rotor Speed (RPM)	Vane Configuration	$(\eta_{t\text{-}s})_{peak}$	$(U/C_{is})_{\eta\text{-}peak}$	iEGR rate (%)
30k	S51_L51	0.6	0.6	7.9
	S51_L66	0.646	0.6	0
	S51_L71	0.621	0.6	8
	S66_L51	0.66	0.6	16
	S66_L66	0.698	0.605	5.4
	S66_L71	0.724	0.6	0
	S71_L51	0.671	0.62	19.9
	S71_L66	0.7	0.6	11
	S71_L71	0.688	0.587	8
48k	S66_L66	0.744	0.656	6.4
	S66_L71	0.737	0.643	0
	S71_L71	0.723	0.572	4
	S71_L66	0.742	0.639	11.3

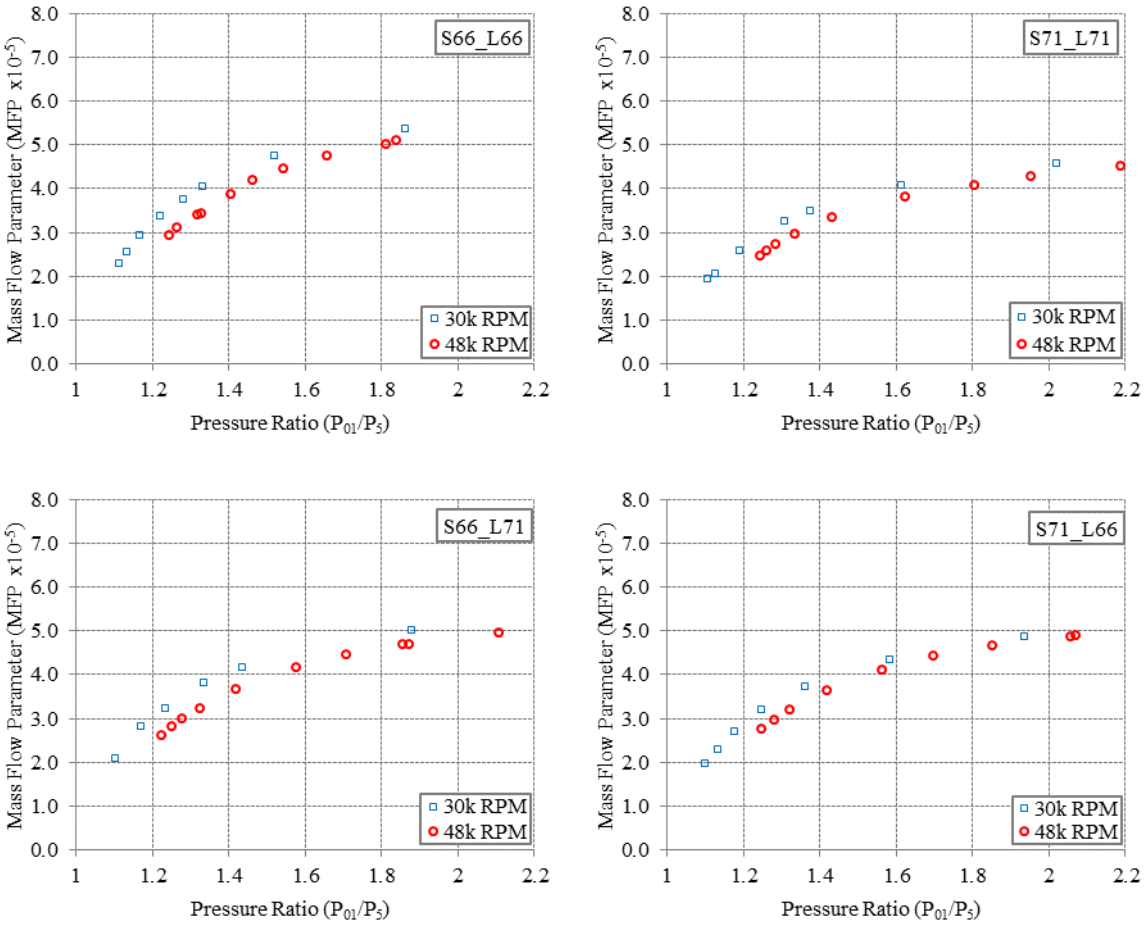


Figure 5.9 Overall turbine swallowing capacity plot for various SL nozzle vane opening

Table 5.5 List of swallowing capacity and pressure ratio corresponding to peak efficiency of SL nozzle configuration

Rotor Speed (RPM)	Vane Configuration	$(MFP)_{\eta\text{-peak}}$ (x 10^{-5})	$(P_{01}/P_5)_{\eta\text{-peak}}$
30k	S51_L51	5.26	1.3
	S51_L66	4.63	1.31
	S51_L71	4.27	1.31
	S66_L51	4.64	1.32
	S66_L66	3.75	1.28
	S66_L71	3.82	1.34
	S71_L51	3.97	1.26
	S71_L66	3.71	1.36
	S71_L71	3.25	1.308
48k	S66_L66	5.1	1.84
	S66_L71	4.7	1.86
	S71_L71	4.53	2.185
	S71_L66	4.66	1.85

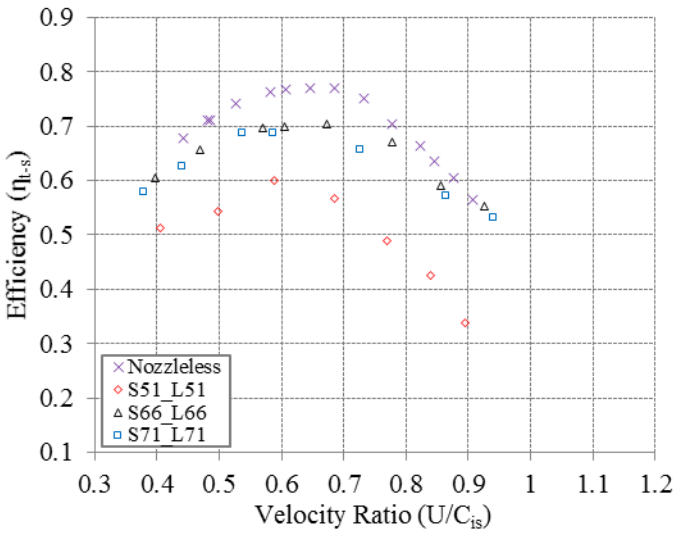


Figure 5.10 Total to static efficiency plot comparison between SL nozzle and nozzleless configuration at 30k RPM

Swallowing capacity curves of configuration with equal nozzle vane angle setting in both scrolls are presented in Figure 5.11. As expected S51_L51 and S71_L71 has recorded the highest and lowest mass flow parameter respectively.

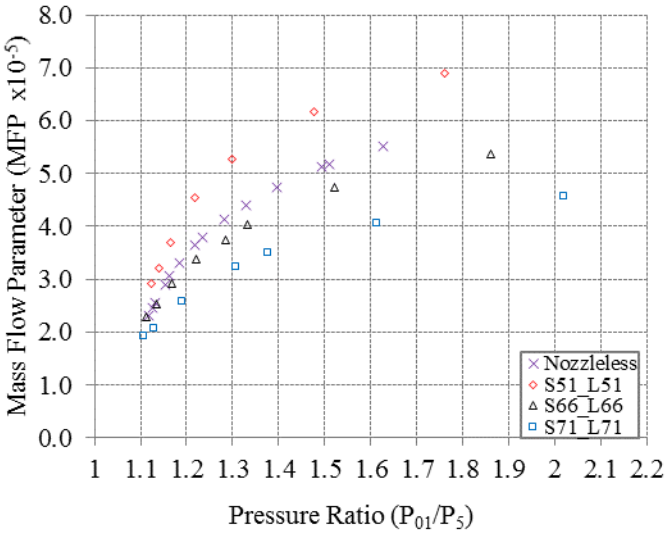


Figure 5.11 Overall turbine swallowing capacity plot comparison between SL nozzle and nozzleless configuration at 30k RPM

Figure 5.12 shows efficiency characteristics of asymmetric double entry turbine with distinct nozzle vane opening in each scroll. Efficiency curve of S nozzle settings are only presented in Figure 5.12 (a). All settings presented in Figure 5.12 (a) has similar nozzle vane angle in small scroll, while that of Figure 5.12 (b) has same nozzle vane angle in large scroll. Both figures represent experimental data from the same test.

S71_L66 (nozzle vane in small scroll with an angle of 71° and nozzle vane in large scroll with an angle of 66°) configurations has displayed similar efficiency characteristic compared to S71_L71 setting, despite having different nozzle vane angle setting in the large scroll. Peak efficiency of both configurations have departed by 3 percentage point from that of S71 vane angle setting. In order to understand the loss mechanism accountable for this phenomenon, some important findings in section 5.1.2 are worth repeating here. With vane angle of 71° and 66° in the small scroll, flow is observed to be within the optimum incidence angle range. This was clearly depicted by optimum efficiency characteristics of S61 and S77 configurations. Going by the same observation, similar incidence angle characteristic is expected when 71° and 66° vane angle openings are configured in the large scroll of S71_L71 and S71_L66 configurations. Hence, this rules out the influence of losses due to flow separation in the rotor passage. Additionally, with optimum flow condition in both scrolls of these two configurations, unsteadiness in the flow as rotor rotates from one sector to another is also dismissed. Therefore, additional

skin friction force due to presence of nozzle vanes in large scroll is solely responsible for the deficit in the total to static efficiency in these settings.

S71_L51 (nozzle vane in small scroll with an angle of 71° and nozzle vane in large scroll with an angle of 51°) settings, despite having lowest skin friction effect, has recorded the lowest peak efficiency, penalty of 3% and 6% compared to S71_L71 and S71 settings, respectively. Radially arranged nozzle vane in large scroll of S71_L51 settings causes separation on blade suction surface which contributes to secondary flow generation in the rotor passage. Apart from that, as the rotor rotates from small scroll to large scroll sector, it experiences abrupt mismatch in the flow direction; both scroll having distinct vane angle opening. The unsteadiness in flow coupled with secondary flow are believed to be the reason for efficiency departure from that of S71 settings.

S66_L71 and S66_L66 configuration have recorded 2% penalty in peak efficiency compared to S61 setting. As observed earlier, the performance deficit is believed to be caused by significant skin friction force, consequence of nozzle vanes presence in the large scroll. On the other hand, secondary flow in rotor passage and uneven incidence angle distribution between scrolls are believed to have more profound influence than skin friction force in the S61_L51 setting, which has recorded the lowest peak efficiency.

Despite having uniform incidence angle distribution around the entire rotor inlet circumference, S51_L51 (nozzle vane with an angle of 51° around full circumference of rotor inlet) setting has recorded the lowest efficiency characteristic. When the more open nozzle vane setting of 51° is configured in large scroll, higher flow separation loss due to deviation from optimum incidence angle has reduced the peak efficiency by 5%. This secondary flow is believed to be the main contributor to the losses encountered in this configuration. This observation is strongly supported by the efficiency curve displayed by S51, S51_L66 & S51_L71 configurations. In these settings, nozzle vane arrangement in the small scroll section contribute to flow separation on the suction surface in the rotor passage, while the favorable incidence angle encountered at the large scroll sector causes flow to pass smoothly in the rotor passage without separating on either surface of the rotor blade. This gain (incidence angle improvement in large scroll) in performance offsets the additional skin friction and non-uniform incidence angle losses. The gain due to well

matched flow at the rotor leading edge, is believed to be large enough to offset the losses due to skin friction and unequal incidence angle between scrolls.

Figure 5.13 shows mass flow parameter of all the settings presented in Figure 5.12. S51_L71, S71_L51 and S66 settings swallow the same amount of mass as that of nozzleless configuration. S51 and S51_L51 too exhibit similar swallowing capacity. S66_L51 and S51_L66 settings have same overall swallowing capacity characteristic.

5.2 Partial Admission characteristics

The real engine exhaust flow in a multiple entry turbine pulses in an out of phase mode; it is thus important to perform steady tests at different levels of flow in the two entries, called commonly as unequal admission. In this condition, each scroll of the double entry turbine is subjected to different pressures and mass flow rates. The extreme of unequal admission is what we call partial admission where one side is fully flowing while the other side is not flowing. The findings in this section is expected to answer one of the hypothesis in this thesis; whether partially admitted flow in small scroll would have same influence on the turbine rotor as that admitted in large scroll.

5.2.1 Nozzleless

Partial admission results of configuration without nozzle vanes are presented in this section. Nozzleless asymmetric double entry turbine was tested with two types of partial admission settings; small scroll flowing (SSF) and large scroll flowing (LSF). As in the case of full admission condition, the nozzleless partial admission findings serves as the baseline for other configurations subjected to similar admission condition. Apart from comparison between different nozzle vane configurations subjected to partial admission, assessment is also made against nozzleless full admission results.

In reality this partial admission condition does not occur, as the exhaust gas continuously feeds the turbine. Nevertheless, in the case of the asymmetric double entry turbine, the closest partial admission condition that would be experienced by the turbine is when the

small scroll has no mass flowing, as this scroll is accountable for EGR extraction. As such partial admission condition with large scroll flowing is a better representation of the lowest efficiency that would be experienced by this turbine with 50% EGR operation.

Figure 5.14 shows total-to-static partial admission efficiency plotted against velocity ratio for two speed lines. As observed in the full admission condition of the nozzleless settings, turbine speed has again shown little influence on efficiency performance when flow is admitted partially. Increase in turbine speed would have caused the incidence angle to become more negative, thus contributed in minimizing secondary flow in the rotor passage. It is worth noting that, this reduction in secondary flow only occurred along rotor inlet circumferential area, in the flowing scroll. However, as the rotor passage rotates from one circumferential division to another, it will be subjected to the sudden change in total pressure and mass. This abrupt mismatch creates unsteadiness in the flow as turbine continues to rotate. Since the frequency of this unsteadiness is a function of turbine speed, the increased unsteadiness in the higher turbine speed balances the gain obtained from reduced secondary flow in the rotor passage.

Apart from shift in peak efficiency velocity ratio, turbine speed does not cause any marked changes in the efficiency. Peak efficiency point of partial admission has shifted to velocity ratio in the range of 0.53 – 0.55 for 30k RPM speed. As for the 48k RPM speed, new peak efficiency has moved to velocity ratio of 0.6.

Figure 5.15, which shows partial admission efficiency for 30k RPM is used to illustrate the drop in efficiency in partial admission relative to full admission. Test which was conducted with no flow in the large scroll, has recorded lowest efficiency, the drop being 25 point (calculated between A1 and C1). The deficit in peak efficiency measured with large scroll flowing is 17 point (calculated between A1 and B1). Peak efficiency points (B1 and C1) for partial admission has shifted to a velocity ratio between 0.55 and 0.57. Table 5.8 shows percentage point drop of partial admission condition relative to full admission state.

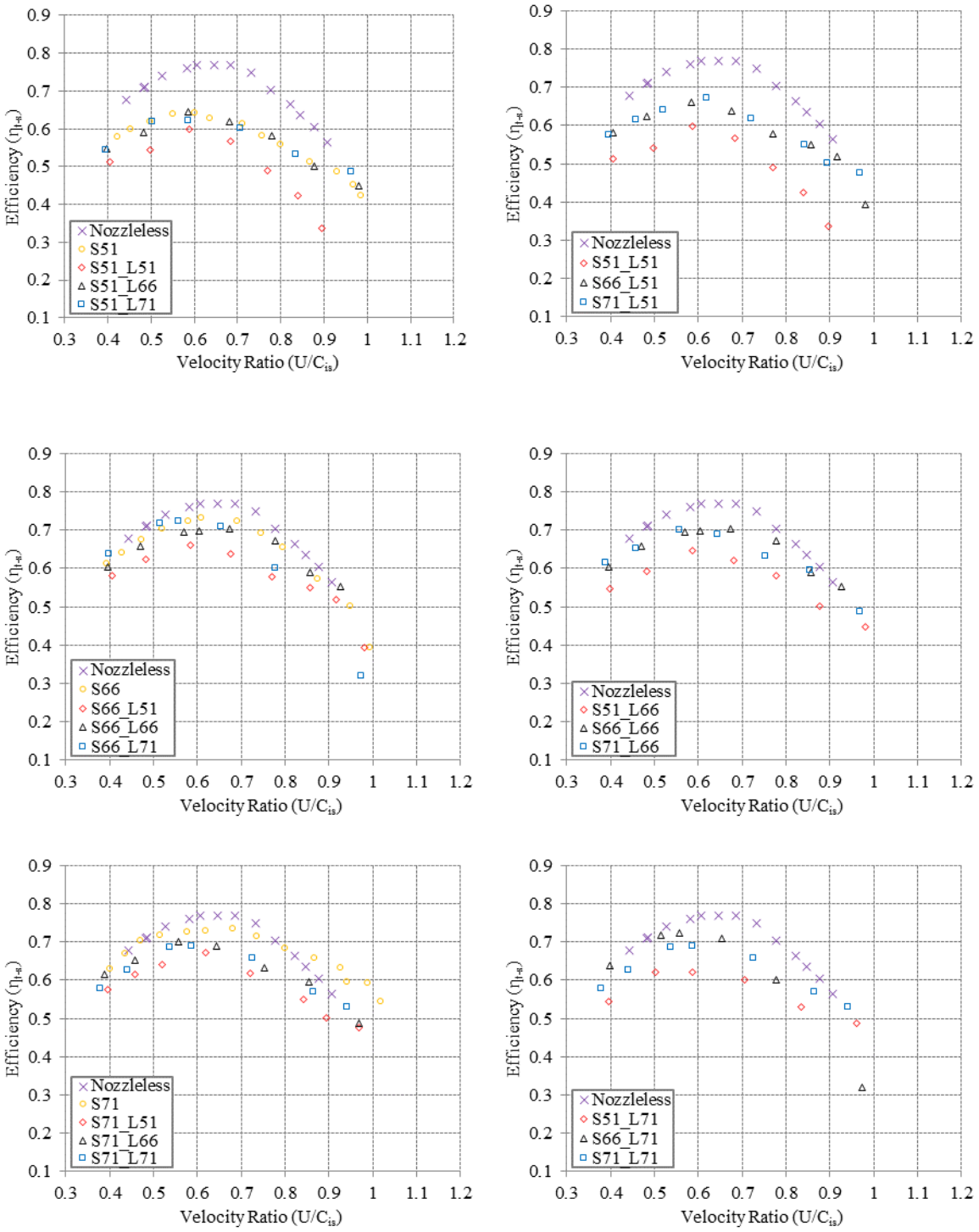


Figure 5.12 Total to static efficiency plot for various nozzle vane configuration under full admission condition at 30k RPM

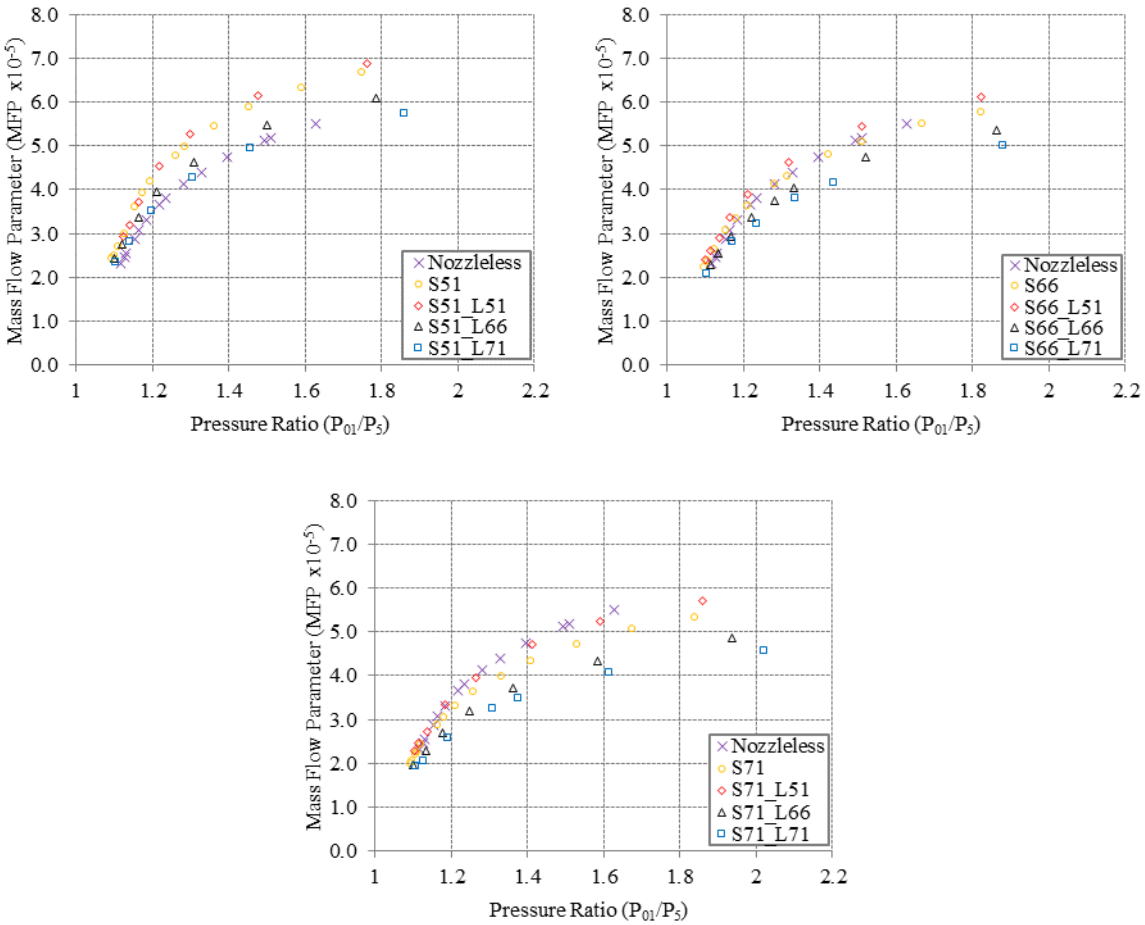


Figure 5.13 Overall turbine swallowing capacity plot various nozzle vane configuration under full admission condition at 30k RPM

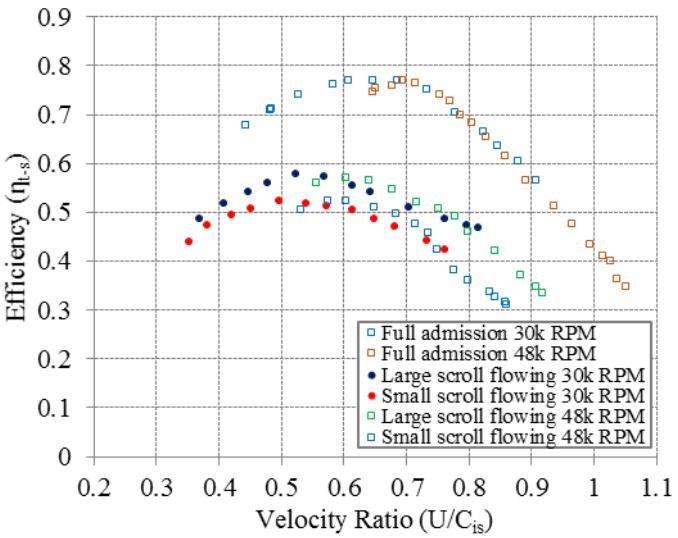


Figure 5.14 Total to static efficiency plot comparison between full and partial admission condition for nozzleless configuration

When comparing two cases of partial admission (small scroll flowing vs large scroll flowing), it is evident that the impact of the shear layer is most significant when the small scroll is flowing (25 point drop relative to full admission, refer Table 5.6) than when the large scroll is flowing (17 point drop relative to full admission, refer Table 5.6). Since simulation would be beneficial in understanding mechanism behind this significant difference, CFD analyses carried out by Newton [18] and Copeland [53] are being referred here. The CFD analyses conducted by Newton [18] and Copeland [53] have clearly shown that vorticity generated in the interspace volume between nozzle exit and rotor inlet is responsible for the efficiency penalty in a symmetric double entry turbine. If we assume the same phenomena observed by Newton [18] and Copeland [53] occurs here, the flow from small scroll (flowing) moves towards the low pressure region (large scroll, non-flowing). The difference in velocity magnitude between the two regions causes a strong shear flow, originating at the first tongue (azimuth angle = 0°), which continues to grow in the non-flowing interspace region. This results in vorticity generation in the flow. Vorticity flows into the interspace volume and subsequently into rotor passage. At the second tongue region (azimuth angle = 160°), shear layer is again formed due to difference in flow velocities. This shear layer produces second movement of vortices that moves into non-flowing interspace and rotor passage. Since the large scroll feeds a rotor circumferential area that subtends angle of 200° at the rotor center (Figure 5.16), the effect of vorticity is felt over a relatively larger circumferential area in the large scroll. This is the reason why highest drop in efficiency is recorded when there is no mass flowing in the large scroll.

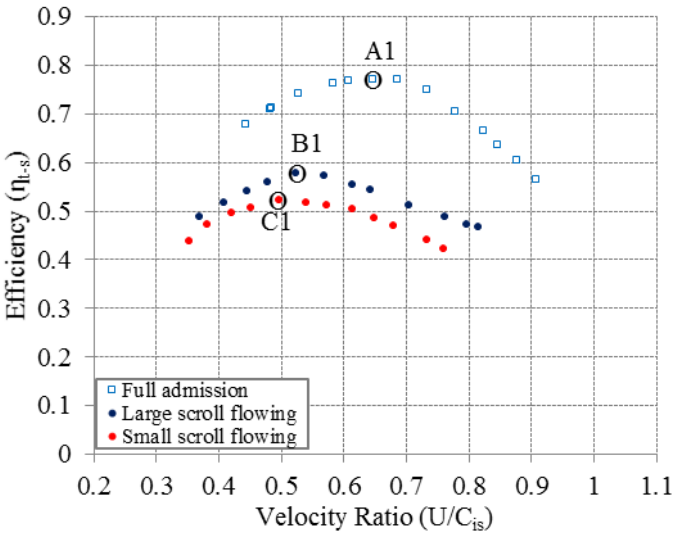


Figure 5.15 Total to static efficiency plot comparison between full and partial admission condition at 30k RPM for nozzleless configuration

Table 5.6 Drop in partial admission efficiency relative to full admission for nozzleless configuration

Speed (RPM)	Large scroll Flowing		Small scroll flowing	
	Drop in η_{ts}	$\frac{U}{C_{is}}$	Drop in η_{ts}	$\frac{U}{C_{is}}$
30k	17	0.55	25	0.53
48k	18	0.6	25	0.6

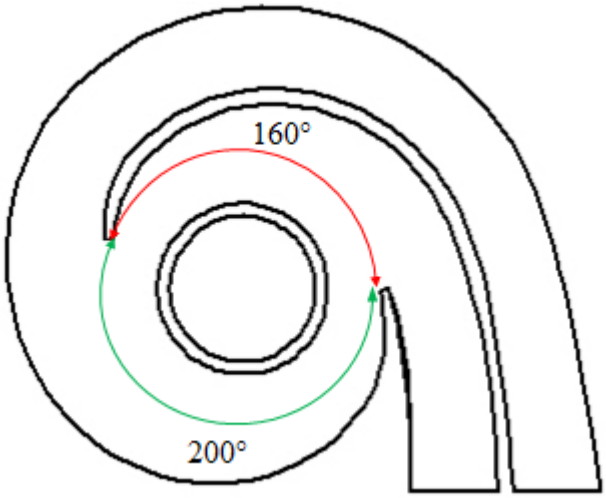


Figure 5.16 Nozzleless configuration

Figure 5.17 shows swallowing capacity of partial admission compared to full admission condition. With the zero mass in the large scroll, small scroll was only able to deliver maximum of 3.8 x 10^{-5} ($kgs^{-1}K^{1/2}$). Pa^{-1} mass flow parameter at pressure ratio of 2.5 for an average rotor speed of 48k RPM. On the other hand, for the same rotor speed, mass flow parameter saw an increase of 10.5 % (($MFP_{Lmax} - MFP_{Smax}$)/ MFP_{Smax})) to 4.2 x ($kgs^{-1}K^{1/2}$). Pa^{-1} at pressure ratio of 2.24 with air flowing only in large scroll. Besides the mass flow parameter, pressure ratio at choking point too has increased for the two speeds lines in partial admission condition. The volute which has one scroll with smaller circumferential area than the other, is responsible for the difference in mass flow parameter, as noted above.

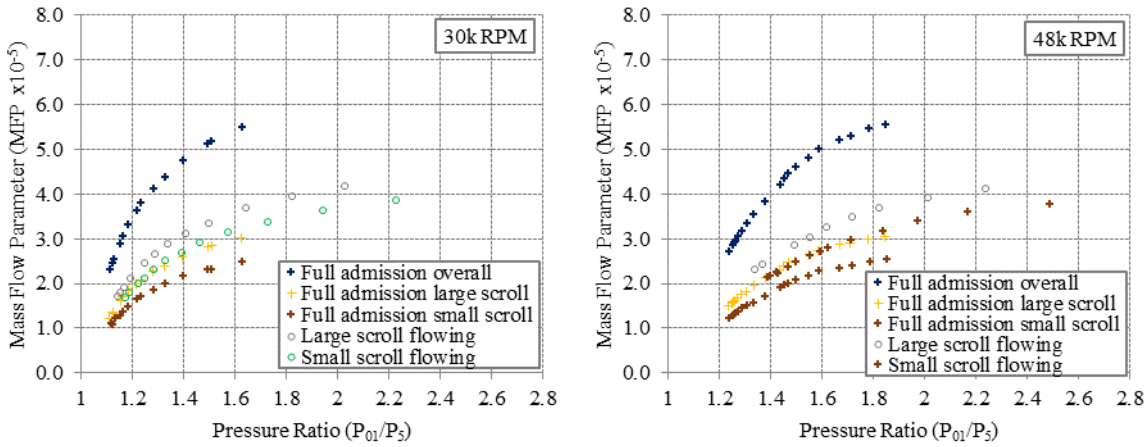


Figure 5.17 Overall turbine swallowing capacity plot comparison between full and partial admission condition for nozzleless configuration

5.2.2 Nozzle Vanes in small scroll (S nozzle configuration)

Full admission test results on 3 different nozzle vane openings, has revealed a very similar trend between S66 and S71 configurations in all the five turbine speed tested. The peak efficiency plot of all 3 nozzle vane settings shown in Figure 5.4 clearly demonstrates the similarity. Based on this full admission findings, the S nozzle testing in partial admission condition has been limited to S51 and S66 configurations. In the quest to investigate the influence of nozzle vanes on the partial admission performance, comparison between nozzleless and S nozzle configuration are made. Apart from that, full admission is assessed against partial admission of the same configuration, to understand the underlying principles which causes performance difference.

Figure 5.18 shows partial admission efficiency for S nozzle configuration. Turbine speed has more profound effect on partial admission efficiency of the S nozzle configuration, compared to nozzleless setting. Partial admission efficiency curve shows clear improvement with increase in turbine speed, as the nozzle vane opening approaches optimum angle. Peak efficiency point of partial admission has shifted to lower velocity ratio than that of the full admission in all vane angle openings. At higher turbine speed, drop in efficiency in partial admission relative to full admission, has decreased as nozzle vane angle setting changes from 51° to 71°.

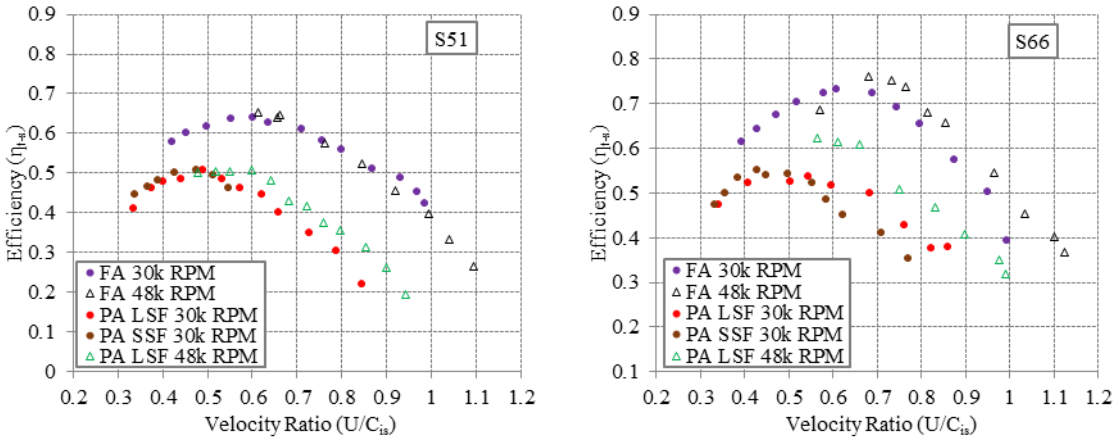


Figure 5.18 Total to static efficiency plot comparison between full and partial admission condition for two S nozzle configuration

Figure 5.19, which shows the partial admission efficiency for S51 configuration at 30k RPM speed, is used to illustrate the drop in efficiency in partial admission relative to full admission. Both partial admission conditions, large scroll flowing (LSF) and small scroll flowing (SSL), have recorded similar drop in peak efficiency, 13.2 percentage point (calculated between A2 and B2; between A2 and C2 respectively). The peak efficiency points (B2 and C2) for partial admission has shifted to a velocity ratio between 0.47 and 0.49. Table 5.7 shows drop in partial admission condition relative to full admission for various S nozzle configuration.

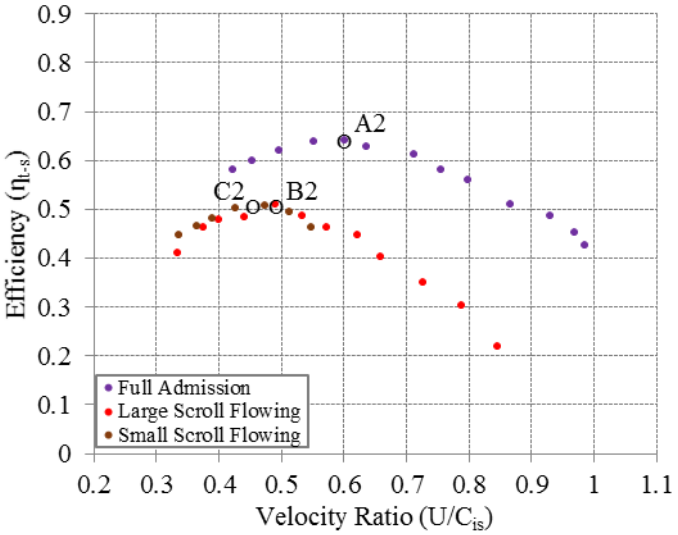


Figure 5.19 Total to static efficiency plot comparison between full and partial admission condition at 30k RPM for S51 configuration

Table 5.7 Drop in partial admission efficiency relative to full admission for S nozzle configuration

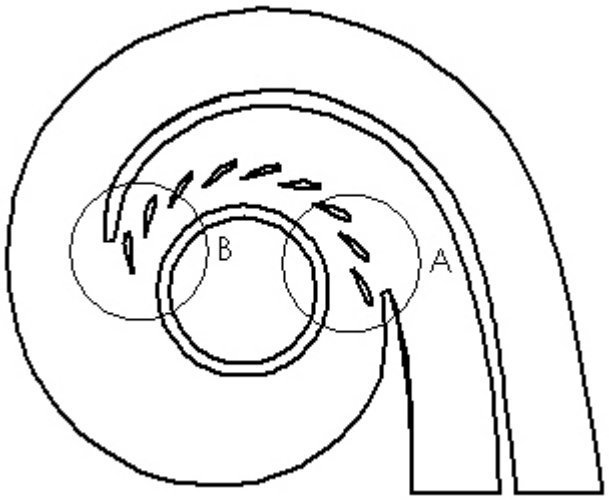
Speed (RPM)	S nozzle Configuration	Large scroll Flowing		Small scroll flowing	
		Drop in η_{ts}	$\frac{U}{C_{is}}$	Drop in η_{ts}	$\frac{U}{C_{is}}$
30k	S51	13.2	0.49	13.2	0.47
	S66	19.7	0.545	19.1	0.498
48k	S51	14.3	0.599		
	S66	14.6	0.611		

Figure 5.21 (a) shows partial admission efficiency characteristics when flow is admitted only in the small scroll at 30k RPM speed. S66 has higher overall partial admission efficiency characteristic below velocity ratio of 0.58. Beyond this velocity ratio, nozzleless setting outperforms the S66 configuration. Peak efficiency of S51 and S66 configurations are 50.8%, and 54.1% respectively. Both nozzle vanes efficiency peaks at velocity ratio between 0.47 and 0.50. As shown in Figure 5.21 (b), S51 mass flow parameter is higher than S61 setting, differing from the full admission condition where both settings swallowed equal mass.

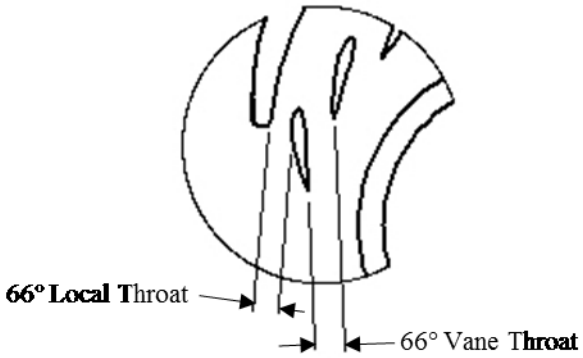
In Section 5.1.2, it has been observed that correctly matched flow to the rotor inlet leading edge produces the highest overall turbine performance. Reduced secondary flow (as a result of flow separation minimization on the pressure surface) is suggested to be the mechanism behind this outcome. Therefore, it comes as no surprise that the partially admitted S nozzle setting with 66° vane angle opening (S66) displayed better efficiency characteristics compared to the S51 setting based on the same postulation. Moreover, the presence of nozzle vanes in the vicinity of the tongue region, decreases local throat area between tongue and adjacent nozzle vane. This is shown in Figure 5.20. Despite increasing the local velocity magnitude at the tongue region, nozzle vanes tend to minimize the interaction between two regions with significant pressure difference. As a result, vorticity into non-flowing region is reduced. The performance gain due to reduced secondary flow and minimized vorticity in the flow, have significantly reduced the penalty in efficiency of S66 setting. This explains why S66 setting performs better than nozzleless configuration by 2 percentage point.

On the other hand, introduction of nozzle vanes with opening angle of 51° has created negative impact on the partial admission performance, when small scroll is flowing. Local throat area between the tongue and nozzle vane in S51 configuration is much smaller than in S66 setting. Refer Figure 5.20. This translates to reduced vorticity flow into the non-flowing region and subsequently minimizing the loss due to entropy generation. Furthermore, the abrupt mismatch between rotor and scrolls (flowing and non-flowing scroll) experienced in S51 setting is believed to be lower as opposed to S61 nozzle vane angle. This suggestion is premised based on mass flow parameter plot in Figure 5.21 (b). Despite having equal turbine speed, S51 has recorded lower back pressure for a given mass flow rate. Therefore smaller pressure gradient between flowing and non-flowing section in the S51 setting. However, the flow becomes less tangential and incidence angle becomes more positive. Positive incidence angle causes the flow to separate on the suction surface, as observed in the full admission condition. This gives rise to secondary flow formation in the rotor passage. Therefore, the magnitude of the gain is insufficient to offset losses due to increase in secondary flow. Thus resulting in 2 percentage point lower peak efficiency than the nozzleless setting. This assumption shows that losses arising due to incorrect incidence angle has more profound influence on the overall asymmetric double entry turbine efficiency, when flow is partially admitted.

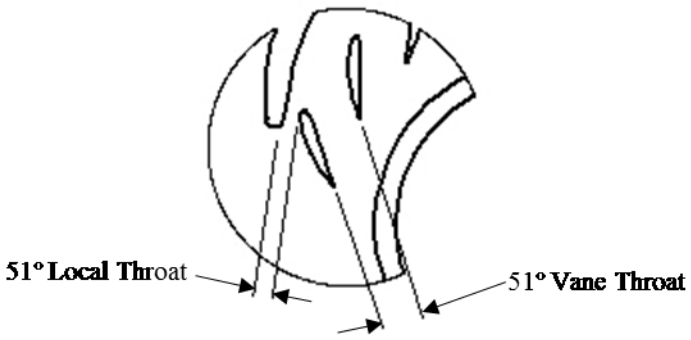
Figure 5.22 (a) presents efficiency curves of various S nozzle configuration at 48k RPM, with flow being admitted only in the large scroll. Peak efficiency of S66 and S51 configurations are 61.5% and 50.9% respectively. Both nozzle vanes efficiency peaks at velocity ratio between 0.590 and 0.611. Although swallowing capacity of both configurations are identical as shown in Figure 5.22 (b), S66 performance partial admission condition is far superior to S51 setting. With a peak efficiency difference of approximately 3 percentage point relative to the nozzleless setting, S66 configuration has displayed highest overall efficiency characteristics. As nozzle vane in small scroll closes, from 51° to 66°, overall partial admission efficiency improves at higher turbine operating speed, relative to nozzleless setting, when flow is only admitted in large scroll.



(a)

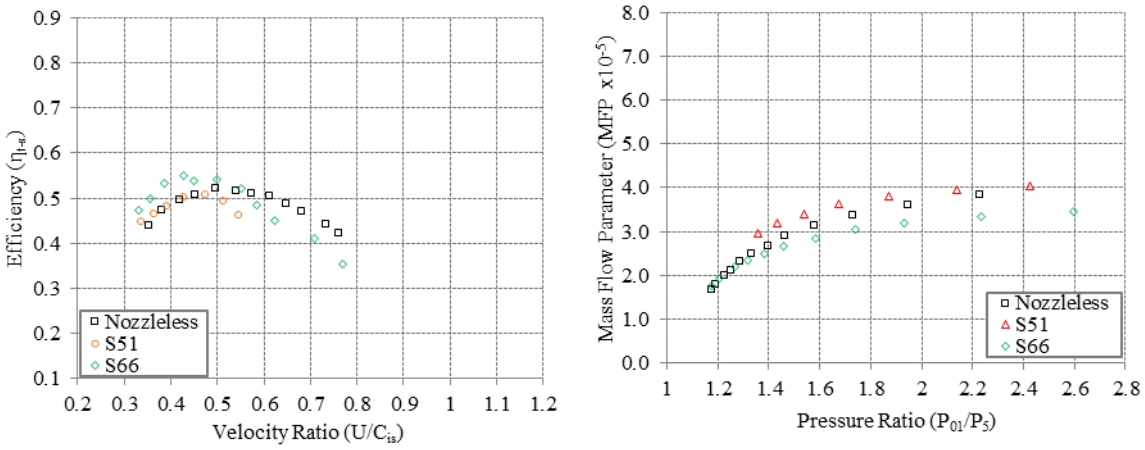


(b)



(c)

Figure 5.20 (a) S nozzle configuration (b) S66 detail view B
(c) S51 detail view B

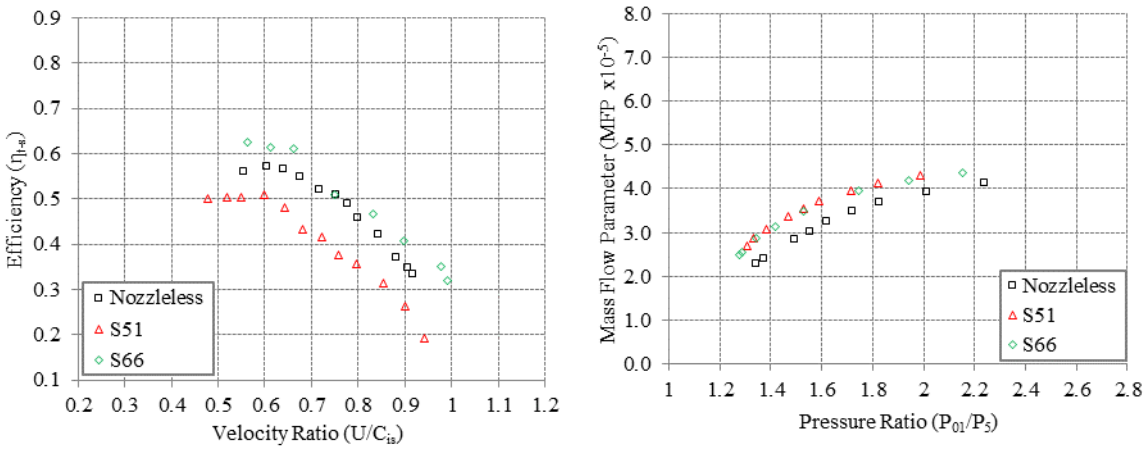


(a) (b)

Figure 5.21 Partial Admission Perfomance comparison map between S nozzle and nozzleless configuration when small scroll is flowing at 30k RPM

With the presence of nozzle vanes in the non-flowing region, the effective nozzle throat area in that region reduces, as opposed to the nozzleless setting. This is shown in Figure 5.20. Therefore less vorticity flow enters the rotor in the small scroll (non-flowing sector) section in the S nozzle setting as opposed to nozzleless configuration. However, the marked difference in efficiency between S51 and S66 settings is closely related to the distinct local tongue throat area and nozzle vane throat area in each setting. The local tongue throat area effect in S51 setting is much lesser than in S66 setting. Nonetheless, greater vorticity effect is felt in S51 (nozzle vane on small scroll with an angle of 51°) as opposed to S66 (nozzle vane on small scroll with an angle of 66°). The greater nozzle vane opening in S51 setting causes more vortices to be moved into rotor passage, hence higher losses due to entropy generation in S51 settings compared to S66.

Identical swallowing characteristic portrayed by both configurations, in Figure 5.22 (b) does not only imply similar back pressure; in addition identical absolute flow magnitude and angle (identical velocity triangle). Hence, pressure difference between flowing and non-flowing, and incidence angle at rotor inlet in both settings are same. As such influence of these parameters in each S nozzle setting is presumed to be alike.



(a) (b)

Figure 5.22 Partial Admission Perfomance map comparison between S nozzle and nozzleless configuration when large scroll is flowing at 48k RPM

5.2.3 Nozzle Vanes in both scrolls (SL nozzle configuration)

The same approach used to determine the configuration in the full admission testing of the SL setting has been adopted in this section. One configuration involves nozzle vanes with equal opening angles around the entire circumference of the rotor inlet, and another combination with distinct opening angles in each scroll. The only difference in this partial admission assessment is the number of total configurations, which now have been reduced to four. The four configurations comes from two nozzle vane openings, 51° and 66°, that were experimentally investigated in S nozzle configuration testing of the partial admission condition. The testing is expected to provide some insights on effects of different nozzle vane angle (in the non-flowing sector), on the turbine efficiency.

Figure 5.23 which shows efficiency characteristic of S66_L66 configuration at 30k RPM speed, is used to illustrate difference in performance between partial and full admission. A drop of 13.9 percentage point (calculated between A3 and B3) in peak efficiency has been observed when the flow was admitted only in the large scroll. When flow was partially admitted in the small scroll, the peak efficiency has dropped by 15.8 percentage point (calculated between A3 and C3). Peak efficiency points (B3 and C3) for partial admission has shifted to a velocity ratio between 0.506 and 0.517. Table 5.10 shows drop in partial admission condition relative to full admission for various SL nozzle configuration.

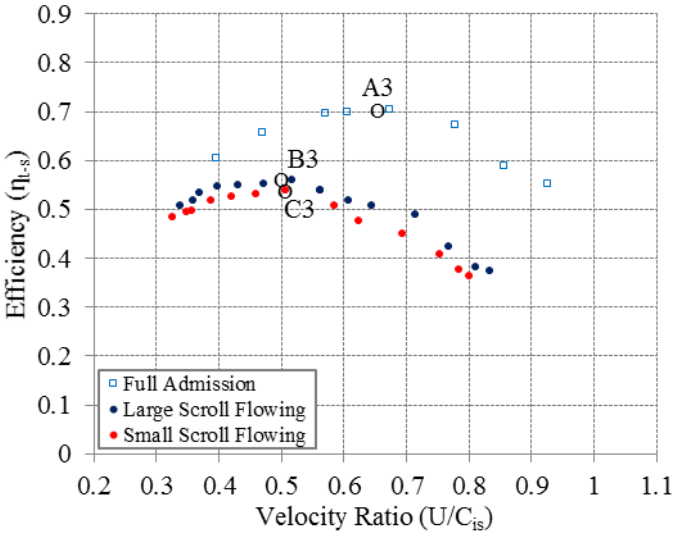


Figure 5.23 Total to static efficiency plot comparison between full and partial admission condition at 30k RPM for S66_L66 configuration

In order to qualitatively assess partial admission efficiency of the SL nozzle configuration with full nozzle vanes, the results of Newton [18] are shown in Figure 5.24. For the same speed, the symmetric configuration has recorded a drop of 19.6 point (calculated between D and E). Partial admission curve peaks (E) at a velocity ratio of 0.5 for this configuration. The results of symmetric double entry turbine and S51_L51 configuration in asymmetric double entry turbine (when the large scroll is flowing) are almost identical (19.6 vs 19.5, Table 5.8). But when the same comparison is made with other settings, asymmetric double turbine has shown to have much lower deficit in efficiency at 50% EGR (large flow flowing).

Figure 5.25 shows efficiency characteristic of SL nozzle configurations when flow is partially admitted in the small scroll. S66_L66 has highest overall partial efficiency characteristic below velocity ratio of 0.5, beyond which the curve overlaps efficiency curve of nozzleless settings. S51_L51 and S51_L66 configurations have displayed lowest overall efficiency among all four nozzle vane configuration tested. Peak efficiencies of S66_L66, S66_L51, S51_L51 and S51_L66 are 54%, 50.8%, 47.7% and 47.2% respectively.

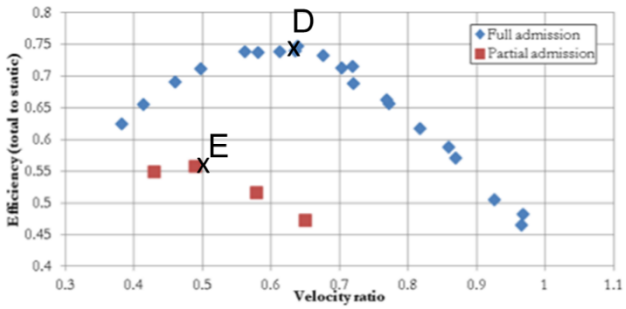


Figure 5.24 Comparison Between Full And Partial Admission Efficiency Of Symmetric Double Entry Turbine At 30k RPM *(extract from Newton [18])*

Table 5.8 Drop in partial admission efficiency relative to full admission for SL nozzle configuration

Speed (RPM)	Symmetric Turbine [12]		Asymmetric Turbine				
			SL nozzle Configuration	Large scroll Flowing		Small scroll flowing	
	Drop in η_{ts}	$\frac{U}{C_{is}}$		Drop in η_{ts}	$\frac{U}{C_{is}}$	Drop in η_{ts}	$\frac{U}{C_{is}}$
30k	19.6	0.5	S66_L66	13.9	0.517	15.8	0.506
			S66_L51	15.3	0.532	15.2	0.457
			S51_L51	19.5	0.519	18.5	0.505
			S51_L66	11.2	0.516	17.4	0.471

Figure 5.26 (a) shows S66_L66 setting having almost identical efficiency characterisitcs as S66 setting in the velocity ratio range of 0.349 - 0.624. Beyond velocity ratio of 0.624, efficiency curve of S66_L66 is higher than S66 setting. Presence of nozzle vanes in large scroll of S66_L66 is believed to be the reason for this difference. All three nozzle settings (S66, S66_L66 and S66_L51) swallowed equal mass, as shown in Figure 5.26 (b). This indicates that effect of abrupt mismatch between rotor and scrolls in all three settings are similar for a given turbine speed. In addition to that, presence of nozzle vanes with 66° opening angle (in small scroll) is accountable for equivalent incidence angle at rotor inlet in all three settings. Despite this, S66_L66 setting has outperformed S66_L51 setting. This marked difference in efficiency is caused by distinct vane angle setting in the large scroll (L66 opposed to L51).

S66_L66 and S66_L51 has similar local tongue throat area (Figure 5.27), hence identical shear layer strength at tongue regions in both configuration (equal mass and flowing into small scroll with nozzle vane at an angle of 66°). Nevertheless, the magnitude of vorticity in the flow felt by the rotor passage in the non-flowing region is expected to be different.

S66_L51 which has bigger effective nozzle throat area in the non-flowing region (nozzle vane at an angle of 51°) is the cause for this phenomena. More vorticity flow moves into the rotor passage of the S66_L51 settings, which translates to higher entropy generation. Thus the penalty experienced by the S66_L51 settings.

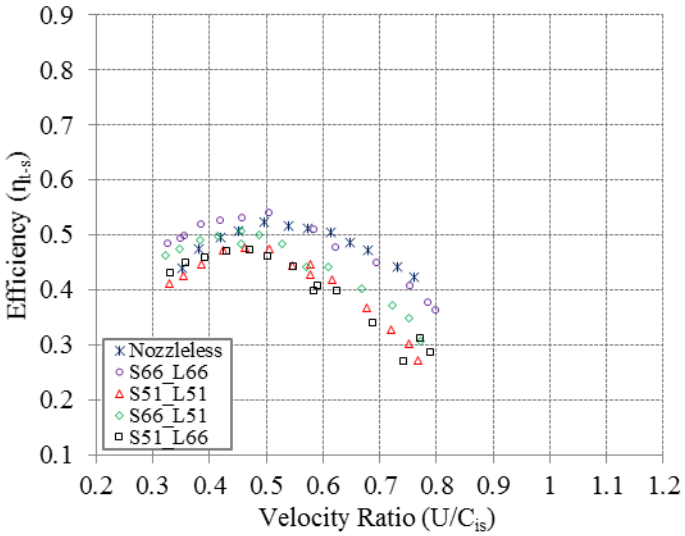
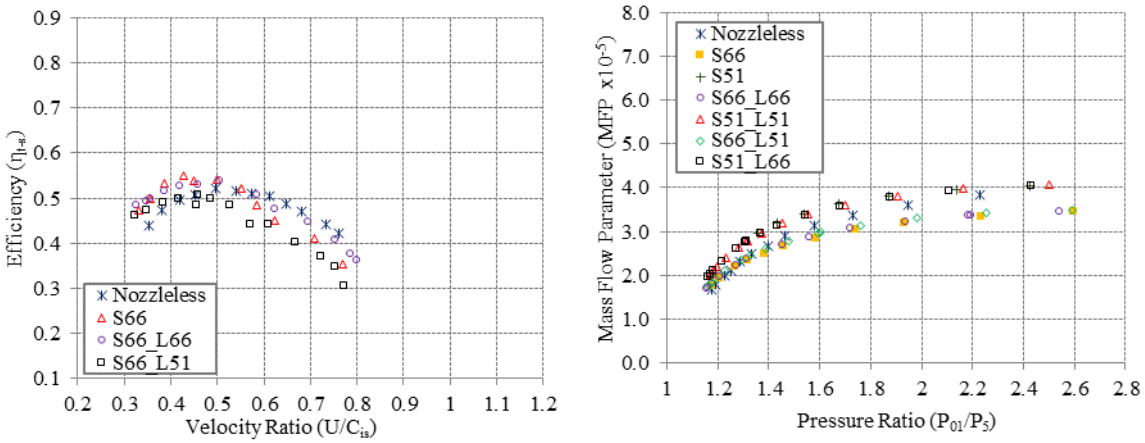
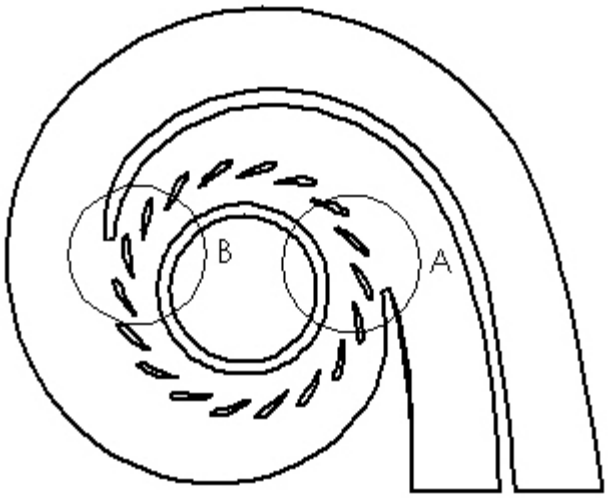


Figure 5.25 Total to static efficiency plot comparison between nozzleless and SL nozzle configuration with small scroll flowing at 30k RPM

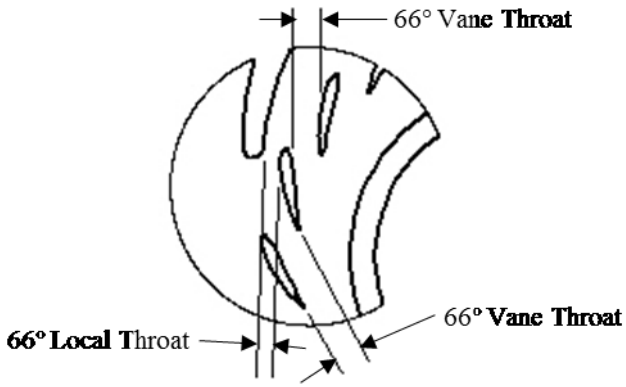


(a) (b)

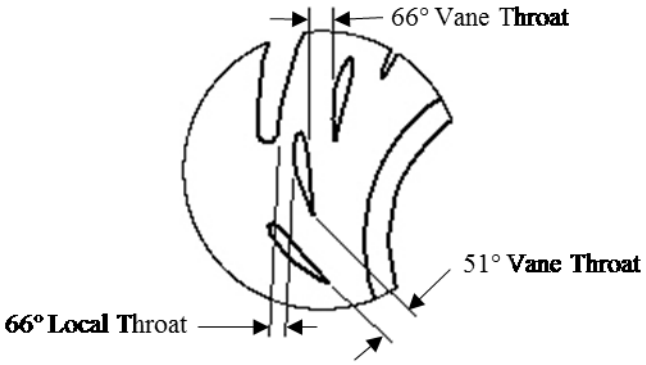
Figure 5.26 Partial Admission Perfomance map for various nozzle vane configuration with small scroll flowing at 30 k RPM



(a)



(b)



(c)

Figure 5.27 (a) SL nozzle configuration (b) S66_L66 detail view B
(c) S66_L51 detail view B

Figure 5.28 shows efficiency characteristic of SL nozzle vane configurations when flow is partially admitted in the large scroll at 30k RPM. S66_L66 has highest overall partial efficiency characteristic below velocity ratio of 0.517. Above this velocity ratio nozzleless setting has the highest overall efficiency. S51_L51 configuration has recorded lowest

overall efficiency among all four nozzle vane configuration tested. Peak efficiencies of S66_L66, S66_L51, S51_L51 and S51_L66 are 55.3%, 50.7%, 46.6% and 52.7% respectively.

In Figure 5.29 (a), S66_L66 setting has displayed higher efficiency characteristics over S66 setting in the velocity ratio range of 0.338 – 0.607. S66 and S66_L66 efficiency curves overlaps each other beyond velocity ratio of 0.607. This difference is believed to be caused by the presence of nozzle vanes in large scroll of S66_L66, which provides flow guidance that was not available in the S66 setting. But when nozzle vane is set to 51° in large scroll, represented by S66_L51 curve, drop in turbine efficiency becomes more significant. Unfavorable incidence angle in large scroll sector of S51 setting is the reason for this observation.

S66 and S66_L51 swallows equal amount of mass, and higher than S66_L66, as shown in Figure 5.29 (b). Hence, pressure difference between flowing and non-flowing region at both tongue region is expected to be same in S66 and S66_L51 settings; lower than that of S66_L66. Due to this reason, shear layer strength of higher order orginates from two tongue regions in S66_L66 settings, despite equal effective local tongue throat area in all three configurations. This causes should lead to more vorticity flow to be passed through the rotor passage in S66_L66 configuration. In addition to that nozzle throat area in the non-flowing region is similar for all the settings. The presence of nozzle vane with 66° opening angle in the large scroll (flowing sector) of the S66_L66 has significant influence in bringing down deficit in overall turbine performance. On the other hand, the flow becomes less tangential and flow separates on the rotor suction surface with vane angle of 51° in the large scroll of the S66_L51 setting. This effect of more positive incidence angle increases secondary flow in the rotor passage, and complements the entropy generation losses due to vorticity flow.

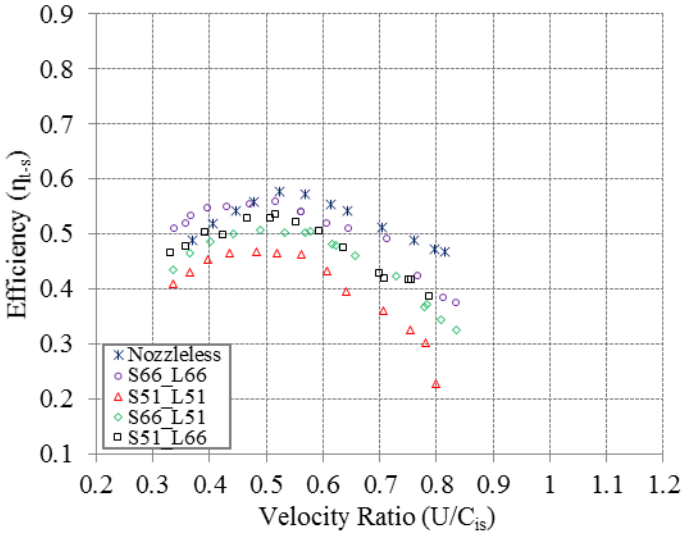
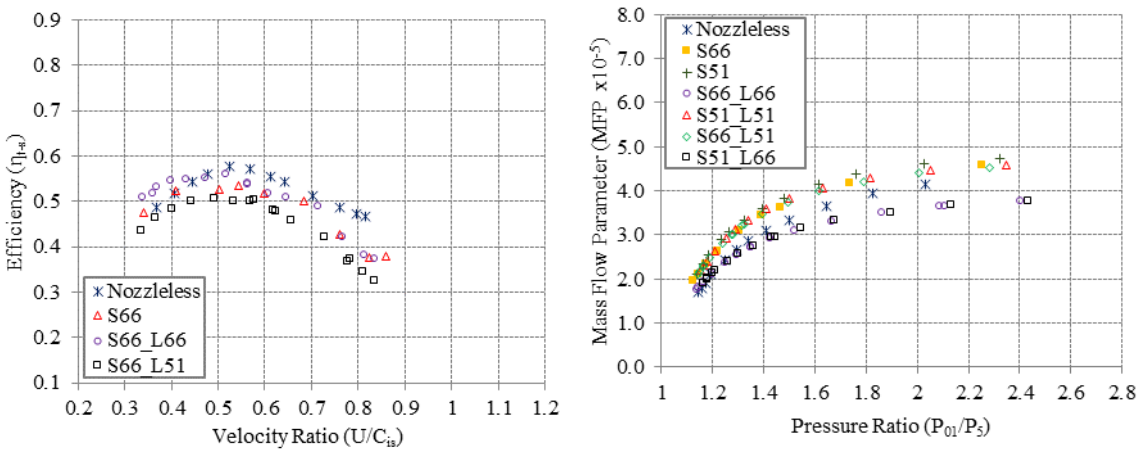


Figure 5.28 Total to static efficiency plot comparison between nozzleless and SL nozzle configuration with large scroll flowing at 30k RPM



(a) (b)

Figure 5.29 Partial Admission Perfomance map for various nozzle vane configuration with large scroll flowing at 30 k RPM

5.3 Unequal Admission Characteristics

In Sections 5.1 & 5.2, two extreme operating conditions of asymmetric double entry turbine were explored. The operating condition between the full and partial admission state is known as unequal admission. In the unequal admission testing, each scroll of the asymmetric double entry turbine is subjected to different total pressure in order to investigate the effect of relative pressure difference between scrolls, on the efficiency of the turbine. This was achieved by having one scroll flowing (valve fully opened), while the flow in the other scroll is varied at constant velocity ratio and pressure ratio, which

typically sets the speed parameter at constant value. Due to the nature of the test methodology chosen in this thesis, all unequal admission performance characteristics are represented by plot of normalized efficiency against Ratio of Pressure Ratios (RPR). The normalized efficiency is obtained by dividing the measured efficiency in unequal condition by the maximum efficiency at full admission condition for the same velocity ratio and pressure ratio. RPR is the ratio between Pressure Ratio (PR) in small scroll and PR in large scroll, or simply the ratio between small scroll inlet and large scroll inlet stagnation pressure.

Figure 5.30 shows the normalized efficiency plotted against RPR to illustrate how to make sense of the plots in this section. The abscissa represent RPR, where value of 1 represents full admission. Away from this value, on either side of the vertical axis, the inequality between scroll increases. Curves on the right side of the vertical axis represent effect of inequality on small scroll (flow in small scroll is fixed while flow in large scroll is varied), where else the left side shows that of large scroll for the equivalent velocity ratio.

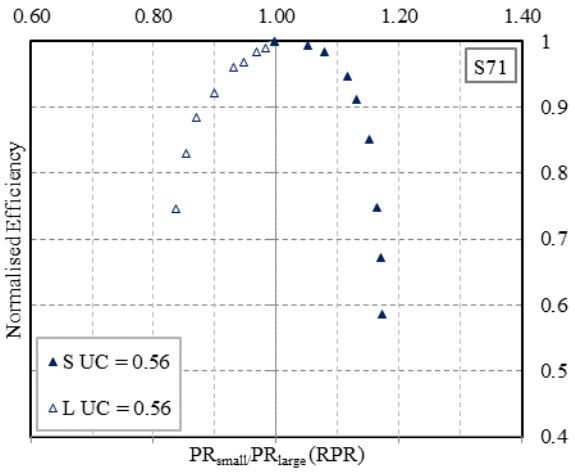


Figure 5.30 Normalised efficiency

5.3.1 Nozzleless

Nozzleless unequal admission findings are presented in this section. Apart from being used as a baseline for other nozzle vane configurations subjected to unequal admission condition, the nozzleless unequal admission experiment is beneficial in establishing relationship between two unequal scrolls (whether symmetric behavior exist). Since

absence of nozzle vanes gives the actual scroll area, nozzleless setting results would relate this relationship directly to the turbine geometry.

Figure 5.31 (a) and (b) show normalized efficiency characteristics of nozzleless configuration at 30k RPM and 48k RPM respectively. The right side of the efficiency is symmetrical about the vertical axis and vice versa. The symmetrical efficiency characteristic displayed by this asymmetric turbine in an unequal admission operating condition shows that scroll circumferential area does not have any impact on efficiency in the unequal admission condition as it did in the partial admission.

A downward trend in efficiency is clearly evident as the inequality of inlet pressure ratio between the scrolls increases. As noted previously in the full admission condition, the unequal rotor circumferential division, which was instrumental in relative flow angle and incidence angle difference between scrolls, has been identified as the main reason for formation of shear layer at the tongue regions. When the inlet stagnation pressure inequality between scrolls increases gradually, the formation of shear layer becomes more significant as a result of gradual change in both magnitude and direction of absolute flow. This potentially causes rise in vorticity generation in the flow which should lead to an increase in entropy generation. In addition to that, as the rotor passage rotates from one circumferential division to another, it will be subjected to significant absolute flow velocity changes, as observed in the partial admission condition. The deficit in efficiency due to this unsteadiness becomes greater as the inequality between the scrolls increases. Unlike the partial admission condition, there is always flow in both scrolls in the unequal admission condition. Therefore the strength of shear layer that originates from volute tongues is not as intensified as in the case of partial admission. Furthermore, the level of unsteadiness experienced by the rotor due to difference in pressure between scrolls is milder.

The efficiency drops even further when the velocity ratio increases, which suggest that effect of the inlet pressure inequality increases drastically as the velocity ratio increases. As pressure ratio is inversely related to the velocity ratio, a lower velocity ratio corresponds to higher turbine pressure ratio operation during which more energy is extracted from the flow. This greater actual work absorption subsequently translates to higher efficiency. The reverse is true when turbine operates at lower pressure ratio (higher

velocity ratio), where lesser amount of energy is absorbed by the turbine. This explains the reason for the drop in efficiency when velocity ratio increases.

On the other hand, when the turbine speed increases, the effect of inequality of inlet pressure ratio reduces. This can be clearly seen for RPR = 1.05 for U/C = 0.644 at 30k RPM and 0.654 at 48k RPM. U/C = 0.644 records 0.87 normalized efficiency while that of U/C = 0.654 is 0.97, 10 points higher. Increase in rotor speed causes the incidence angle to become more negative. This typical turbine characteristic has been presented in the previous sections. Despite the difference in absolute flow between scrolls, and associated losses, the improvement in incidence angle (incidence angle become more negative) has reduced the formation of secondary flow in the rotor blade passage. This has substantially improved the turbine efficiency.

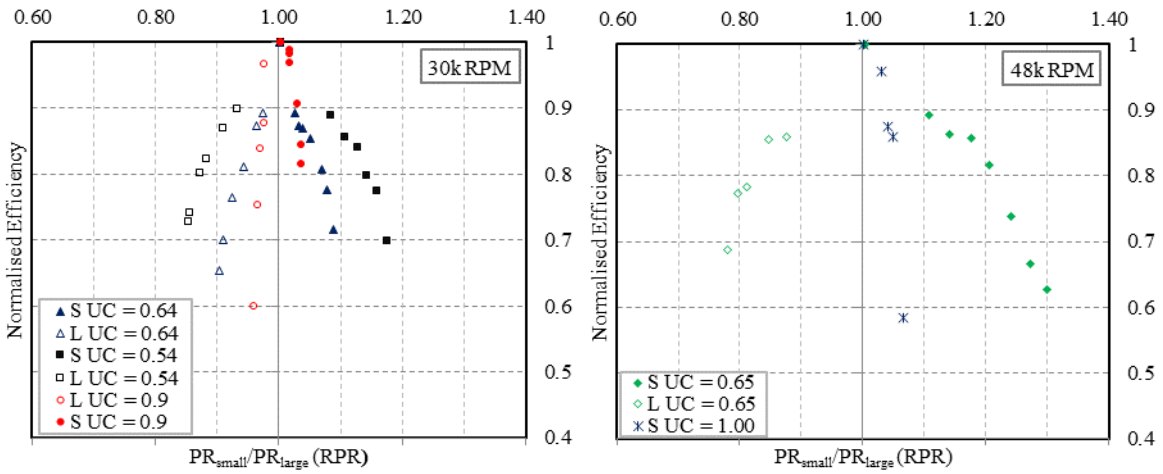


Figure 5.31 Unequal Admission normalized efficiency for nozzleless configuration

5.3.2 Nozzle Vanes in small scroll (S nozzle configuration)

The nozzleless unequal admission findings has evidently ruled out the scroll circumference geometry (area) influence, which was very significant when the flow was admitted fully and partially, on turbine efficiency. Nevertheless it has shown an important resemblances with full and partial admission findings; effect of change in magnitude and direction of absolute flow on overall stage performance. But it is important to state here that, this effect was only demonstrated by varying the velocity ratio, and not the nozzle vane angle opening. Therefore in this section, the direct impact of vane angle opening on turbine

performance, as the inequality between scrolls increases, is investigated. Both S66 and S71 settings were evaluated, despite both vane angle opening having similar efficiency map in the full admission. These settings would be the best candidates to picture the sensitivity of nozzle vane angle change, as the vane opening angles between them only differs by 5°.

Figure 5.32 presents unequal admission efficiency for S66 and S71 nozzle configuration at 30k RPM turbine speed. Since the volute has been designed to deliver flow at an angle of 71°, flow approaching the rotor in the nozzleless large scroll is assumed to be equal to the volute exit flow angle. With flow in both scrolls set to approach rotor inlet at equivalent flow angle (approximately close in the case of S66) symmetrical efficiency characteristic is observed in both S66 and S71 efficiency plots.

Figure 5.33 shows normalized efficiency of nozzleless, S66 and S71 settings plotted on the same scale. With the presence of nozzle vanes in small scroll, the deficit in normalized efficiency has reduced, when flow is fixed in the small scroll (U/C = 0.62 _S nozzle vs U/C = 0.64_Nozzleless). The apparent inequality in the stagnation pressure between scrolls, enables postulation found in section 5.2.2 (where flow was partially admitted into small scroll section of the volute of S nozzle configuration with nozzle vanes in the small scroll) to be adopted to understand the mechanism responsible for this improvement. Based on this idea, the presence of the nozzle vanes reduces the throat area at volute tongue region, thus dampening the shear layer flow into rotor passage. Therefore, reduced tongue throat area improves efficiency in unequal admission condition. To picture the influence of tongue throat area, comparison is made between S71 and S66. S71 settings has recorded lower drop in efficiency as opposed to S66 vane angle opening. One would initially assume that the comparison in Figure 5.33 to be unfair, as both settings performance were measured at different velocity ratio. However a closer look would reveal that difference (in U/C) between U/C = 0.62 (S66) and U/C = 0.56 (S71) are insignificant. Small vane angle (opening) difference of 5° has indeed created obvious changes in efficiency trend, especially in the RPR between 0.9 and 1.1.

Moreover, with vane angle setting of 66° and 71° in the small scroll, the incidence angle becomes more negative and level of unsteadiness experienced by the rotor reduces. The

influence of incidence angle on flow separation and circulation has been clearly explained in the full and partial admission section.

When the turbine speed increases to 48k RPM, curves on either sides of efficiency plot are not symmetrical about the vertical axis. This is clearly demonstrated in Figure 5.34. Curves on right side of efficiency plot has recorded higher normalized efficiency. One obvious reason for this observation is incidence angle becomes more negative as turbine speed increases. This effect becomes very significant with the presence of nozzle vanes in the small scroll. Therefore reduction in secondary flow in the rotor blade passage translates to higher efficiency.

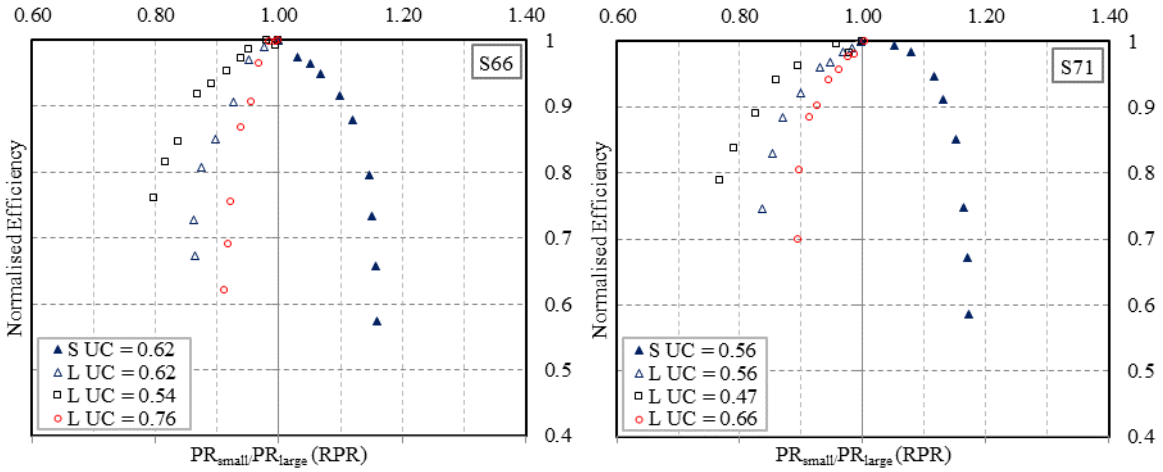


Figure 5.32 Unequal Admission normalized efficiency for S nozzle configuration at 30k RPM

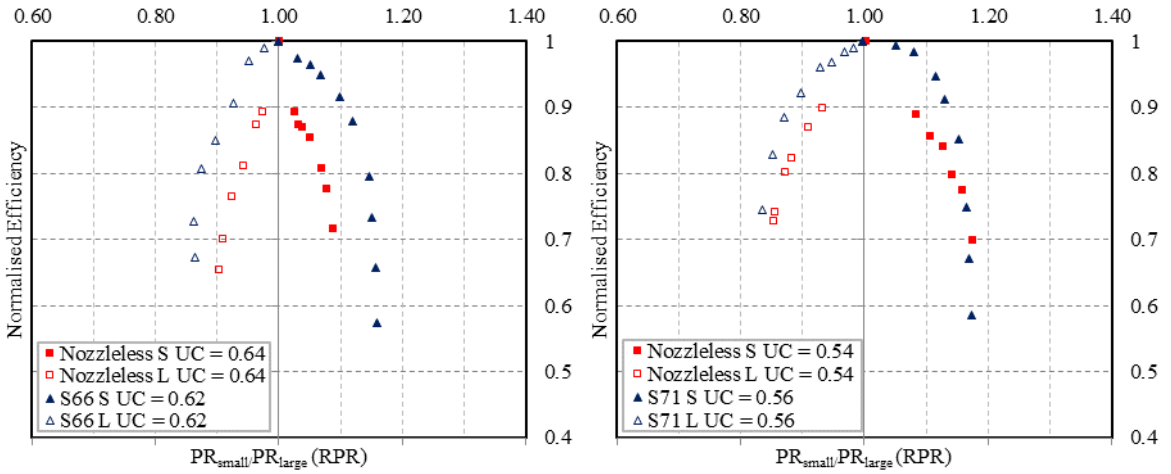


Figure 5.33 Comparison between nozzleless and S nozzle configuration at 30k RPM

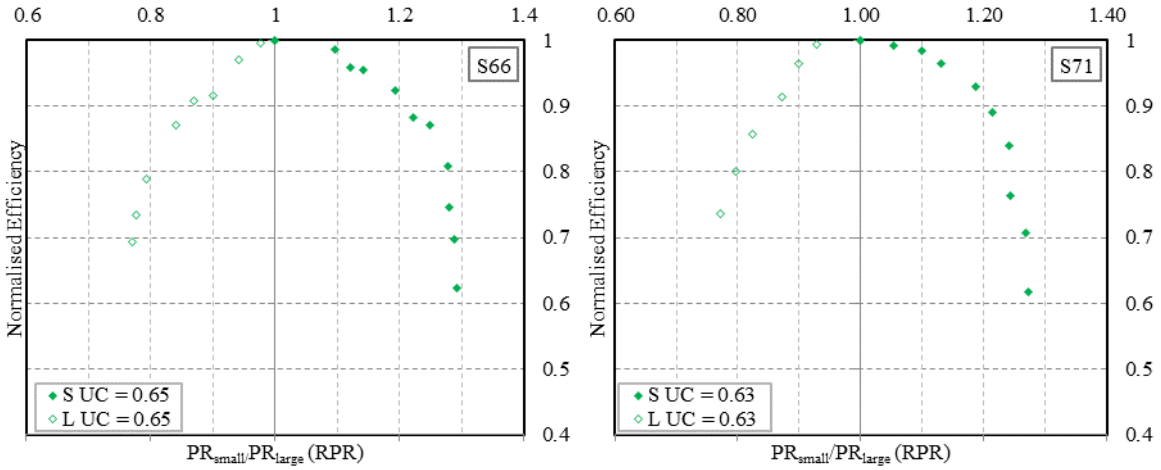


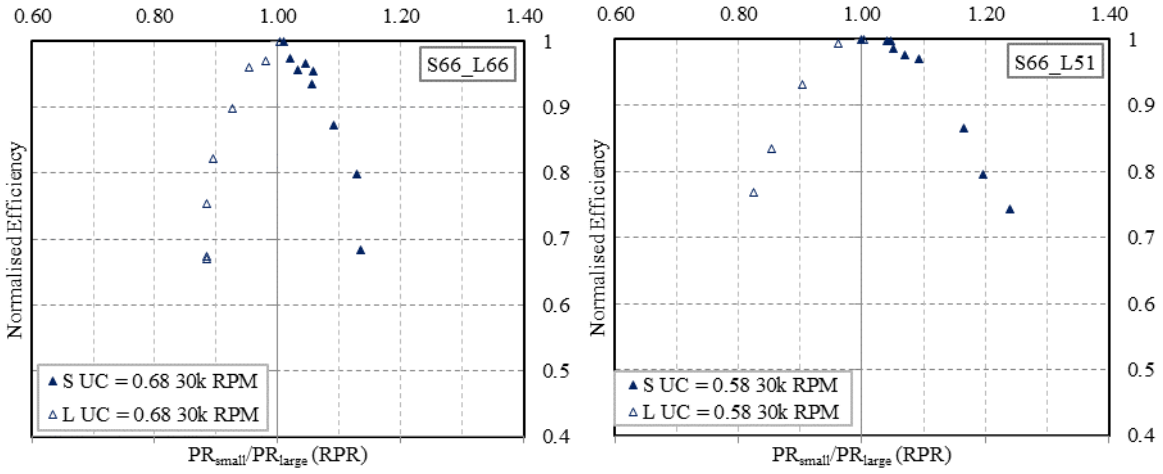
Figure 5.34 Unequal Admission normalized efficiency for S nozzle configuration at 42k RPM

5.3.3 Nozzle Vanes in both scrolls (SL nozzle configuration)

S66_L66 settings has recorded the closest efficiency characteristic to the nozzleless configuration, while S66_L51 and S51_L66 efficiency curves are close to each other in the partial admission experiment. Therefore, S66_L66 and S66_L51 are evaluated in the unequal admission testing of the SL nozzle vane configuration to assess the influence of nozzle vane opening in each scroll, on the level of symmetry in the efficiency characteristics.

Figure 5.35 presents unequal admission efficiency for S66_L66 and S66_L51 nozzle configuration. Curves on either sides of efficiency plot in Figure 5.35 (a) are symmetrical about the vertical axis, while that of Figure 5.35 (b) are not symmetrical. The symmetric normalized efficiency characteristic displayed by S66_L66 setting is believed due to equal vane angle opening in both scrolls of the asymmetric double entry turbine. Comparison to S66 configuration, measured at a slightly higher velocity ratio, further strengthen this assumption. Both normalized efficiency curve of S66 and S66_L66 are close to each other, as shown in Figure 5.36. In S66 settings, the flow in the large scroll (nozzleless sector) approaches the rotor with absolute angle of 71° (volute exit flow angle). Although flow in each scroll approaches rotor with slightly different absolute flow angle, the normalized efficiency of S66 settings are symmetrical. On the other hand, the significant dissimilarity in nozzle vane angle is assumed to be the reason the efficiency characteristic in S66_L51 configuration is not symmetrical. The symmetric characteristic in unequal admission

condition of this asymmetric turbine are governed by flow angle approaching the rotor inlet in the scroll with fixed flow and overall turbine speed.



(a) (b)

Figure 5.35 Unequal Admission normalized efficiency for SL nozzle configuration at 30k RPM

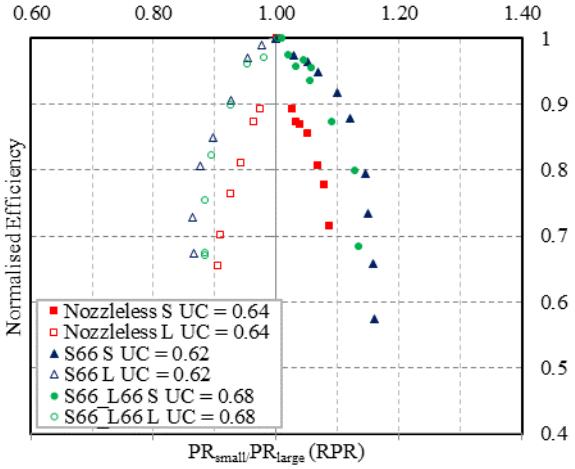


Figure 5.36 Unequal Admission normalized efficiency for various nozzle vane configuration at 30k RPM

5.4 Summary

Asymmetric double entry turbine steady flow experimental results are presented in this chapter for three different admission conditions: full, partial and unequal admission. All admission condition results presented here consist of nozzleless, nozzle vanes in small scroll (S nozzle configuration) and nozzle vanes in both scrolls (SL nozzle vane configuration). The peak recorded efficiencies in full admission condition are 78%, 77.6%

and 74.4%, respectively for nozzleless, S71 and S66_L66 settings; the corresponding velocity ratios were 0.72, 0.694 and 0.656. As the nozzle vane angle opening changed from the most open position (51°) to mid open position (71°) an increase in stage efficiency is observed in S nozzle setting testing.

Measured partial admission efficiency are compared against that of full admission. In the nozzleless testing, the deficit in peak efficiency measured with large scroll flowing (LSF) is 17 point, while the drop in peak efficiency measured with small scroll flowing (SSF) is 25 point. The significant difference has been suggested due to profound shear layer when small scroll is flowing. When nozzle vanes are introduced only in the small scroll sector, LSF and SSF has recorded similar drop in peak efficiency. Contrary to the S nozzle findings, SL nozzle, S66_L66 has recorded deficit of 15.8% and 13.9%, with small scroll flowing and large scroll flowing respectively.

As for the unequal admission testing, the symmetrical efficiency characteristic displayed by the nozzleless configuration shows that scroll circumferential area does not have any impact on efficiency in the unequal admission condition as it did in the partial admission. Symmetrical efficiency characteristic are also displayed by the S nozzle configuration. S nozzle configuration, S71 has outperformed S66, similar to the full admission findings. This is attributed to reduced tongue throat area that has subsequently improved efficiency in unequal admission condition.

CHAPTER 6

UNSTEADY FLOW EXPERIMENT

The asymmetric double entry turbine experimental findings and analysis under wide range of unsteady flow test conditions are presented in this chapter. Various nozzle vane openings and configurations between two scrolls were explored in the steady flow investigation, as presented in Chapter 5. However, in this chapter, the number of nozzle vane settings has been reduced based on full, partial and unequal performance characteristic obtained from the steady flow testing. Each of these configurations were evaluated at peak efficiency of the steady flow characteristic presented in Chapter 5, which corresponds to mid load condition. Besides that, the time average turbine speed and the inlet mean temperature were set to correspond to the equivalent steady condition, for every pulsating flow condition investigated.

In order to investigate effect of instantaneous pressure inequality between scrolls on turbine unsteady flow performance, out of phase unsteady flow has been investigated in addition to the in phase flow condition. This is achieved by setting the chopper plate in each limb of the test rig (Figure 4.1 and 4.2) in opposing direction, as explained in Chapter 4. Apart from varying the phase angle between pulsating flow in each limb, the testing was also conducted at different rotor speeds, at 50% and 90% of the equivalent turbine speed. Unfortunately, for the S51 setting, maximum speed has been limited to 42k RPM (70% equivalent turbine speed), due to high frequency of hot wire breakdown, owing to the high back pressure in this setting. Finally, 3 different frequencies were tested, namely 20Hz, 40Hz and 60Hz, to evaluate the influence of pulsating flow frequency on each of the settings.

6.1 Nozzleless

Figure 6.1 shows instantaneous swallowing capacity of the small scroll during in phase pulsating condition for 20Hz, 40Hz and 60Hz at two different rotor speed. Operating

hysteresis loop in 30k RPM for all pulsating frequency tested is closer to the steady state curve, compared to that of the higher speed at 48k RPM. With exception of 40Hz operating loop, pressure ratio range for all other orbits in 30k RPM are relatively smaller than 48k RPM.

Looking at 30k RPM turbine speed, the operating loop although closer to the steady state curve, the former does not overlap the latter, except for 40Hz and 60Hz flow frequency, during the emptying process. Turbine emptying loop is clearly seen tracing the steady state curve in the pressure ratio range of 1.35 – 1.55 and 1.29 – 1.41 in 40Hz and 60Hz test condition respectively. The difference between high pressure and low pressure ratio of the hysteresis loop apparently decreases with increase in flow pulsating frequency. However, the range of mass flow parameter increases for the same increase in flow frequency. Similarly, increase in mass flow rate and decrease in range of pressure ratio is observed as flow frequency increases in 48k RPM speed condition. Turbine emptying loop traces the steady curve only during 60Hz pulse operation, between pressure ratio of 1.54 and 1.65. The rise in pressure over one pulse cycle increases (become too rapid) in the small scroll as the flow frequency is increased. This is the reason for emptying curve tracing the steady curve in 40Hz and 60Hz unsteady flow.

Both speed condition has shown choking phenomena in the 40Hz pulsating flow testing. This is shown by a plateau line in the mass flow parameter curve between pressure ratio of 1.51 – 1.63 and 1.73 – 1.80, corresponding to 30k RPM and 48k RPM. Apart from that, presence of secondary loop is noticed in both speed conditions, at lower flow frequency of 20Hz. The occurrence of secondary loop which is significant in the low pressure and mass flow region of the swallowing capacity map, indicates effect of wave action within the turbine volute. This phenomenon has been reported by Newton [18] in the experimental work involving a conventional double entry turbine.

Instantaneous swallowing capacity of the large scroll during in phase pulsating condition for 20Hz, 40Hz and 60Hz at two different rotor speed is shown in Figure 6.2. Hysteresis loci in 30k RPM turbine speed tested traces closely the steady state characteristic. Maximum unsteady pressure ratio experienced by the turbine decreases as the flow frequency increases. Apart from that, the presence of secondary loop is more profound than that in the small scroll unsteady flow. This is clearly seen in all flow frequencies

tested for both speed line, with an exception in 60Hz unsteady flow at 30k RPM. The secondary loop, which occurs in the slightly higher pressure ratio region, relative to that of the small scroll, indicates greater influence of wave action in the large scroll within the

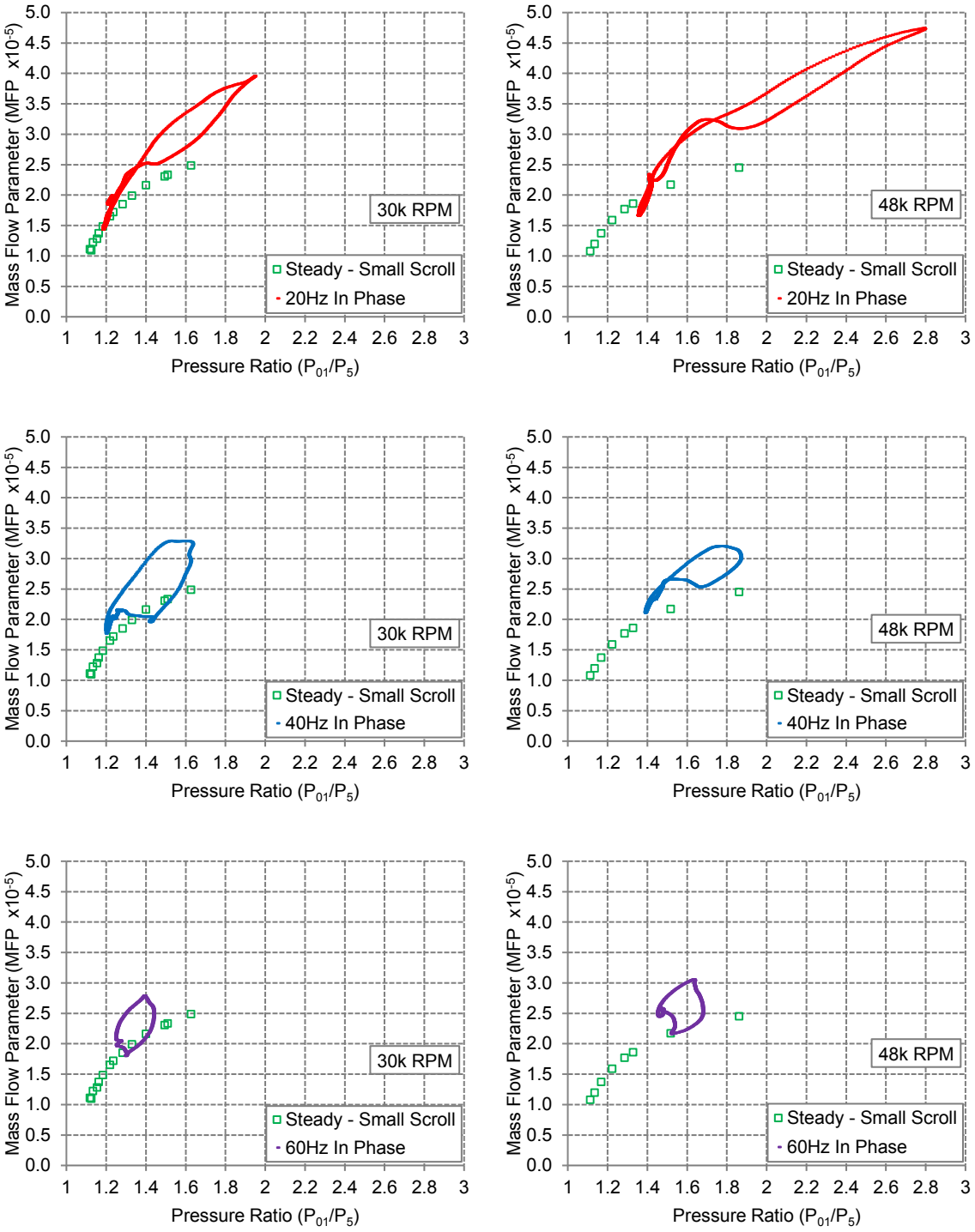


Figure 6.1 In-Phase Small Scroll Instantaneous Swallowing Capacity for nozzleless configuration

volute. The 20Hz operating loop is the smallest, with traces of volute filling and emptying closely following and encapsulating steady state trace. On the other hand, with bigger hysteresis loop in 48k RPM, the 20Hz operating orbit has slightly rotated away from steady curve.

Although the operating loop remains aligned to the steady curve trend, there is an obvious presence of bigger loop in 40Hz compared to 20Hz flow, at 30k RPM turbine speed. This is depicted by a volute filling trace that is much closer to the steady state curve than the emptying trace. Conversely, the operating orbit in the 48k RPM traces the steady curve closely with much smaller loop. When the flow frequency increases to 60Hz, operating loci envelopes the steady state trace with minimum orbit size. Emptying trace still remains below steady state curve. A trend observed for both turbine speed.

The rise and fall in pressure is consistent over the entire pulse cycle for a given unsteady frequency. In the high pressure ratio region of the hysteresis loop, the pressure rise is proportional to increase in mass flow, thus the reason for low mass storage. And this pressure rise increases when turbine is subjected to higher frequency flow.

Figure 6.3 shows instantaneous swallowing capacity of the small scroll during out of phase condition for 20Hz, 40Hz and 60Hz at two different rotor speed. Apparent secondary loops, with bigger operating orbit are present in all pulsating frequencies tested. Operating orbits in the higher pressure ratio region are rotated away from steady curve. This is most significant in 20Hz pulsating flow condition in both turbine speed tested. Maximum unsteady pressure ratio experienced by the turbine did not see any changes with different flow frequency. However, the high pressure ratio operating loci has moved closer to the steady trace. As for the lower pressure ratio orbit, the position is closely related to the secondary phase orbit in Figure 6.1, which traced steady state curve with a reasonable agreement.

The rise and fall in pressure is not consistent over the entire pulse cycle for a given unsteady frequency, which is clearly depicted by the size of operating loop between high and low pressure ratio region. In the high pressure ratio region of the hysteresis loop, the rapid pressure rise has caused delay between pressure and mass flow, thus the reason for high mass storage. And this pressure rise increases when turbine is subjected to higher

frequency flow. On the other hand, in the low pressure ratio region, the relatively smaller operating orbit is produced by a slow pressure rise. This pressure rise tend to be in the reducing order as the unsteady frequency increases, contrary to the phenomena observed in the high pressure ratio region.

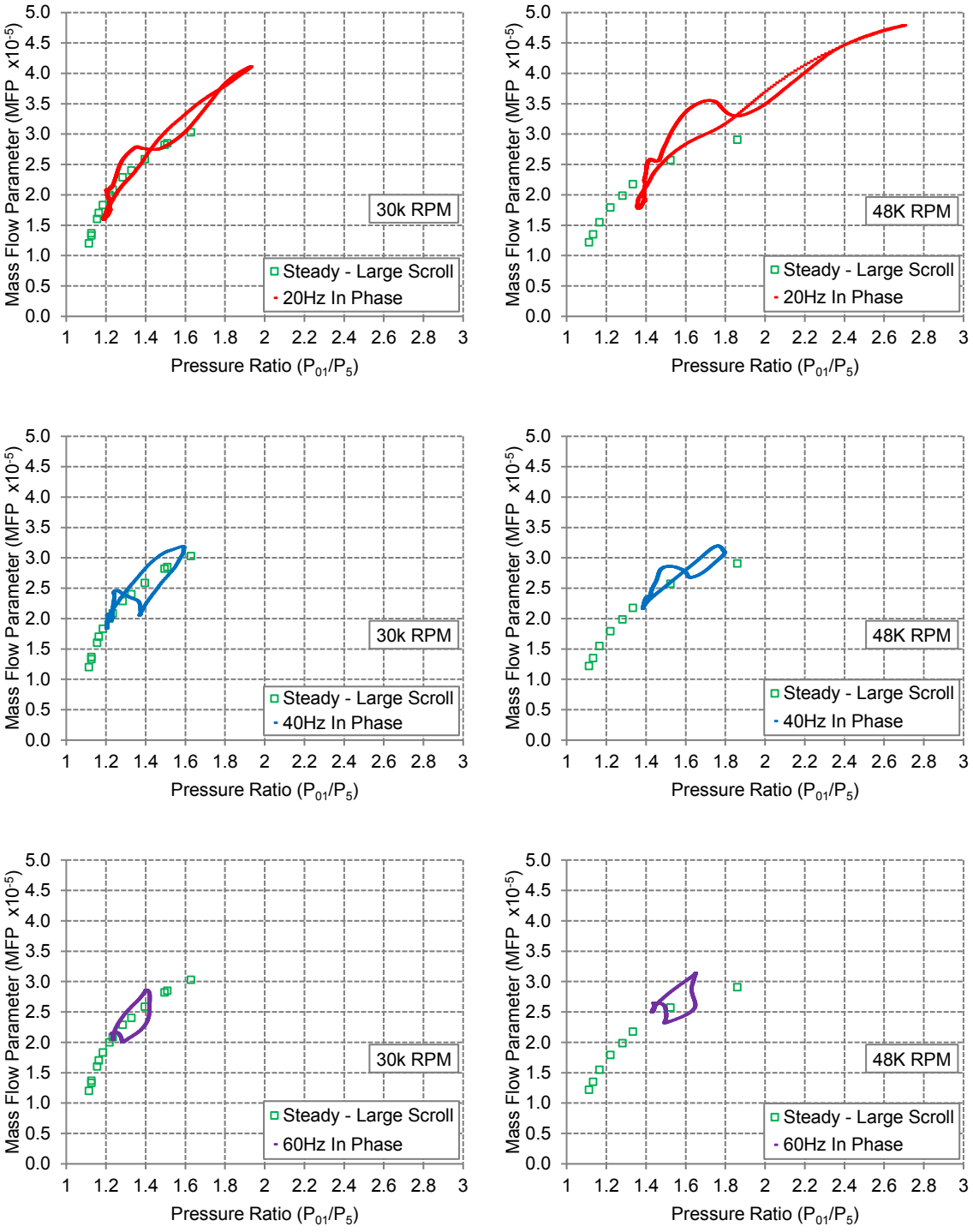


Figure 6.2 In-Phase Large Scroll Instantaneous Swallowing Capacity for nozzleless configuration

Figure 6.4 presents instantaneous swallowing capacity of the large scroll during out of phase pulsating condition for 20Hz, 40Hz and 60Hz at two different rotor speed. While two hysteresis loops are still present, the influence of out of phase unsteadiness has reduced tremendously in the large scroll. The delay between filling and emptying in the higher pressure ratio has reduced, especially in 20Hz and 40Hz flow regime. This is clearly depicted by unsteady trace which traces the trend of steady curve, with some clear offset between them. As observed in the small scroll, flow frequency has no influence on the maximum unsteady pressure ratio in the turbine volute.

Figure 6.5 shows small scroll instantaneous isentropic power for nozzleless configuration. When flow in both scrolls are in phase (measured at measurement plane), 20 Hz flow frequency allows the highest isentropic power into the small scroll at 30k RPM and 48k RPM. The in phase instantaneous isentropic power reduces as flow frequency increases. As for the out of phase testing results, the greatest isentropic power is allowed into the small scroll, during 60Hz and 20Hz pulsating frequency for 30k RPM and 48k RPM speed line. Out of phase testing at 30k RPM, has shown slight increase in isentropic power with frequency. On the other hand, as flow frequency is increased during 48k RPM turbine speed operation, out of phase isentropic power available in the small scroll has shown downward trend.

Large scroll instantaneous isentropic power for this configuration is presented in Figure 6.6. As in the case of small scroll, for both turbine speed, the large scroll has recorded greatest isentropic power when pulsating flow pulsation is set at 20Hz, during in phase operation. Highest isentropic energy available during out of phase condition in 30k RPM increases, while that in 48k RPM decreases, as flow frequency increases.

Figure 6.7 and 6.8 shows in phase and out of phase instantaneous actual power absorbed by rotor shaft. For the 30k RPM turbine speed, 20Hz flow pulsation has recorded greatest actual power during in phase operation. When turbine speed is increased to 48k RPM, the highest power absorbed by turbine is recorded during 40Hz flow condition. During out of phase operation, 20Hz flow pulsation has recorded highest actual power absorbed by turbine, for both turbine speeds tested.

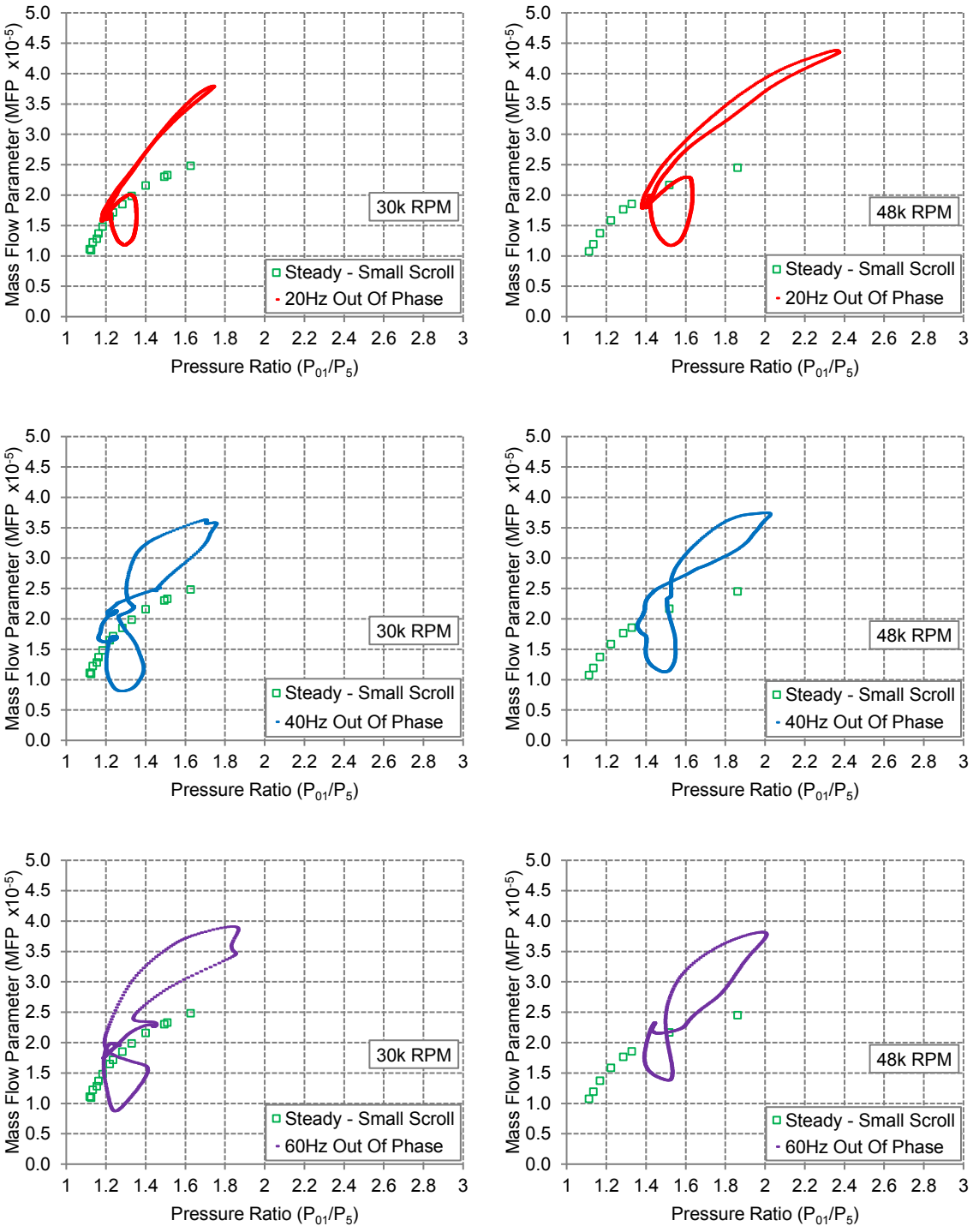


Figure 6.3 Out of phase Small Scroll Instantaneous Swallowing Capacity for nozzleless configuration

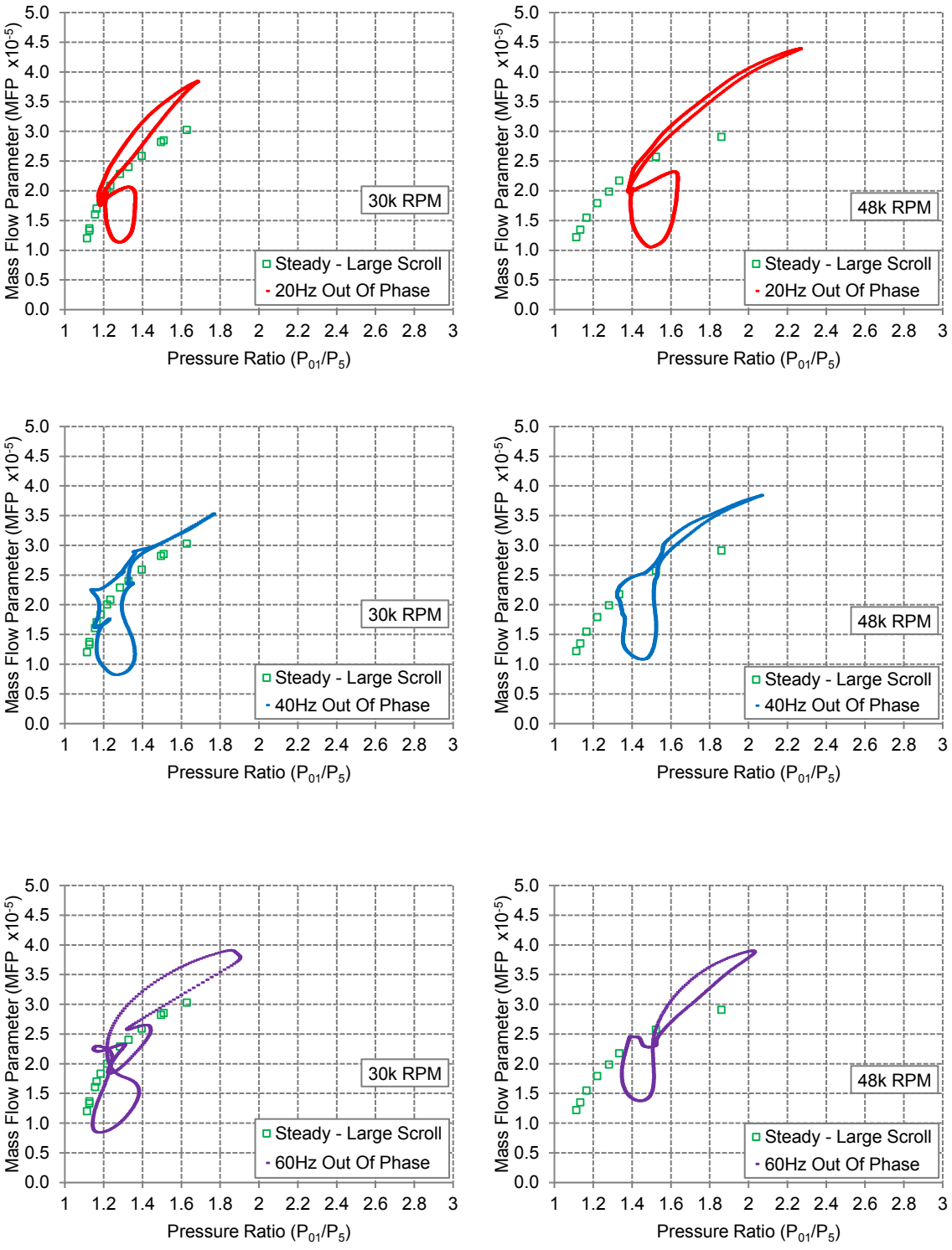


Figure 6.4 Out of phase Large Scroll Instantaneous Swallowing Capacity for nozzleless configuration

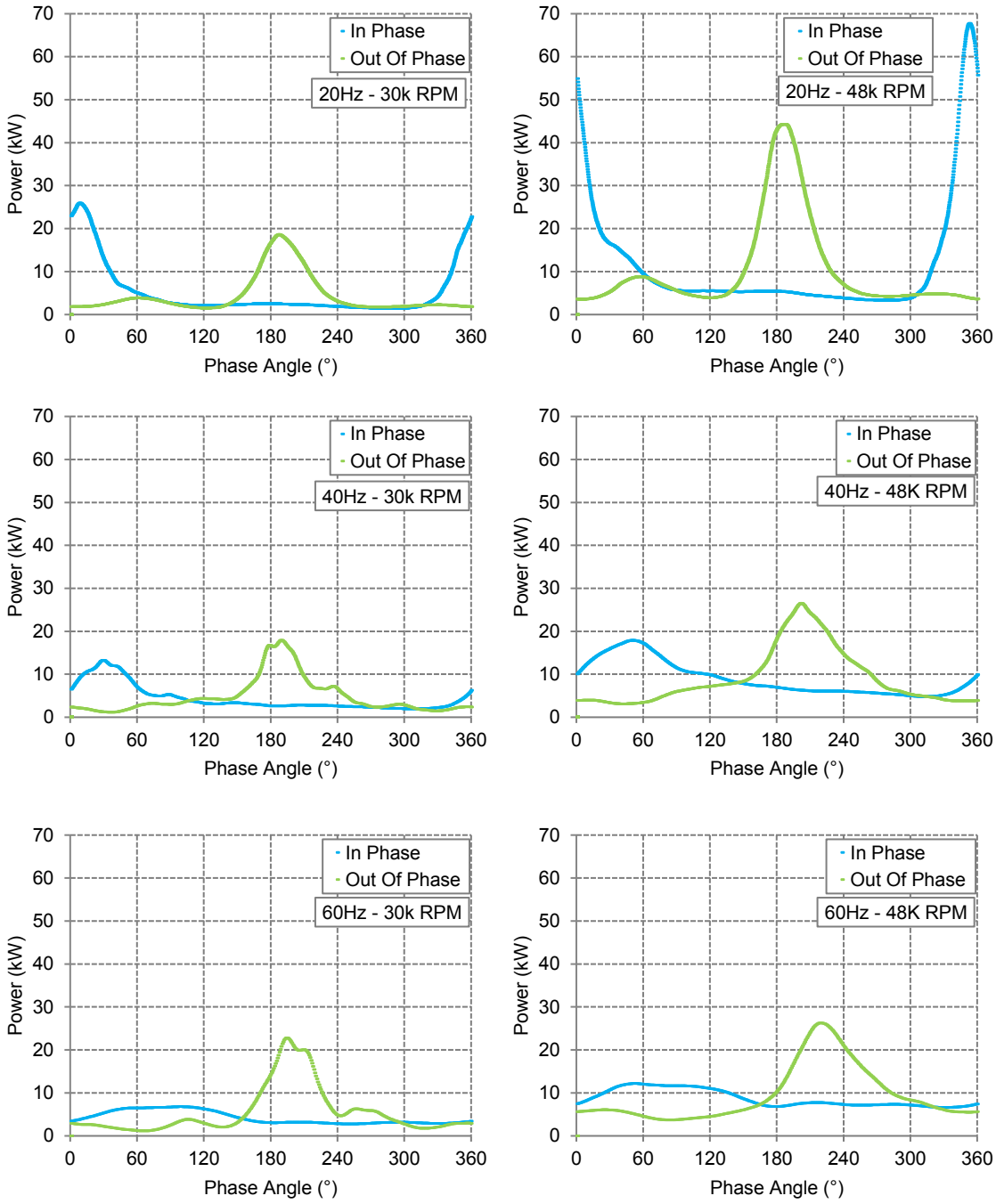


Figure 6.5 Small Scroll Instantaneous Isentropic Power for nozzleless configuration

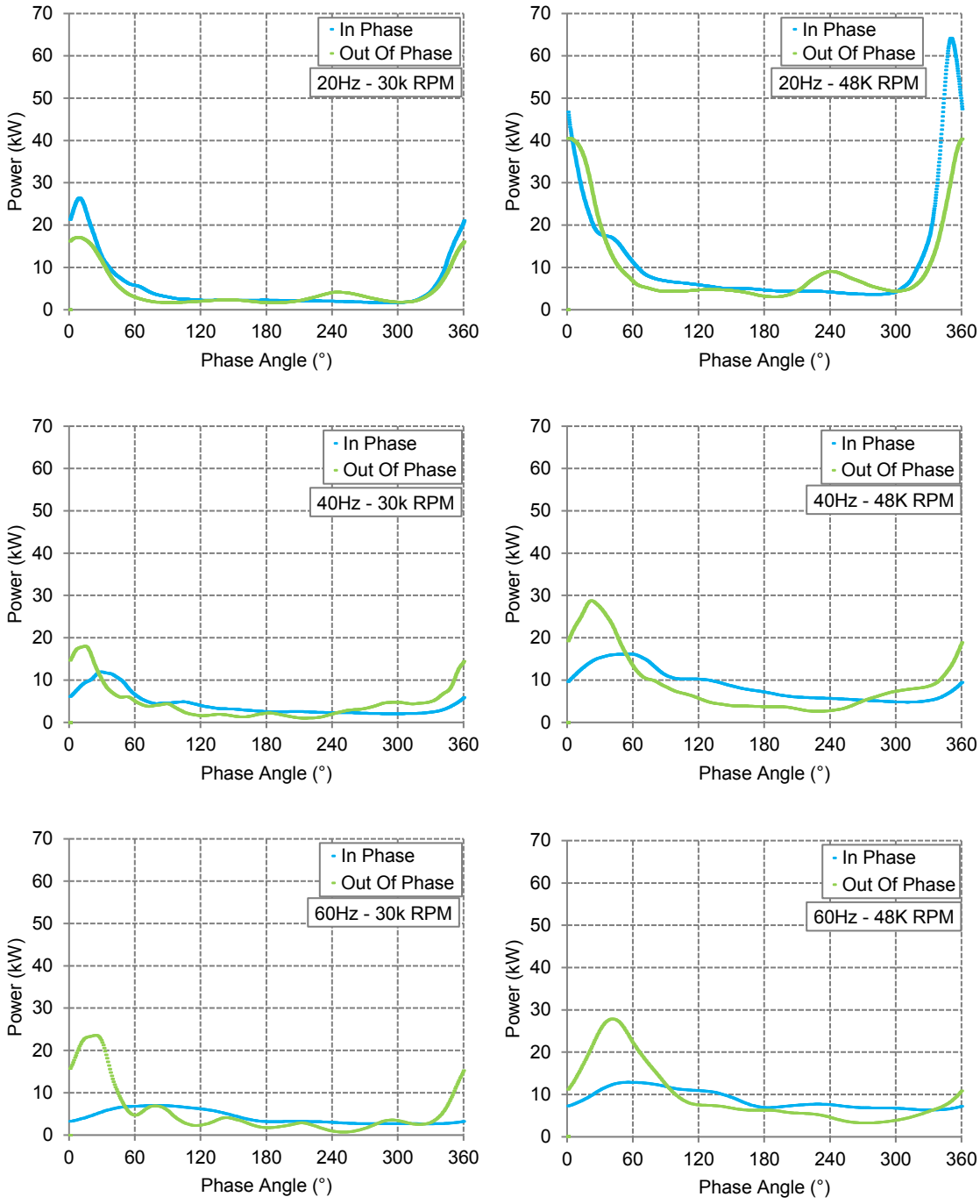


Figure 6.6 Large Scroll Instantaneous Isentropic Power for nozzleless configuration

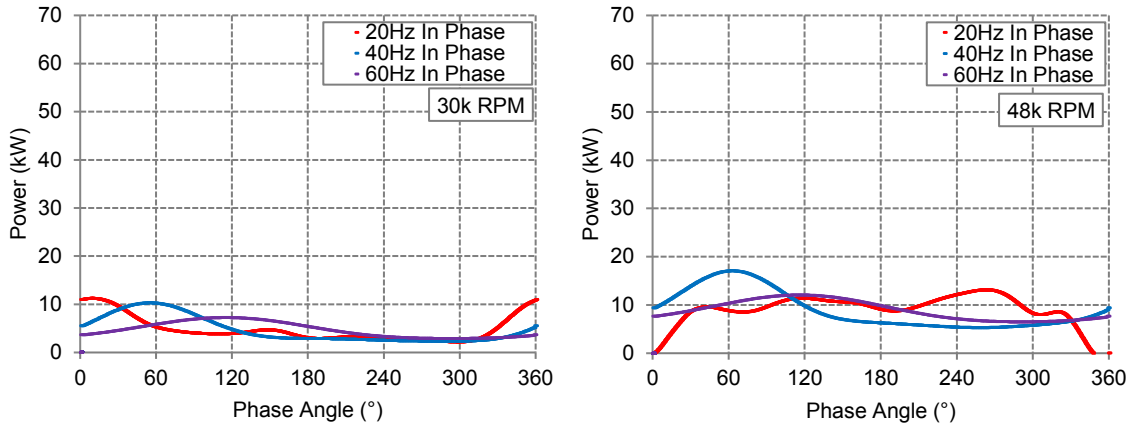


Figure 6.7 In Phase Instantaneous Actual power for nozzleless configuration

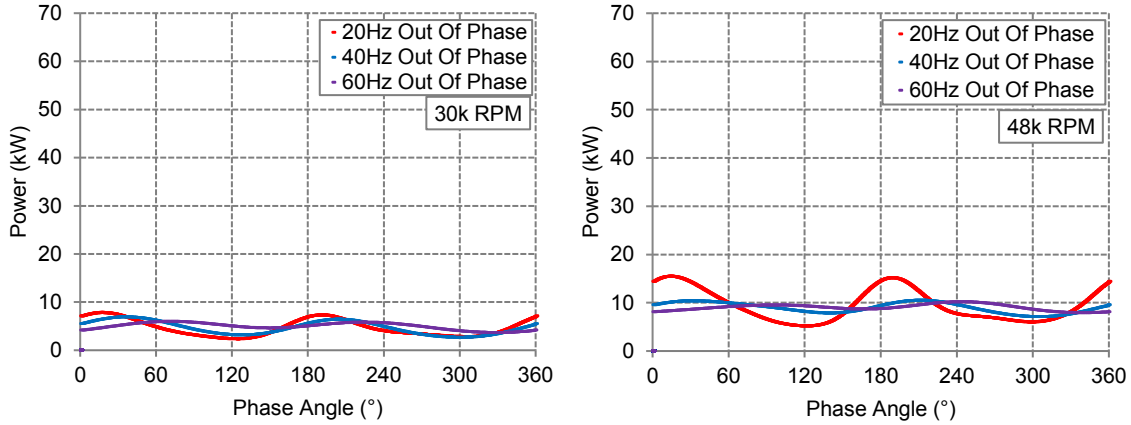


Figure 6.8 Out of Phase Instantaneous Actual power for nozzleless configuration

6.2 Nozzle Vanes in small scroll

Instantaneous swallowing capacities of the small scroll in the S51 setting (nozzle vanes in small scroll with an angle of 51°) during in phase pulsating condition for 20Hz, 40Hz and 60Hz at two different rotor speed are presented in Figure 6.9. Operating loop in 30k RPM for all pulsating frequency tested is closer to the steady state curve, compared to that of 42k RPM speed. Pressure ratio range for all other orbits in 30k RPM are relatively smaller than 42k RPM.

Although the operating loop of the 30k RPM is closer to the steady state curve, only 20Hz flow frequency traces the latter, during emptying process in the pressure ratio range of 1.15 – 1.5. 60Hz flow frequency encompasses the steady state curve in the pressure ratio range of 1.25 – 1.55. As observed in the nozzleless setting (in phase of the small scroll), pressure

ratio range for the hysteresis loop reduces as flow frequency increases in both speed conditions. Operating loop size in the 30k RPM speed is relatively smaller than that of the nozzleless setting. Apart from that, presence of secondary loop is more significant in both speed conditions, compared to the nozzleless configuration. This is especially true at lower flow frequency of 20Hz. Operating orbits of the 42k RPM are rotated away from steady curve. This can be seen in all flow frequencies tested at this rotor speed.

Instantaneous swallowing capacity of the large scroll in the S51 setting during in phase pulsating condition for 20Hz, 40Hz and 60Hz at two different rotor speed is shown in Figure 6.10. All the hysteresis loop in 30k RPM turbine speed tested traces closely the steady state characteristic. The 20Hz and 40Hz operating loops encapsulates steady state trace in the pressure ratio range of 1.2 – 1.6 and 1.2 – 1.75 respectively. The difference between high pressure and low pressure ratio of the hysteresis loop clearly decreases with increase in flow pulsating frequency. Secondary loop is not as visible as the small scroll unsteady flow in Figure 6.9. Presence of nozzle vanes in the small scroll has evidently reduced the influence of wave action in the large scroll, when compared to nozzleless unsteady flow as presented in Figure 6.2. Conversely, the 42k RPM operating loop has departed from the steady state trace, with bigger hysteresis loops. Turbine speed has more profound influence in the S51 configuration, than nozzleless setting, during in phase pulsating flow.

Figure 6.11 shows instantaneous swallowing capacity of the small scroll in the S51 configuration during out of phase condition for 20Hz, 40Hz and 60Hz at two different rotor speed. The filling and emptying trace are very close to each other. The size of the operating loop has significantly reduced compared to nozzleless out of phase unsteady flow, shown in Figure 6.3. Although all the operating orbits have departed from steady state trace, the effect is more significant in 42k RPM speed hysteresis loop. The rise and fall in pressure is consistent over the entire pulse cycle for a given unsteady frequency. The pressure rise is proportional to increase in mass flow, thus the reason for low mass storage; indicated by smaller operating orbits.

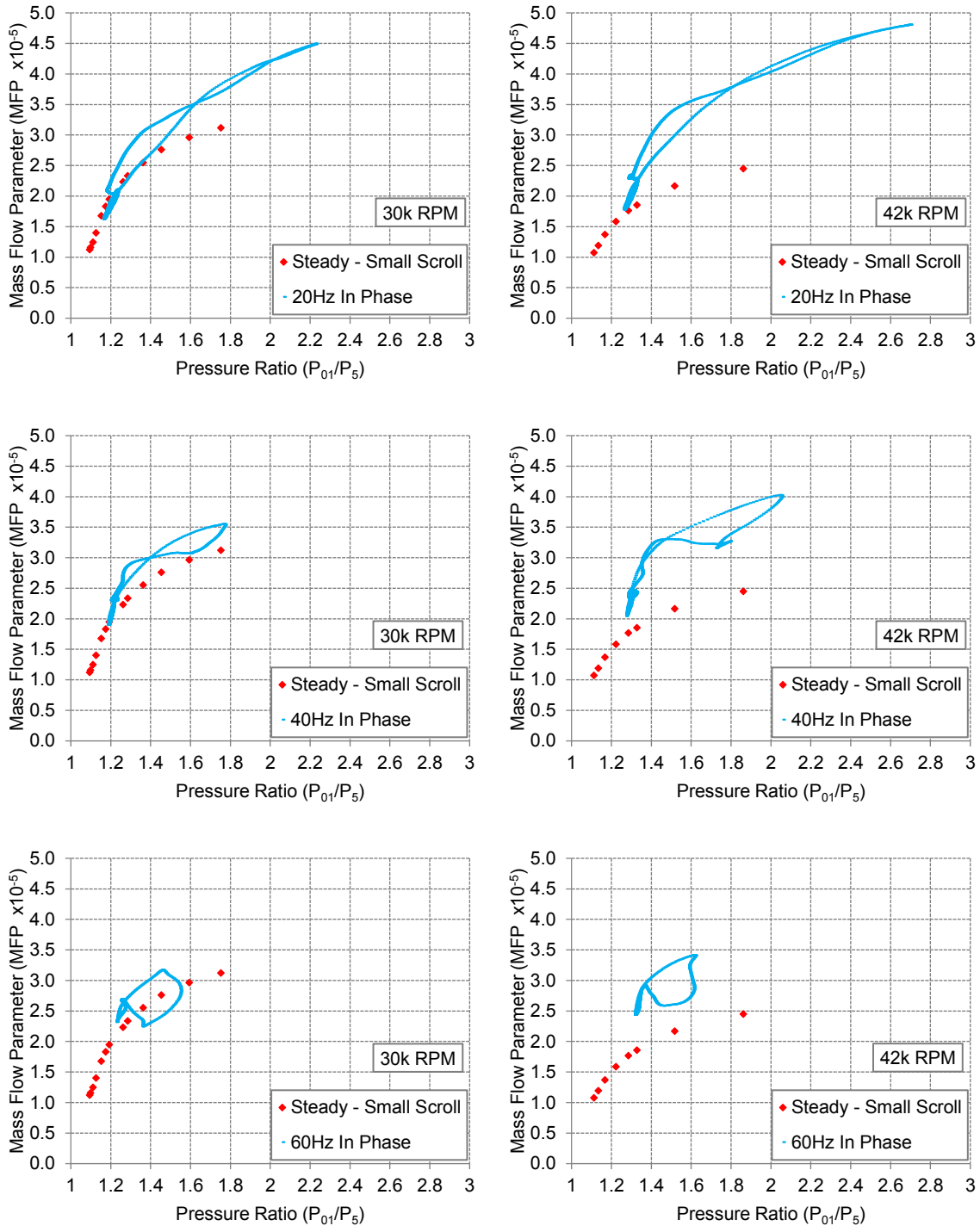


Figure 6.9 In-Phase Small Scroll Instantaneous Swallowing Capacity for S51 configuration

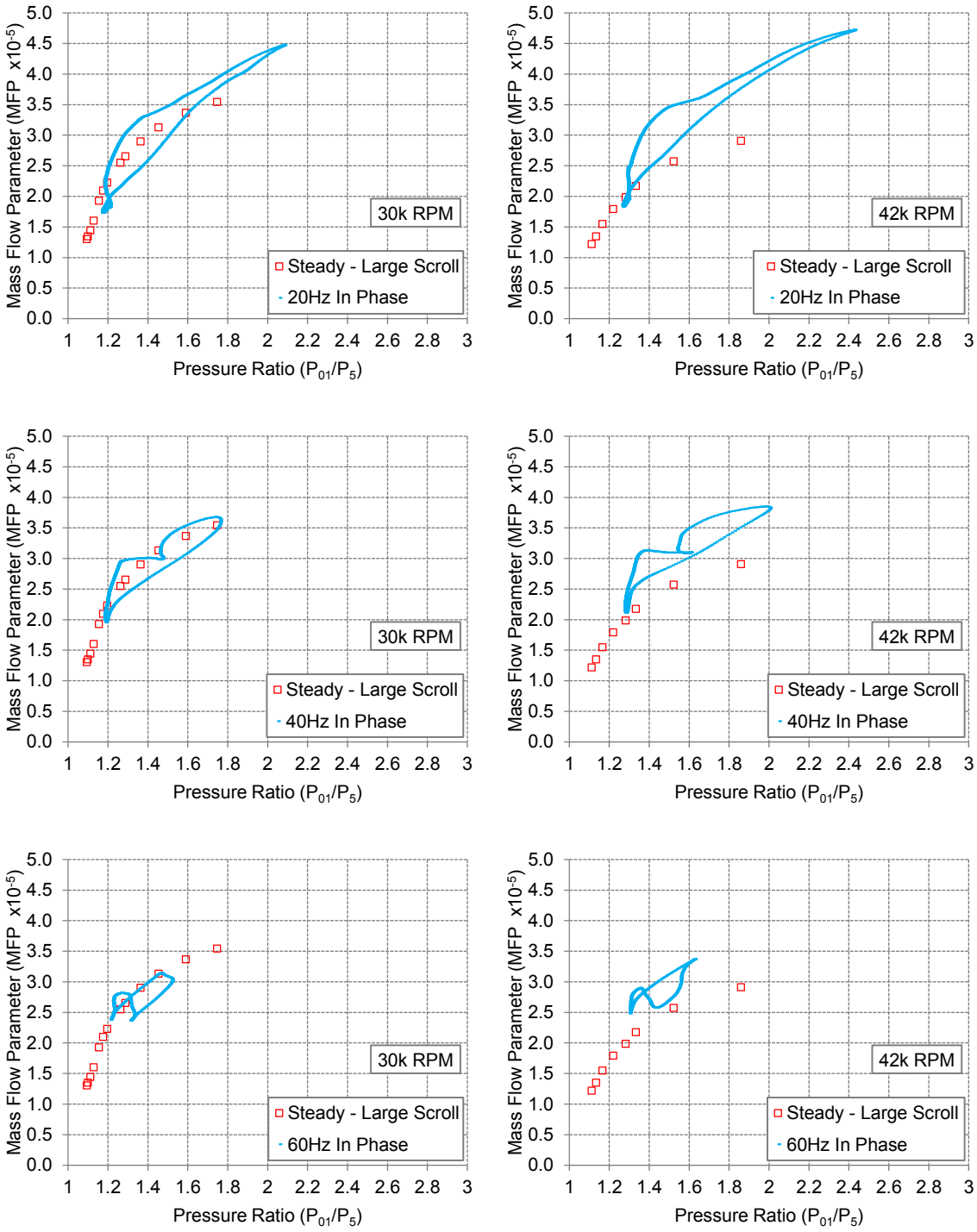


Figure 6.10 In-Phase Large Scroll Instantaneous Swallowing Capacity for S51 configuration

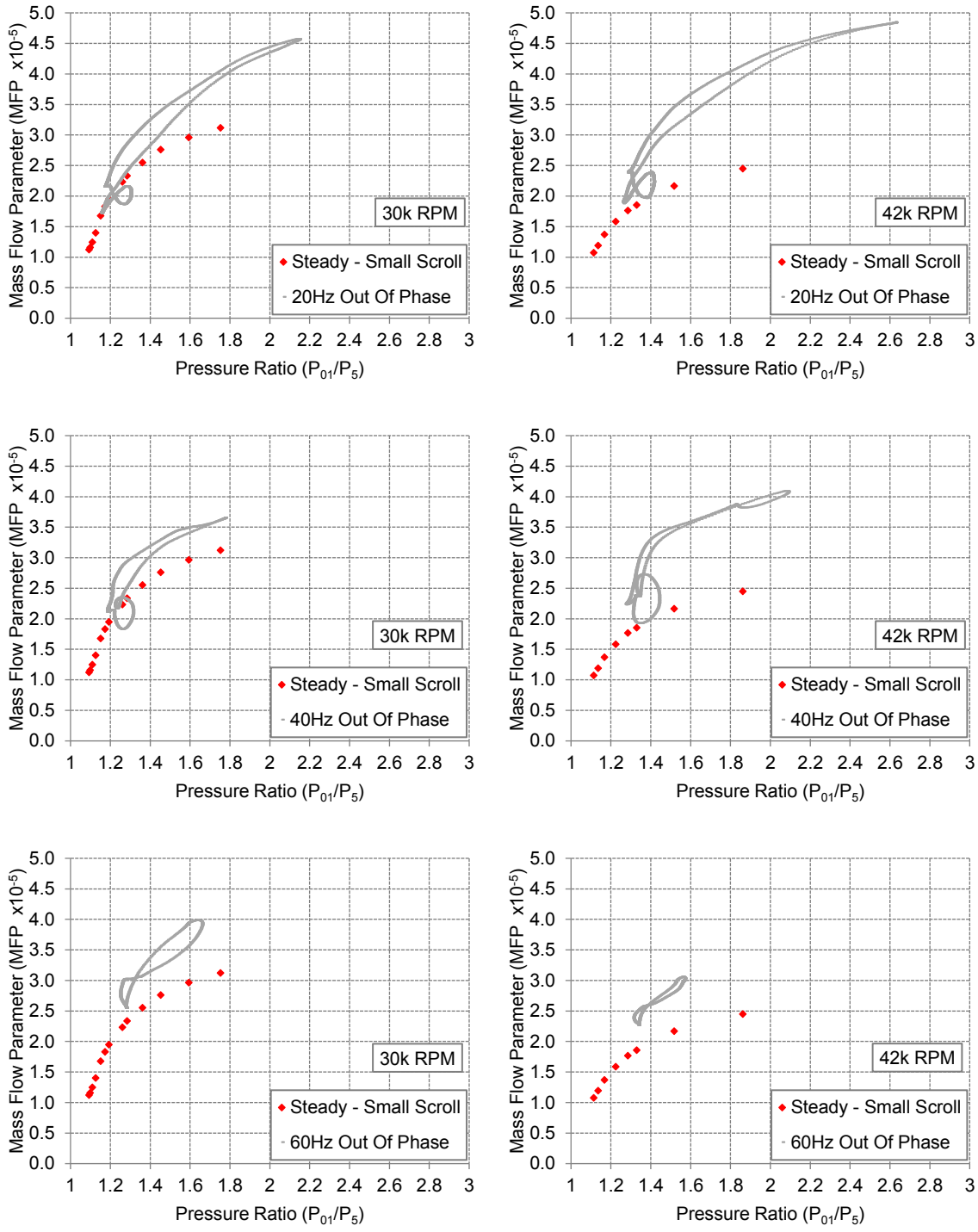


Figure 6.11 Out of phase Small Scroll Instantaneous Swallowing Capacity for S51 configuration

Figure 6.12 presents instantaneous swallowing capacity of the large scroll scroll in the S51 setting during out of phase pulsating condition for 20Hz, 40Hz and 60Hz at two different rotor speed. The delay between filling and emptying process has increased, which is depicted by a bigger operating loop. Nevertheless, both filling and emptying trace gets closer to each other as the flow frequency increases. This is very apparent in the 60Hz

pulsating flow frequency. Furthermore, the hysteresis loci in 30k RPM turbine speed tested traces closely the steady state characteristic. With the presence of nozzle vanes in the small scroll, the influence of out of phase unsteadiness has reduced tremendously in the large scroll. However, turbine speed has more influence on out of phase unsteadiness, compared to flow frequency. This can be clearly seen in 42k RPM unsteady flow plots. Although 42k RPM characteristics is similar to that of 30k RPM, the hysteresis orbit in former has departed significantly from steady state trace.

Figure 6.13 shows instantaneous swallowing capacity of the small scroll in the S66 setting (nozzle vanes in small scroll with an angle of 66°) during in phase pulsating condition for 20Hz, 40Hz and 60Hz at two different rotor speed. Operating hysteresis loop in 30k RPM for all pulsating frequency tested is closer to the steady state curve, compared to that of the higher speed at 48k RPM. With exception of 60Hz operating loop, pressure ratio range for all other orbits in 30k RPM are relatively smaller than 48k RPM.

At 30k RPM turbine speed, the operating loop although appears closer to the steady state curve, the former does not overlap the latter. Nevertheless, the hysteresis orbit in 40Hz and 60Hz flow frequency, encapsulates steady state trace in the pressure ratio range of 1.3 – 1.45 and 1.3 – 1.4 respectively. The difference between high pressure and low pressure ratio of the hysteresis loop apparently decreases with increase in flow pulsating frequency. This is also observed in the 48k RPM speed condition. The rise in pressure over one pulse cycle increases (become too rapid) in the small scroll as the flow frequency is increased. This is the reason for emptying curve tracing the steady curve in 40Hz and 60Hz unsteady flow at 30k RPM turbine speed. Presence of secondary loop is more profound in 48k RPM speed conditions. The occurrence of secondary loop which is significant in the low pressure and mass flow region of the swallowing capacity map, indicates effect of wave action within the turbine volute.

The in phase unsteady flow characteristic demonstrated by small scroll in S66 setting resembles that of the nozzleless configuration. As observed in Chapter 5, both nozzleless and S66 settings swallows equal amount of mass in the steady flow condition at both turbine speed tested. In other words, the opening in S66 small scroll circumference has equivalent area as in the nozzleless configuration. Therefore, this could be one reason why similar unsteady characteristic observed in both settings.

Instantaneous swallowing capacity of the large scroll in the S66 setting during in phase pulsating condition for 20Hz, 40Hz and 60Hz at two different rotor speed is shown in Figure 6.14. Hysteresis loci in 30k RPM turbine speed tested traces closely the steady state characteristic. Maximum unsteady pressure ratio experienced by the turbine decreases as the flow frequency increases. Apart from that, the presence of secondary loop is more profound than that in the small scroll unsteady flow. Traces of volute filling and emptying closely follows and encapsulates steady state trace at 30k RPM speed.

The unsteady characteristics similarity displayed by small scroll in both settings (nozzleless and S66) during in phase unsteady flow at 48k RPM, has not been echoed by the large scrolls. The presence of nozzle vanes (with an angle of 66°) in the small scroll has significantly influenced the unsteadiness in the large scroll of the volute. The operating loop has grown bigger in the S66 settings and has departed from steady state curve, especially at 20Hz pulsating flow.

Figure 6.15 shows instantaneous swallowing capacity of the small scroll in the S66 setting during out of phase phase condition for 20Hz, 40Hz and 60Hz at two different rotor speed. Apparent secondary loops, are present in all pulsating frequencies tested. When comparing the nozzleless setting, S66 configuration hysteresis loops have departed from steady curve for both turbine speeds tested. However, operating orbit has reduced in size, depicting the decrease in delay between filling and emptying, especially at 48k RPM speed.

Figure 6.16 presents instantaneous swallowing capacity of the large scroll in the S66 setting during out of phase pulsating condition for 20Hz, 40Hz and 60Hz at two different rotor speed. While two hysteresis loops are still present, the influence of out of phase unsteadiness has reduced tremendously in the large scroll. The delay between filling and emptying process has increased, which is depicted by a bigger operating loop, at 48k RPM speed. Apart from that, the hysteresis loci in both turbine speed tested traces closely the steady state characteristic. With the presence of nozzle vanes in the small scroll, the influence of out of phase unsteadiness has reduced tremendously in the large scroll.

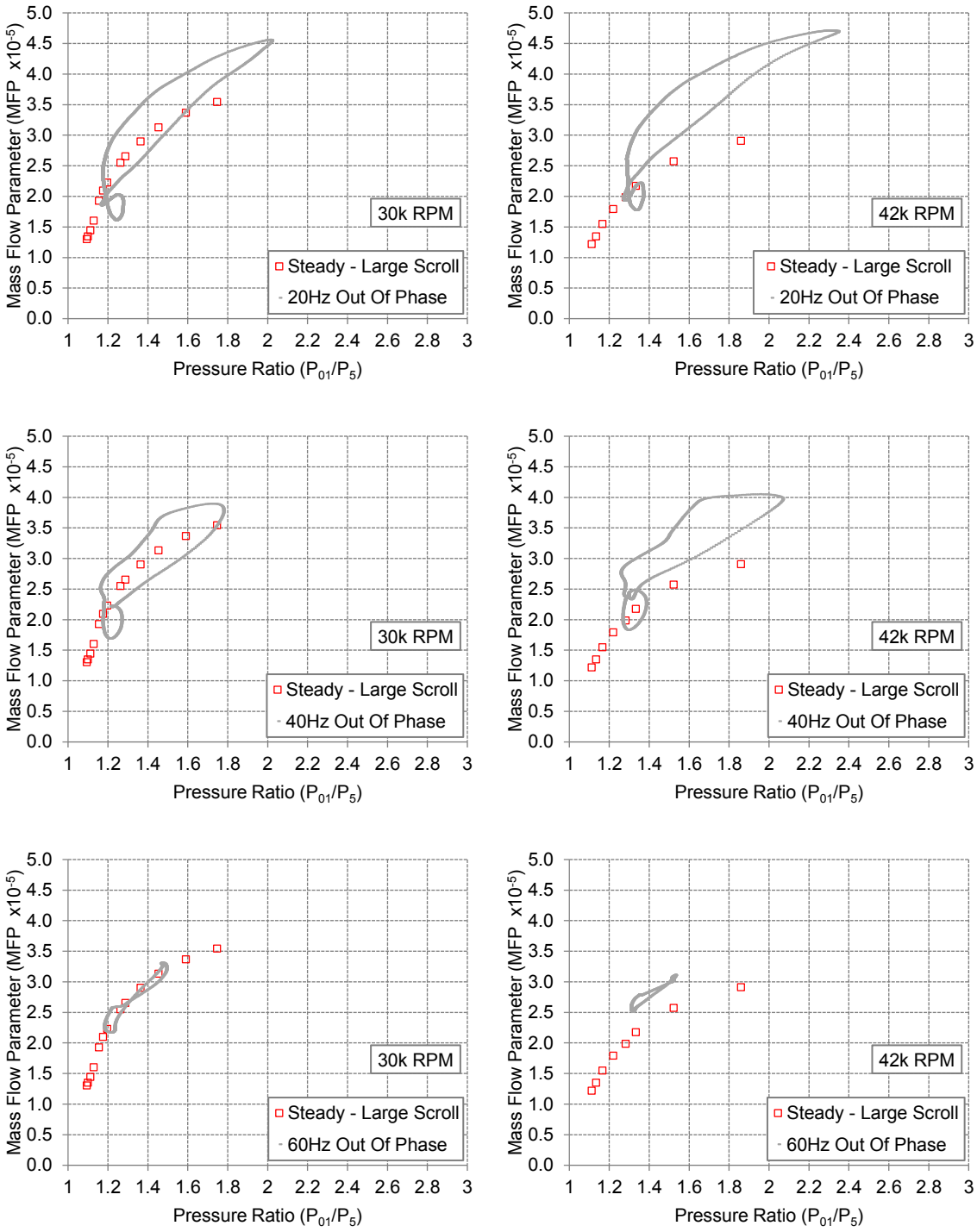


Figure 6.12 Out of phase Large Scroll Instantaneous Swallowing Capacity for S51 configuration

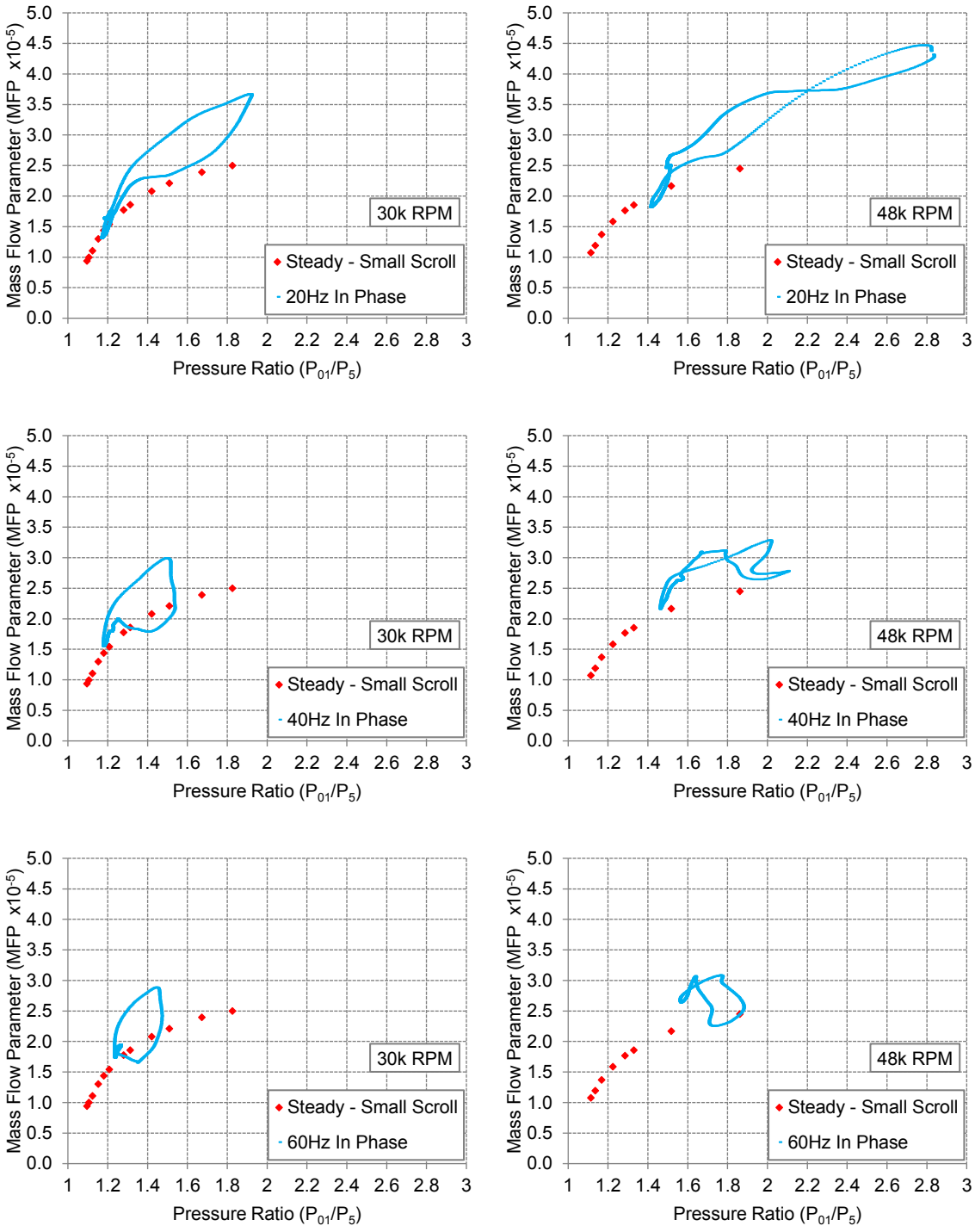


Figure 6.13 In-Phase Small Scroll Instantaneous Swallowing Capacity for S66 configuration

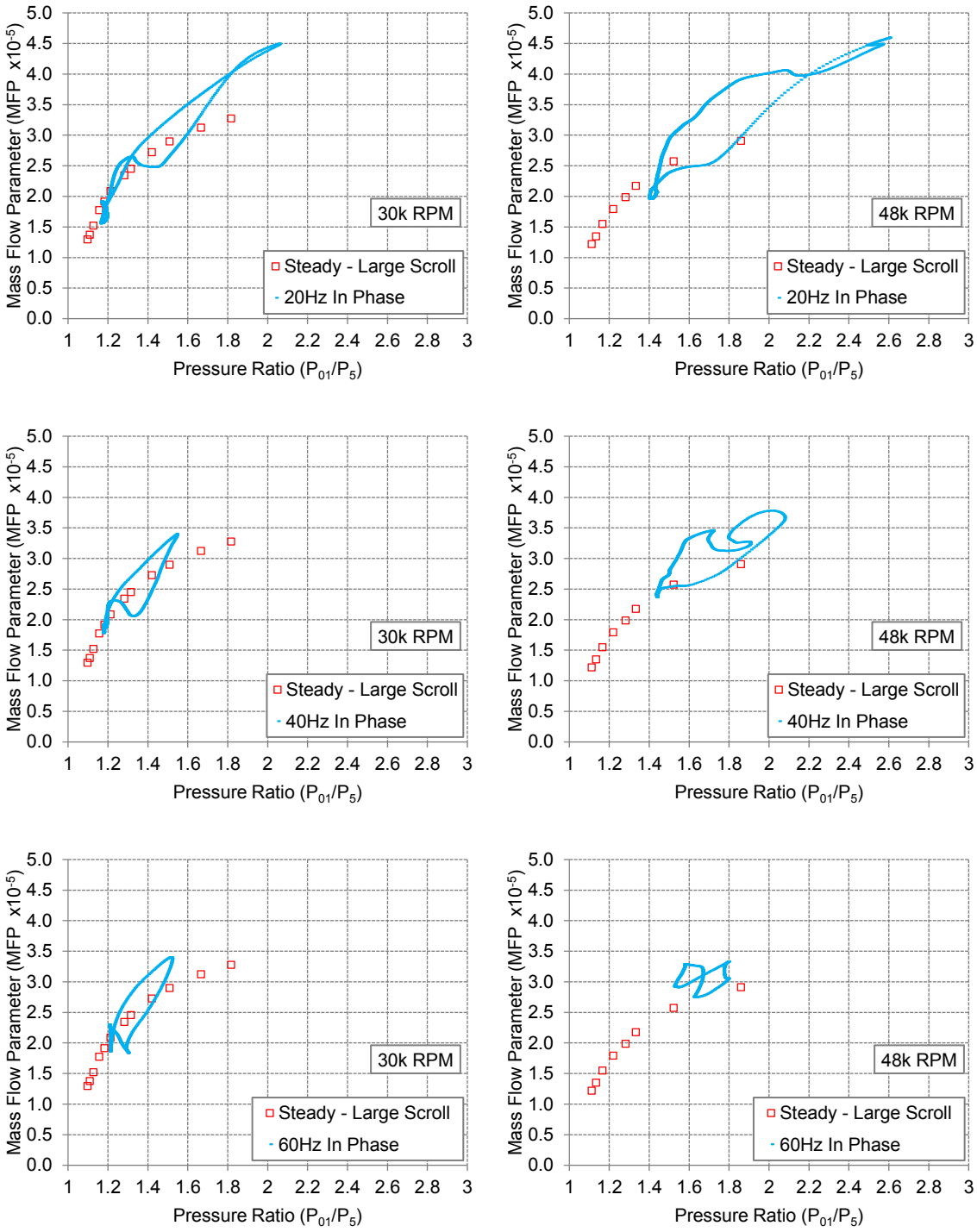


Figure 6.14 In-Phase Large Scroll Instantaneous Swallowing Capacity for S66 configuration

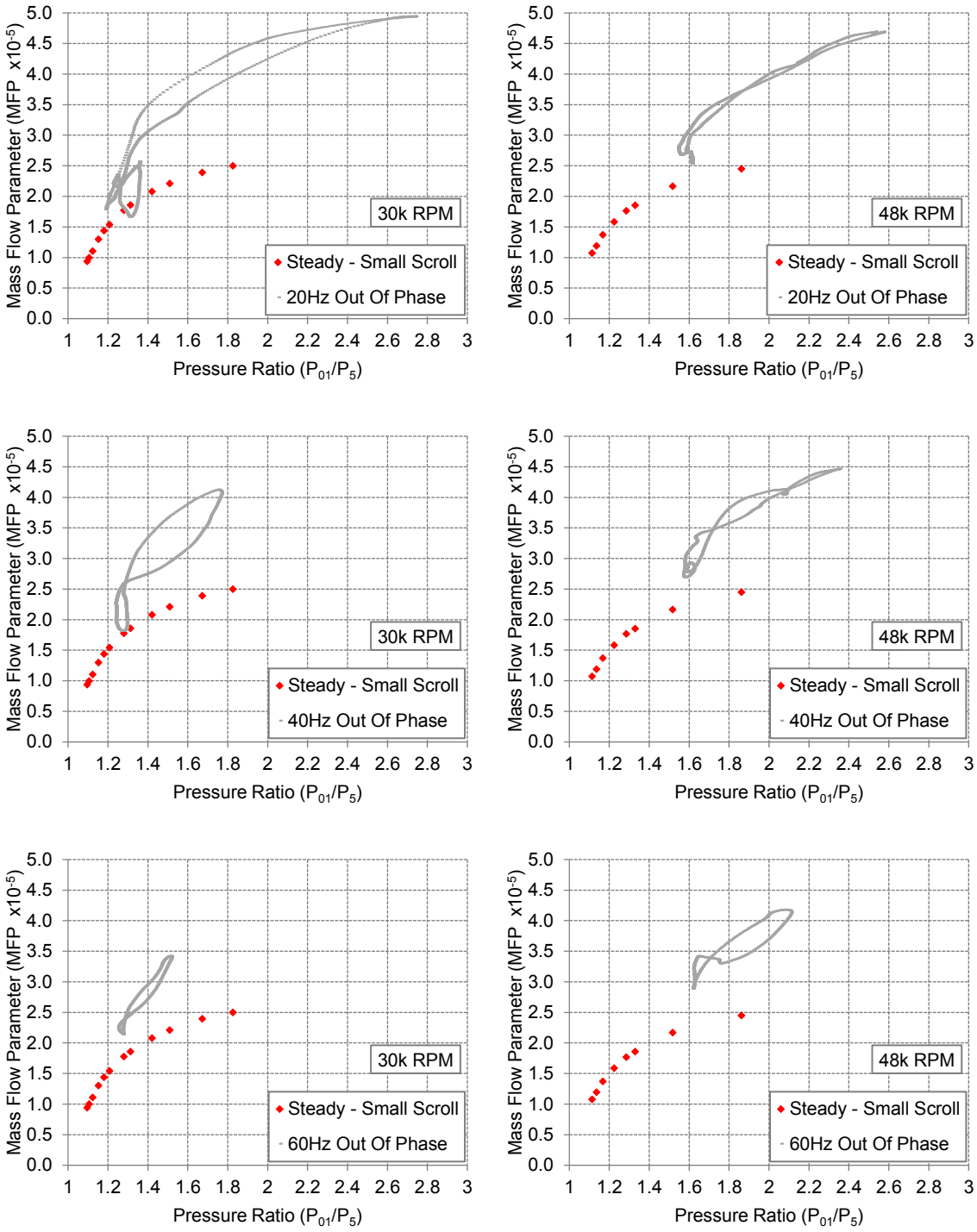


Figure 6.15 Out of Phase Small Scroll Instantaneous Swallowing Capacity for S66 configuration

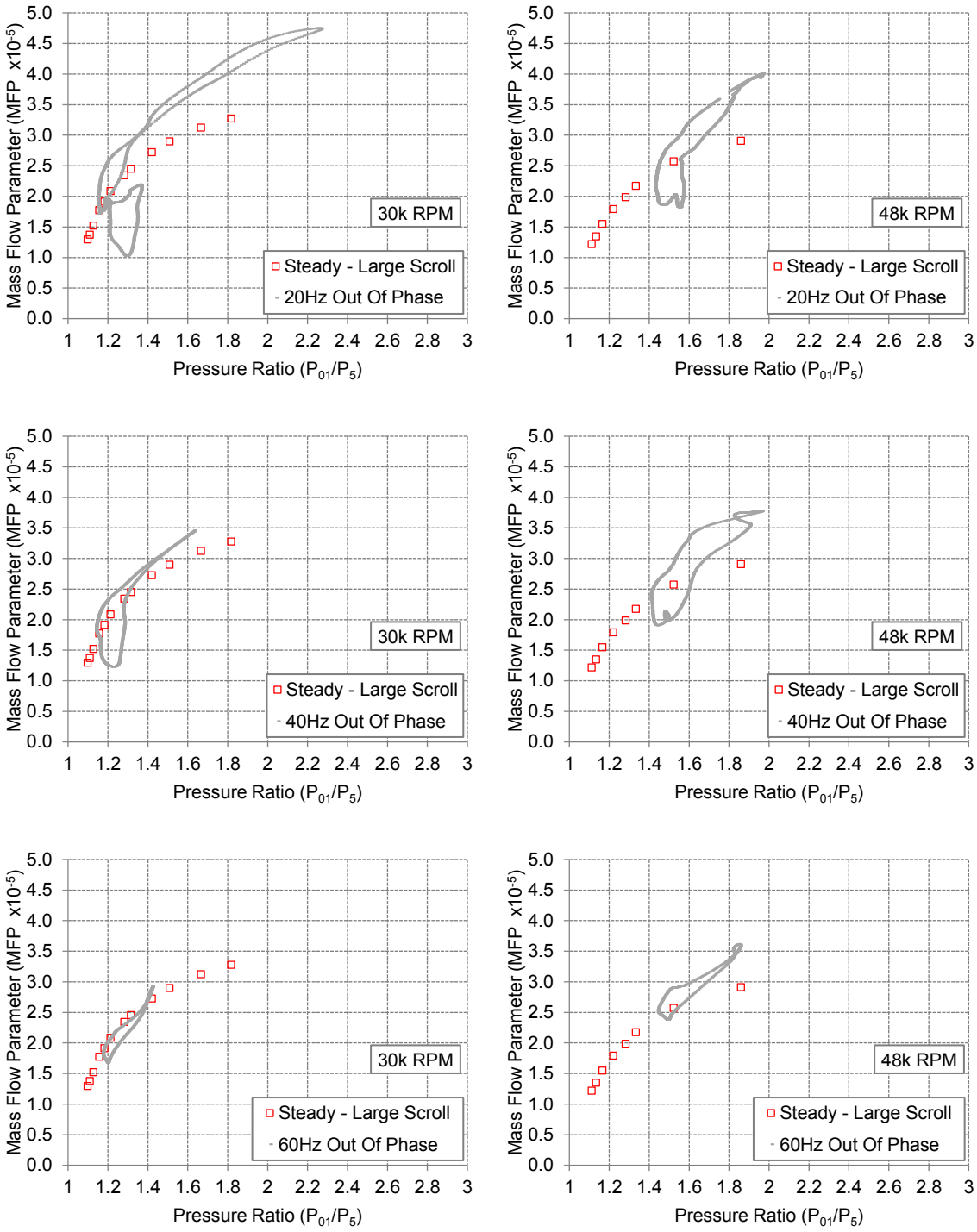


Figure 6.16 Out of Phase Large Scroll Instantaneous Swallowing Capacity for S66 configuration

Figure 6.17 shows instantaneous swallowing capacity of the small scroll in the S71 setting (nozzle vanes in small scroll with an angle of 71°) during in phase pulsating condition for 20Hz, 40Hz and 60Hz at two different rotor speed. As observed in S66 setting (small scroll during in phase pulsating condition) operating orbit in 30k RPM for all pulsating frequency

tested is closer to the steady state curve. compared to that of the higher speed at 48k RPM. With exception of 20Hz operating loop, other orbits in 48k RPM have departed from steady state trace. Both 40Hz and 60Hz operating loop in 48k RPM is located below steady state curve. At 30k RPM turbine speed, the hysteresis orbit in 40Hz and 60Hz, encapsulates steady state trace in the pressure ratio range of 1.25 – 1.65 and 1.3 – 1.45 respectively. Presence of secondary loop is more profound in 48k RPM speed conditions. The in phase unsteady flow characteristic demonstrated by small scroll at 30k RPM turbine speed in S71 setting resembles that of the nozzleless configuration.

Instantaneous swallowing capacity of the large scroll in the S71 setting during in phase pulsating condition for 20Hz, 40Hz and 60Hz at two different rotor speed is shown in Figure 6.18. Operating loop in both turbine speed tested traces closely the steady state characteristic. The presence of nozzle vanes (with an angle of 71°) in the small scroll has significantly reduced the unsteadiness in the large scroll of the volute, especially at higher turbine speed. The size of the operating loop in 48k RPM rotor speed has reduced with comparison to that of 30k RPM for all pulsating flow frequencies tested.

Figure 6.19 shows instantaneous swallowing capacity of the small scroll in the S71 setting during out of phase condition for 20Hz, 40Hz and 60Hz at two different rotor speed. S71 setting hysteresis loop resembles that of small scroll in the S66 configuration during out of phase condition, for all testing conditions. Apparent secondary loops, are present in all pulsating frequencies tested.

Figure 6.20 presents instantaneous swallowing capacity of the large scroll in the S71 setting during out of phase pulsating condition for 20Hz, 40Hz and 60Hz at two different rotor speed. The delay between filling and emptying process has increased, which is depicted by a bigger operating loop, in both turbine speed tested. Compared to the large scroll in the S66 setting during out of phase pulsating condition, the influence of out of phase unsteadiness has increased significantly in the S71 configuration, especially at 48k RPM turbine speed.

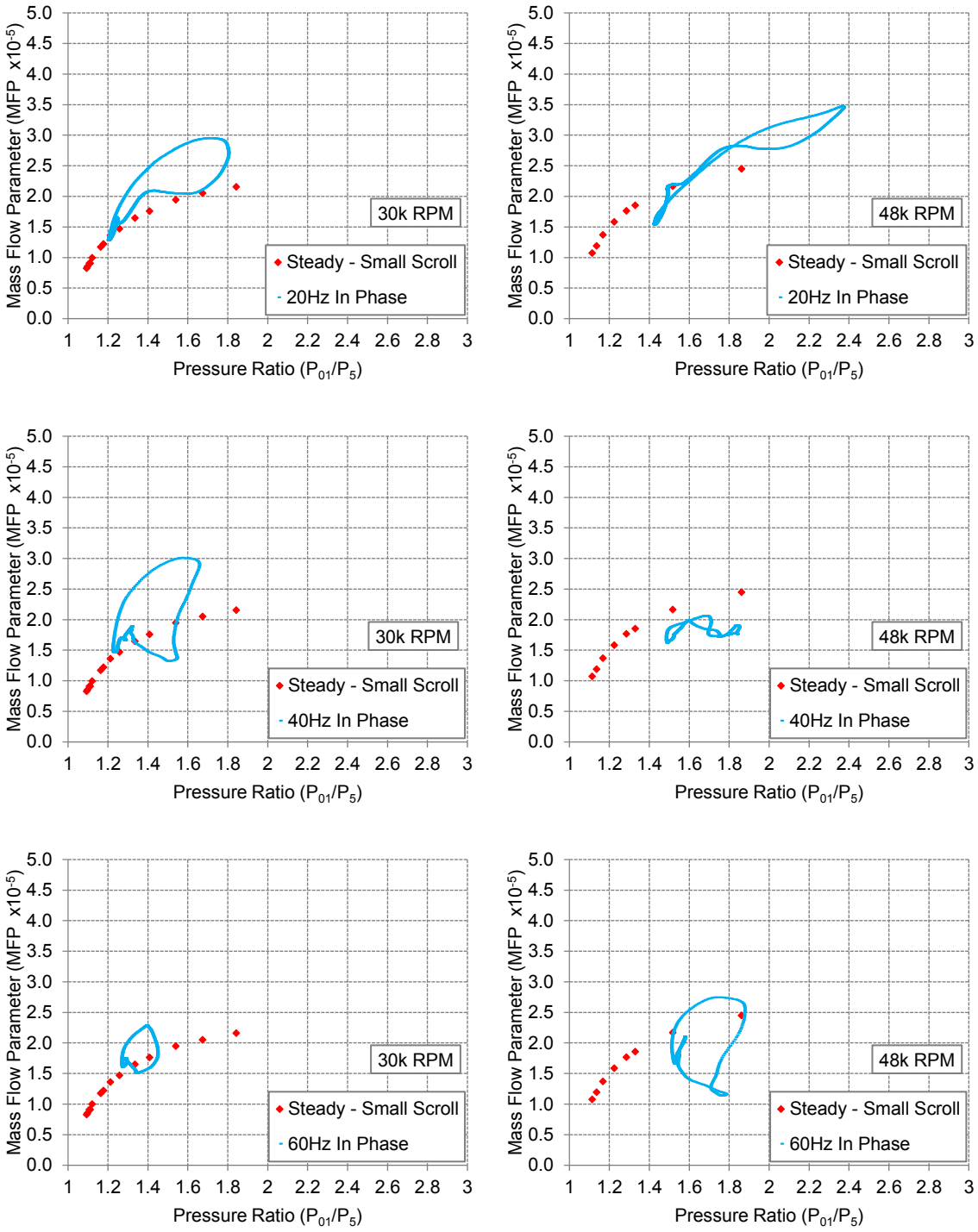


Figure 6.17 In-Phase Small Scroll Instantaneous Swallowing Capacity for S71 configuration

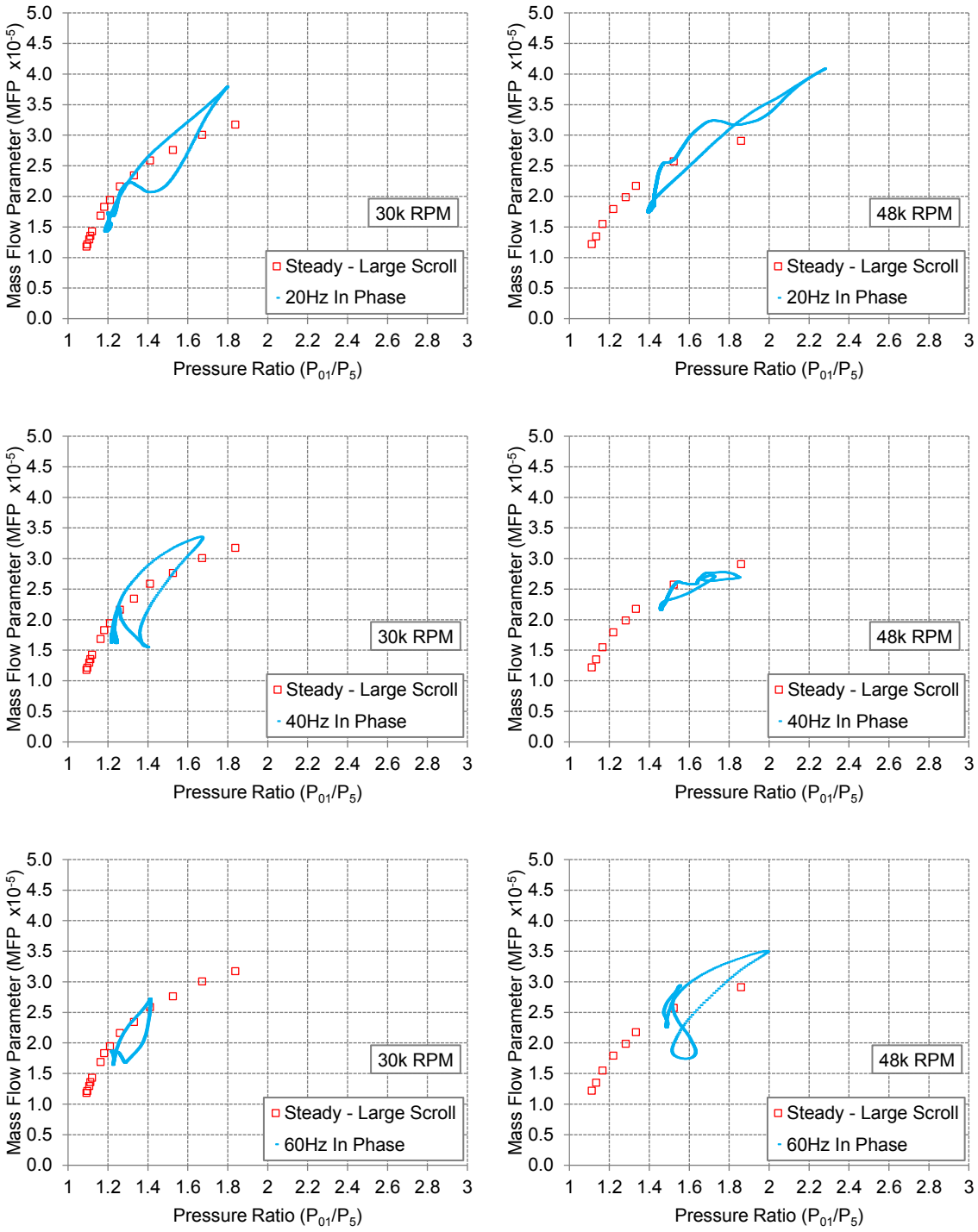


Figure 6.18 In-Phase Large Scroll Instantaneous Swallowing Capacity for S71 configuration

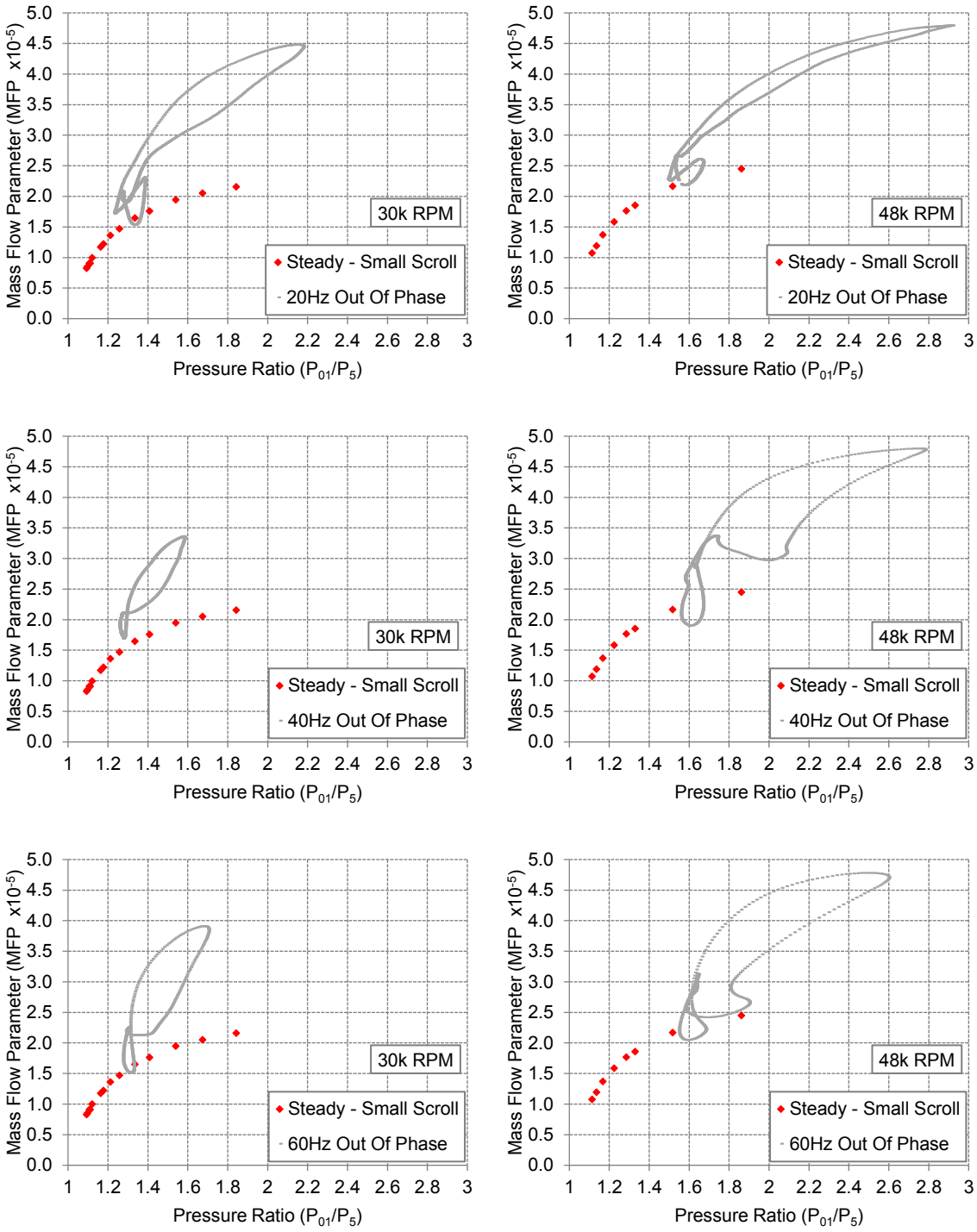


Figure 6.19 Out of Phase Small Scroll Instantaneous Swallowing Capacity for S71 configuration

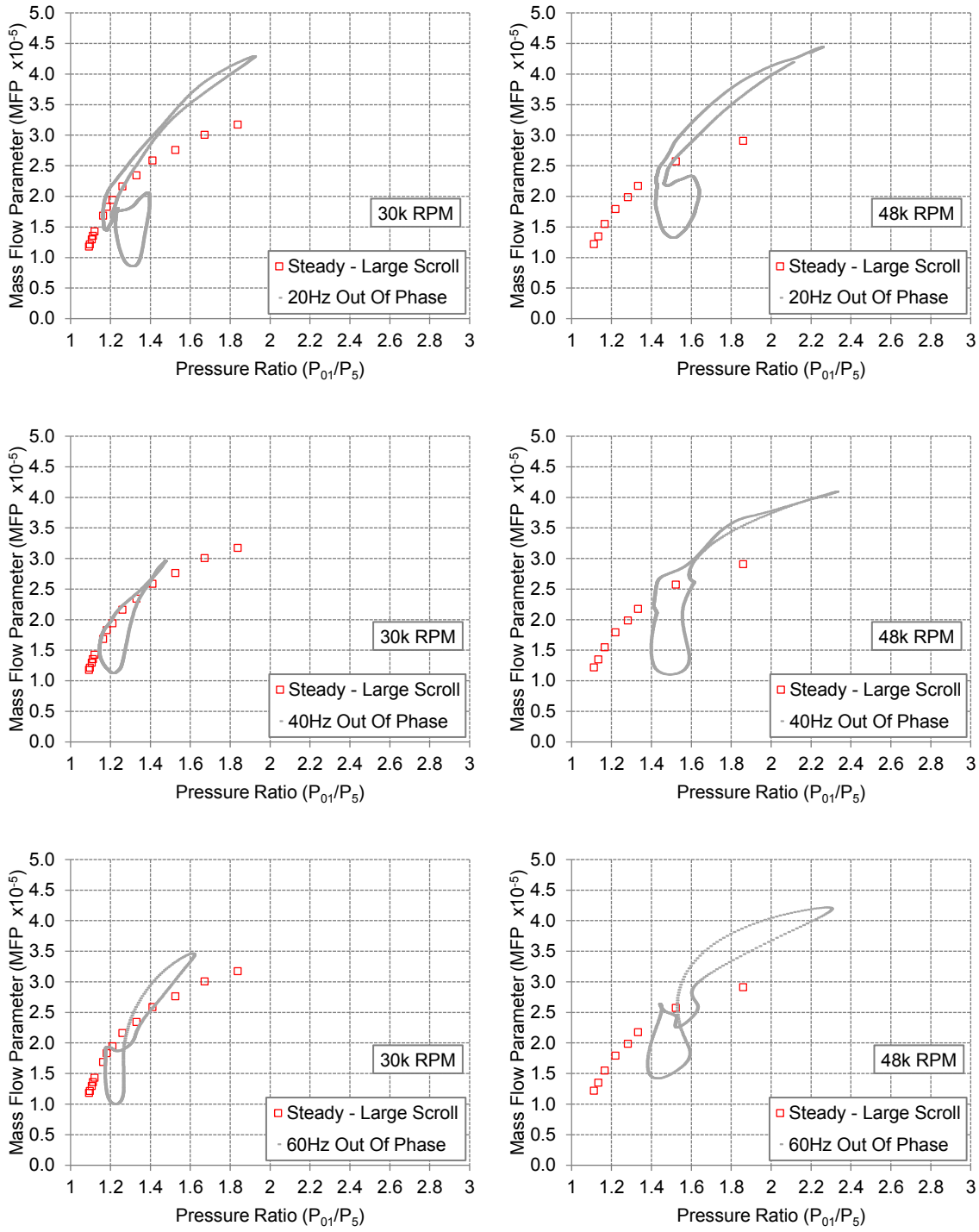


Figure 6.20 Out of Phase Large Scroll Instantaneous Swallowing Capacity for S71 configuration

Presence of nozzle vanes in small scroll has reduced flow unsteadiness in both scrolls. This is clearly presented in Figure 6.21. In the small scroll, during in phase operation, S71 configuration has shown the smallest operating orbit, which envelopes the steady trace in the mid pressure ratio region. During out of phase testing, S66 configuration has reduced unsteadiness most effectively compared to other vane angle settings, in the small scroll. In

the large scroll, S66 configuration again emerges as the setting which has operating loci tracing closely the equivalent steady curve.

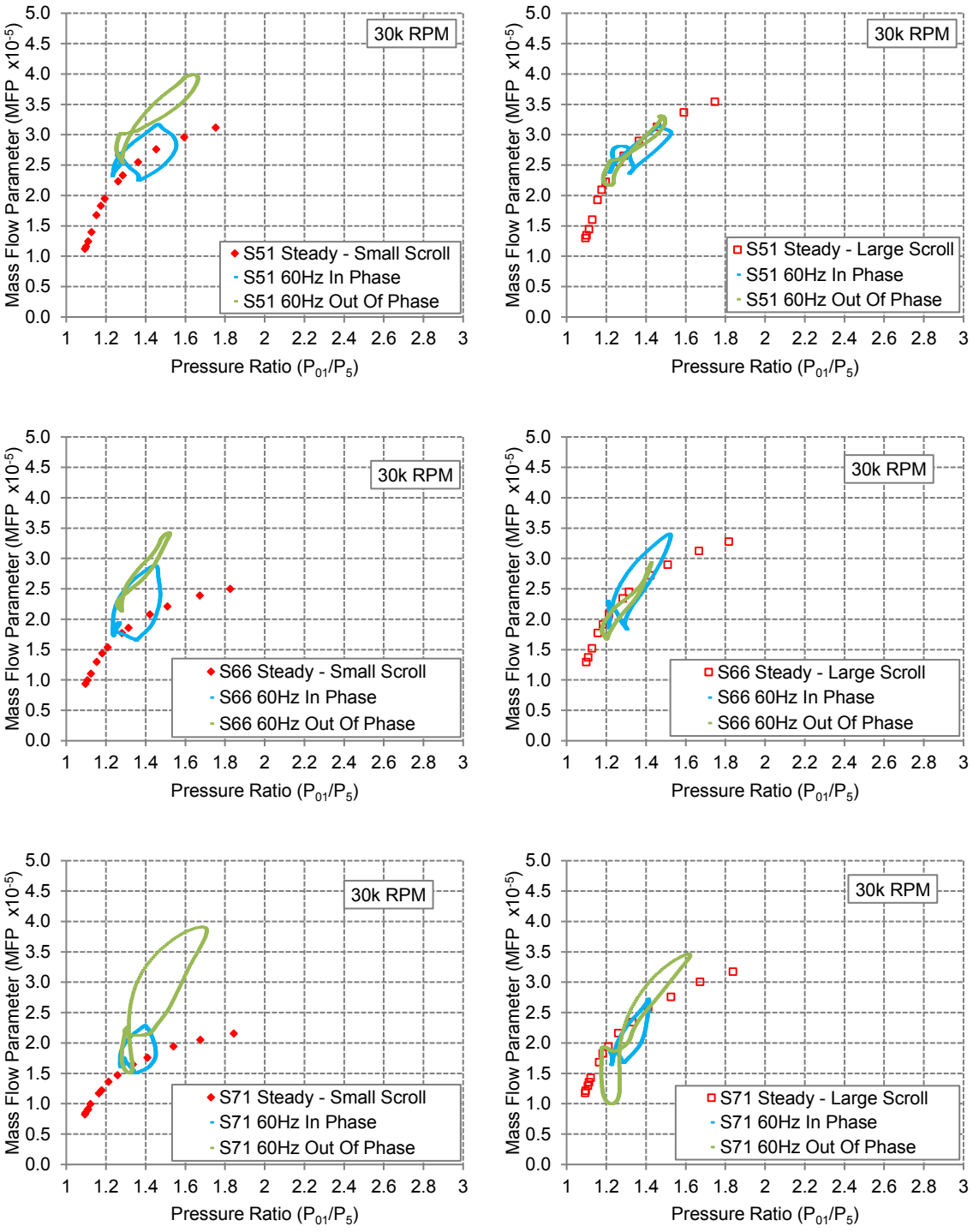


Figure 6.21 Instantaneous Swallowing Capacity for various S nozzle nozzleless configuration at 60Hz

Figure 6.22 shows instantaneous swallowing capacity comparison between nozzleless and S66. Since both settings has recorded equal swallowing capacity at 30k RPM and 48k RPM turbine speed in full admission condition, the unsteady comparison between the two will provide a fair assessment.

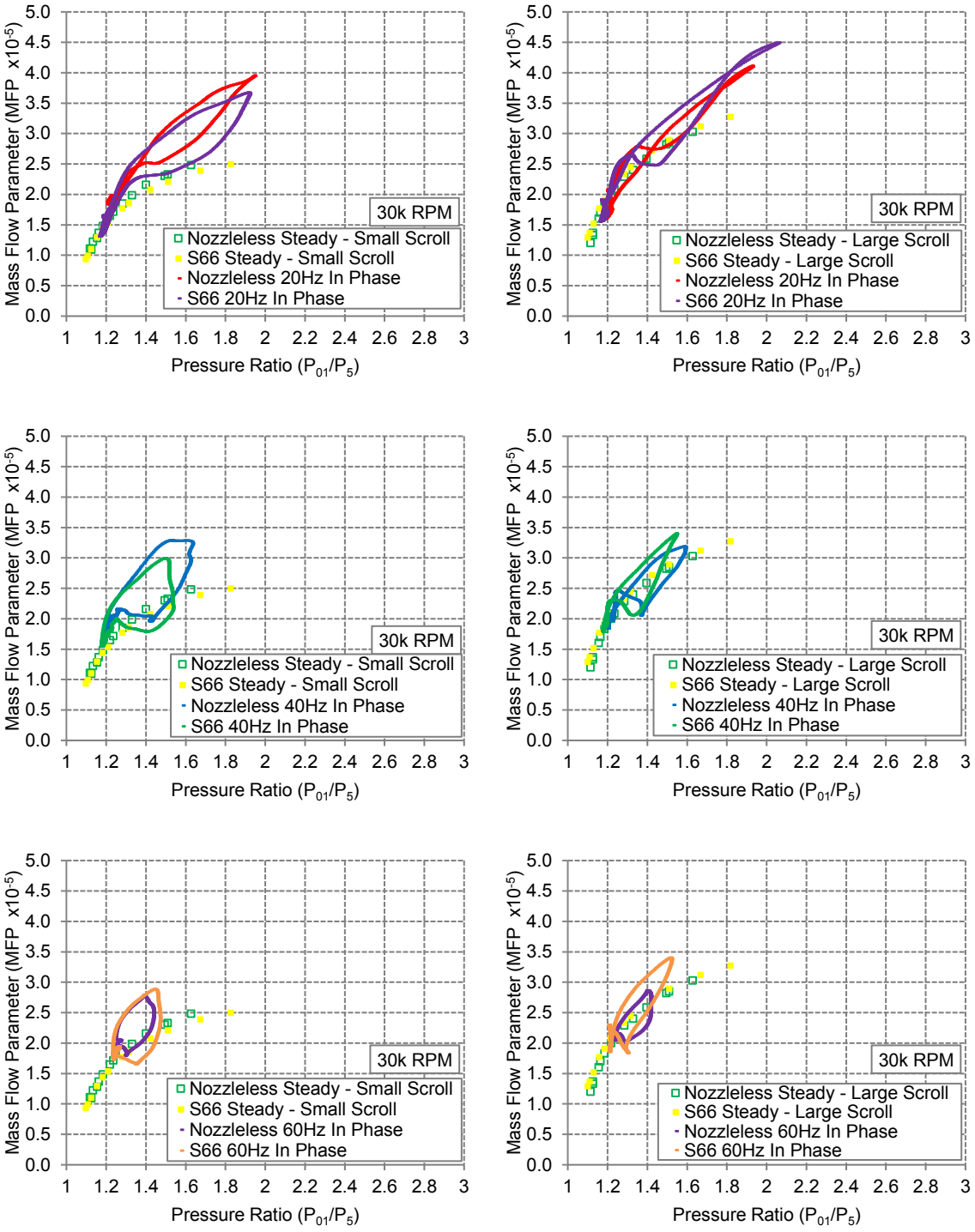


Figure 6.22 In-Phase Instantaneous Swallowing Capacity for S66 nozzle configuration

6.3 Cycle Average Parameters

Cycle average parameter are discussed in this section. The cycle average values are energy weighted cycle averaged as shown in equations (4.40) and (4.41), presented in Chapter 4. The change in cycle average efficiency of S and SL settings relative to nozzleless configuration during in phase unsteady flow for 20Hz, 40Hz and 60Hz at 30k RPM rotor speed are shown in Table 6.1, 6.2 and 6.3. The cycle average swallowing capacity difference between nozzleless and nozzle settings are also presented with the respective efficiency change. The purpose of presenting cycle average mass flow parameter difference here is to provide clarity and fair comparison when two settings are compared. Presence of nozzle vanes has apparently improved the cycle average efficiency of the asymmetric double entry turbine. This is true for all frequencies tested during in phase pulsating flow experiment. This clearly indicates the value of introducing nozzle vanes, either in the S nozzle or SL nozzle settings. S65.9 setting which has shown the minimum swallowing capacity difference with respect to nozzleless configuration, during 20Hz and 60Hz in phase unsteady test, has recorded the lowest improvement in cycle average efficiency of 1.3 and 3.3 point respectively. The minimum change in cycle average swallowing capacity agrees well with the similar mass flow characteristic portrayed by both setting under steady flow condition.

Table 6.1 Cycle Average properties at 20Hz In Phase

Configuration	Changes in Cyc. Ave. MFP. (relative to Nozzleless) (%)	Changes in Cyc. Ave. Effi. (relative to Nozzleless) (Point)
S66	-0.9	1.3
S51_L71	-9.5	1.3
S66_L71	-14.4	6.1
S66_L66	-16.4	12.6
S71_L71	-29.9	13.8

Table 6.2 Cycle Average properties at 40Hz In Phase

Configuration	Changes in Cyc. Ave. MFP. (relative to Nozzleless) (%)	Changes in Cyc. Ave. Effi. (relative to Nozzleless) (Point)
S66_L51	0.8	3.2
S66	-4.1	3.4
S66_L71	-12.5	7.3
S66_L66	-13.3	12.0
S71_L71	-24.5	13.7

Table 6.3 Cycle Average properties at 60Hz In Phase

Configuration	Changes in Cyc. Ave. MFP. (relative to Nozzleless) (%)	Changes in Cyc. Ave. Effi. (relative to Nozzleless) (Point)
S66	0.7	3.3
S66_L71	-9.6	5.1
S66_L66	-2.6	6.6
S71_L71	-19.0	9.9

The change in cycle average efficiency of S and SL settings relative to nozzleless configuration during out of phase unsteady condition for 40Hz and 60Hz at 30k RPM rotor speed are shown in Table 6.4 and 6.5. S66_S71 setting cycle average efficiency has increased by almost 2 efficiency points at 40Hz flow frequency. Unfortunately, when the unsteady flow frequency was increased to 60Hz, this configuration has recorded a drop of 2.5 efficiency points (between in phase and out of phase condition at 60Hz flow frequency). When comparing S66_L66 settings cycle average performance between in phase and out of phase condition at 40Hz pulsating frequency, the later again has recorded an improvement of 1 point. The same configuration has recorded an increase in cycle average efficiency of 7 points, when out of phase flow frequency increased to 60Hz. As for the S71_L71 settings, the out of phase cycle average efficiency has dropped by 4 points, when compared against in phase flow condition at 40Hz frequency. Surprisingly, when the pulsating flow frequency is increased to 60Hz, the S71_L71 setting out of phase cycle average efficiency has shown 9 points improvement over in phase unsteady flow.

Table 6.4 Cycle Average properties at 40Hz Out of Phase

Configuration	Changes in Cyc. Ave. MFP. (relative to Nozzleless) (%)	Changes in Cyc. Ave. Effi. (relative to Nozzleless) (Point)
S71_L66	-7.1	3.9
S71_L51	-11.6	7.0
S71_L71	-10.5	7.9
S66_L71	-6.8	9.2
S66_L66	-3.4	12.7

Table 6.5 Cycle Average properties at 60Hz Out of Phase

Configuration	Changes in Cyc. Ave. MFP. (relative to Nozzleless) (%)	Changes in Cyc. Ave. Effi. (relative to Nozzleless) (Point)
S66_L71	-9.4	2.5
S71_L66	-12.4	9.7
S71_L51	-17.3	13.0
S66_L66	-6.0	13.4
S71_L71	-20.9	18.8

6.4 Summary

Nozzleless hysteresis loop shows higher mass accumulation, especially under out of phase pulsation, with presence of significant secondary loop. This influence of wave action was reduced with the introduction of nozzle vanes in the small scroll interspace. S66 configuration swallowing capacity operating loop traces closely the equivalent steady state curve, especially at flow frequency higher than 40Hz in out of phase condition. Significant improvement was observed in the large scroll swallowing capacity operating loop. Introduction of vanes in both scrolls, however did not make any significant improvement to reduce the unsteadiness in the flow. During unsteady flow admission at 30k RPM for all frequencies showed that the nozzle configurations recorded higher cycle average efficiency than the base line nozzleless unit. Test results at 20 Hz and 40 Hz have shown higher cycle average efficiency than 60 Hz. Interestingly when nozzles were present on both scrolls the cycle average efficiency increased by almost 13 percentage point higher than nozzleless indicating the value of introducing nozzles, despite not reducing the flow unsteadiness.

CHAPTER 7

CONCLUSION

Presented in this thesis presents are the design and experimental evaluation of asymmetric double entry turbine under steady and unsteady flow condition for 3 different nozzle vane configurations; nozzleless, nozzle vane in small scroll (S nozzle vanes) and nozzle vane in both scrolls (SL nozzle vanes). The experimental finding includes the turbine performance for full, partial and unequal admission during steady flow. Additionally, it also includes the experimental evaluation and results for pulsating flow. This chapter will include the main conclusions of the thesis with suggestions for future work.

7.1 Conclusions

7.1.1 Asymmetric double entry turbine design

This novel asymmetric double entry volute was designed and fabricated with *A/r* ratio of 13.33 and 16.67 in the small and large scroll respectively. Each scroll in the volute has identical volute exit flow angle of 71°. The small scroll feeds the rotor between azimuth angle of 0° and 160°, beyond which the large scroll proceeds to deliver the exhaust gas to the remaining 200° directly into the inlet of the rotor. NACA0015 specification was used to design a novel nozzle vane with equal inlet and exit flow angle. The pivoting range of the nozzle vane between 51° and 91°, is achieved via a pivoting mechanism. Rotor used in this investigation is a mixed flow rotor consisting 12 blades with a constant inlet blade angle of +20°, a cone angle of 50° and tip diameter of 95.2 mm.

The nozzle vane interspace can accommodate 18 vanes, 9 on each scroll. These vanes are connected to a dual ring vane control unit via the pivoting mechanism. This dual ring vane control has the capability to regulate the vane angle opening in each scroll independently. An inverted link bar is used to rotate each ring to the desired vane angle, which is displayed on the indicator plate. The linear motion to extend or retract the link bar, exerts a tangential force on the pins, which is then converted into radial traverse of the siding lever.

This subsequently translates to rotation of nozzle vanes. Linear motion in the link bar is done manually at the moment.

7.1.2 Steady flow experiment

Extensive steady state performance results are presented for vane angle opening of 51°, 66° and 71°. Testing was carried out to characterise the novel turbine under various steady flow conditions; full admission, unequal and partial admission. Turbine speed tested ranges between 30k RPM and 54k RPM. The nozzleless setting has been used as the baseline for comparison with other configurations. The peak recorded efficiency for the full admission nozzleless condition was found to be 78%. When a nozzle was present in the small scroll the efficiency had a similar magnitude (77.6%); while when nozzles were present in both scrolls a lower efficiency was found (74.4%). Considering nozzles only on the small sector: as the vane angle opening changes from most open position (51°) to mid open position (71°) an increase in stage efficiency was observed. Under partial admission, the nozzleless unit showed a very significant deficit in peak efficiency: 17 points with large scroll flowing and 25 points with small scroll flowing. When nozzle vanes are introduced in the small scroll sector a similar drop was found; but when vanes were present in both scrolls the deficit during partial reduced (13.9% for the best performing configuration). During unequal admission the nozzleless and small nozzle setting displayed a symmetrical efficiency characteristic.

7.1.3 Unsteady flow experiment

Asymmetric double entry turbine was tested under pulsating flow condition at 30k RPM and 48k RPM turbine speed. Pulse generator was used to simulate the Internal Combustion Engine exhaust gas pulsation at different flow frequencies; 20Hz, 40Hz and 60Hz. Flow was introduced under two different conditions; in phase and out of phase. Nozzleless configuration was used as the baseline for S66 settings, as both displayed equal swallowing capacity under full admission condition. Results for S51 and S71, alongside four other SL nozzle vane configurations are also presented.

Nozzleless hysteresis loop shows higher mass accumulation, especially under out of phase pulsation, with presence of significant secondary loop. This influence of wave action was reduced with the introduction of nozzle vanes in the small scroll interspace. S66 configuration swallowing capacity operating loop traces closely the equivalent steady state curve, especially at flow frequency higher than 40Hz in out of phase condition. Significant improvement was observed in the large scroll swallowing capacity operating loop. Introduction of vanes in both scrolls, however did not make any significant improvement to reduce the unsteadiness in the flow. During unsteady flow admission at 30k RPM for all frequencies showed that the nozzle configurations recorded higher cycle average efficiency than the base line nozzleless unit. Test results at 20 Hz and 40 Hz have shown higher cycle average efficiency than 60 Hz. Interestingly when nozzles were present on both scrolls the cycle average efficiency increased by almost 13 percentage point higher than nozzleless indicating the value of introducing nozzles, despite not reducing the flow unsteadiness.

7.2 Future Work

This thesis has presented an extensive experimental investigation and analysis to address the objectives presented at the beginning. There are however, areas for further investigation in order to better understand asymmetric double entry turbine and the influence of steady and unsteady flow. The suggestions have been categorize into 4 parts, namely Computational Fluid Dynamics, 1 dimensional calculation, Lean nozzle vane design and Rotating nozzle vane design.

7.2.1 Computational model

The steady and unsteady results presented in this thesis, were done entirely based on experimental measurements. Postulation based on conventional double entry turbine and other computational work were used to provide explanation pertaining to the losses and flow dynamics in this asymmetric entry. In order to investigate and validate these postulations on, a fluid computational dynamics (CFD) simulation should be undertaken. A full CFD model to simulate steady and unsteady condition would provide great deal of information related to turbomachinery understanding of this novel turbine and related loss

mechanism. This numerical study would in turn provide opportunity to further improve performance of the asymmetric double entry turbine.

The steady state work presented in Chapter 5 has the potential to be the first future work in the computational analysis. Although full steady state turbine characteristic has been made available through the work of the current research, the flow physics responsible for the turbine performance is yet to be understood. Measurements obtained from experimental work were very valuable in evaluating turbine efficiency and swallowing capacity. Unfortunately, additional pressure tapping in the nozzle interspace or other region of the volute were not possible due to the presence of dual nozzle vane control mechanism module on the shroud side of the volute housing. These additional measurements have immense potential to provide further understanding of the flow within the turbine. However, CFD research work provides better flow visualization and understanding of the flow physics. What more, when the investigation involves different vane angle setting and configuration, under full, unequal and partial admission conditions; each presenting a different turbine characteristic as seen in Chapter 5.

7.2.2 Active Control Turbocharger

The experimental work in this thesis was primarily based on conventional variable geometry turbine concept. The design of dual ring allows the vane angle opening in each scroll to be unique. The results obtained should be analyzed further to survey the viability of introducing an active control turbocharger (A.C.T) system to maximize pulsating energy extraction during unsteady flow. Rajoo [7] has successfully investigated the concept of A.C.T on a single entry turbine, with an overall power and efficiency improvement of 1.6%. Although applying A.C.T concept to the asymmetric double entry turbine would create further complication in the design, it is nevertheless important, to redress the dynamic incoming flow into the turbine at various pulsation frequencies. With A.C.T coupled to the dual vane control mechanism, vane angle in each scroll can be regulated in either passive or active mode.

7.2.3 Exhaust Gas Recirculation

The ideal Exhaust Gas Recirculation (iEGR) used throughout the current work represents assumed mass flow at a turbine loading condition. Although it has provided a great deal of assessment in the current research, it really does not correspond to actual varying engine condition, apart from the pulsating flow generated by the chopper plates. It would be intriguing to explore the full potential of the turbocharger test rig at the Mechanical Engineering Department of Imperial College London, by installing additional piping upstream of the turbine inlet to replicate actual EGR operation. EGR valves can be used to vary the amount of extraction from the inner limb (connected to the small scroll) corresponding to actual engine operation. The mass imbalance created between scrolls will then require the dual nozzle vane control mechanism to respond to the dynamically changing flow into the turbine, very rapidly. Both large and small scroll rings need to be actuated by means of motor or A.C.T. as discussed above. Apart from cold flow test, the turbine can also be tested on a hot gas stand. This, with the help of necessary EGR valve and piping will require a more robust dual nozzle vane control mechanism module, owing to the high temperature of the flow.

REFERENCES

[1] European Automobile Industry: Committed To Bringing Down Emissions, *European Automobile Manufacturers' Association*, [accessed 9th December 2013].

[2] Fuel Efficiency : A Key Objective, *European Automobile Manufacturers' Association*, [accessed 9th December 2013].

[3] Baines, N. C., and Lavy, M., 1990. Flows in Vaned and Vaneless Stators of Radial-Inflow Turbocharger Turbines. *Proceedings of the International Conference on Turbocharging and Turbochargers*, **(***IMechE***)**, pp. 7-12.

[4] Martinez-Botas, R. F., Pesiridis, A., and Yang, M. Y., 2011. Overview of boosting options for future downsized engines. *Science China Technological Sciences*, 54(2), pp. 318–331.

[5] Japikse, D., and Baines, N.C., 1994. *Introduction to turbomachinery*. Norich Vt and Oxford UK: Concepts ETI.

[6] A. Kusztelan, A., Yao, Y.F., Marchant, D.R., and Wang, Y., 2011. A Review of Novel Turbocharger Concepts for Enhancements in Energy Efficiency. *International Journal of Thermal and Environmental Engineering*, 2(2), pp. 75-82.

[7] Rajoo, S., 2007. *Steady and pulsating performance of a variable geometry mixed-flow turbocharger turbine.* PhD thesis, Imperial College of Science, Technology, and Medicine - University of London.

[8] Moustapha, H., Zelesky, M.F., Baines, N.C., Japikse, D., 2003. *Axial and Radial Turbines*. Concepts ETI

[9] Heywood, J.B., 1988. *Internal Combustion Engine Fundamental*. McGraw-Hill Book Company.

[10] Logan, E. Jr., and Roy, R., 2003. *Handbook of Turbomachinery*. New York. Marcel Dekker Inc.

[11] Watson, N., And Janota, M.S., 1982. *Turbocharging the Internal Combustion Engine.* London. The Maxmillan Press Ltd.

[12] Directive 98/69/EC of the *European Parliament and of the Council* of 13 October 1998 relating to measures to be taken against air pollution by emissions from motor vehicles and amending Council Directive 70/220/EEC.

[13] Commission Regulation (EU) No. 566/2011 of 8 June 2011 amending Regulation (EC) No 715/2007 of the *European Parliament and of the Council* of 20 June 2007 on type approval of motor vehicles with respect to emissions from light passenger and commercial vehicles (Euro 5 and Euro 6) and on access to vehicle repair and maintenance information.

[14] Wei. H, Zhu. T, Shu. G, Tan. L, and Wang. Y, 2012. Gasoline engine exhaust gas recirculation – A review. *Applied Energy Journal*, 99, pp 534-544.

[15] Woolley N. H. and Hatton, A. P., 1973. Viscous flow in radial turbomachine blade passages. *Proceedings of the Institution of Mechanical Engineers Conference,* 3, pp 175-181.

[16] Muller, M. et al., 2011. The Asymmetric Twin Entry Scroll Turbine for Exhaust Gas Turbochargers. *Proceedings of the ASME Turbo Expo*, GT2008-50614.

[17] Sakai, M., Romagnoli, A., and Martinez-Botas, R. F., 2014. Performance and Flow-Field Assessment of an EGR Pulse Optimised Asymmetric Double-Entry Turbocharger Turbine. *Proceedings of the International Conference on Turbochargers and Turbocharging (IMechE*), pp. 321-332.

[18] Newton, P. J., 2013. *An Experimental and Computational Study of Pulsating Flow within a Double-entry Turbine with Different Nozzle Settings*. PhD thesis, Imperial College London.

[19] Rajoo, S., Martinez-Botas, R. F., 2008. Mixed Flow Turbine Research: A Review. *Journal of Turbomachinery*, 130, pp. 1-12.

[20] Wallace, F. J., and Pasha, S. G. A., 1972. Design, Construction and Testing of a Mixed Flow Gas Turbine. *The 2nd International JSME Symposium on Fluid Machinery and Fluids,* pp. 213–224.

[21] Baines, N. C., Wallace, F. J., and Whitfield, A., 1979. Computer Aided Design of Mixed-Flow Turbines for Turbochargers. *Journal of Turbomach*inery, 101, pp. 440–449.

[22] Abidat, M., Chen, H., Baines, N. C., and Firth, M. R., 1992. Design of a Highly Loaded Mixed Flow Turbine. *Proceedings of the Institution of Mechanical Engineers,* 206, pp. 95–107.

[23] Yamaguchi, H., Nishiyama, T., Horiai, K., and Kasuya, T., 1984. High Performance Komatsu KTR150 Turbocharger. *SAE Paper* No. 840019.

[24] Chou, C. C., and Gibbs, C. A., 1989. The Design and Testing of a Mixed Flow Turbine for Turbochargers. *SAE Paper* No. 890644.

[25] Naguib, M., 1986. Experience with the Modern RR 151 Turbocharger for High-Speed Diesel Engines. *Proceedings of the International Conference on Turbochargers and Turbocharging (IMechE)*, Paper No. 99/86.

[26] Minegashi, H., Matsushita, H., and Sakakida, M., 1995. Development of a Small Mixed-Flow Turbine for Automotive Turbochargers. *ASME International Gas Turbine and Aeroengine Congress and Exposition,* Paper No. 95-GT-53.

[27] Chen, H., and Baines, N. C., 1992. Analytical Optimization Design of Radial and Mixed Flow Turbines. *Proceedings of the Institution of Mechanical Engineers,* 206, pp. 177–187.

[28] Whitfield, A., 1990. The Preliminary Design of Radial Inflow Turbines. *Journal of Turbomach*inery, 112, pp. 50–57.

[29] Flaxington, D. And Szuzupak, D. T., 1982. Variable Area Radial-Inflow Turbine. *Proceedings of the International Conference on Turbochargers and Turbocharging (IMechE)*, Paper No. C36/82.

[30] Hawley, J. G., Wallace, F. J., Cox, A., Horrocks, R. W., and Bird, G. L., 1999. Variable Geometry Turbocharging for Lower Emissions and Improved Torque Characteristics. *Proceedings of the Institution of Mechanical Engineers, Journal of Automobile Engineering*, 213 (2), pp.145-159.

[31] Walsham, B. E., 1990. Alternative Turbocharger Systems for the Automotive Diesel Engine. *Proceedings of the International Conference on Turbochargers and Turbocharging (IMechE)*, pp. 39-50.

[32] Hiett, G. F., and Johnston, I. H., 1963. Experiments Concerning the Aerodynamic Performance of Inward Flow Radial Turbines. *Proceedings of the Institution of Mechanical Engineers*, 178 (3I(ii)), pp. 28-42.

[33] Hiett, G.F. and Palmer, R.M., 1956. D.I.G.T. radial inflow turbine – cold tests on turbine B. *Ricardo Internal Report No. 1381*, Ricardo & Co., Sussex.

[34] Maki, H., and Mori, Y., 1973. On the Study of Flow Through an Impeller of Mixed and Inward-Flow Radial Turbines. *Bulletin of the JSME*, 16 (91), pp. 81-92.

[35] Ribaud, Y., and Mischel, C., 1986. Study and Experiments of a Small Radial Turbine for Auxiliary Power Units. *ASME International Gas Turbine Conference and Exhibition,* Paper No. 86-GT-23.

[36] Reichert, A. W., and Simon, H., 1994. Numerical Investigations on the Optimum Design of Radial Inflow Turbine Guide Vanes. *ASME International Gas Turbine and Aeroengine Congress and Exposition,* Paper No. 94-GT-61.

[37] Simpson, A.T., Spence, S.W.T. and McCullough, G., 2006. Experimental And Numerical Investigation Of Varying Stator Design Parameters For A Radial Turbine. *Proceedings of the ASME Turbo Expo*, Paper No. GT-2006–90152.

[38] Simpson, A.T., Spence, S.W.T. and Ealy, J., 2009. A Numerical And Experimental Study Of The Rotor Inlet Flow Fields Of Radial Turbines Using Vaned And Vaneless Stators. *Proceedings of* the *ASME Turbo Expo*, Paper No. GT-2009–59998.

[39] Simpson, A.T., Spence, S.W.T. and Watterson, J.K., 2012. Numerical and Experimental Study of the Performance Effects of Varying Vaneless Space and Vane Solidity in Radial Turbine Stators. *Proceedings of the ASME Turbo Expo*, Paper No. GT-2012–59998.

[40] Palfreyman, D., and Martinez-Botas, R. F., 2004. The Pulsating Flow Field in a Mixed-Flow Turbocharger Turbine: An Experimental and Computational Study. *Proceedings of the ASME Turbo Expo*, Paper No. GT-2004–53143.

[41] Baets, J., Bernard, O., Gamp, T., and Zehnder, M., 1998. Design and Performance of ABB Turbocharger TPS57 with Variable Turbine Geometry. *Proceedings of the International Conference on Turbochargers and Turbocharging (IMechE)*, pp. 315 - 325.

[42] Ishino, M. And Bessho, A., 2000. Mixed-flow variable nozzle turbine. *R&D review of Toyota CRDL*, Vol. 35, No. 3, Special Issue: *Variable Geometry Turbocharger for Automotive.*

[43] Rajoo, S., and Martinez-Botas, R. F., 2008. Variable Geometry Mixed Flow Turbine for Turbochargers: An Experimental Study A. *International Journal of Fluid Machinery and Systems*, 1(1), pp. 155-168.

[44] Zweifel, O., 1945. *The spacing of turbomachine blading, especially with large angular deflection*. Brown Boveri Rev., 32, pp 12.

[45] Rajoo, S., and Martinez-Botas, R. F., 2010. Unsteady Effect in a Nozzled Turbocharger Turbine. *Journal of Turbomach*inery, 132, pp. 1-9.

[46] Benson, R. S., and Scrimshaw, K. H., 1965. An Experimental Investigation of Non-Steady Flow in a Radial Gas Turbine. *Proceedings of the Institution of Mechanical Engineers*, 180 (3J), pp. 74-85.

[47] Timmis, P. H., 1969. *A Study of the Performance of a Twin-Entry Radial Turbine Operating Under Steady and Unsteady Flow Conditions*, M.Sc Thesis, UMIST, Manchester.

[48] Wallace, F. J., Cave, P. R., and Miles. J., 1969. Performance of inward radial flow turbines under steady flow conditions with special reference to high pressure ratios and partial admission. *Proceedings of the Institution of Mechanical Engineers*, 184(1(56)), pp. 1027-1042.

[49] Pischinger, F., and Wunsche, A., 1977. The characteristic behavior of radial turbines and its influence on the turbocharging process. *12th International Congress on Combustion Engines*, Tokyo.

[50] Mizumachi, N., Yoshiki, H., and Endoh, T., 1979. A Study on Performance of Radial Turbine Under Unsteady Flow Conditions. University of Tokyo, 28.

[51] Copeland, C. D., Seiler. M., and Martiez-Botas, R. F., 2012. Unsteady Performance of a Double-entry Turbocharger Turbine with a Comparison to Steady Flow Conditions. *Journal of Turbomachinery*, 134.

[52] Copeland, C. D., Martiez-Botas, R. F., and Seilar, M., 2011. Comparison Between Steady Unsteady Double-Entry Turbine Performance Using the Quasi-Steady Assumption. *Journal of Turbomach*inery, 133(3).

[53] Copeland, C.D., 2009. *The Evaluation of Steady and Pulsating Flow Performance of a Double entry Turbocharger Turbine*. PhD thesis, Imperial College London.

[54] Wallace, F. J., and Blair, G. P., 1965. The Pulsating-Flow Performance of Inward Radial-Flow Turbines. *Gas Turbine Conference, Washington D.C*.

[55] Kosuge, H., Yamanaka, N., Ariga, I., and Wantabe, I., 1976. Performance of Radial Flow Turbines Under Pulsating Flow Conditions. *Journal of Engineering for Power (ASME)*, pp.53-59.

[56] Benson, R. S., 1974. Nonsteady Flow in a Turbocharger Nozzleless Radial Gas Turbine. *National Combined Farm, Construction & Industrial Machinery and Powerplant Meetings, Milwaukee.*

[57] Dale, A., and Watson, N., 1986. Vaneless Radial Turbine Performance. *Proceedings of the International Conference on Turbochargers and Turbocharging (IMechE),* pp. 65-76.

[58] Szymko, S., 2006. *The development of an eddy current dynamometer for evaluation of steady and pulsating turbocharger turbine performance*. PhD Thesis, Imperial College of Science, Technology, and Medicine—University of London.

[59] Dale, A., 1990. *Radial, vaneless, turbocharger turbine performance*. PhD Thesis, Imperial College of Science, Technology, and Medicine—University of London.

[60] Yeo, J., and Baines, N. C., 1990. Pulsating Flow Behavior of a Twin Entry Vanelesss Radial-Inflow Turbine. *Proceedings of the International Conference on Turbochargers and Turbocharging (IMechE)*, pp.113-122

[61] Baines, N. C., Hajilouy-Benisi, A., and Yeo, J. H., 1994. The pulse flow performance and modelling of radial inflow turbines. *Proceedings of the International Conference on Turbocharging and Turbochargers (IMechE)*, pp 209-220

[62] Acoumanis, C., Hakeem, I., Khezzar, L., Martinez-Botas, R. F., and Baines, N. C., 1995. Performance of a mixed flow turbocharger turbne under pulsating flow conditions. *International Gas Turbine and Aeroengine Congress and Exposition*, Paper No. 95-GT-210.

[63] Karamanis, N., Martinez-Botas, R. F., and Su, C. C., 2001. Mixed Flow Turbines: Inlet and Exit Flow Under Steady and Pulsating Conditions. *Journal of Turbomach*inery, 123, pp. 359–371.

[64] Szymko, S., Martinez-Botas, R.F., Pullen, K. R., McGlashan, N.R., and Chen, H., 2002. A high-speed, permenant magnet eddy-current dynamometer for turbocharger research. *Proceedings of the International Conference on Turbochargers and Turbocharging (IMechE)*, pp. 213-221.

[65] Costall, A., Szymko, S., Martinez-Botas, R.F., Filsinger, D., and Ninkovic, D., 2006. An assessment of unsteady behavior in turbocharger turbines. *Proceedings of the ASME Turbo Expo,* Paper No. GT2006-90348.

[66] Chen, H., and Winterbone, D. E., 1990. A Method to Predict Performance of Vaneless Radial Turbine Under Steady and Unsteady Flow Conditions. *Proceedings of the International Conference on Turbochargers and Turbocharging (IMechE)*, pp. 13–22.

[67] Chen, H., Hakeem, I., and Martinez-Botas, R. F., 1996. Modelling of a Turbocharger Turbine Under Pulsating Inlet Conditions. *Proceedings of the Institution of Mechanical Engineers,* Part A : Journal of Power and Energy, 210(A5), pp. 397–408.

[68] Abidat, M., Hachemi, M., Hamidou, M. K., and Baines, N. C., 1998. Prediction of the Steady and Non-Steady Flow Performance of a Highly Loaded Mixed Flow Turbine. *Proceedings of the Institution of Mechanical Engineers*, Part A : Journal of Power and Energy, 212(3), pp. 173–184.

[69] Hellstrom, F., 2008. *Numerical computations of the unsteady flow in a radial turbine*. PhD thesis, Royal Institute of Technology: KTH Mechanics, Stockholm, Sweden.

[70] Copeland, C. D., Newton, P., Martinez-Botas, R.F., and Seiler, M., 2012. The Effect of Unequal Admission on the Performance and Loss Generation in a Double Entry Turbocharger Turbine. *Journal of Turbomachinery*, 134(1).

[71] Padzillah, M.H., Rajoo, S., and Martinez-Botas, R.F., 2012. Numerical Assesment of Unsteady Flow Effects on a Nozzled Turbocharger Turbine. *Proceedings of the ASME Turbo Expo*, Paper No. GT2012-6906.

[72] Abidat, M., 1991. *Design and Testing of a Highly Loaded Mixed Flow Turbine.* PhD thesis, Imperial College of Science, Technology, and Medicine - University of London..

[73] Romagnoli, A. and Martinez-Botas, R., 2011. Performance prediction of a nozzled and nozzleless mixed-flow turbine in steady conditions. *International Journal of Mechanical Sciences, 53,* pp. 557-574.

[74] Padzillah, M.H., 2014. *Experimental and Numerical Investigation of an Automotive Mixed Flow Turbocharger Turbine under Pulsating Flow Conditions*. PhD thesis, Imperial College London.

[75] Abbott, I., Von Doenhoff, A.E., and Stivers, L.S.Jr., 1945. *Summary of Airfoil Data.* NACA-TR- 824, NASA Technical Reports Server (NTRS), U.S.A.

[76] Wan Salim, W.S.I., 2015. *Study of Externally Waste-gated Turbine Performance under Steady and Pulsating Inlet Conditions for Improved Turbocharger Matching*. PhD thesis, Imperial College London.

[77] Yahya, S.M., 1982. *Fundamentals of Compressible Flow*. New York: Wiley

[78] McCrometer Inc. 2011. *V-Cone Flow Meter Technical Brief*. California.

[79] Lomas, C. G., 1986. *Fundamentals of hot-wire anemometry*. Cambridge University press.

[80] Brunn. H. H., 1995. *Hot-wire anemometer – Principles and signal analysis*. Oxford University Press.

[81] British Standards, 1983. *Measurement of fluid flow in closed conduits*, BS 1042: Section 2.1, ISO3966-1977.

[82] Cumpsty, N. A., and Horlock, J. H., 2005. Averaging Nonuniform Flow for a Purpose. *Proceedings of the ASME Turbo Expo,* Paper No. GT2005-68081.

[83] Potter, C.M., and Wiggert, C.D., 2002. *Mechanics of Fluids*. Brooks/Cole Thomson Learning, USA.

[84] Szymko, S., Martinez-Botas, R.F. and Pullen, K.R., 2005. Experimental Evaluation of Turbocharger Turbine Performance under Pulsating Flow Conditions. *Proceedings of the ASME Turbo Expo*, Paper No. GT 2005-68878.

[85] Kirkup, L., 1994. *Experimental Methods: An introduction to the analysis and presentation of data*. Queensland, Australia, John Wiley & Sons Australia.